



SAPIENZA  
UNIVERSITÀ DI ROMA

# Measurement of the helicity of the $W$ boson with the CMS experiment

Facoltà di Scienze Matematiche Fisiche e Naturali  
Dottorato di Ricerca in Fisica – XXXI Ciclo

Candidate

Marco Cipriani  
ID number 1399000

Thesis Advisor

Prof. Shahram Rahatlou


A thesis submitted in partial fulfillment of the requirements  
for the degree of Doctor of Philosophy in Physics  
December 2018

Thesis defended on 12 February 2019  
in front of a Board of Examiners composed by:  
Prof. Marumi Kado (chairman)  
Prof. Bruno Giacomazzo  
Prof. Jerzy Kowalski-Glikman

---

**Measurement of the helicity of the W boson with the CMS experiment**

Ph.D. thesis. Sapienza – University of Rome

 2019 Marco Cipriani

Released under a Creative Commons Attribution - Non Commercial - Share Alike License

This thesis has been typeset by  $\text{\LaTeX}$  and the Sapthesis class.

Version: February 2019

Author's email: marco.cipriani@cern.ch

*Dedicated to Suor Cecilia,  
my first teacher at the primary school,  
for teaching me that learning is marvelous*

“In experimental particle physics, there exist only two possible states:  
negligible and not negligible”

**Anonymous**



# Contents

Introduction . . . . .	viii
<b>1 Measurement of the W-boson mass</b>	<b>1</b>
1.1 State of the art . . . . .	1
1.2 Production of W bosons at the LHC . . . . .	2
1.2.1 Phenomenology of hadron collisions . . . . .	2
1.2.2 Parton distribution functions . . . . .	4
1.2.3 Pileup . . . . .	6
1.2.4 Kinematics of W bosons . . . . .	6
1.3 Traditional measurement technique . . . . .	8
1.3.1 Systematic uncertainties . . . . .	9
1.3.2 The ATLAS measurement . . . . .	11
1.4 A new measurement method . . . . .	12
<b>2 Measurement of the W-boson helicity and rapidity</b>	<b>15</b>
2.1 Theoretical foundations . . . . .	15
2.2 Analysis strategy . . . . .	18
2.3 Helicity fractions . . . . .	19
<b>3 The CMS experiment at the CERN LHC</b>	<b>25</b>
3.1 The Large Hadron Collider . . . . .	25
3.2 The Compact Muon Solenoid . . . . .	27
3.2.1 Coordinate system . . . . .	27
3.2.2 Tracker . . . . .	28
3.2.3 Electromagnetic calorimeter . . . . .	29
3.2.4 Hadronic calorimeter . . . . .	29
3.2.5 Magnet . . . . .	30
3.2.6 Muon chambers . . . . .	30
3.2.7 Trigger system . . . . .	31
3.3 Physics objects reconstruction . . . . .	32
3.3.1 Particle Flow reconstruction . . . . .	32
3.3.2 Muons . . . . .	32
3.3.3 Electrons . . . . .	33
3.3.4 Jets and missing transverse energy . . . . .	34

<b>4</b>	<b>Data sample and event selection</b>	<b>35</b>
4.1	Data sample and trigger . . . . .	36
4.2	Monte Carlo samples . . . . .	37
4.3	Pileup reweighting . . . . .	38
4.4	Selection criteria . . . . .	38
4.4.1	Electrons . . . . .	39
4.4.2	Muons . . . . .	44
4.4.3	Further event selection . . . . .	45
4.5	Lepton momentum scale corrections . . . . .	46
4.6	Efficiency corrections . . . . .	49
4.6.1	Tag-and-probe method . . . . .	50
4.6.2	Efficiency scale factors . . . . .	50
4.6.3	Validation of the corrections . . . . .	54
4.6.4	Systematic uncertainties . . . . .	57
<b>5</b>	<b>Background estimation</b>	<b>61</b>
5.1	Fake-rate method . . . . .	62
5.2	Fake-rate measurement . . . . .	63
5.2.1	Electrons . . . . .	64
5.2.2	Muons . . . . .	66
5.3	Fake-rate validation . . . . .	67
5.4	Systematic uncertainties . . . . .	68
<b>6</b>	<b>Maximum likelihood fit</b>	<b>73</b>
6.1	Extraction of the W-boson helicity . . . . .	74
6.2	Signal and background templates . . . . .	78
6.3	Systematic uncertainties . . . . .	82
6.3.1	Normalization uncertainties . . . . .	83
6.3.2	Shape uncertainties . . . . .	83
6.4	W-boson double-differential cross section . . . . .	86
<b>7</b>	<b>Results and interpretation</b>	<b>89</b>
7.1	Helicity and rapidity . . . . .	90
7.2	Charge asymmetry . . . . .	94
7.3	Constraint on PDFs . . . . .	95
7.4	Double-differential cross section . . . . .	97
7.5	Results on data . . . . .	99
7.5.1	Helicity and rapidity . . . . .	103
7.5.2	Double-differential cross section . . . . .	104
7.5.3	Impacts of systematic uncertainties . . . . .	105
<b>8</b>	<b>Conclusions and perspectives</b>	<b>111</b>
	<b>Appendices</b>	<b>113</b>

<b>A</b>	<b>ECAL inter-calibration with <math>\pi^0 \rightarrow \gamma\gamma</math></b>	<b>115</b>
A.1	ECAL detector . . . . .	116
A.2	ECAL geometry . . . . .	116
A.3	ECAL energy reconstruction . . . . .	117
A.3.1	Corrections to clustered energy . . . . .	119
A.3.2	Crystals response monitoring . . . . .	119
A.3.3	Crystals inter-calibration . . . . .	120
A.3.4	ECAL selective readout algorithm . . . . .	122
A.3.5	Data formats in the ECAL software . . . . .	123
A.4	ECAL inter-calibration with the $\pi^0$ method . . . . .	124
A.4.1	The $\pi^0$ trigger stream . . . . .	125
A.4.2	Clustering algorithm . . . . .	126
A.4.3	Selection criteria . . . . .	128
A.4.4	Derivation of the inter-calibration constants . . . . .	129
A.4.5	Convergence of inter-calibration constants . . . . .	130
A.4.6	Statistical uncertainty . . . . .	132
A.4.7	Containment corrections . . . . .	134
A.4.8	Residual corrections . . . . .	141
A.5	Inter-calibration campaign using 2017 data . . . . .	143
A.6	Prospects for calibration of full Run II dataset . . . . .	145
	<b>Bibliography</b>	<b>147</b>

## Introduction

The Standard Model (SM) of particle physics is a renormalizable quantum field theory that describes matter in terms of fundamental spin-1/2 fermions (quarks and leptons) and their interactions mediated by spin-1 vector bosons. This picture is completed by the spin-0 Higgs boson, that allows to generate the mass of the other particles [1–4]. The fundamental constituents of the SM are shown in Fig. 0.1.

The elegant theoretical framework provided by the SM has been extremely successful in describing a wide range of experimental observations. At the same time, the theory has shown astonishing predictive power, representing a solid guide for the experimental community. For instance, the mediators of the weak interaction, the W and Z bosons, were theorized in the early '60s [5], but were discovered only in 1983 at CERN [6, 7]. Last but not least, the ultimate brick of the SM was laid in 2012 with the announcement of the discovery of the Higgs boson by the ATLAS and CMS Collaborations [8–10] at the CERN Large Hadron Collider (LHC).

Despite its extraordinary success, the SM is unable to explain dark matter, the masses on neutrinos, the observed matter-antimatter asymmetry or the gravitational interaction. Many theories beyond the SM have tried to cope with these issues by enriching the spectrum of known particles with new candidates, typically with expected masses ranging from the GeV to the TeV scale. The search for these particles has been pursued at the LHC in proton-proton collisions at the unprecedented center of mass energy of 13 TeV, scanning a wide energy range never explored before. Unfortunately, no direct evidence of their existence has been found so far.

However, even though the LHC has not led to the discovery of new particles beyond the SM, it has allowed to consolidate and improve our understanding of the electroweak and strong sectors. Moreover, the large amount of LHC data that is currently available allows to measure with unprecedented precision the properties of known SM particles. In the current scenario, where the reach in the energy scale is limited by the available technology and is not expected to improve significantly in the near future, precision measurements can play a key role in probing new physics beyond the SM.

This thesis describes the measurement of the helicity of W bosons as a function of the W-boson rapidity in the  $W \rightarrow \mu\nu$  and  $W \rightarrow e\nu$  decay channels. The analysis is based on a dataset of  $35.9 \text{ fb}^{-1}$  at  $\sqrt{s} = 13 \text{ TeV}$  collected in 2016 by the CMS experiment [11] at the LHC. The thesis also presents the measurement of the W-boson double-differential cross section as a function of the transverse momentum and pseudorapidity of the decay charged lepton unfolded to stable-particle level. Both measurements are carried out for each W-boson charge through a simultaneous fit and are complemented by the measurement of the charge asymmetry of W bosons produced at the LHC. All these measurements are performed using an innovative method that allows to unfold the cross section and charge asymmetry directly as a function of stable-particle-level quantities.

The experimental techniques and statistical analysis tools adopted to perform the helicity measurement have been developed to pave the way towards the precision measurement of the W-boson mass ( $m_W$ ) with CMS data. The SM prediction for  $m_W$  has an uncertainty of 7 MeV, while the uncertainty of the current experimental world average is twice as large and is dominated by theoretical systematic uncertainties.

Achieving the same precision as the prediction in a direct measurement of  $m_W$  is a challenging goal. In this respect, the results presented in this thesis hold promise to provide



stringent in-situ constraints on the main theoretical uncertainties that degrade the precision on  $m_W$  measured at hadron colliders. Therefore, some prospects regarding this topic are discussed as well.

The work presented in this thesis is organized as follows: chapter 1 offers an overview of the phenomenology of hadron collisions and provides an introduction about the W-boson production at the LHC. The theoretical motivations and the experimental techniques for the  $m_W$  measurement at hadron colliders are illustrated, and the current status and prospects are presented.

Chapter 2 introduces the measurement of the W-boson helicity and rapidity, that is the main topic of this work. It illustrates the theoretical elements on which the measurement is devised and discusses the analysis strategy.

The LHC accelerator and the CMS detector are briefly described in chapter 3. Particular emphasis is given to the electron and muon reconstruction algorithms.

Chapter 4 describes the dataset and simulated samples used for the analysis, as well as the event selection. Significant emphasis is given to the accurate measurement of the lepton reconstruction efficiency in data and simulations.

The helicity measurement requires an accurate estimation of the backgrounds. Chapter 5 provides a description of the various background sources, focusing on the data-driven technique adopted to estimate the dominant component due to multijet production.

The statistical analysis tools that are adopted to extract the parameters of interest are presented in chapter 6 and results are finally shown in chapter 7.

Eventually, the conclusions are drawn in chapter 8 and some prospects for future improvements and developments in view of the W-boson mass measurement with CMS data are discussed as well.

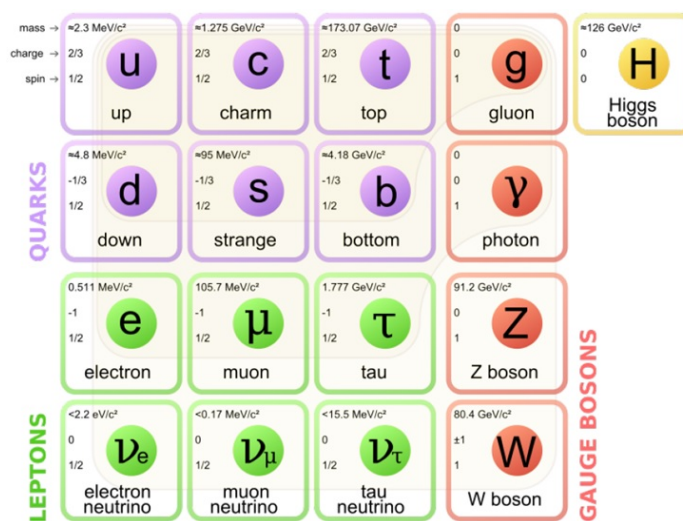


Figure 0.1. Fundamental constituents of the Standard Model.



# Chapter 1

## Measurement of the W-boson mass

The W boson is one of the fundamental particles of the SM. At the lowest order in the electroweak theory, its mass ( $m_W$ ) is related to that of the Z boson ( $m_Z$ ), the fine-structure constant ( $\alpha$ ) and the Fermi constant ( $G_F$ ) by the following equation:

$$m_W^2 \left(1 - \frac{m_W^2}{m_Z^2}\right) = \frac{\pi\alpha}{\sqrt{2}G_F} (1 + \Delta r) \quad (1.1)$$

The term  $\Delta r$  in eq. (1.1) summarizes additional contributions to  $m_W$  arising from higher order corrections that depend on the gauge couplings and the masses of heavy particles in the SM, such as the top quark and the Higgs boson. New particles and interactions, often implied by theories beyond the SM, would have a non-negligible effect on  $m_W$  through these corrections. Therefore, the precise measurement of  $m_W$  represents an extraordinary handle to test the internal consistency of the SM and probe the possible existence of new physics.

### 1.1 State of the art

The experimental world average for the W-boson mass is  $m_W = 80385 \pm 15$  MeV [12], dominated by the direct measurements carried out by the CDF and D0 collaborations at the Tevatron collider [13] in proton-antiproton ( $p\bar{p}$ ) collisions at a center-of-mass energy of 2 TeV ( $\sqrt{s} = 1.96$  TeV). The theoretical value comes from a global fit to experimental measurements of SM electroweak parameters and yields an indirect estimate of  $m_W = 80354 \pm 7$  MeV [15]. Although the experimental and theoretical values agree within  $2\sigma$ , the former has a larger uncertainty than the latter. This occurrence has motivated the need for an additional independent measurement, targeting the same precision as the prediction.

The ATLAS experiment at the CERN Large Hadron Collider (LHC) has recently measured  $m_W = 80370 \pm 19$  MeV [16] in proton-proton ( $pp$ ) collisions at  $\sqrt{s} = 7$  TeV. After combining this measurement with the previous world average, the current best value is  $m_W = 80379 \pm 13$  MeV [17], in closer agreement with the expected value. It should be noted that this combination does not fully take into account correlations between the two measurements, so that the reported value should be considered as a weighted average of the two, to be taken with a grain of salt. The CMS experiment at the LHC [11] has hitherto performed feasibility studies using events with a Z boson decaying into a pair of oppositely charged muons [18], neglecting one muon and trying to measure  $m_Z$  in a W-like manner, but no measurement of  $m_W$  has been performed with CMS data so far.

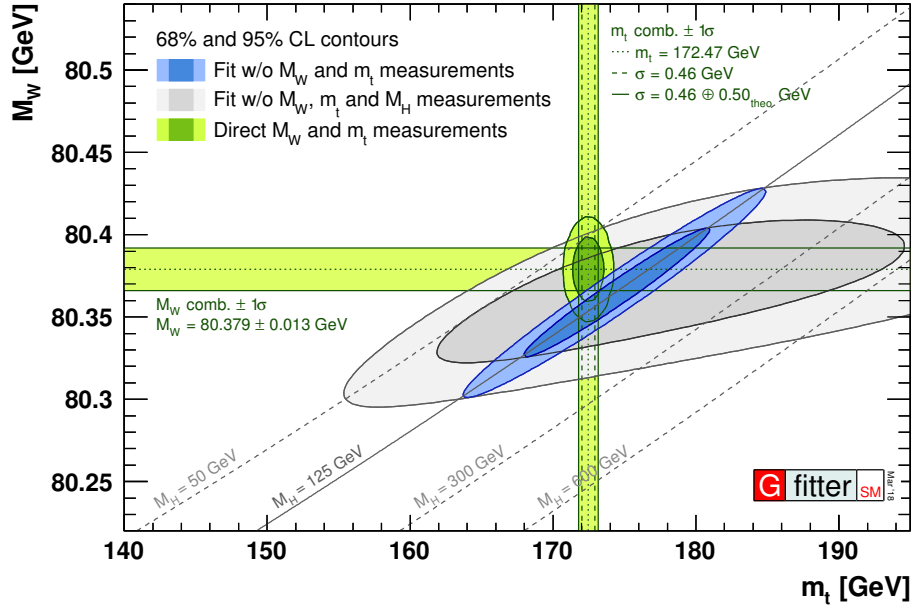


**Figure 1.1.** Relation among the masses of the top quark ( $m_t$ ), the Higgs boson ( $m_H$ ) and the W boson ( $m_W$ ) within the SM. The grey contour represents the allowed phase-space without including the direct measurements of  $m_W$ ,  $m_t$  and  $m_H$ . The direct measurements of these parameters restrict the range to the horizontal and vertical green bands and the blue ellipse.

Figure 1.1 shows the relation among the masses of the top quark, the Higgs boson and the W boson in the SM. This plot is obtained from a global fit to electroweak parameters in the SM, including also the information from direct measurements of  $m_W$  and the masses of the Higgs boson ( $m_H$ ) and the top quark ( $m_t$ ). The value of  $m_W$  in the plot represents the combination of the world average and the ATLAS measurement. The phase space allowed by the theory without considering the direct measurements of  $m_W$ ,  $m_H$ , and  $m_t$  is given by the grey contour, while the measurements of these three masses yield the horizontal and vertical green bands and the blue ellipse, respectively. The green bands and the blue region are expected to cross each other: indeed, this is the case within the uncertainties, although it is also evident that a more precise measurement of  $m_W$  might either confirm or disprove this observation. It is also interesting to note that, among the masses mentioned above,  $m_W$  is the only parameter whose theoretical uncertainty is lower than the experimental one.

## 1.2 Production of W bosons at the LHC

### 1.2.1 Phenomenology of hadron collisions

The proton is not a fundamental particle. It can be seen as a composite object made of three valence quarks (two up-quarks and a down-quark) surrounded by a sea of gluons emitted by quarks and  $q\bar{q}$  pairs from gluon splitting. Therefore, whenever two protons collide, the real interaction involves their fundamental constituents, namely quarks and gluons (generally referred to as partons).

Following the scheme in Fig. 1.2a, the interaction is characterized by a sequence of

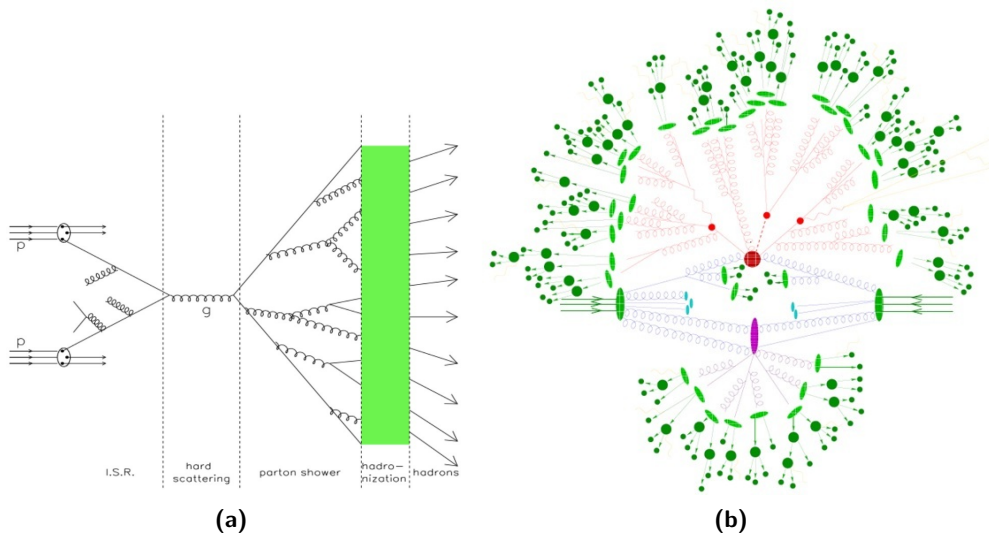


**Figure 1.2.** Scheme of parton interactions (left). The image on the right shows a sketch of a hadron-hadron collision as simulated by a Monte Carlo event generator. The red blob in the center represents the hard collision. The light green blobs represent the formation of hadrons from partons, while dark green blobs indicate the hadron decays. These processes can also be accompanied by soft photon radiation, indicated by the yellow lines. The purple blob is a second (softer) hard scattering process making the underlying event, along with the azure blobs.

different phases described by the theory of Quantum Chromodynamics (QCD):

- possible **emission of initial state radiation** (ISR) from the incoming partons, before they actually interact with each other;
- **hard scattering process**: it represents the fundamental interaction between partons, out of which other particles are produced;
- **parton shower**: in case colored particles are produced from ISR or the hard scattering process, they generate additional gluons and quarks, giving rise to a QCD shower;
- **hadronization**: as the QCD shower evolves, momentum transfers get lower until the non-perturbative regime is reached. At this point, partons recombine into color-singlet states, thus forming hadrons.

A pictorial representation of these steps is given in Fig. 1.2b, where it can be seen that the chain of reactions ends up with the formation of bunches of stable particles, either hadrons or leptons. These are experimentally observed as jets. A jet is a “spray” of particles, primarily hadrons, but also photons and leptons, produced from the hadronization. It is a composite object defined by a clustering algorithm, which groups the jet constituents according to their kinematic properties.

In some cases, a second hard scattering process can take place as well. The hard scattering is also accompanied by additional softer activity generated by the other partons in the same protons. Indeed, those partons that did not participate in the hard scattering must neutralize their color charge. They will generate additional parton showers and subsequent

hadronization. This activity is known as *underlying event* and is represented by the purple and azure blobs in Fig. 1.2b.

The center-of-mass energy in the hard scattering process ( $\sqrt{\hat{s}}$ ) is related to the one of the  $pp$  collision ( $\sqrt{s}$ ) by the following expression

$$\hat{s} = (x_1 p_1 + x_2 p_2)^2 \approx x_1 x_2 s \quad (1.2)$$

where  $p_1$  and  $p_2$  are the 4-momenta of the two colliding protons, while  $x_1$  and  $x_2$  are the fractions of these 4-momenta carried by the interacting partons. These fractions are not fixed a priori, but are distributed according to characteristic probability density functions known as parton distribution functions (PDFs).

The cross section  $\sigma_{AB \rightarrow X}$  for the production of the final state  $X$  from two colliding protons  $A$  and  $B$  can be written in terms of the parton-level cross section  $\hat{\sigma}_{ab \rightarrow X}$  involving partons  $a$  and  $b$  as:

$$\sigma_{AB \rightarrow X} = \sum_{a,b} \int_0^1 dx_a dx_b f_a(x_a, Q^2) f_b(x_b, Q^2) \cdot \hat{\sigma}_{ab \rightarrow X}(x_a, x_b, Q^2, \mu_F, \mu_R) \quad (1.3)$$

where:  $Q^2$  is the momentum transfer in the hard scattering process between partons (equivalent to  $\hat{s}$ );  $f_i$  is the PDF for parton  $i$ ;  $\mu_F$  is the factorization scale, which separates the long-distance, non-perturbative interactions from the hard scattering;  $\mu_R$  is the renormalization scale. The  $\mu_F$  and  $\mu_R$  scales are arbitrary parameters of a fixed-order QCD calculation, while at all orders of the perturbative expansion the cross section should not depend on them. The sum in eq. (1.3) runs over all the possible pairs of partons which can contribute to the process of interest, while the integral is over the fraction of the proton momenta carried by the considered partons.

The parton-level cross section  $\hat{\sigma}_{ab \rightarrow X}$  can be written as

$$\hat{\sigma}_{ab \rightarrow X} = \int d\phi_X \frac{1}{2\hat{s}} |\mathcal{M}_{ab \rightarrow X}|^2 \quad (1.4)$$

where  $\mathcal{M}_{ab \rightarrow X}$  denotes the matrix element given by the sum over all the Feynman diagrams that contribute to the process being analyzed, and  $d\phi_X$  is the differential phase space element over the  $X$  final-state particles.

It should be stressed that QCD multijet production is the process with the highest cross section at a hadron collider. Therefore, it constitutes the dominant source of background for the production of a W boson in the final state, whose cross section is several orders of magnitude lower. The difference in the cross section originates mainly from the corresponding matrix element, which is proportional to either the strong or weak coupling constants.

### 1.2.2 Parton distribution functions

The aleatoric nature of the momenta of the colliding partons due to the PDFs has some important experimental consequences:

- the center-of-mass energy is not the same for all collisions: this allows to scan a wide range of energies without the need to modify the energy of the beams (unlike the case of lepton colliders where beams are made of fundamental particles);

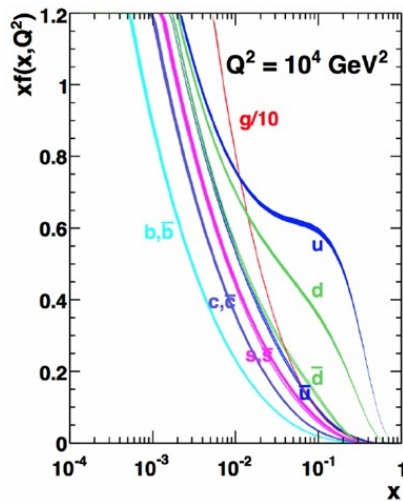


**Figure 1.3.** Example of PDFs at  $Q^2 = 10^4 \text{ GeV}^2$  for some parton flavors. The PDFs are shown multiplied by the fraction  $x$  of the proton momentum, as they tend to diverge at low  $x$ . It can be seen that valence quarks have larger probability to carry a substantial fraction of the proton momentum. It should be noted that gluons (in red) have the largest probability to initiate the hard scattering. Also, when low values of  $x$  are considered, the different (anti)quark flavors have roughly the same probability to be found inside the proton, so that the hard scattering is mainly initiated by sea partons.

- the total longitudinal momentum (along the beams) in the hard scattering process is unknown for each event: this implies that it is not possible to exploit the conservation of the total momentum between the initial and final state to set a constraint on the kinematics of the final state;

On the other hand, it should be noted that the total transverse momentum (orthogonal to the beam axis) in the initial state is zero to a very good approximation. This allows for the definition of the missing transverse energy ( $E_T^{\text{miss}}$ ) as the magnitude of the vector sum of the transverse momenta of all the detected final-state particles compatible with the interaction vertex. The  $p_T$  of an undetected neutrino in the event can thus be estimated through the  $E_T^{\text{miss}}$ , while its longitudinal momentum cannot be resolved because of the PDFs.

The functional forms of the PDFs do not descend from first principles and have to be experimentally determined. Fixing a value for  $Q^2$ , PDFs can be derived from precision measurements of cross sections in *deep inelastic scattering* processes, for example in lepton-hadron interactions, as done at HERA [19]. Given the experimental measurements of PDFs, a fit is made to obtain the model that provides the best description of data. PDFs are typically well described by polynomials. Examples of PDFs for gluons and different quark species at  $Q^2 = 10^4 \text{ GeV}^2$  (corresponding to  $\sqrt{\hat{s}} \approx m_W$ ) are shown in Fig. 1.3. There exist several sets of PDFs named after the collaborations that provided them, like CTEQ [20] or NNPDF [21].

Once the PDFs are known for a specific value of  $Q^2$ , it is possible to extrapolate them to different values of  $Q^2$  exploiting the PDFs evolution equation, known as the Dokshitzer-Gribov-Lipatov-Altarelli-Parisi (DGLAP) equation [22–24].

The choice of the model to describe the PDFs reflects into an uncertainty in the measured cross section. The PDF uncertainties have a peculiar nature, as they represent variations in a space of functions. There exist two main methods to provide a representation of these uncertainties in a more convenient form: the Hessian method and the Monte Carlo (MC) method [25].

In the former, a parametrization based on a fixed functional form is introduced, and a multigaussian probability distribution is assumed in the space of parameters. Uncertainties are then given as the inverse of the covariance matrix of this multigaussian distribution. This is usually obtained as the Hessian matrix with respect to the parameters of a figure of merit at its minimum. In the latter, PDFs are delivered as an ensemble of replicas which

provide a discrete (Monte Carlo) representation of the underlying probability distribution: uncertainties are then simply obtained as moments of this probability distribution.

The Hessian method has the advantage that the orthogonal eigenvectors of the Hessian matrix may be treated as nuisance parameters. This is particularly suited for experimental analyses, as the result of a measurement is typically obtained from a maximum likelihood fit in which uncertainties are treated as nuisance parameters.

### 1.2.3 Pileup

The picture described so far for pp collisions assumes that a single pp collision takes place. Actually, LHC beams are made of a large number of protons (order of  $10^{11}$ ) collimated in a needle-shaped bunch with transverse (longitudinal) dimension of the order of few  $\mu\text{m}$  (cm). Therefore, there is a high chance that multiple simultaneous interactions take place while the proton bunches move through each other.

Among them, only one interaction would generally generate an interesting physics event with high- $p_T$  particles: in experimental analyses, the corresponding hard-scattering interaction point is called the primary vertex. The other concurrent interactions (pileup, PU) produce low- $p_T$  particles whose energy deposits can overlap with those originating from the primary vertex, degrading the performance of the reconstruction of the interesting event. Particle reconstruction and correct assignment to the primary interaction vertex among tens of PU vertices is paramount and represents a serious challenge for the detectors.

In addition to that, detectors need a finite amount of time to read out the signals formed by the passage of particles. If this time is comparable to the time spacing between consecutive bunch crossings, there can also be a contamination from energy deposits induced by particles belonging to early or later bunch crossings. This is the source of the so-called *out-of-time* PU (distinguished from the *in-time* component that includes multiple collisions inside the same in-time bunches).

### 1.2.4 Kinematics of W bosons

At the lowest order in perturbation theory, W bosons are produced with zero transverse momentum ( $p_T^W = 0$ ) from a collision of a quark-antiquark pair. The associated Feynman diagram is reported in Fig. 1.4a. However, due to higher order corrections in the theory, a W boson is most often produced in association with one or more quarks or gluons in the final state, as shown in Fig. 1.4b. In this case, the W boson can have substantial transverse momentum, which is balanced by the vector sum of the transverse momenta of all the other particles produced in the hard scattering process. These particles are generally referred to as the *recoil*.

The most probable value of  $p_T^W$  for W bosons produced at LHC is around 5 GeV, as shown in Fig. 1.4c. From the experimental point of view, this implies that the kinematics of W-boson production is far from the real “jet regime”. Indeed, the typical  $p_T$  threshold applied to the physics objects produced by the jet clustering algorithm to have them identified as jets is few tens of GeV. As a consequence, in most of the selected events the recoil consists of low energy hadrons.

Focusing on the  $\ell\nu$  decay channel and denoting as  $\vec{h}$  the vector representing the recoil, the following relation holds:

$$\vec{p}_T^W = \vec{p}_T^\nu + \vec{p}_T^\ell = -\vec{h} \quad (1.5)$$



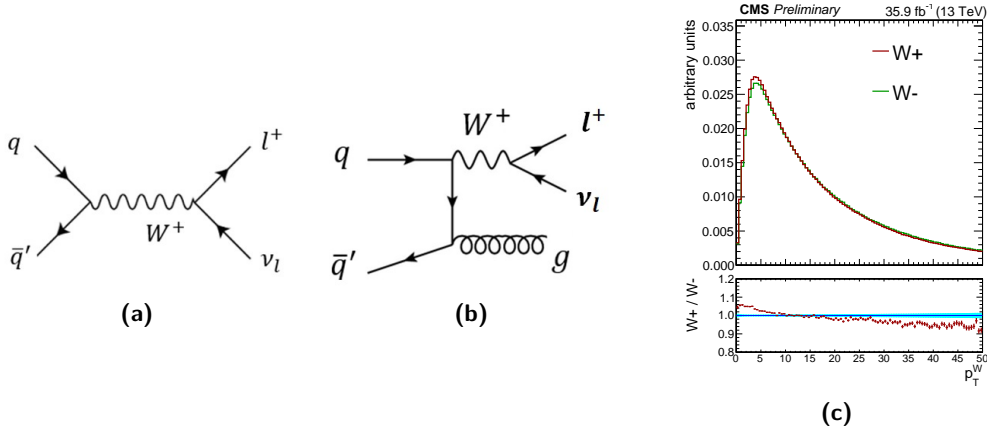


**Figure 1.4.** Feynman diagram for the production of a W boson with  $p_T = 0$  (a) and  $p_T > 0$  (b). In (c) the typical distribution of  $p_T^W$  produced at LHC is shown for both charges. The slightly different quark-composition in the initial state between the two charges results in a different  $p_T$  spectrum.

where  $p_T^\ell$  and  $p_T^\nu$  are the transverse momenta of the neutrino and the charged lepton.

Although the production is most often initiated by collisions of  $u\bar{d}$  ( $\bar{u}d$ ) for a  $W^+$  ( $W^-$ ), there is also a non-negligible contribution from second generation quarks (strange and charm quarks), as it can be inferred from Fig. 1.3. For proton collisions at a center-of-mass energy of 13 TeV, the fraction of heavy-quark-initiated production is as high as 20%. This fraction depends on the PDFs and has an impact on the  $p_T^W$  distribution, which in turn reflects into the observables used to measure  $m_W$ . For the sake of comparison, at the Tevatron collider second generation quarks contribute to approximately 5% of the total production rate, as the production is mostly initiated by valence  $q\bar{q}$  pairs. This implies that the impact of PDFs on the final  $m_W$  uncertainty is higher at the LHC than at the Tevatron.

The production and decay of W bosons at the LHC can be characterized by a 5-dimensional differential cross section according to the following expression:

$$\begin{aligned} \frac{d^5\sigma}{dp_T^2 dY dm d\cos\theta d\phi} &= \frac{3}{16\pi} \frac{d^3\sigma}{dp_T^2 dY dm} \\ &\times \left[ (1 + \cos^2\theta) + A_0 \frac{1}{2} (1 - 3\cos^2\theta) \right. \\ &+ A_1 \sin 2\theta \cos\phi + A_2 \frac{1}{2} \sin^2\theta \cos 2\phi \\ &+ A_3 \sin\theta \cos\phi + A_4 \cos\theta \\ &+ A_5 \sin^2\theta \sin 2\phi + A_6 \sin 2\theta \sin\phi \\ &\left. + A_7 \sin\theta \sin\phi \right] \end{aligned} \quad (1.6)$$

where  $p_T$ ,  $Y$ ,  $m$  are the transverse momentum ( $p_T^W$ ), rapidity ( $Y_W$ ), and mass of the W boson, respectively. The angles  $\theta$  and  $\phi$  are the lepton angles in a given W boson rest frame. For the definition of the angle, the lepton is taken as either  $\ell^-$  for the  $W^-$  or the neutrino in case of a  $W^+$ .

The cross section in eq. (1.6) is decomposed as the product of the unpolarized (angular-integrated) cross section  $d^3\sigma/dp_T^2 dY dm$  and a linear combination of nine harmonic polynomials with weights  $A_i$ . The dimensionless angular coefficients  $A_i$  depend on  $p_T^W$ ,  $Y_W$ ,  $m_W$  and represent the helicity cross sections divided by the unpolarized cross section [26]. The  $A_5$ - $A_7$  coefficients are non-zero only at order  $O(\alpha_s^2)$  and above ( $\alpha_s$  is the QCD strong coupling constant), and are small in the low- $p_T$  region compared to the others.

### 1.3 Traditional measurement technique

The measurement of  $m_W$  at hadron colliders is traditionally performed in events where a W boson decays into a charged lepton (electron or muon) and the corresponding neutrino ( $W \rightarrow \mu\nu$  and  $W \rightarrow e\nu$  events). For the sake of brevity, the charged lepton will be referred to as the lepton in the event, unless differently specified in the text.

The production of a lepton provides a clean experimental signature, helping suppress the large background component originating from QCD multijet production. Moreover, the lepton momentum can be measured with high resolution and accuracy, allowing for precision measurements of the observables reflecting the underlying value of  $m_W$ . However, the neutrino is not detected and prevents the measurement of the W-boson invariant mass on an event-by-event basis.

On the other hand, the decay of a W boson into a quark-antiquark pair would provide a final state with a pair of jets which, in principle, can be completely reconstructed. Although it is possible to define an invariant mass of the jet pair system, the resolution on the measurement of the jet momenta is generally larger than 10% and would not guarantee sufficient precision to measure  $m_W$ . Moreover, even the hadronic decay mode can produce genuine  $E_T^{miss}$  due to semi-leptonic decays of hadrons inside the jets.

Similarly, events with  $W \rightarrow \tau\nu$  are not considered. Indeed, a  $\tau$  lepton is unstable and decays within the detector in either a quark-antiquark pair (and a neutrino) or a lighter lepton and neutrinos. The former decay mode has the same experimental disadvantages of the W-boson hadronic decay mode, while the latter is relatively clean but generates larger amounts of  $E_T^{miss}$  from the production of two neutrinos as well as electrons or muons with a different kinematics than those originating directly from the decay of a W boson.

In summary, only the electron and muon final states are considered, and  $m_W$  is measured exploiting two observables defined in the transverse plane:

- the charged lepton transverse momentum ( $p_T^\ell$  or simply  $p_T$ );
- the transverse mass of the  $\ell\nu$  system (it will be referred to as the W-boson transverse mass,  $m_T$ ).

The  $m_T$  variable is defined as the invariant mass of the  $\ell\nu$  system computed with the projections of their energies and momenta in the transverse plane:

$$m_T = \sqrt{2 \cdot p_T^\ell \cdot p_T^\nu \cdot (1 - \cos\phi_{\ell\nu})} \quad (1.7)$$

where  $\phi_{\ell\nu}$  is the angle between the transverse momenta of the neutrino and the charged lepton. The definition in (1.7) is obtained with the approximation of zero mass for both the

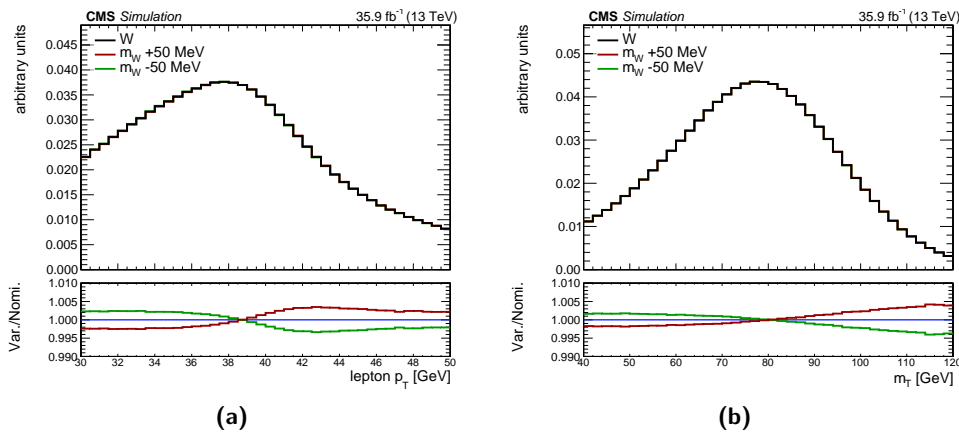


**Figure 1.5.** Kinematic distributions of  $p_T$  (a) and  $m_T$  (b) in simulated events for the  $W$ -boson mass  $m_W = 80420 \text{ MeV}$ , which is the default value in the MC, and the shifted values defined as  $m_W \pm 50 \text{ MeV}$ . Events are simulated with *aMC@NLO\_MadGraph5* with *NNPDF3.0 PDF set* (see Sect. 4.2).

decay products. An alternative expression for  $m_T$  is obtained by substituting eq. (1.5) into eq. (1.7), resulting in the following equation:

$$m_T = \sqrt{2p_T|\vec{p}_T + \vec{h}| + 2\vec{p}_T \cdot (\vec{p}_T + \vec{h})} \quad (1.8)$$

where it is explicitly shown that  $m_T$  only depends on  $p_T$  and the recoil.

The distributions of  $p_T$  and  $m_T$  present a Jacobian peak at  $m_W/2$  and  $m_W$ , respectively. For each observable,  $m_W$  is measured by comparing the measured distribution in data with several simulated templates obtained for different mass hypotheses. For each of them, a likelihood ratio is computed and the mass is evaluated as the value that minimizes the likelihood ratio distribution.

This technique requires a perfect mastering of the Monte Carlo (MC) simulations and a deep understanding of both the detector response and the theoretical uncertainties on the  $W$ -boson production and decay kinematics. In addition, one also has to consider the presence of background processes that contribute to the measured distribution in data, modifying its shape and potentially leading to a severe bias in the measurement.

### 1.3.1 Systematic uncertainties

There are several sources of uncertainties that affect the measured value of  $m_W$ , with different impact depending of the specific observable. In Fig. 1.5 it is shown that variations of 50 MeV on  $m_W$  in simulated events can induce changes on the distributions of  $p_T$  and  $m_T$  which are generally lower than 0.4%. This evidence strongly suggests that all potential sources of uncertainties should be carefully evaluated and motivates the stringent need to keep them as low as possible.

### Experimental uncertainties

Experimental uncertainties are related to the reconstruction, identification and imperfect measurements of physics object kinematics. They stem from:

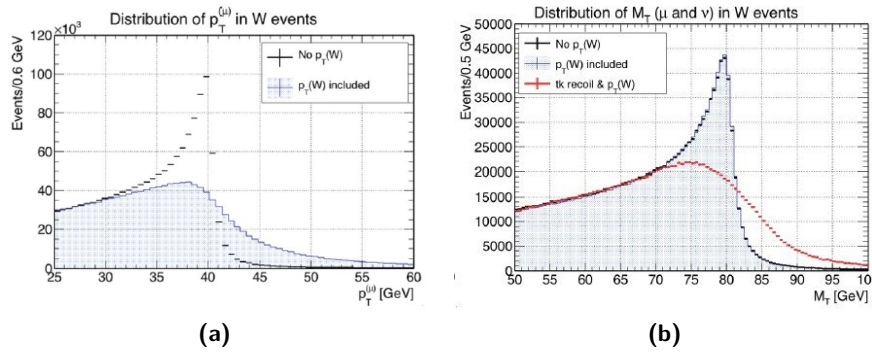


**Figure 1.6.** (a) impact of the W-boson transverse momentum ( $p_T^W$ ) on the  $p_T$  distribution of the charged lepton in the decay: the sharp jacobian peak is smeared by the spread in  $p_T^W$ . (b) impact of the energy scale and resolution of the recoil on the W-boson transverse mass distribution ( $m_T$ ). The uncertainty on  $p_T^W$  has little or no impact on  $m_T$ . The distributions with or without  $p_T^W$  are obtained using generator-level quantities, where events with no  $p_T^W$  are simulated at tree-level as in Fig. 1.4a. The red dots in Fig. 1.6b are obtained using reconstructed quantities and include the experimental resolution.

- calibration of the energy and momentum scale of the lepton;
- resolution and energy scale on the measurement of the recoil;
- contribution of background processes to selected events in data;
- difference between data and simulations in the efficiencies for the identification and selection of the lepton;

The word *scale* refers to the displacement of a measured quantity with respect to its true value. The precision on the lepton momentum scale is paramount for the measurement based on  $p_T$ , as the non-perfect calibration of the scale modifies the shape of this observable by moving the position of the Jacobian edge reflecting the measured value of  $m_W$ . In order to keep the associated uncertainty on  $m_W$  below 10 MeV, the scale must be tuned to the level of  $10^{-4}$ . The lepton efficiencies depend on the lepton  $p_T$  and position in the detector (i.e., on the lepton pseudorapidity  $\eta$ , defined in eq. (3.3)) and affect the shape of the kinematic distributions as well.

The measurement of the recoil in the low- $p_T^W$  phase space characterizing the  $m_W$  analysis suffers from worse performance regarding both the energy response and resolution with respect to the high- $p_T^W$  regime. This directly affects the measurement based on  $m_T$ .

### Theoretical uncertainties

Theoretical uncertainties arise from the imperfect knowledge of the W-boson production kinematics and are mainly related to the following items:

- the PDFs;
- the modeling of  $p_T^W$ ;
- the modeling of the  $A_i$  coefficients in eq. 1.6;

**Table 1.1.** Result of the ATLAS measurement of  $m_W$  and the corresponding uncertainty split in different experimental and theoretical sources. The dominant uncertainty is given by the PDFs, while the second largest one, denoted by “QCD unc.”, arises from QCD higher order corrections reflecting in the modeling of  $p_T^W$ .

Combined categories	Value [MeV]	Stat. Unc.	Muon Unc.	Elec. Unc.	Recoil Unc.	Bckg. Unc.	QCD Unc.	EWK Unc.	PDF Unc.	Total Unc.	$\chi^2/dof$ of comb.
$m_T$ - $p_T^\ell$ , $W^\pm$ , $e$ - $\mu$	80369.5	6.8	6.6	6.4	2.9	4.5	8.3	5.5	9.2	18.5	29/27

- missing higher orders in EWK and QCD calculations;
- the modeling of QED radiation, i.e., of photons emitted by the charged lepton.

where PDFs and  $p_T^W$  represent the main sources of uncertainty.

The PDFs affect the W-boson rapidity distribution, as they define the boost of the W boson along the beam axis. While at Tevatron the PDF uncertainties on  $m_W$  are primarily related to the finite acceptance of the detector, at the LHC they mainly arise from the subsequent uncertainties on the lepton polarizations, which in turn affect the shape of the observables. Indeed, the fact that a W boson is a spin-1 particle implies a correlation between the kinematics of the decay and the production mechanism. This point is further developed in chapter 2.

PDFs and  $p_T^W$  induce a significant smearing of the lepton  $p_T$  distribution, thus broadening the corresponding Jacobian edge, while their effect on  $m_T$  is negligible. This is illustrated in Fig. 1.6. On the other hand, the same figure also shows that  $m_T$  is primarily sensitive to the resolution on the recoil in the low- $p_T$  regime.

The experimental resolution on the recoil degrades the precision on the direct measurement of the  $p_T^W$  distribution. At the same time, the theoretical prediction of the low- $p_T$  region of the  $p_T^W$  spectrum ( $p_T^W \approx 15$  GeV) cannot rely solely on fixed-order perturbative QCD. Indeed, at such low values of  $p_T^W$ , large logarithmic terms of the type  $\log(m_W/p_T^W)$  appear in calculations, which originate from soft gluon radiation and must be treated with resummation techniques [27–31]. Hence, the low- $p_T^W$  region is affected by large theoretical uncertainties.

For these reasons, the prediction of the  $p_T^W$  distribution is generally based on the direct measurement of the Z-boson  $p_T$  spectrum and the extrapolation to the W-boson phase space through the theoretical ratio of the bosons’  $p_T$  spectra. While it is possible to measure  $p_T^Z$  with high precision due to the decay into two charged leptons, for which the  $p_T$  is measured with high resolution, the theoretical transfer factor from  $p_T^Z$  to  $p_T^W$  still suffers from many uncertainties. These arise from the differences in the production mechanism, which is particularly sensitive to the contribution of second and third generation quarks.

### 1.3.2 The ATLAS measurement

The ATLAS experiment at LHC has published the first measurement of  $m_W$  made with LHC data [16], based on  $4.6 \text{ fb}^{-1}$  collected at a center-of-mass energy of 7 TeV. The ATLAS measurement has been carried out exploiting both  $p_T$  and  $m_T$  in different categories of lepton  $\eta$  for the two distinct charges and for both the muon and electron channel.

The uncertainty on the final measurement combining all the categories is reported in Table. 1.1, also split in the experimental and theoretical sources. The total uncertainty quoted

by ATLAS is 18.5 MeV. The dominant contribution is given by the PDFs (9.2 MeV), while the second largest one, denoted by ‘‘QCD unc.’’, is mainly driven by the modeling of  $p_T^W$  (8.3 MeV). The conclusion is that the measurement of  $m_W$  at LHC is expected to be limited by the theoretical uncertainty.

The uncertainty attributed to the modeling of  $p_T^W$  strongly depends on the degree of correlation that is assumed between Z-boson and W-boson production in the extrapolation from  $p_T^Z$  to  $p_T^W$ . A certain degree of uncorrelation can be expected due to the different amounts of heavy-quark-initiated production. If the  $\mu_F$  variations were treated as correlated between all quark flavors, but uncorrelated between W- and Z-boson production, the systematic uncertainty on  $m_W$  would rise up to approximately 30 MeV.

The approach followed by ATLAS in the determination of the uncertainty associated to  $p_T^W$  consists in assuming that the contribution of the light-flavor-quark initial states between  $p_T^W$  and  $p_T^Z$  is correlated (heavy flavors are treated independently), while stating explicitly what would happen if a more conservative assumption were made. This is actually justified by the lack of a precise prescription from the theoretical community regarding how the aforementioned correlation should be treated. Nevertheless, this circumstance highlights the importance of providing in-situ constraints on the theoretical uncertainties to reduce their impact on  $m_W$ .

## 1.4 A new measurement method

The  $m_W$  measurement from ATLAS and the W-like  $m_Z$  measurement made by CMS [18] have shown that the experimental uncertainty can be kept to a sufficiently low level. On the other hand, it is now evident that improving the precision of an  $m_W$  measurement at LHC requires an outstanding effort to reduce the theoretical systematic uncertainties.

Based on the current status, it is unlikely that in the near future there will be a substantial breakthrough in the development of theoretical calculations. Therefore, it is up to the experimental community to tackle the issue and find a way to exploit at best the available data in order to improve the current measurements. This goal can be achieved by arranging the measurement in such a way to exploit in-situ constraints as much as possible to reduce the dependence on theoretical assumptions.

As detailed in eq. 1.6, the production and decay of the W boson at the LHC is completely determined by the 5-dimensional differential cross section, that depends on  $p_T^W$ ,  $Y_W$ ,  $m_W$ ,  $\cos\theta$ ,  $\phi$ . From the experimental point of view, a more suited basis to define the problem in the laboratory frame is  $p_T^\ell$ ,  $\eta_\ell$ ,  $m_T$ ,  $p_T^V$ . The latter quantities contain all the information on the underlying W-boson kinematics and can be used to extract  $m_W$  up to uncertainties associated to  $Y_W$ ,  $p_T^W$  and the PDFs.

In this respect, the strategy followed by CDF, D0 and ATLAS was based on separate fits to the  $p_T^\ell$  or  $m_T$  distributions in few bins of lepton  $\eta$  and charge, then combined together. Instead, a simultaneous measurement of  $m_W$ ,  $d^2\sigma/(dp_T^W dY_W)$  and angular coefficients can be achieved with looser theory assumptions by exploiting the intrinsic correlations with the reconstructed lepton kinematics,  $p_T$ - $\eta$ , and  $m_T$ . In fact, the CMS approach to measure  $m_W$  foresees an in-situ constraint of PDFs and W production kinematics based on a fit to the 2-dimensional  $p_T$ - $\eta$  distribution, with the possible extension in a 3-dimensional space by including the recoil.

The CMS collaboration has investigated the potential of this alternative method by

applying it to the measurement of the helicity of the W boson as a function of the W-boson rapidity. The  $Y_W$  measurement in CMS was set up during 2018 with my major contribution and constitutes the main topic of this thesis. It exploits the strong correlation between the lepton  $p_T$ - $\eta$  and the W-boson rapidity and polarization to unfold the joint  $p_T$ - $\eta$  distribution measured in data into the underlying  $Y_W$  distribution. This is achieved through a maximum likelihood fit of the  $p_T$ - $\eta$  distribution in data with several simulated signal templates obtained in bins of  $Y_W$  for each helicity state, also taking into account the presence of background processes.

The  $Y_W$  analysis shares many common tools with the  $m_W$  measurement, such as the precise measurement of the lepton reconstruction efficiencies and the background estimation techniques. It is therefore the first concrete step in the development of a comprehensive analysis framework. Moreover, as it will be shown in this thesis, the  $Y_W$  measurement provides in-situ constraints on the PDFs, representing an important breakthrough in terms of physics reach in view of the forthcoming measurement of  $m_W$ .

The analysis framework developed for the helicity measurement also allows to carry out other interesting measurements characterizing the W-boson production, such as the W-boson charge asymmetry in each helicity state. The fit was also adapted to measure the W-boson double-differential cross section as a function of the lepton  $p_T$  and  $\eta$  unfolded to generator-level (which will be described in this thesis as well).

The 2-dimensional fit based on  $p_T$ - $\eta$  to measure  $m_W$  is still dependent on the  $p_T^W$  modeling. The plan to overcome this limitation relies on the direct measurement of  $p_T^W$ , that CMS is currently carrying out using a dedicated dataset collected in 2017 during a special physics run with low intensity beams, entailing less PU and therefore allowing for a better experimental resolution on the recoil. A more refined approach will involve the extension of the  $Y_W$  measurement to include  $p_T^W$  in a simultaneous fit to the  $p_T$ - $\eta$  distribution.

At the same time, the sensitivity on  $m_W$  can be further improved by also adding the experimental measurement of the recoil in the fit. This item requires a dedicated recoil calibration, which is already being worked on using multivariate analysis techniques. The precision of the ATLAS measurement is driven by  $p_T$  due to the worse recoil resolution, about 13 GeV, that degrades the performance of the measurement based on  $m_T$ . Therefore, it is expected that improving the recoil calibration will lead to a significantly better precision on the final  $m_W$  measurement.





## Chapter 2

# Measurement of the W-boson helicity and rapidity

The PDFs affect the measurement of  $m_W$  through their impact on the W production kinematics, which in turn reflects into variations of the observable quantities in the decay. The associated uncertainty on  $m_W$  can be constrained with dedicated in-situ measurements of other correlated kinematic quantities. The PDFs define the fraction of proton momentum carried by the incoming partons in the hard scattering process. Therefore, at first order they affect only the longitudinal component of the W-boson momentum in the laboratory frame, hence its rapidity distribution ( $Y_W$ ). This implies that a precision measurement of this distribution can in turn be used to provide a constraint on the PDFs.

It was shown in [32] that the  $Y_W$  measurement has the potential of constraining the PDF uncertainty, leading to a better precision on  $m_W$ . The authors have investigated the possibility to perform the measurement differentially in the W-boson helicity states. It must be stressed that such a measurement has never been performed at the LHC in the phase space which is relevant for the  $m_W$  measurement, i.e., for  $p_T^W \lesssim 30$  GeV.

The work presented in [32] is based only on generator-level information and neglects the effect of backgrounds and several systematic uncertainties. Instead, the one presented in this thesis extends the original idea using full-simulation MC samples and comparing with data, featuring a careful estimation of backgrounds and all relevant systematic uncertainties.

### 2.1 Theoretical foundations

The method adopted to measure  $Y_W$  is based on the correlation of the W-boson production kinematics and the charged lepton in the decay. As already stated for the  $m_W$  measurement, only the decays into electrons or muons are considered. The correlation arises from the spin conservation between the initial and final state. For the sake of an example, let's consider a  $W^+$ : as shown in Fig. 2.1a, assuming that a  $W^+$  is produced from the collision of a  $u\bar{d}$  pair, most of the  $W^+$  will be produced in the same direction as the u-quark. Indeed, based on Fig. 1.3, it can be assumed that a valence quark would carry a larger fraction of the proton momentum than the antiquark on average. This results in a  $Y_W$  distribution like the one shown in Fig. 2.1b, where one can see that most of the W-bosons are produced with negative helicity ( $h_W < 0$ , or equivalently left polarization). The helicity is defined as the projection of the spin of a particle along the direction of its momentum: it is negative if the

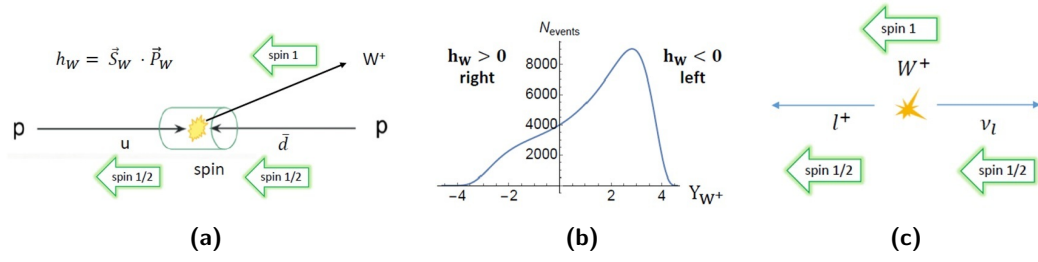


**Figure 2.1.** Scheme of W-boson production and decay (the picture refers to a  $W^+$ ). The production mechanism is illustrated on the left and results in the rapidity distribution in the middle plot (it assumes that the quark arrives from the left side of the x axis). Finally, the plot on the right shows the correlation of the spin of the W-boson and the lepton in the decay.

spin points oppositely to the direction of  $p_T^W$ . A smaller fraction of W bosons has positive helicity ( $h_W > 0$ , or equivalently right polarization).

The left and right polarization states are the most relevant in the phase space interesting for the  $m_W$  measurement, where the W-boson is mainly produced with low  $p_T^W$  ( $\lesssim 20$  GeV). The longitudinal polarization ( $h_W = 0$ ), for which the spin of the W-boson is orthogonal to its momentum, becomes important as the boson acquires higher values of transverse momentum, and is therefore a fully next-to-leading order (NLO) effect.

Similarly, following the picture in Fig. 2.1c showing the W-boson decay, spin conservation forces the leptons to be produced inside a well-defined portion of the phase space in terms of lepton  $p_T$  and pseudorapidity ( $\eta$ ). Fixing the W-boson helicity and rapidity, the lepton is emitted with  $\eta = Y_W \pm \eta_0$ , where  $\eta_0$  is the lepton pseudorapidity in the W-boson rest frame. The most probable value of  $\eta_0$  is 0.5 (the actual value also depends on  $p_T$ ) and the sign depends on the W-boson charge and helicity.

A  $W^+$  with left polarization tends to send the muon/electron in the opposite direction with respect to the boson momentum, while a  $W^+$  with right polarization sends the lepton along the same direction as its momentum. For a  $W^-$ , the opposite behaviour holds.

As a consequence, the double-differential distribution of the lepton  $p_T$  and  $\eta$  manifests characteristic patterns depending on the W-boson helicity state and rapidity. This feature arises from the V-A coupling structure of the weak interactions, which correlates the spin of the W-boson to the direction of motion of the lepton in the decay. Figure 2.2 shows the inclusive  $p_T$  vs.  $\eta$  distributions for the case of a  $W^+$  or  $W^-$  with left, right or longitudinal polarization. In addition, Fig. 2.3 shows an example of the lepton  $p_T$  vs.  $\eta$  distribution for three rapidity bins with different polarizations. Some relevant features can be observed:

- for a given helicity, the distributions have similar shapes but shift towards larger  $|\eta|$  as  $|Y_W|$  increases;
- different helicities entail different shapes for the  $p_T$ - $\eta$  distribution;
- the correlation between  $p_T$  and  $\eta$  depends on the polarization state;
- there is a significant overlap of the distributions for close  $Y_W$  bins, both for the same and for different helicities.

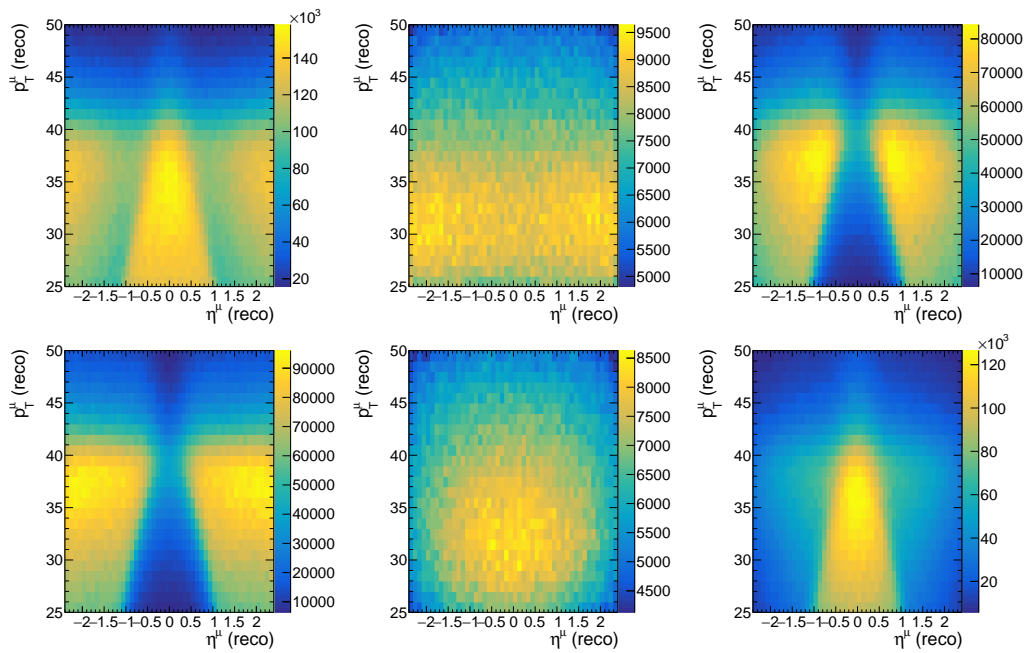


**Figure 2.2.** Simulated distributions of  $p_T$  vs.  $\eta$  of a muon from the  $W$ -boson decay. Top (bottom) plots refer to the positive (negative) charge channel. Plots from left to right are relative to the left, longitudinal, and right polarization states, respectively. These distributions are filled with the kinematic quantities of the generator-level muon passed through a simulation of the detector (“reco” label in the axis).

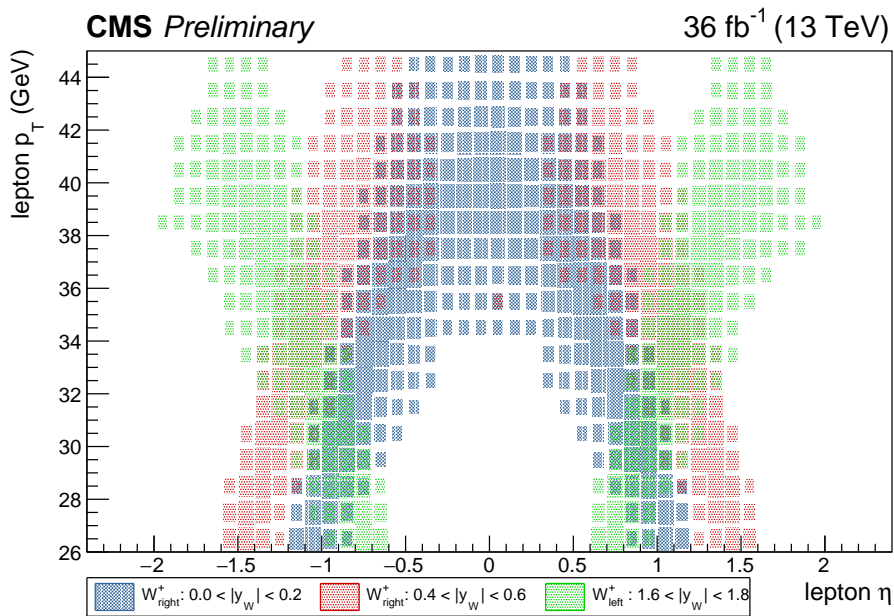


**Figure 2.3.** Comparison of the lepton  $p_T$  vs.  $\eta$  distribution for three  $Y_W$  bins for a  $W^+$ .

## 2.2 Analysis strategy

While  $Y_W$  is not directly observable due to the presence of the undetected neutrino, which prevents the reconstruction of the W-boson four-momentum, the lepton  $p_T$  and  $\eta$  can both be measured with high precision. In particular,  $\eta$  represents the position of the particle in the detector and is characterized by an excellent resolution. Therefore, the basic idea of the  $Y_W$  measurement is to split the inclusive simulated distributions shown in Fig. 2.2 in several bins of  $|Y_W|$  for each helicity state, so to obtain characteristic  $p_T$  vs.  $\eta$  distributions, which will be referred to as *templates*.

$Y_W$  is then measured by fitting the measured  $p_T$  vs.  $\eta$  distribution in data with these signal templates, taking into account the contribution from background processes as well. The fit extracts the stable-particle-level cross section of each signal component, one for each helicity state and  $Y_W$  bin, therefore yielding the  $Y_W$  distribution for each polarization state.

The symmetry in the initial state ( $pp$  collisions) reflects into a symmetric  $Y_W$  distribution with respect to  $Y_W = 0$ , which in turn implies that the lepton  $p_T$  vs.  $\eta$  templates for opposite bins in  $Y_W$  contain the same number of events. Therefore, opposite rapidity bins can be merged into a single template in the fit.

The procedure outlined above can be performed independently for each charge to obtain the measurement of the differential W-boson cross section as a function of  $Y_W$  and  $h_W$ . The predicted cross section depends on the parametrization of the PDFs implemented in the simulated samples and on the corresponding uncertainty. On the other hand, as soon as the cross section is fixed to the expected value for each bin of  $|Y_W|$ , one can recast the measurement into a direct fit of the PDFs. Performing the fit in this configuration would then result in a direct constraint on the PDF uncertainty.

The sensitivity of the analysis to the PDFs arises from the variation of the shape and normalization of the binned signal templates. Further constraining power on the PDFs can be achieved if the fit is performed simultaneously on both charges, due to the strong anti-correlation between the expected number of  $W^+$  and  $W^-$ . The anti-correlation is a consequence of the fact that the total light-quark sea PDF is well constrained by deep inelastic scattering data, while the PDFs for  $u$ -,  $d$ - and  $s$ -quarks in the sea are less precisely known [33]. Therefore, an increase in the  $\bar{u}$  PDF is at the expense of the  $\bar{d}$  PDF, entailing opposite effects in the dynamics of positively and negatively charged W bosons [34].

In addition, the analysis sensitivity is improved by the simultaneous fit in the muon and electron channel with respect to the fit in a single channel, as the two are characterized by some independent experimental systematic uncertainties.

This analysis requires:

- a good calibration of the lepton momentum scale;
- an accurate measurement of the reconstruction efficiencies in data and MC;
- a robust control of the background processes;
- a fitting framework that can reliably extract the parameters of interest and the associated uncertainty;
- a careful evaluation of the systematic uncertainties.

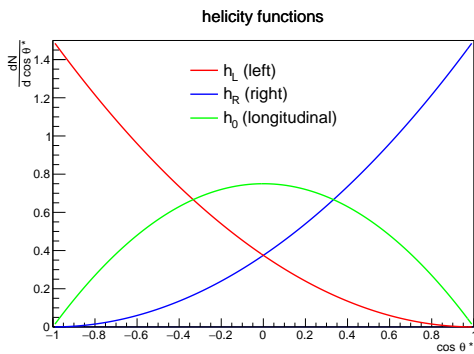


**Figure 2.4.** Helicity functions  $h_i$  for left-handed, right-handed, and longitudinal  $W$  bosons, shown with a red, blue and green line, respectively.

These aspects of the analysis are shared with the  $m_W$  measurement, although the precision that needs to be achieved is generally not as high. The aforementioned items will be discussed in next chapters.

## 2.3 Helicity fractions

The experimental setup to extract the measurement of  $Y_W$  requires signal templates obtained for each  $W$ -boson helicity state independently. However, the helicity is a piece of information that is generally not available in Monte Carlo (MC) simulations. Therefore, one has to devise a general procedure to extract this information from any MC sample starting from other quantities available in the simulations. It is possible to accomplish this task by exploiting the analytical expression of the  $W$ -boson cross section in the Collins-Soper (CS) frame [35].

The cross section is written as a function of the  $W$ -boson three helicity fractions and the decay angle  $\theta^*$  of the lepton, which is defined with respect to the axis that bisects the angle between the direction of the quark and the reversed direction of the antiquark. In this context, the word *lepton* refers to  $\mu^-/e^-$  in the negative charge channel or the neutrino for the positive charge case. In the case where  $p_T^W = 0$ , the axis used to define the angle is oriented as the  $W$ -boson momentum.

The analytical expression of the differential cross section in the CS frame is given by the following relation:

$$\frac{1}{\sigma} \frac{d\sigma}{d\cos\theta^*} \simeq \frac{3}{8}(1 + \cos\theta^*)^2 \cdot f_L + \frac{3}{8}(1 - \cos\theta^*)^2 \cdot f_R + \frac{3}{4}\sin^2\theta^* \cdot f_0 \quad (2.1)$$

where the coefficients  $f_L, f_R, f_0$  represent the aforementioned helicity fractions for the left, right, and longitudinal polarization, respectively [36]. It can be seen that the left polarization is maximal for  $\theta^* = 0$ , which corresponds to the case where the momenta of the  $W^+$  ( $W^-$ ) and the neutrino (charged lepton) are aligned, as expected based on the spin orientation.

The helicity functions  $h_i$ , i.e. the terms containing  $\cos\theta^*$  for each helicity state, are shown in Fig. 2.4. Therefore, by fitting the  $\cos\theta^*$  spectrum of the inclusive MC sample it is possible to compute the three  $f_i$  parameters. Once they are known, each event can be reweighted three times to obtain three pure samples of right-handed, left-handed, and longitudinally polarized  $W$ -bosons.

In order to fit the distribution of  $\cos\theta^*$ , it is imperative to implement a consistent stable-particle-level definition of the charged lepton. The so-called pre-FSR lepton definition is used, which represents the lepton before the emission of final-state radiation (FSR), also

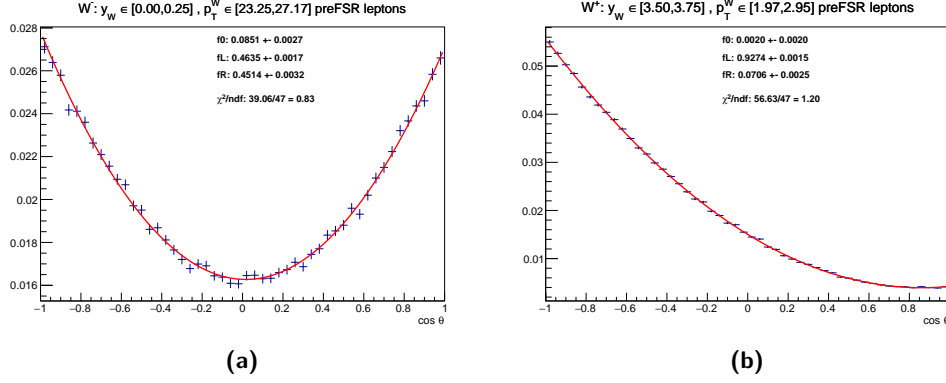


**Figure 2.5.**  $\cos \theta^*$  spectrum for  $W^-$  at low rapidity and high  $p_T^W$  (left) and for  $W^+$  at high rapidity and low  $p_T^W$ . The y axis is in arbitrary units.

known as Born lepton definition. The neutrino to be associated to the W-boson decay is chosen as the hardest neutrino in the simulated event.

There are two fundamental points to observe:

- the helicity fractions in eq. (2.1) strongly depend on both  $p_T^W$  and  $Y_W$ ;
- the  $\cos \theta^*$  distribution must be derived from a set of simulated events without any kinematic selection applied at generator level, even prior to the passage of the particle through the simulation of the detector, in order not to bias the stable-particle definition.

The former implies that the helicity fractions have to be derived differentially in  $p_T^W$  and  $Y_W$ . The reason for the latter is that any requirement on the generated charged leptons in terms of  $p_T$  or  $\eta$  would break the theoretical relation of eq. (2.1) and distort the shape of  $\cos \theta^*$ .

An example of two  $\cos \theta^*$  distributions in two bins of  $Y_W$  and  $p_T^W$  are shown in Fig. 2.5. The left plot shows a fit to the  $\cos \theta^*$  spectrum for  $W^-$  with low  $Y_W$  and high  $p_T$ , while the right plot shows a fit to a  $\cos \theta^*$  spectrum at high value of  $Y_W$  and low  $p_T$  for  $W^+$ . As already mentioned, the helicity fractions have a strong dependence on the W-boson kinematics. In particular, at low  $p_T^W$  the longitudinal polarization is almost negligible (Fig. 2.5b), while it increases to substantial values at higher transverse momentum. Similarly, as expected from Fig. 2.1b, the left and right helicity fractions are very similar at low values of  $Y_W$ . Indeed,  $f_R$  and  $f_L$  are predicted to be identical at  $Y_W = 0$ , which is consistent within the uncertainties of the fit in Fig. 2.5b.

The distributions of the helicity fractions as a function of  $p_T^W$  and  $Y_W$  are reported in Fig. 2.6. It can be observed that  $f_0$  increases towards higher  $p_T^W$  and is relatively flat as a function of  $Y_W$ , while  $f_R$  and  $f_L$  are less dependent on  $p_T^W$  but change significantly as a function of  $Y_W$ . These fractions were computed separately for the electron and muon decay channel, and no significant difference was observed between the two cases. This evidence supports the goodness of the pre-FSR lepton implementation, which is expected to provide a flavor-independent definition of the lepton.

An alternative method to compute the helicity fractions relies on the relation between these fractions and some of the angular coefficients characterizing the W-boson differential

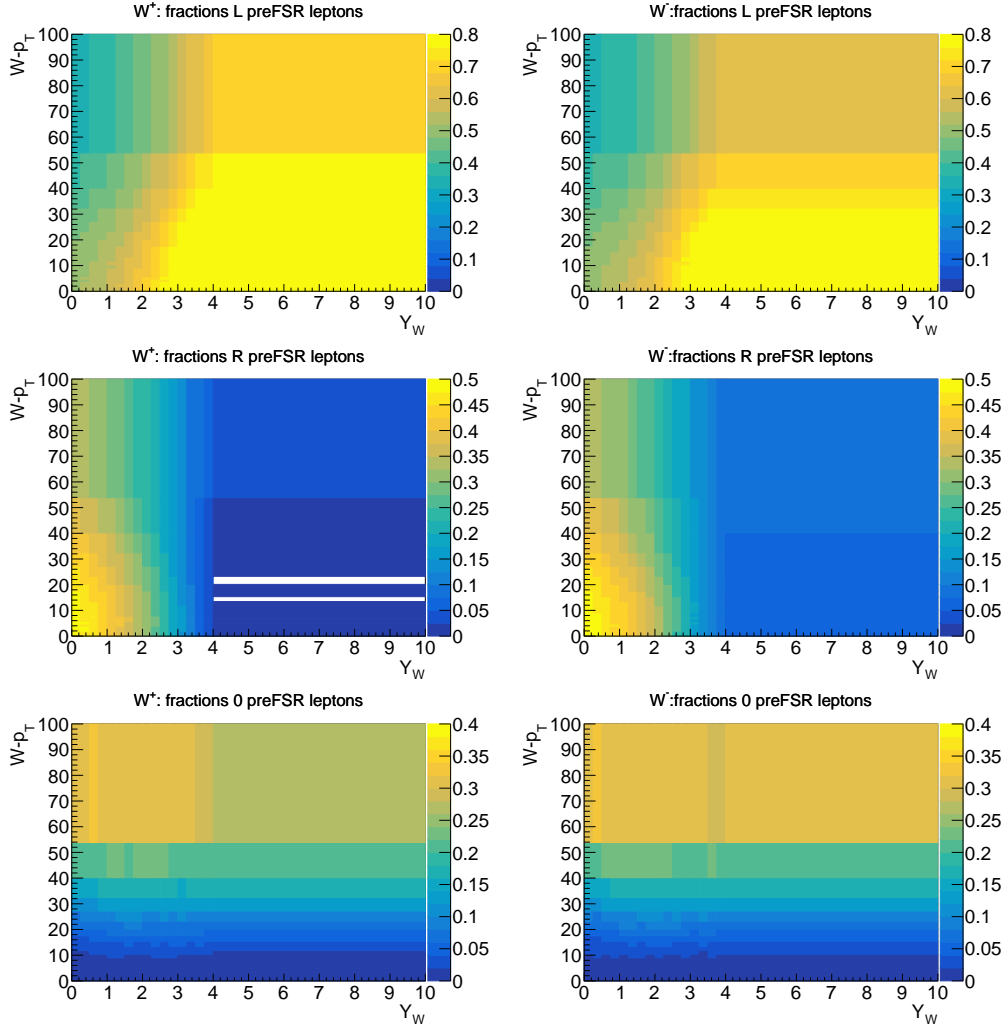


**Figure 2.6.** Helicity fractions for  $W^+$  (left) and  $W^-$  (right) as a function of  $Y_W$  and  $p_T^W$ , for left, right, and longitudinal polarization (from top to bottom, respectively).

cross section reported in eq. (1.6):

$$\begin{aligned}
 f_L(Y_W, p_T^W) &= \frac{1}{4} [2 - A_0(Y_W, p_T^W) + A_4(Y_W, p_T^W)] \\
 f_R(Y_W, p_T^W) &= \frac{1}{4} [2 - A_0(Y_W, p_T^W) - A_4(Y_W, p_T^W)] \\
 f_0(Y_W, p_T^W) &= \frac{1}{2} A_0(Y_W, p_T^W)
 \end{aligned} \tag{2.2}$$

Therefore, the helicity fractions can be obtained from the  $A_0$  and  $A_4$  coefficients as a function of  $Y_W$  and  $p_T^W$ .  $A_0$  and  $A_4$  can be derived through the following analytical formulas:

$$\begin{aligned}
 A_0 &= \frac{2}{3} + \frac{10}{3} \langle 1 - 3 \cos^2 \theta^* \rangle \\
 A_4 &= 4 \langle \cos \theta^* \rangle
 \end{aligned} \tag{2.3}$$

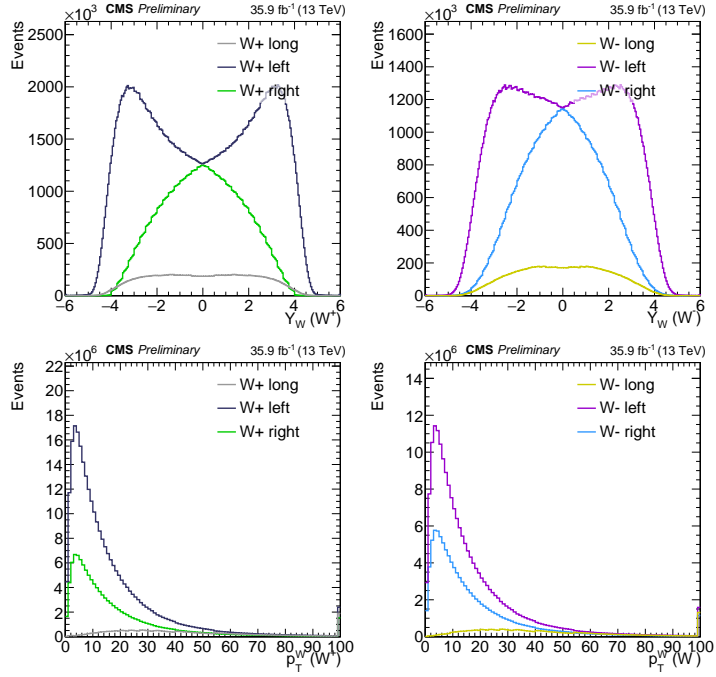


**Figure 2.7.**  $W$ -boson  $Y_W$  (top) and  $p_T^W$  (bottom) for each helicity states for  $W^+$  (left) and  $W^-$  (right).

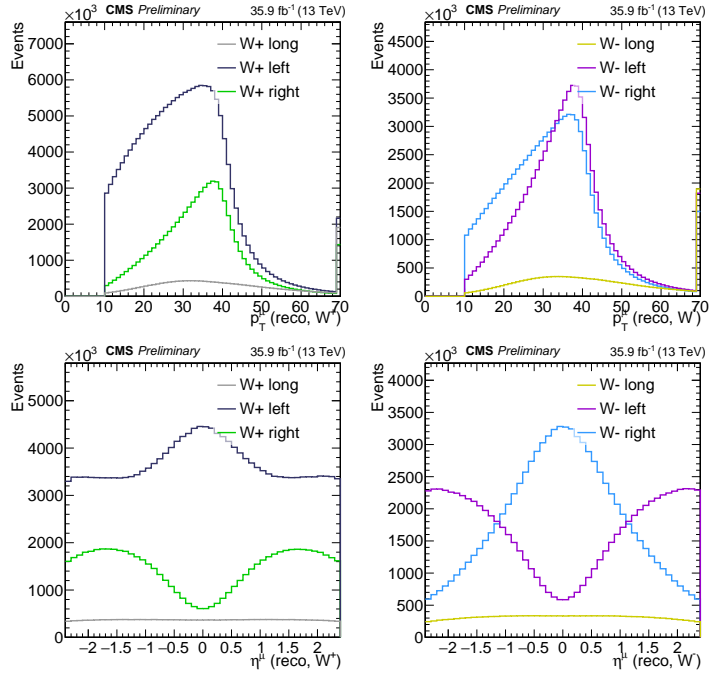


**Figure 2.8.** Distributions of the reconstructed muon  $p_T$  (top) and  $\eta$  (bottom) for  $W^+$  (left) and  $W^-$  (right), split in the helicity state.



where  $\langle \cdot \rangle$  denotes the mean of the distribution of the argument. Both methods were used to derive the helicity fractions and no significant difference was observed in the results.

The helicity fractions can be used to build any kinematic distribution exclusive with respect to the W-boson helicity state. This is accomplished by reweighing simulated events according to the weight defined in the following expression:

$$\omega_i = \frac{f_i \cdot h_i(\cos \theta^*)}{\sum_i f_i \cdot h_i(\cos \theta^*)} \quad (2.4)$$

Some relevant distributions are shown in Fig. 2.7 for W bosons, while Fig. 2.8 shows some distributions for the charged lepton in the muon decay channel. The former are obtained without applying any kinematic selection, while the latter are produced after applying some identification criteria to the reconstructed lepton (these will be outlined in chapter 4). When talking about MC, a reconstructed lepton represents the generated lepton passed through a simulation of the detector. This includes any possible kinematic selection or identification criteria implemented in the reconstruction algorithm to identify a particle based on the outputs of the detector. For instance, an object can be reconstructed only inside the geometrical acceptance of the detector. Also, as shown in Fig. 2.8, the candidate lepton is required to have  $p_T > 10$  GeV to be identified as a muon.

The selection requirements on the reconstructed lepton modify the fraction of events belonging to each helicity state. For example, the majority of the events in the negative charge case prior to any selection originates from  $W^-$  with left polarization, while the relative fraction of left and right W bosons becomes almost identical after the selection (see top right plot in Fig. 2.8). This can be easily explained by looking at the bottom right plot in Fig. 2.8: a large fraction of leptons from a left-handed  $W^-$  is produced with  $|\eta| > 2.4$ , outside the detector acceptance.

It should be highlighted that the finite detector acceptance partially limits the potential of the measurement. Indeed, signal templates obtained for W bosons produced with  $Y_W \gtrsim 3.0$  tend to be depleted due to the fact that a large fraction of the corresponding leptons are produced outside acceptance and therefore cannot be detected.



## Chapter 3

# The CMS experiment at the CERN LHC

This chapter provides a brief description of the Large Hadron Collider (LHC) accelerator facility and the CMS experiment.

### 3.1 The Large Hadron Collider

LHC is the largest and most powerful particle accelerator at CERN and in the world. It is located around 100 m below the surface across the French-Swiss border, close to Geneva, and occupies the 27 km long tunnel that was previously hosting the LEP collider.

Inside the accelerator, two beams made of thousands of bunches of protons travel in opposite directions in separate beam pipes, kept at ultrahigh vacuum. The trajectory followed by protons is bent by strong magnetic fields of up to 8.33 T generated by superconducting electromagnets operating at 1.9 K.

Protons are produced from ionized hydrogen and are accelerated up to 50 MeV by the LINAC2; then, they are injected in the first ring (the Booster) where they reach 1.4 GeV; afterwards, they pass into the Proton Synchrotron (PS) and Super Proton Synchrotron (SPS), which accelerate them up to 26 and 450 GeV, respectively; finally, they enter the LHC beam pipe, where they can be progressively accelerated up to the maximum design energy of 7 TeV, albeit the highest energy reached so far was 6.5 TeV. Proton collisions take place in four interaction points and are recorded by 4 experiments: ATLAS (A Toroidal LHC ApparatuS), CMS (Compact Muon Solenoid), LHCb (Large Hadron Collider bPhysics), ALICE (A Large Ion Collider Experiment). Figure 3.1 shows the complex of accelerators used to inject protons inside the LHC.

Physics collisions started in 2010 at a center of mass energy of 7 TeV (3.5 per beam), brought up to 8 TeV in 2012. Data taking operation lasted until the end of 2012. This phase, named *Run 1*, has led to the discovery of the Higgs boson, officially announced on the 4th of July 2012. Data taking started again in 2015 at a center of mass energy of 13 TeV and went on up to the end of 2018. This phase is known as *Run 2*. During *Run 2*, the intensity of collisions has reached unprecedented luminosity values, above  $10^{34} \text{ cm}^{-2} \text{ s}^{-1}$ , with time spacing between proton bunches of 25 ns (resulting in a collision frequency of 40 MHz).

The instantaneous luminosity is an important figure of merit for a particle accelerator. It

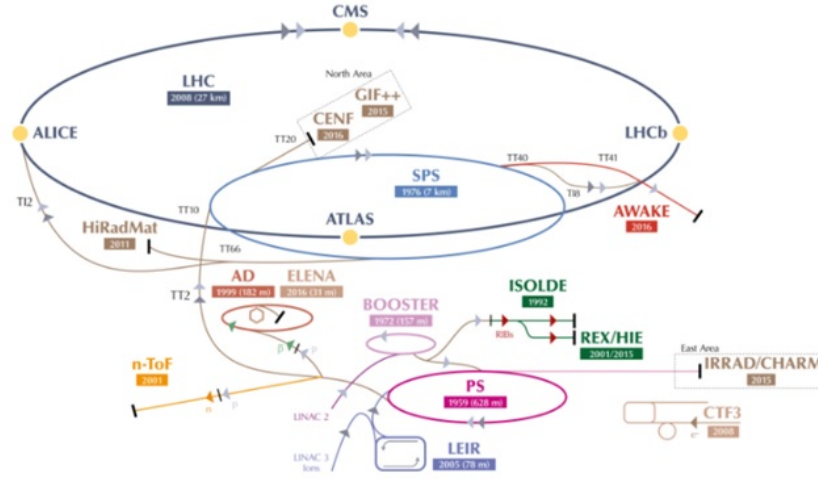


Figure 3.1. LHC injection scheme.

depends on the properties of the beams according to the following relation:

$$\mathcal{L} = \frac{n^2 f k}{4\pi \zeta_x \zeta_y} \quad (3.1)$$

where

- $n$  is the number of protons inside each bunch (of the order of  $10^{11}$ , but potentially different for the two bunches);
- $k$  is the number of bunches forming the beams (of the order of  $2 \cdot 10^3$ );
- $f = 1.1 \times 10^4 \text{ Hz}$  is the revolution frequency of a single bunch;
- $\zeta_x$  and  $\zeta_y$  represent the RMS of the transverse dimensions of a bunch along the  $x$ - and  $y$ -axis ( $\sqrt{\zeta_x \zeta_y} \approx 15 \mu\text{m}$ , while the spread along the  $z$ -axis is of the order of some cm);

The revolution frequency is known with high precision. The number of particles is continuously measured with beam current transformers which reach an accuracy of about 1% for the LHC nominal beam parameters. The transverse dimensions of the beams are measured with dedicated Van Der Meer scans [37], which consist in scanning the two beams through one another in the transverse plane of the detector. This technique allows to derive an absolute calibration for the luminosity scale.

Given a physics process with cross section  $\sigma$ , the expected number of such events produced during collisions is given by the product of the cross section and the instantaneous luminosity integrated over the time of data taking, namely:

$$N = \sigma \int dt \mathcal{L} = \sigma L \quad (3.2)$$

The total integrated luminosity  $L$  delivered by the LHC in  $pp$  collisions at 13 TeV amounts to more about  $180 \text{ fb}^{-1}$ . The fraction collected during 2016 operations is around  $36 \text{ fb}^{-1}$ .

The proton-proton cross section at 13 TeV at the LHC amounts to about  $80 \text{ mb}$  ( $1 \text{ b} = 10^{-24} \text{ cm}^2$ ). Assuming a beam luminosity of  $10^{34} \text{ cm}^{-2} \text{ s}^{-1}$  and given the bunch crossing

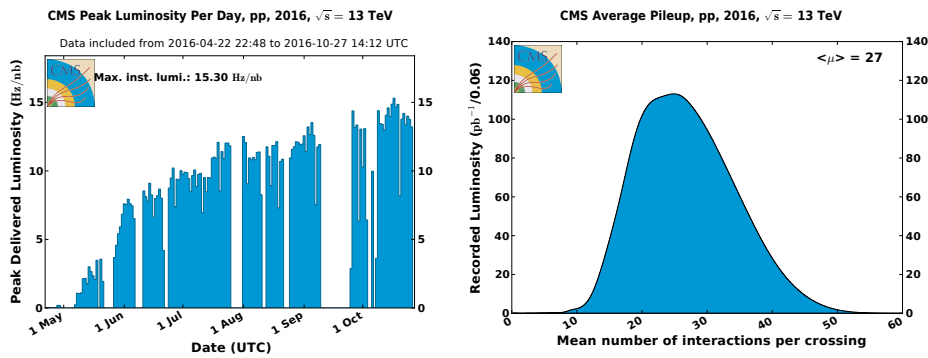


**Figure 3.2.** (left) Peak instantaneous luminosity on a day-by-day basis,  $1 \text{ Hz/nb} = 10^{-33} \text{ cm}^{-2} \text{ s}^{-1}$ . (right) Mean number of interactions per bunch crossing for the 2016 pp run at 13 TeV. The cross section is taken to be 80 mb.

frequency of 40 MHz, eq. (3.2) yields about 20 proton-proton simultaneous interactions for each bunch crossing. Figure 3.2 reports the instantaneous luminosity delivered by the LHC and the mean number of pileup interactions per bunch crossing during 2016. The instantaneous luminosity increased steadily during the year, leading to higher PU, as visible from the asymmetry of the PU distribution.

Actually, the PU is not constant even during physics runs, but decreases as a function of time during a fill, which denotes the time period between the moments when the beams are injected in the accelerator and have reached stable conditions, and when they are dumped. Indeed, proton bunches are slowly depleted as protons interact during collisions. The typical lifetime of beams at LHC is of the order of 10 hours.

## 3.2 The Compact Muon Solenoid

The Compact Muon Solenoid (CMS) is a general purpose detector designed to discover the Higgs boson and search for new physics beyond the SM [11]. Particles produced in the collisions interact in different ways with the several layers of the detector according to their nature. Starting from the interaction vertex, the CMS detector comprises:

- the tracker;
- the electromagnetic and hadronic calorimeters;
- the superconducting solenoid;
- the muon detectors.

The inner structure of the CMS detector is shown in Fig. 3.3.

### 3.2.1 Coordinate system

CMS uses a right-handed coordinate system with the origin at the nominal interaction point in the centre of CMS. The  $x$ -axis points to the center of the LHC, the  $y$ -axis points vertically up (perpendicularly to the LHC plane) and the  $z$ -axis along the anticlockwise beam direction.

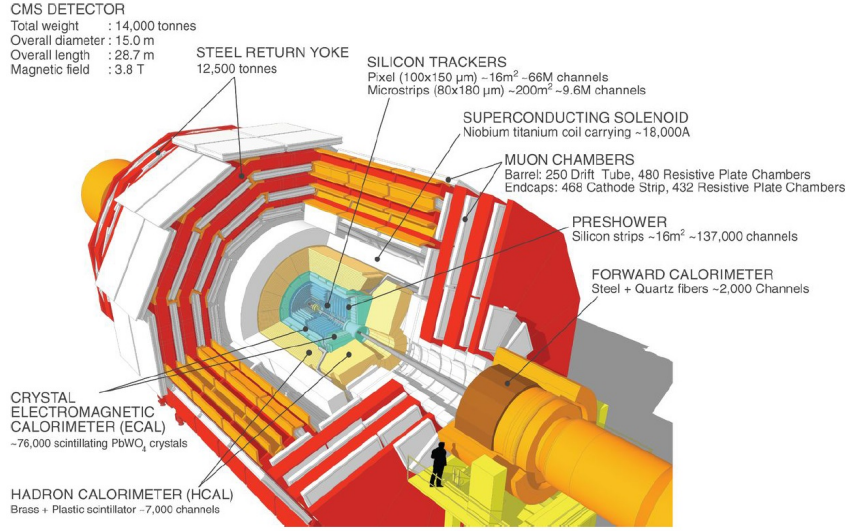


**Figure 3.3.** Inner structure of the CMS detector.

The azimuthal angle ( $\phi$ ) is measured in the  $xy$ -plane from the positive side of the  $x$ -axis, such that  $\phi = \pi/2$  along the positive side of the  $y$ -axis, while the polar angle ( $\theta$ ) is measured from the  $z$ -axis. The angle  $\theta$  allows to define projection of the energy  $E$  and momentum  $\vec{p}$  on the transverse plane (orthogonal to the  $z$ -axis) as  $E_T = E \sin \theta$  and  $\vec{p}_T = \vec{p} \sin \theta$ . For massless objects,  $E_T$  and the magnitude of  $\vec{p}_T$  (denoted as  $p_T$ ) are often used as synonyms.

The angle  $\theta$  is used to define the pseudorapidity ( $\eta$ ) of a particle as

$$\eta = -\ln \tan \frac{\theta}{2} \quad (3.3)$$

The  $\eta$  coordinate is widely used at LHC: it represents a zoomed version of the angle  $\theta$  and is more suited to quantify the angular distribution of particles, especially for  $\theta \rightarrow 0$  and  $\theta \rightarrow \pi$ . From eq. (3.3) one can observe that  $\eta$  is 0 for  $\theta = \pi/2$  and tends to  $\infty(-\infty)$  for  $\theta \rightarrow 0(\pi)$ . In addition, in the kinematic regime where the mass of a particle can be neglected (which is often the case at LHC), the pseudorapidity tends to the rapidity  $Y$ , which is a relativistic kinematic variable defined as

$$Y = \frac{1}{2} \ln \frac{E + p_z}{E - p_z} \quad (3.4)$$

where  $E$  and  $p_z$  represents the energy of the considered particle and the projection of its momentum along the  $z$ -axis.

In relativistic kinematics, the difference in rapidity between two particles is an invariant quantity under Lorentz transformations with boost along the  $z$ -axis. Finally, the two angular coordinates  $\phi$  and  $\eta$  are used to define a distance between particles in the detectors, denoted as  $\Delta R = \sqrt{(\Delta\phi)^2 + (\Delta\eta)^2}$ .

### 3.2.2 Tracker

The tracker detector has the purpose of measuring the momentum of charged particles. These are detected as a series of energy deposits in the different layers of the tracker. The momentum of a particle is measured from the curvature of its reconstructed track, which is bent by the magnetic field provided by the solenoid.

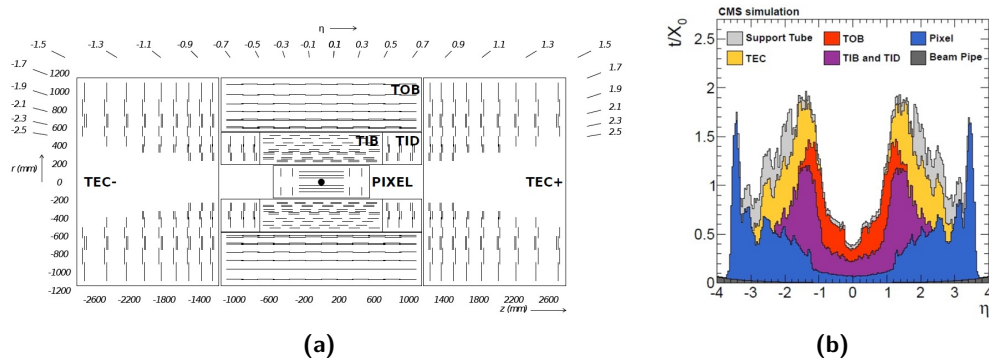


**Figure 3.4.** (left) View of the tracker and its partitions in the  $rz$ -plane: Tracker Inner Barrel (TIB), Tracker Inner Disks (TID), Tracker Outer Barrel (TOB), Tracker Endcaps (TEC). (right) Tracker material budget in units of radiation length  $X_0$ .

The CMS tracker is entirely based on silicon detector technology: it covers the region within  $|\eta| = 2.5$  and comprises an inner Pixel Detector based on silicon pixels and an outer Silicon Strip Tracker made of several layers of silicon microstrips arranged in a central (barrel) structure closed by two endcaps at each side. A sketch of the tracker is shown in Fig. 3.4a, while Fig. 3.4b shows the amount of material represented by the tracker upstream of the electromagnetic calorimeter. The material budget of the tracker entails significant energy losses for electromagnetic particles, as it can lead to electron bremsstrahlung or photon conversions into electron pairs, degrading the energy resolution for these particles.

The spacial resolution of the tracker is of the order of  $15 \mu\text{m}$ , resulting in a momentum resolution below 2% (6%) in the barrel (endcap) for muons with  $20 \text{ GeV} < p_T < 100 \text{ GeV}$ , and better than 10% for  $p_T$  up to 1 TeV.

### 3.2.3 Electromagnetic calorimeter

The electromagnetic calorimeter (ECAL) is the detector where electrons and photons deposit their energy. It is a high-resolution, homogeneous electromagnetic calorimeter made of 75848 scintillating crystals of lead tungstate ( $PbWO_4$ ) arranged in a barrel detector (EB) covering  $|\eta| < 1.479$  and 2 endcaps (EE) extending the coverage up to  $|\eta| = 3.0$ .

A preshower detector (ES), based on lead absorbers equipped with silicon strip sensors, is placed in front of EE. ES covers the region  $1.65 < |\eta| < 2.6$  and helps resolve the signals of high-energy photons from the decays of neutral pions into two close photons, improving also the measurement of the position of the electromagnetic deposit in EE. A more detailed description of ECAL is provided directly in appendix A, which is fully dedicated to the ECAL calibration.

### 3.2.4 Hadronic calorimeter

The hadronic calorimeter (HCAL) devoted to the measurement of the energy of hadrons. It is a sampling calorimeter made of alternating layers of brass absorber and fluorescent scintillator materials and covering the region up to  $|\eta| = 3.0$ . The coverage is extended up to  $|\eta| = 5.0$  by the hadronic forward calorimeter (HF), which employs a Cherenkov-based

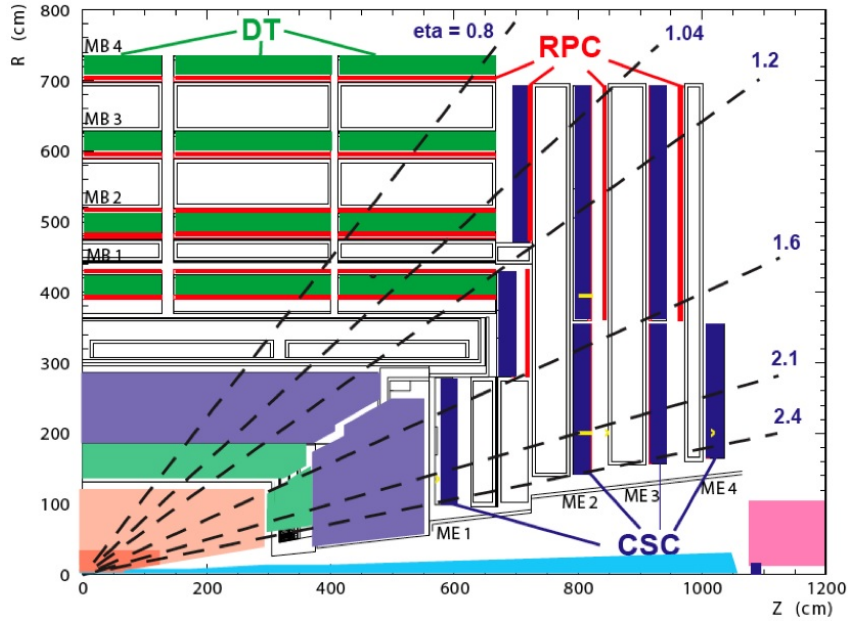


Figure 3.5. Muon detectors in CMS.

radiation-hard technology with quartz fibres as active medium. The combined ECAL and HCAL resolution, limited by HCAL, can be expressed as:

$$\frac{\sigma(E)}{E} = \frac{100\%}{\sqrt{E[\text{GeV}]}} \oplus 5\% \quad (3.5)$$

which is above 20% for hadrons with 25 GeV of energy.

### 3.2.5 Magnet

CMS features a 13 m long solenoid composed of a superconducting cylindrical Niobium-Titanium coil with a diameter of 5.9 m. The magnet provides a magnetic field of 3.8 T at its center, allowing for the precise measurements of the momenta of charged particles through the curvature of their tracks. The magnet flux is returned by a saturated iron yoke located outside the solenoid, which also works as mechanical support structure of the detector.

### 3.2.6 Muon chambers

Neglecting neutrinos, muons are the only particles that manage to escape the calorimeters. They are identified by the external muon chambers embedded in the magnet iron yoke. Different detector technologies are employed:

- drift tubes (DT), covering the region with  $|\eta| < 1.2$ ;
- resistive plate chambers (RPC), covering the region with  $|\eta| < 1.6$ ;
- cathod strip chambers (CSC), supplying the region with  $0.9 < |\eta| < 2.4$ .

Muon chambers are characterized by high time resolution (3 ns for RPC) and a good space resolution. These properties make them the optimal solution for a fast high-efficiency trigger system. The location of muon detectors in CMS is illustrated in Fig. 3.5.



### 3.2.7 Trigger system

The collision frequency of 40 MHz times the number of PU interactions results in a rate of events of about 1 GHz, which is impossible to record, as the interesting events are only a small fraction of the total one.

Therefore, a dedicated trigger system is necessary to reduce the rate of selected events to lower values, so to comply with the intrinsic limits of the CMS readout bandwidth and storage space. The allowed bandwidth is  $\approx 2$  GB/s. Since the typical physics event size is about 1 MB, the trigger system must reduce the initial rate down to about 1 kHz, six order of magnitude lower than the input.

The trigger system [38] is structured in two levels:

- **Level-1 Trigger (L1):** it is made of a series of hardware processors able to perform fast logical operations on the signals generated by some detectors;
- **High-Level Trigger (HLT):** it is a software system implemented as a multiprocessor computer farm, which operates on the output passed by the L1 stage.

The L1 trigger has a latency time of  $3.2 \mu\text{s}$  and reduces the input rate to 100 kHz. It exploits coarse information from only the calorimeters and the muon chambers, as the track reconstruction algorithm is too slow for this stage.

The L1 features several algorithms (L1 bits, or seeds) to store a general description of the event content. For example, the L1\_SingleEG35 bit is switched on if an energy deposits with transverse energy above 35 GeV is detected in ECAL. There exist different families of L1 bits which record the presence of either a muon, an electromagnetic particle, hadronic activity or even  $E_T^{miss}$ . At the same time, there are several bits implementing different threshold within each family. The accepted event, condensed in a list of L1 bits, is passed to the HLT for further event processing.

The HLT employs reconstruction algorithms very similar to those used for offline analysis (including track reconstruction). The HLT software system is implemented as a list of algorithms (named HLT paths) consisting of several steps (software modules). Each module performs a well-defined task, like reconstructing higher-level physics objects (for example, a track or an energy cluster in ECAL) or taking a decision to either accept or reject an event.

The guiding principles of an HLT path are regional reconstruction and fast event veto. They are operatively implemented as a sorted array of producer and filter modules working according to the following criteria:

- particle candidates are built from detector information located only in the nearby of interesting activity identified by the L1;
- the event is rejected if it doesn't satisfy the specific requirements of the path before passing to the next module, minimizing CPU time usage and freeing the processors to evaluate another event;
- if accepted by a filter, the event passes through subsequent modules that might apply more sophisticated (and time-consuming) reconstruction algorithm to identify candidate particles (an electron from a track and a cluster in ECAL) or apply further filtering.

At the end of this chain, the output rate is as low as 1 kHz and the selected events are stored in different Primary Dataset (PD) to be used for offline data analysis. A PD collects events with similar topology (for instance, the presence of at least one high energy electron) and is generally fed by more than one HLT paths, just like a single HLT path is potentially seeded by more than one L1 bits. For example, data used for the W-boson rapidity measurement in the electron channel is stored in the SingleElectron PD, which collects events selected by the logical OR of several SingleElectron HLT paths.

In order to keep the output rate below the sustainable level, *prescales* might be used at either L1 or HLT level. A prescaled trigger saves only a fraction of the otherwise accepted events, without applying a physics selection. For instance, a prescale of 3 means that only one out of three candidate events is actually accepted. Prescales reduce the effective amount of integrated luminosity available for the analysis, and are clearly not suited in searches for rare processes. The trigger menu that is deployed online during data taking is actually composed of several “prescale columns” featuring different prescale values for the L1 algorithms and HLT paths. Within an LHC fill, the trigger menu switches among these columns to optimize the rate of selected events as the instantaneous luminosity decreases during the fill. For instance, a specific L1 algorithm with low thresholds might be disabled in the beginning of the fill and get enabled, in case prescaled, in the middle on the fill.

### 3.3 Physics objects reconstruction

#### 3.3.1 Particle Flow reconstruction

Particle reconstruction in CMS is based on the particle-flow (PF) algorithm [39]. The PF exploits an optimized combination of the basic information from the different sub-detectors (energy deposits in ECAL, hits in the pixel detector or in the muon chambers) to build higher-level objects (tracks, energy clusters). Finally, these ingredients are combined to form PF candidates.

The PF algorithm is also implemented at HLT level. It starts from segments in the external muon chambers and tries to associate them to tracks in the tracker to form muons. In this way, the remaining tracks can be used to form other charged PF candidates. Those that are associated to clusters in ECAL are identified as electrons. ECAL clusters not associated to tracks form photon candidates. The remaining objects are used to build charged or neutral hadrons. Finally, these PF objects can be clustered together to build jets.

#### 3.3.2 Muons

Muons are detected by the dedicated chambers located outside the magnet. At the same time, they also interact with the tracker which, thanks to its excellent spatial resolution and the high magnetic field, allows for a very precise measurement of muon momentum. The track reconstruction is based on the Kalman Filter algorithm [40].

From the point of view of the reconstruction, three categories of muons are defined in CMS:

- standalone muons: they are obtained from tracks made only with hits in the muon chambers;

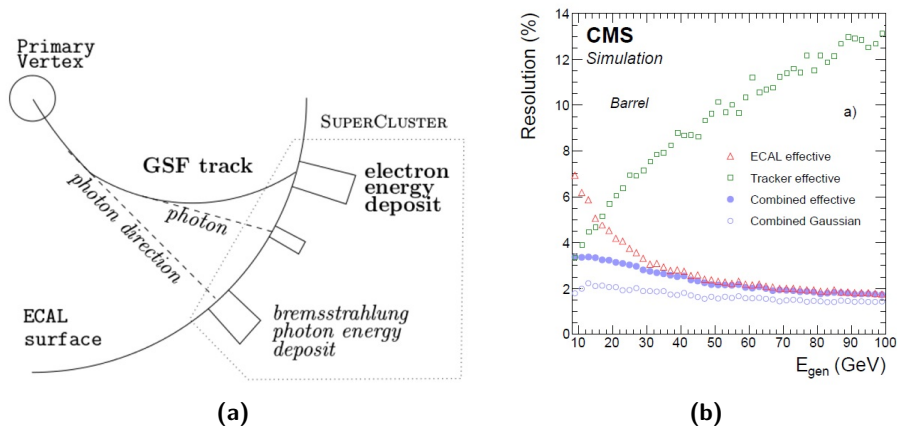


**Figure 3.6.** (left) Schematic view of an electron reconstruction: the track is reconstructed by the GSF algorithm taking into account the kinks due to breemstrahlung. The supercluster recovers this radiation and merges it with the electron cluster. (right) Electron energy resolution in simulations, as obtained using only the tracker (green squares), ECAL (red triangles) or their combination (circles).

- global muons: they are obtained from the matching of standalone muons with tracks in the tracker;
- tracker muons: basically the opposite of global muons, since the algorithm starts from inner tracks and extrapolates them to the muon system (taking into account the magnetic field, the average expected energy losses, and multiple Coulomb scattering in the detector material), eventually trying to match them with hits in the muon chambers (without necessarily requiring a complete track in the muon system);

The last case is particularly suited for low- $p_T$  muons ( $p_T \lesssim 10$  GeV) which might hardly reach the muon chambers or leave only few hits there.

### 3.3.3 Electrons

Electrons are identified as a cluster of energy in ECAL that is associated to a track in the tracker, with little or no energy deposits in HCAL. A more detailed description of the ECAL energy measurement is reported in appendix A.

Electron tracks can be reconstructed in the tracker using the standard Kalman filter procedure used for all charged particles. However, the large radiative losses for electrons in the tracker material compromise this procedure and lead to a reduced hit-collection efficiency. Indeed, hits can be lost when the change in curvature is large because of bremsstrahlung. For this reason, the gaussian-sum filter (GSF) algorithm is used instead [41] to improve the performance on electron track reconstruction.

It should be noted that the ECAL clustering algorithm is able to recover the emitted radiation by extending the width of the electron cluster along the  $\phi$  direction to form a supercluster (SC). This is illustrated in Fig. 3.6a. Nevertheless, photon radiation degrades the performance on the energy measurement, such as the resolution. For this reason, it is convenient to define some quantities to categorize electrons based on the amount of emitted

radiation. The shower shape variable  $R_9$  serves this purpose: it is defined as the ratio of the energy measured in a  $3 \times 3$  matrix of ECAL crystals centered on the SC crystal with the highest energy and the total SC energy. Electrons with  $R_9 > 0.94$  are characterized by low emitted bremsstrahlung.

The final electron energy is obtained from the combination of the momentum measured with the tracker and the energy of the SC measured with ECAL. The excellent energy resolution of ECAL drives the precision in the combination already for electron  $p_T$  above 20 GeV. This is shown in Fig. 3.6b for simulated electrons in EB.

### 3.3.4 Jets and missing transverse energy

A jet is a spray of particles produced in the hadronization process of quarks and gluons: it is typically composed of hadrons, but can also include leptons or photons produced in the decay chain of other jet constituents. This (mostly) collimated swarm of particles appears in the detector in the form of clusters of energy in ECAL and HCAL, with associated tracks in the tracker.

Technically, a jet is actually not a well-defined physics object, but rather the output of a jet clustering algorithm that tries to gather the primary and secondary products of the hadronization. Ideally, the kinematic properties of the jet should mirror those of the original parton from which it originated.

Jets in CMS are reconstructed through the ‘‘anti-kt’’ clustering algorithm [42] with distance parameter  $R = 0.4$ . The algorithm builds a jet from PF candidates in a cone with radius  $\Delta R$  around a given candidate, starting from particles with the highest  $p_T$  and proceeding with the clustering of softer ones until all candidates are used.

Several corrections must be applied to the energy of jets to account and correct for spurious energy deposits from PU interactions or the non-uniformity of the detector response as a function of the jet  $p_T$  and  $\eta$ . Not surprisingly, the accuracy and resolution on the jet energy is not competitive with the one of muons and electrons.

The missing energy, denoted as  $E_T^{miss}$ , is defined as the absolute value of the missing transverse momentum, which in turn is computed as

$$\vec{p}_T^{miss} = - \sum_i \vec{p}_{T,i} \quad (3.6)$$

The sum above is over all detected PF objects associated to the primary vertex. It goes without saying that PU rejection is fundamental not to degrade the measurement of  $E_T^{miss}$ . Moreover, the accuracy and resolution of the  $E_T^{miss}$  measurement clearly depend on those of the other PF objects in the event.

## Chapter 4

# Data sample and event selection

This chapter describes the dataset and MC samples used to carry out the measurement. The event selection is presented as well.

Signal events are characterized by the presence of a muon or electron originating from the primary vertex,  $E_T^{miss}$  due to the neutrino, and hadronic activity composing the recoil. The most probable value for the lepton  $p_T$  is about 40 GeV. Similar values of  $E_T^{miss}$  are expected, as the kinematics of the neutrino is the same as the one of the charged lepton.

The lepton is selected requiring certain quality criteria meant to ensure high signal purity and efficient background rejection. These requirements include a set of predefined identification criteria (ID) and isolation: the former group several cuts on discriminating quantities based on the different interaction of hadrons and electromagnetic particles with the tracker and the calorimeters; the latter is a condition on the amount of energy from additional particles around the candidate lepton. The detailed selection is described in Sec. 4.4.

The background originates from all SM processes that produce real or misidentified leptons in the final state. It consists of:

- QCD multijet production, referred to as QCD for simplicity. QCD events contain genuine leptons generated from in-flight decays of hadrons. In addition to that, a jet can also be misidentified as a lepton by the reconstruction algorithm. Although the misidentification probability, larger for electrons than for muons, is only of the order of  $10^{-6}$ , the QCD cross section is several orders of magnitude higher than for signal events. This makes QCD the dominant background for any inclusive measurement of W bosons decaying into leptons;
- Drell-Yan (DY) dilepton production ( $Z/\gamma^* \rightarrow \ell\ell$ ), where one lepton is either not reconstructed or lost outside the detector acceptance;
- $Z \rightarrow \tau\bar{\tau}$  and  $W \rightarrow \tau\nu_\tau$ : a small background contribution arises from the decays of  $\tau$  leptons into electrons or muons: these leptons tend to be less energetic than signal ones and are largely suppressed by the  $p_T$  selection
- top quark pairs or single top production: these processes are a source of genuine leptons from top quark semileptonic decays ( $t \rightarrow Wb$  with  $W \rightarrow \ell\nu$ ). The decay of the b-quark can also produce a real lepton. However, this will less likely be isolated or compatible with the primary vertex because the b-quark has a relatively long lifetime and decays in flight far from the interaction vertex;

**Table 4.1.** Run eras of the 2016  $p$ - $p$  run with their integrated luminosities.

Era	RunB	RunC	RunD	RunE	RunF	RunG	RunH	total
$\mathcal{L}_{int}$ [ $\text{fb}^{-1}$ ]	5.75	2.57	4.24	4.03	3.11	7.58	8.65	35.93

- diboson production consisting of WW, WZ, and ZZ events, where the weak bosons decay into leptons. Even though a W boson is produced, these processes are treated as backgrounds because their production mechanism and kinematics are different from the ones of signal events, and the considerations made in chapter 2 regarding the helicity do not hold.

For the electron channel, an additional minor background component is considered, which is made of events where a W boson with a given charge produces a lepton that is reconstructed with the opposite charge. This background is referred to as “charge-flips”. It arises from the emission of bremsstrahlung photons and their possible conversion into electron pairs: the combination of these effects can lead to the wrong reconstruction of the electron track, whose curvature is used to assess the charge. Therefore, the effect is correlated with the tracker material budget and is particularly sensitive to the one of the pixel detector, since the misidentification rate tends to be larger if the conversion happens in the first layers of the tracker. Charge misidentification is negligible for muons, as they emit little or no bremsstrahlung.

## 4.1 Data sample and trigger

The data sample used in this analysis corresponds to an integrated luminosity of  $35.9 \text{ fb}^{-1}$  recorded by the CMS experiment during 2016 at 13 TeV. Data used for the analysis are filtered with the CMS standard selection of runs and luminosity sections that requires high quality data with a good functioning of the different sub-detectors. The luminosity is measured using the Pixel Cluster Counting method and the associated uncertainty is 2.5% [43].

Data are taken from the SingleElectron (SingleMuon) Primary Dataset for the electron (muon) channel, which were obtained using a logical OR of several HLT paths requiring the presence of at least one lepton with predefined quality criteria. In the analysis, events are further selected by requiring the following unrescaled triggers:

- **muons:** HLT\_IsoMu24\_v\* or HLT\_IsoTkMu24\_v\*
- **electrons:** HLT\_Ele27\_WPTight\_Gsf\_v\*

These triggers require at least one isolated muon (electron) with  $p_T > 24$  (27) GeV. They also apply some identification criteria based on the quality of the track and, for the electron, some additional requirements on the energy deposits in the calorimeter.

The total dataset is split in different eras from B to H (era A corresponds to the initial detector commissioning phase and is not used for physics analyses), whose integrated luminosities are reported in Table 4.1. These eras distinguish data taking periods characterized by different trigger conditions, that were rapidly changing during the year, especially for the electron trigger.

**Table 4.2.** List of Monte Carlo samples used in the analysis.

Process	cross section [pb]	generator
$W(\ell\nu)+\text{jets}$	61527	aMC@NLO
$Z(\ell\ell)+\text{jets}$	6025	aMC@NLO
$t\bar{t}+\text{jets}$	182	MadGraph
tW	35.6	POWHEG
Single top (t-channel)	136	POWHEG
Single $\bar{t}$ (t-channel)	80.9	POWHEG
Single top (s-channel)	3.7	POWHEG
WW	115	MadGraph
WZ	47.1	MadGraph
ZZ	16.5	MadGraph

Prompt data collected during 2016 were also affected by minor issues connected to the reconstruction, that were corrected for with a dedicated reprocessing of data at the end of the year. In this respect, the analysis uses the so-called ‘‘Legacy’’ reconstruction version of the data, which includes the best knowledge of the tracker alignment and ECAL calibration.

## 4.2 Monte Carlo samples

MC events are used to model the signal ( $W+\text{jets}$ ) and the other Standard Model background processes except for QCD, which is estimated in a data-driven way as described in chapter 5. Samples of simulated muon- and electromagnetic-enriched QCD events are also available, but their equivalent integrated luminosity is extremely low compared to the one in data. Therefore, they are not used to estimate the QCD background.

Events with either a W or a Z boson produced in the hard scattering are simulated at next-to-leading-order (NLO) accuracy in the strong coupling constant using aMC@NLO\_MadGraph5 [44] with NNPDF3.0 PDF set, and matched to PYTHIA8 [45] for the modeling of the parton shower.

Other background samples are simulated with either aMC@NLO, MadGraph [46], or POWHEG [47]. For the top background, several samples comprising  $t\bar{t}$  and different single top production modes are used. The list of MC processes and their cross sections are reported in Table 4.2. Simulated events are passed through a CMS detector simulation based on the GEANT4 [48] toolkit.

Simulated events have to pass the same selection criteria implemented in the triggers in data. Since the MC production generally starts before the beginning of data taking, the simulated triggers do not fully reproduce those in data. Indeed, the identification requirements applied at HLT level are often adapted during the year to cope with possible changes in the conditions of data taking, like the increase of the instantaneous luminosity provided by LHC, thus demanding for tighter  $p_T$  thresholds or quality restrictions. Moreover, as mentioned in Sec. 3.2.7, the specific prescale column in the trigger menu can be adapted during the fill.

At the same time, the detector simulation does not catch all the features of the real detector. Indeed, differences in the material budget, geometry, calibration or other sources

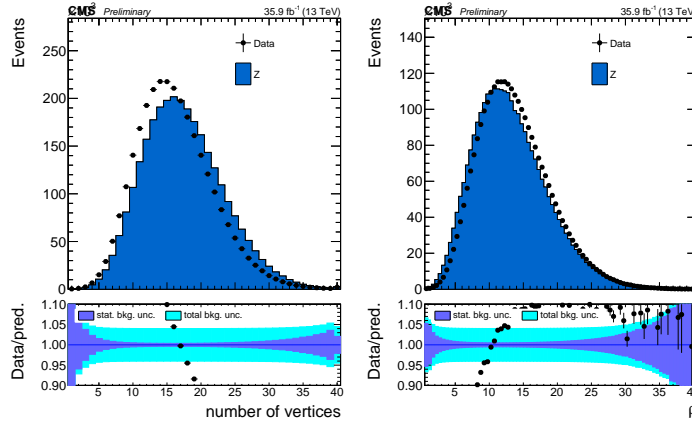


**Figure 4.1.** Distributions of the number of reconstructed vertices (left) and average energy density  $\rho$  in the detector (right) in  $Z \rightarrow ee$  events after the PU reweighting.

of inefficiency in the particle reconstruction are expected. Moreover, there can be some time-dependent effects, such as light yield variations in the ECAL crystals due to radiation damage, that simulations cannot track.

The differences between data and MC concerning the trigger or the particle reconstruction and identification are corrected for a-posteriori by computing dedicated efficiency corrections.

### 4.3 Pileup reweighting

The PU scenario in the MC accounts for both in-time and out-of-time PU, but is generally not identical to the one observed in data. Therefore, MC samples have to be reweighted such that the simulated PU distribution matches the one in data. The PU distribution in data is estimated from the instantaneous luminosity during collisions. The weight is taken from the ratio of the PU distributions in data and MC, and is applied on each simulated event as a function of the number of PU interactions in the event.

The effect of the reweighting procedure is assessed on the distributions of two variables that are sensitive to the number of PU interactions: they are the number of reconstructed vertices and the average energy density  $\rho$  in the event. Their distribution in  $Z \rightarrow ee$  events is shown in Fig. 4.1 after the PU reweighting. The vertex reconstruction efficiency is about 70% and is not linear with PU, as the efficiency is smaller in data than in MC for higher number of PU interactions. This explains the observed discrepancy in the corresponding distribution after the reweighting. Instead, better agreement is seen for the distribution of  $\rho$ . Nevertheless, it should be stressed that the discrepancies between data and MC in Fig. 4.1 do not affect the analysis, as these variables are not used in the measurement.

### 4.4 Selection criteria

Events in data are selected requiring that the primary vertex of the hard scattering process has a distance from the nominal interaction point smaller than 24 cm along the beam axis



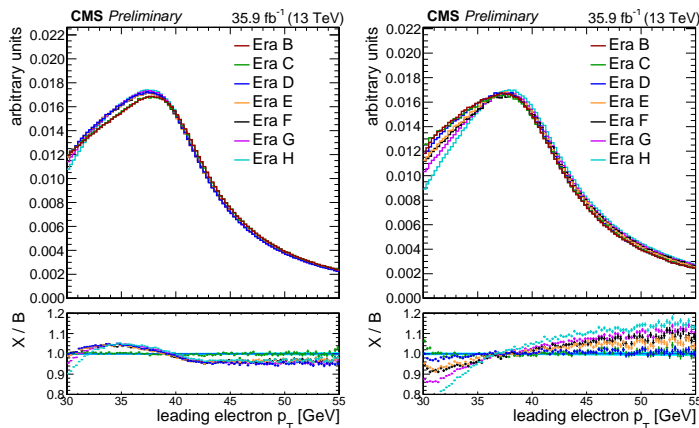


**Figure 4.2.** Electron  $p_T$  spectrum in data for different eras of data taking, as reported in Table 4.1. The distributions are shown separately for EB (left) and EE (right).

and smaller than 2 cm in the transverse plane. Among the PU vertices, the primary vertex is chosen as the one with the largest sum of the squared  $p_T$  of tracks pointing to it.

#### 4.4.1 Electrons

Electrons in data are selected with triggers requiring one electron with  $p_T > 27$  GeV, where the threshold refers to the lowest unrescaled HLT path with  $|\eta|$  coverage up to 2.5. In order to cope with the increasing instantaneous luminosity reached in the  $pp$  collisions, the  $E_T$  threshold of the lowest unrescaled L1 SingleEG bit was raised up during the year. Since summer 2016, roughly corresponding to the beginning of the dataset era E in Table 4.1, the thresholds became tighter than the one of the HLT, arriving up to  $E_T \gtrsim 40$  GeV. This feature reflects in the shape of electron  $p_T$  distribution in different periods of data taking. As it is shown in Fig. 4.2, the largest effect appears in the low- $p_T$  region of the  $p_T$  spectrum, and is enhanced in EE with respect to EB.

It is worth pointing out that the L1 SingleEG algorithms exploit simple information from clustered energy in ECAL, which might be deposited by electrons, photons (the tracker is not used in the L1), jets with large electromagnetic energy fraction, and PU as well. Therefore, keeping the rate within the allotted budget can only be achieved by raising the energy thresholds. An isolation selection is applied as well, but the coarse granularity of the L1 trigger towers does not allow for high discrimination power between electromagnetic particles and jets.

Events in MC have to pass a SingleElectron HLT bit that emulates the trigger used for data. On top of the trigger selection, a special set of identification criteria (generally referred to as HLT-safe ID) is applied. This has the purpose of emulating the HLT and providing homogeneous trigger identification requirements through all the 2016 data taking period. Indeed, similarly to the energy thresholds, the electron identification criteria applied in the SingleElectron HLT paths became more stringent during 2016. As a consequence, at some point they became even tighter than the ones used for offline electron identification.

The HLT-safe ID is applied in both data and MC. The criteria defining it are listed in Table 4.3. The thresholds are provided separately for EB and EE. On top of the trigger requirements, electrons are selected applying some acceptance cuts and identification criteria,

**Table 4.3.** Selection criteria defining the electron 2016 HLT-safe ID.

Variable	EB	EE
full5x5 $\sigma_{\eta\eta}$ <	0.011	0.031
$ \Delta\eta _{\text{InSeed}}$ <	0.004	N/A
$ \Delta\phi _{\text{In}}$ <	0.020	N/A
H/E <	0.060	0.065
$ 1/E - 1/p $ <	0.013	0.013
ECAL PF Cluster Isolation <	0.160	0.120
HCAL PF Cluster Isolation <	0.120	0.120
Tracker Isolation <	0.08	0.0.08
GsfTrack $\chi^2/\text{NDOF}$ <	N/A	3.0

where the latter includes both ID and isolation selections.

The electron identification is based on a selection on a set of discriminating variables that allow the separation of signal leptons from background sources, mainly originating from photon conversions, jets misidentified as electrons, or electrons from semileptonic decays of heavy-flavor quarks. The diverse topologies of background processes demand for the simultaneous usage of different observables. These can be classified into three main categories:

1. variables that compare measurements made with ECAL or the tracker, such as
  - $|1/E - 1/p|$ : it is the difference between the electron energy (E), measured with ECAL, and the electron momentum (p) at the point of closest approach to the vertex, measured with the tracker;
  - $\Delta\eta$  ( $\Delta\phi$ ): it is the difference in  $\eta$  ( $\phi$ ) between the coordinate of the supercluster (SC) and the track, where the track is evaluated close to the interaction vertex;
2. variables based on calorimetric observables that distinguish between genuine electrons (either signal electrons or electrons from photon conversions) and jets:
  - $\sigma_{\eta\eta}$ : it is the transverse shape of the electromagnetic shower along  $\eta$ , which tends to be narrower for single isolated electrons than for hadron deposits;
  - H/E: it is the ratio of the energy measured in HCAL within a cone centered on the electron SC and the energy of the SC. It is expected to be small for real electrons, as their energy is fully contained in ECAL;
3. variables based on the tracker, employed to improve the separation between electrons and charged hadrons, or that require the compatibility with the primary vertex. These exploit the information obtained from the GSF track and the difference between the KF and GSF tracks:
  - $dz$  and  $dxy$ : the electron track is required to point to the primary vertex. This is accomplished by posing a threshold on the impact parameters  $dz$  and  $dxy$ , which are the longitudinal and transverse distance of the track to the vertex;

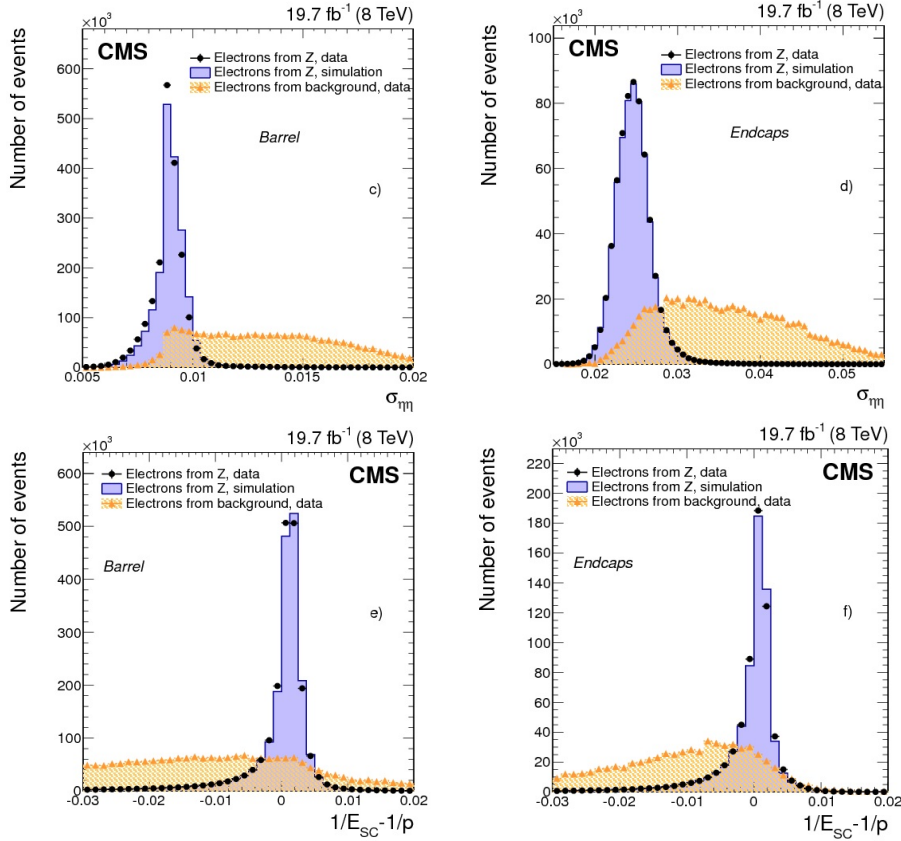


**Figure 4.3.** Comparison of the distributions of some electron discriminating variables in  $Z \rightarrow ee$  events and QCD background:  $\sigma_{ii\eta}$  (top) and  $|1/E - 1/p|$  (bottom) are shown for electrons in EB (left) and EE (right). Taken from [50].

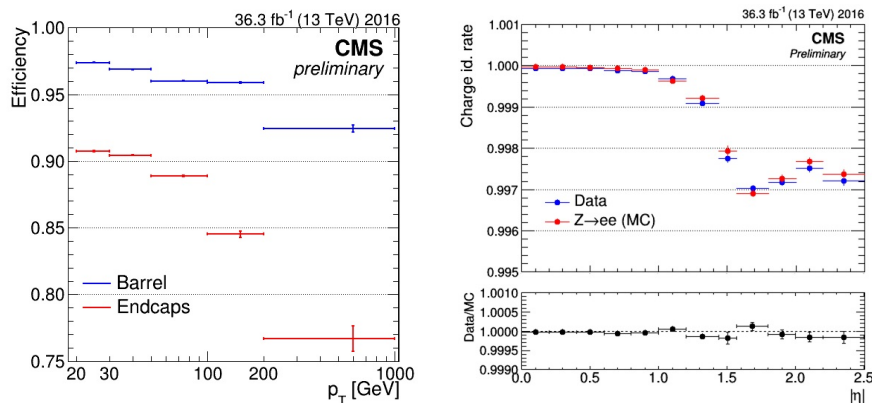
- conversion veto: it is employed to reject photons converting into electron pairs upstream of ECAL. The veto exploits the pattern of track hits, rejecting the electron candidate if there are missing hits in the innermost layer of the tracker. In addition to that, the possible electron track pair is fitted to a common conversion vertex, and the converted photon candidate is rejected according to the  $\chi^2$  probability of the fit.

Some of these discriminating variables are shown in Fig. 4.3, comparing real electrons in  $Z \rightarrow ee$  events and electrons from the QCD background. The distributions, taken from [50], are made using Run I data and are shown here for illustration purpose only.

The previous criteria are complemented by the isolation. This helps reject events where genuine leptons are produced from decays of hadrons inside jets. The isolation is evaluated opening a cone with a predefined radius around the direction of the lepton. Then, the scalar sum of transverse momenta of all PF objects inside the cone is computed. The lepton is considered to be isolated if the ratio of the aforementioned quantity and the electron  $p_T$  is below a given threshold. Contributions from PU interactions are removed from the cone before evaluating the isolation. Charged PU candidates can be easily removed, their track not being associated to the primary vertex. In addition, the average energy expected from PU inside the cone has to be subtracted. This is called effective area (EA) correction [51] and

**Table 4.4.** Selection criteria for electron identification.

Variable	EB	EE
full5x5 $\sigma_{i\eta i\eta} <$	0.011	0.0298
$ \Delta\eta _{\text{InSeed}} <$	0.00477	0.00609
$ \Delta\phi _{\text{In}} <$	0.222	0.045
H/E <	0.298	0.0878
$ 1/E - 1/p  <$	0.241	0.13
number of missing hits $\leq$	1	1
pass conversion veto	yes	yes
$ dxy $ (cm) <	0.05	0.10
$ dz $ (cm) <	0.10	0.20
Relative PF isolation (EA correction) <	0.2	0.0821

**Figure 4.4.** Efficiency for the three charge estimates to agree for electrons in  $Z \rightarrow ee$  events passing the identification criteria of the analysis (left). Probability to assign the correct charge when the agreement of the three methods is required (right). Taken from [49].

accounts for the energy deposited by photons and neutral hadrons from PU. It is obtained as the product of the energy density  $\rho$  and an effective area  $A_{eff}$  proportional to the isolation cone. In summary, the isolation is defined as:

$$ISO_{PF} = \sum p_T^{charged} + \max \left[ 0, \sum p_T^{neutral had} + \sum p_T^\gamma - \rho \cdot A_{eff} \right] \quad (4.1)$$

where the sums run over the charged PF candidates, neutral hadrons and photons inside the cone.

The isolation defined above is referred to as PF isolation to distinguish it from the detector-based isolation that is used at HLT level. The latter relies on the sum, within a cone around the electron, of energy deposits either in ECAL or in HCAL around the electron trajectory, or on the scalar sum of the  $p_T$  of all the tracks compatible with the collision vertex. In the detector-based isolation, the electron energy is removed from the sum by excluding the energy in a smaller cone around the electron candidate.

Ensuring the correct charge assignment is fundamental for the measurement of the charge asymmetry, which is one of the main goals of this analysis. Three methods are used in CMS to assess the electron charge:

- GSF track charge: based on the curvature of the electron GSF track (see Sect. 3.3.3);
- CTF track charge: based on the associated KF track matched to a GSF track when at least one hit is shared;
- SC-pixel match: based on the sign of the  $\Delta\phi$  between the vector joining the beam spot and the SC position and the vector joining the beam spot and the first hit of the electron GSF track;

When the agreement of the three methods is required, the charge misidentification rate is reduced to 0.02% in EB and 0.2% in EE [49]. The efficiency of the charge agreement on signal electrons is about 97% in EB and 90% in EE for  $p_T$  between 30 and 50 GeV. Figure. 4.4 shows the efficiency of the tight charge requirement on genuine electrons and the probability to assign the correct charge when the three methods agree, both measured in  $Z \rightarrow ee$  events.

In CMS, standard selection benchmarks are centrally provided to identify a given type of particles. They correspond to optimizations for several fixed efficiencies. The signal efficiencies for the standard electron loose, medium, and tight ID are approximately 90%, 80%, and 70%, respectively.

The identification criteria and isolation used in the analysis are reported in Table 4.4. It should be noted that the ID variables computed at HLT level may differ slightly from those used in the offline analysis. Therefore, although the effective thresholds implemented in the HLT-safe ID appear to be tighter than those used offline, the latter are still not 100% efficient with respect to the trigger. In summary, electrons used for the W-boson helicity measurement must satisfy the following requirements:

- preselection
  - pass the HLT\_Ele27\_WPTight\_Gsf trigger path;
  - exactly 1 electron with  $p_T > 30$  GeV,  $|\eta| < 2.5$ ;
  - the electron must pass the HLT-safe ID (Table 4.3);
- electron identification criteria
  - Barrel (EB:  $|\eta| < 1.479$ )
    - \* loose cut-based ID (see Table 4.4);
    - \* relative PF isolation less than 0.2 in cone with  $\Delta R < 0.4$  with effective area correction;
  - Endcap (EE:  $|\eta| > 1.479$ )
    - \* medium cut-based ID (see Table 4.4);
    - \* relative PF isolation less than 0.0821 in cone with  $\Delta R < 0.4$  with effective area correction;
  - agreement of the three charge estimates;
- fiducial region: electrons with  $1.4442 < |\eta| < 1.566$  are rejected.

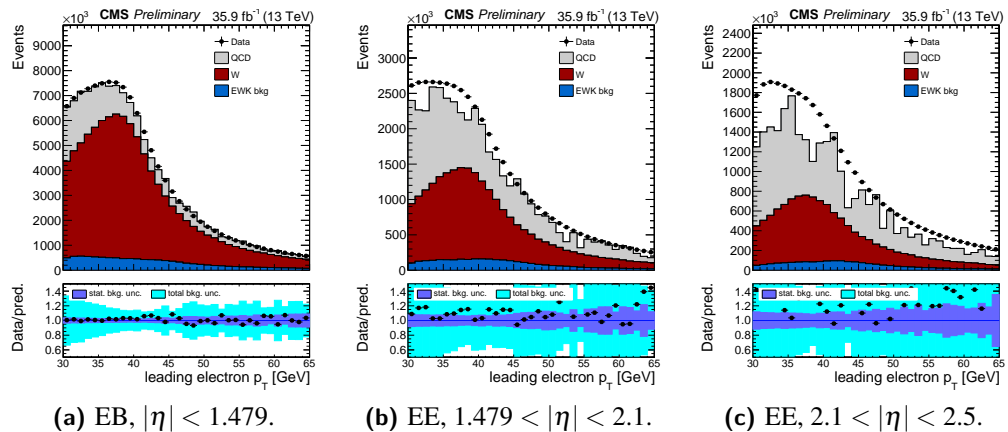


**Figure 4.5.** Distributions of electron  $p_T$  after the trigger and acceptance selection. The QCD background shown here is taken from MC for illustration purpose only. The blue component represents the sum of electroweak backgrounds, i.e., Drell-Yan,  $W \rightarrow \tau\nu_\tau$ , top and dibosons.

The offline  $p_T$  selection is slightly tighter than the one applied by the trigger, ensuring that the phase space of the analysis lies in the plateau of the HLT energy turn-on curve, accounting for the worse energy resolution of the HLT compared to the offline reconstruction.

The fiducial selection in  $\eta$  rejects electrons in the vicinity of the ECAL transition region between EB and EE. This region presents a gap not covered by the calorimeter and is also supplied with cables and other services which are not well modeled by detector simulations.

Figure 4.5 shows the electron  $p_T$  distributions after the preselection, which includes only the trigger and acceptance. The plots also show the relative fraction of QCD and other backgrounds with respect to the signal, which is made of  $W$  + jets events. The signal purity is about 65% in EB and about 35% in EE ( $\approx 40\%$  for  $|\eta| < 2.1$  and  $30\%$  for  $|\eta| > 2.1$ ). The remaining fraction of events comes mainly from QCD, with a small contribution from DY and other electroweak backgrounds. After applying the identification criteria in Table 4.4, the signal purity rises up to about 78% in EB, roughly 60% in EE for  $|\eta| < 2.1$  and 50% for  $|\eta| > 2.1$ .

#### 4.4.2 Muons

The selection adopted for muons exploits similar criteria as for electrons. Due to higher signal purity, the thresholds on the muon  $p_T$  applied at L1 and HLT level are looser than for electrons. Among other advantages, this allows for a lower  $p_T$  threshold in the offline analysis.

Muons used for the analysis are identified as either global or tracker muons (see Sec. 3.3.2). The identification criteria do not depend on  $\eta$  and are mainly based on the quality of the muon track in the tracker. The standard medium muon ID is used, which has an efficiency larger than 95% on signal events. Muons are selected according to the following requirements:

- preselection
  - pass the HLT\_IsoMu24 or the HLT\_IsoTkMu24 trigger paths;

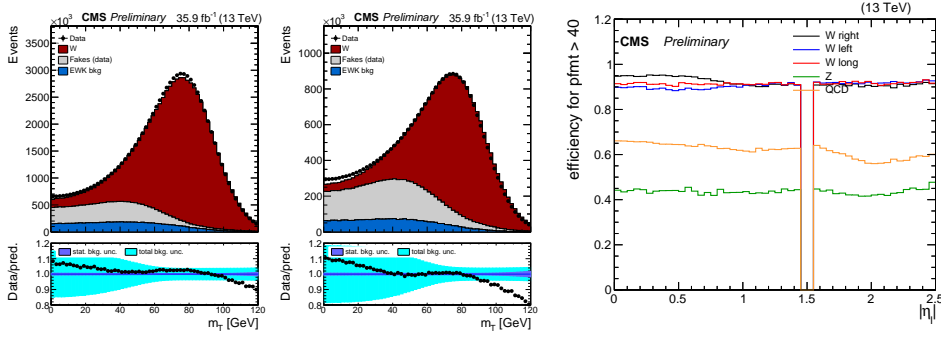


**Figure 4.6.** Distributions of  $m_T$  in the electron channel after the full signal selection in EB (left) and EE (middle). The QCD background, denoted as “fakes”, is estimated using data as described in chapter 5. On the right, efficiency of the  $m_T$  selection versus  $\eta$  on signal and background processes. The signal efficiency in EB depends on the charge and the helicity state.

- exactly 1 muon with  $p_T > 26$  GeV,  $|\eta| < 2.4$ ;
- pass the medium muon ID;
- muon identification criteria
  - relative PF isolation less than 0.15 in cone with  $\Delta R < 0.4$  with PU correction;

The signal purity after the muon selection is above 90%, roughly constant as a function of the muon pseudorapidity.

#### 4.4.3 Further event selection

In addition to the lepton specific criteria described before, the following selection is applied as well:

- events with additional leptons satisfying a looser set of criteria than those adopted for the signal lepton are vetoed;
- $p_T < 45$  GeV for the leading lepton;
- transverse mass  $m_T > 40$  GeV.

The lepton veto suppresses the background component from DY.

The restriction on the lepton  $p_T$  is a fiducial cut to exclude the high  $p_T$  region that does not provide any appreciable contribution to the analysis sensitivity. Indeed, the signal cross section falls rapidly for  $p_T$  above 45 GeV. Moreover, the data-driven estimate of the QCD background for  $p_T > 45$  GeV starts being affected by large uncertainties. Finally, that region is more sensitive to theoretical systematic uncertainties related to QCD and EWK higher order corrections.

The transverse mass is computed from the selected lepton and the  $E_T^{miss}$  in the event. The corresponding selection aims at rejecting a significant fraction of QCD events. At the same time, it also suppresses the Z background (mainly the  $Z \rightarrow \tau\tau$  component). The  $m_T$  distribution for electrons in EB and EE, as well as the efficiency of the  $m_T$  selection as a function of  $\eta$  is shown in Fig. 4.6 for signal and the main backgrounds. The disagreement

between data and prediction in the  $m_T$  distribution is mainly due to non-perfect calibration of  $E_T^{miss}$  response and resolution.

Differences in  $E_T^{miss}$  resolution between data and MC do not have a direct impact on the  $Y_W$  measurement, which is based on a fit to lepton quantities. However, a small migration of events inside or outside the selected  $p_T$  window of the analysis can be induced by the  $m_T$  cut due to resolution effects, resulting in a slight change of the signal templates. The impact of this effect was evaluated in the electron channel by applying a smearing of 20% on the  $E_T^{miss}$  resolution before computing  $m_T$ . It was found to induce a small variation of the inclusive signal template, with a linear dependence on  $p_T$ : the magnitude of the variation is about 1% for  $p_T < 35$  GeV and below 0.5% elsewhere.

## 4.5 Lepton momentum scale corrections

Achieving a precision of 10 MeV of  $m_W$  requires an accurate calibration of the lepton momentum scale, which must be of the order of  $10^{-4}$  for leptons with  $p_T \approx 40$  GeV. Although the measurement of  $Y_W$  does not demand such a high precision, the parameters of interest are extracted by fitting the joint lepton  $p_T$  and  $\eta$  distribution.

The energy scale is calibrated using the position of the Z-boson peak in  $Z \rightarrow ee$  or  $Z \rightarrow \mu\mu$  events as a reference. The method is based on an analytic fit to the Z-boson invariant mass to derive an offset correction between data and simulated events.

There are several effects that can lead to a displacement of the measured Z peak from the expected value. For electrons, the main ones include time dependent variations in the detector response during data taking as well as the non uniformity of the detector response as a function of  $\eta$ . For muons, the dominant effect is due to the alignment of the tracker layers and the muon chambers. The precision of the momentum measurement can substantially vary depending on the lepton kinematics as well, so they are computed as a function of the lepton  $p_T$  and  $\eta$ .

The electron momentum scale corrections are usually computed in different steps. First, the time dependent effects are corrected. Then, additional corrections are computed on top of the former as a function of the lepton  $p_T$ ,  $\eta$ , and the shower shape variable  $R_9$ .

### Electrons

The standard momentum scale corrections described before manifest a dependency on the lepton identification criteria used to compute them. As a consequence, a third step is needed, which consists in deriving residual corrections using exactly the same lepton selection as used in the helicity measurement. This is particularly relevant for electrons, whose identification relies on the combination of several detector quantities.

The residual corrections for the electron momentum scale were specifically derived in the context of the helicity measurement described in this thesis. The technique to derive them is based on a fit to the Z-boson mass spectrum in different categories defined by the  $|\eta| - p_T$  of the leading electron, while integrating over the kinematics of the second lepton. The fit model includes a signal and a background component. The former is defined as the convolution of a Breit–Wigner and a double Crystal Ball (CB) function [52]; the latter is modeled as an empirical falling exponential function, whose exponent is left floating in the fit. In the fit, the width of the Breit–Wigner is kept fixed to that of the Z-boson ( $\Gamma_Z =$



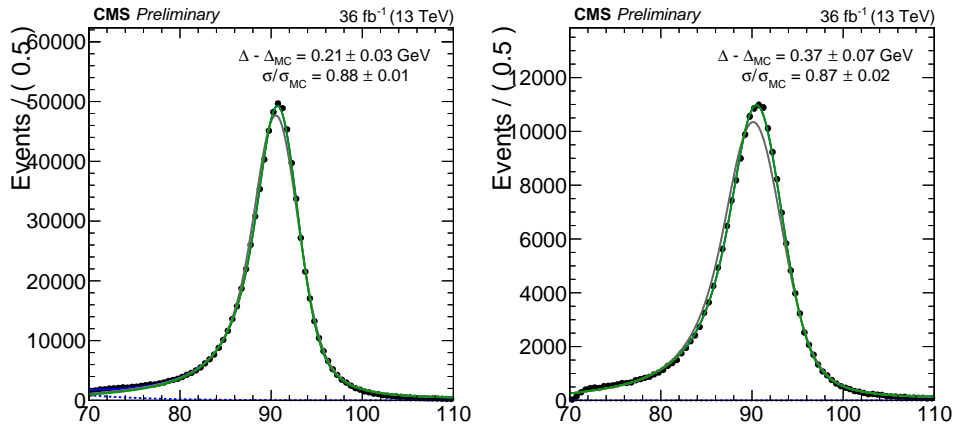


**Figure 4.7.** Reconstructed invariant mass distribution of electron pairs in  $Z \rightarrow ee$  events in data (points). Events are selected with at least one electron with  $30 < p_T < 35$  GeV and  $|\eta| < 1.0$  (left) or  $1.0 < |\eta| < 1.5$  (right). The total fitted PDF in data (solid blue) and the background-only component (dashed blue) are shown as well. For direct comparison, also the signal-only component of the fit in data (dark green) and simulation (dark gray) is superimposed on data as well.

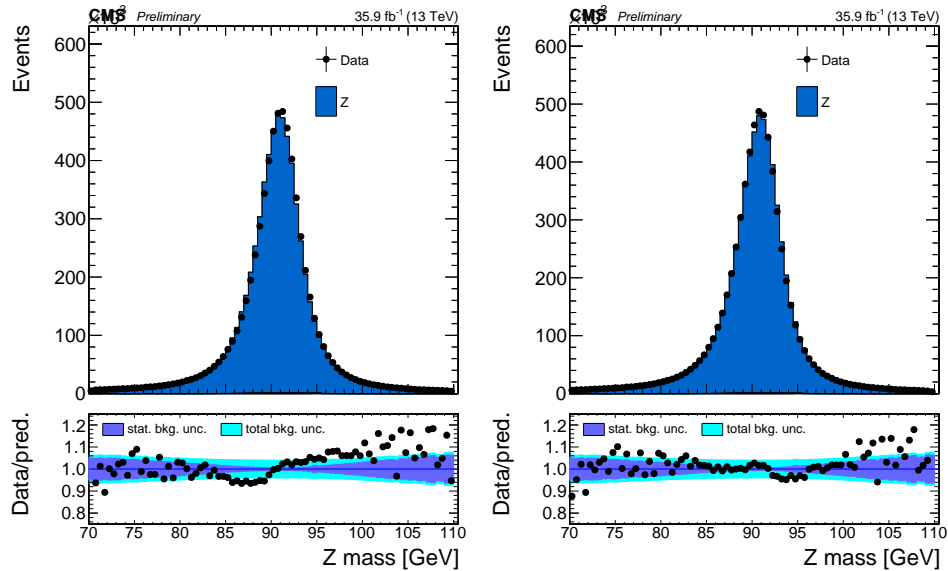


**Figure 4.8.** Reconstructed invariant mass distribution of electron pairs in  $zee$  events in data (points) and in simulation. Events are selected with both electrons in the barrel. The plot on the left is obtained using the standard scale corrections, while the one on the right also implements the residual scale corrections derived for this analysis.

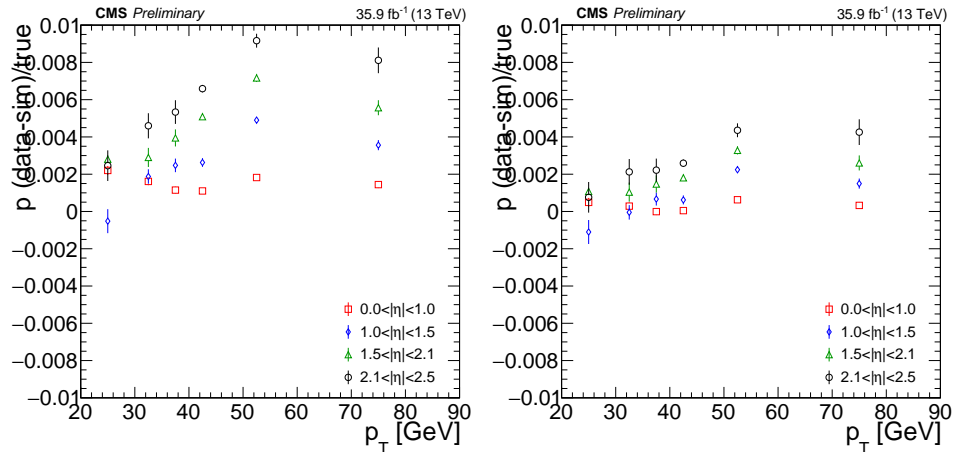


**Figure 4.9.** Closure test of the scale corrections. The difference between the measured  $Z$ -boson mass in data and MC, normalized to the nominal value, is shown as a function of the electron  $p_T$  for the  $|\eta|$  ranges used to derive the corrections. The plot on the left shows the closure of the official corrections, while the one on the right is obtained after applying the residual corrections as well.

2.495 GeV [12]). The CB provides a good description of the calorimeter resolution effects and of bremsstrahlung losses upstream of ECAL. Its parameters are left free in the fit.

The position of the peak is obtained as the mean of the gaussian core of the CB. Distributions obtained from data and from simulated events are fitted separately and the results are compared to extract a scale offset. The fitted width of the CB can be used to derive a data/MC correction for the resolution. Figure 4.8 shows the electron pair invariant mass for the case where both electrons are in EB, before and after applying the residual scale corrections derived on top of the standard ones.

A validation of the method adopted to obtain the corrections was performed by re-deriving the corrections in a sample of  $Z \rightarrow ee$  events on which the residual corrections are already applied. Non-perfect closure is expected because the residual corrections were calculated as a function of the kinematic variables of the leading electron, integrating over all the categories of the second one. The result of the closure are shown in Fig. 4.9 before and after applying the residual corrections. Considering only the  $p_T$  region of the  $Y_W$  analysis ( $30 \text{ GeV} < p_T < 45 \text{ GeV}$ ), the agreement in the scale between data and MC is below 0.2% (0.3%) in EB (EE).

The residual non-closure observed on  $Z \rightarrow ee$  events is taken as a systematic uncertainty on the measured scale corrections. The systematic uncertainty of the momentum scale is propagated to the signal templates used in the fit by varying the lepton  $p_T$  within  $1\sigma$ , where  $\sigma$  is the observed residual difference in the momentum scale between data and MC, taken from the non-closure as a function of the lepton  $p_T$ - $\eta$ .

## Muons

Scale corrections in the muon channel are obtained in the same way as for electrons. As far as the analysis is concerned, the standard muon corrections were found to achieve sufficient precision on the scale. Therefore, no additional work was done in this respect.

Figure 4.10 shows the inclusive  $Z$ -boson mass spectrum after applying the standard

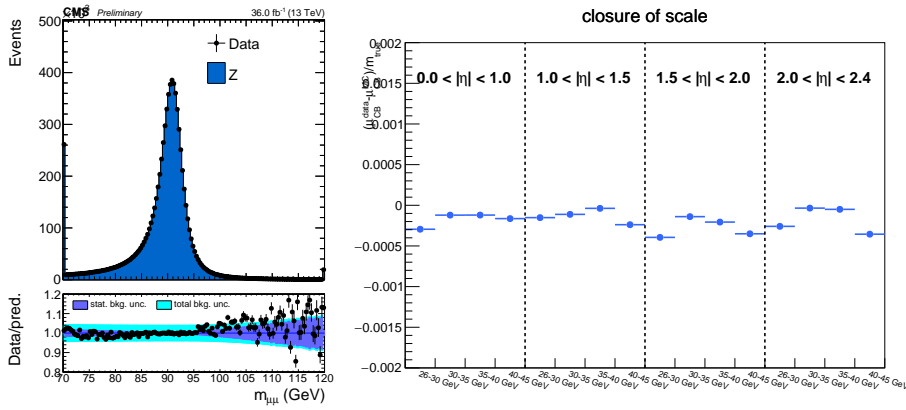


**Figure 4.10.** (left) Z-boson mass spectrum in  $Z \rightarrow \mu\mu$  events after applying the official scale corrections on muons. (right) residual non-closure of the scale corrections as a function of the muon  $p_T$  and  $\eta$ .

scale corrections on muons and the closure achieved as a function of the muon  $p_T$  and  $\eta$ . The residual non-closure is below  $5 \cdot 10^{-4}$  in the entire acceptance region.

## 4.6 Efficiency corrections

The helicity measurement is based on a fit to the lepton  $p_T$  vs.  $\eta$  distribution in data with simulated signal templates. Therefore, it is extremely important that simulations accurately reproduce the efficiency to select and identify leptons as in data. This is generally not the case and a proper reweighting of simulated events must be performed in order to restore the same efficiency in MC as in data. Therefore, dedicated sets of efficiency corrections were derived for the measurements discussed in this work.

The efficiency is computed in both data and MC for different stages of the lepton trigger and offline reconstruction.

- **reconstruction:** it is the probability to build a PF muon (electron) from a track (SC);
- **selection:** it summarizes the probability that a PF lepton passes the isolation and identification criteria;
- **trigger:** it represents the probability that an isolated and well-identified PF lepton satisfies the trigger requirements;

Each stage assumes that the previous one is already satisfied: therefore, the efficiency for the  $i$ -th stage represents the conditional probability that the lepton passes that selection stage having already satisfied all the previous ones. On top of the steps outlined before, an additional correction had to be derived in the electron channel to deal with a detector issue affecting the Level-1 trigger.

Since the efficiency is highly dependent on the lepton kinematics, it is measured as a function of the lepton  $p_T$  and  $\eta$  in granular bins of lepton  $\eta$  and in  $p_T$  in both data and MC. The so-called Tag-and-probe technique [53] is used, as explained in section 4.6.1.

Scale factors are defined as the ratio of the efficiency in data and MC, and are applied as weights to simulated events as a function of the lepton  $p_T$  and  $\eta$ . These scale factors modify

the both the shape and normalization of all the simulated templates that are estimated from MC.

#### 4.6.1 Tag-and-probe method

The Tag-and-probe (TnP) technique uses  $Z \rightarrow \ell\ell$  events to measure the efficiency of a given selection on a clean sample of leptons in data. Events are selected if they contain a pair of oppositely charged leptons with same flavor, whose measured invariant mass falls in a window around the Z mass peak (typically the range  $70 \text{ GeV} < m_{\ell\ell} < 110 \text{ GeV}$  is used). Then, one lepton in the pair is required to satisfy some strict selection criteria (it is referred to as the “tag”), while a more relaxed selection is applied on the other one (which is called the “probe”).

The fraction of probe leptons that pass the selection under scrutiny provides an estimate of its efficiency. The number of events passing or failing the selection on the probe lepton are evaluated through a fit to the Z-boson invariant mass distribution. The purpose of the fit is to allow the subtraction of the background component, which would otherwise bias the measured efficiency. The fit model is analogue to the one described in section 4.5 to derive the lepton momentum scale corrections. The fit is not necessary for the MC, as there is no background to be subtracted. In this case, the efficiency is evaluated by counting the events that pass or fail or not the selection on the probe lepton.

#### 4.6.2 Efficiency scale factors

The efficiencies for the muon and electron selection are shown in Fig. 4.11. The efficiency is relatively flat as a function of  $\eta$  for muons, while there is a strong dependency on  $\eta$  for electrons. This stems from the different electron identification criteria used in EB and EE, while homogeneous criteria are applied to muons.

The trigger efficiencies are shown in Fig. 4.12 for muons and electrons. They present a steep turn-on as a function of  $p_T$ . This is particularly evident in the electron channel, due to the tight energy thresholds applied by the L1 trigger with respect to the HLT.

The choice of a coarse  $p_T$  binning is motivated by the need to minimize the statistical uncertainty on the efficiencies measured in bins of  $\eta$  with width equal to 0.1. However, efficiencies can vary by up to 5% between consecutive  $p_T$  bins and therefore the application of the scale factors would create steps in the  $p_T$  distribution.

To avoid this issue, the discrete behavior of the efficiency is interpolated by fitting it as a function of  $p_T$  for each bin of lepton  $\eta$ . The functional form used in the fit is an error function defined as

$$f(x) = p_0 \cdot \operatorname{erf}\left(\frac{x - p_1}{p_2}\right); \quad \operatorname{erf}(y) = \frac{2}{\sqrt{\pi}} \cdot \int_0^y e^{-t^2} dt \quad (4.2)$$

where  $p_0$ ,  $p_1$ , and  $p_2$  are free parameters in the fit. They represent the plateau, the offset, and the steepness of the error function, respectively.

An example of this procedure is shown in Fig. 4.13 for the muon trigger efficiency in one  $\eta$  bin. The smoothing of the efficiency along  $p_T$  is performed for both data and MC, and the corresponding scale factors are obtained from the ratio of the interpolated efficiencies.

The scale factors are highly dependent on  $\eta$ , and are often characterized by large variations between consecutive  $\eta$  bins. Therefore, an additional smoothing was applied as a

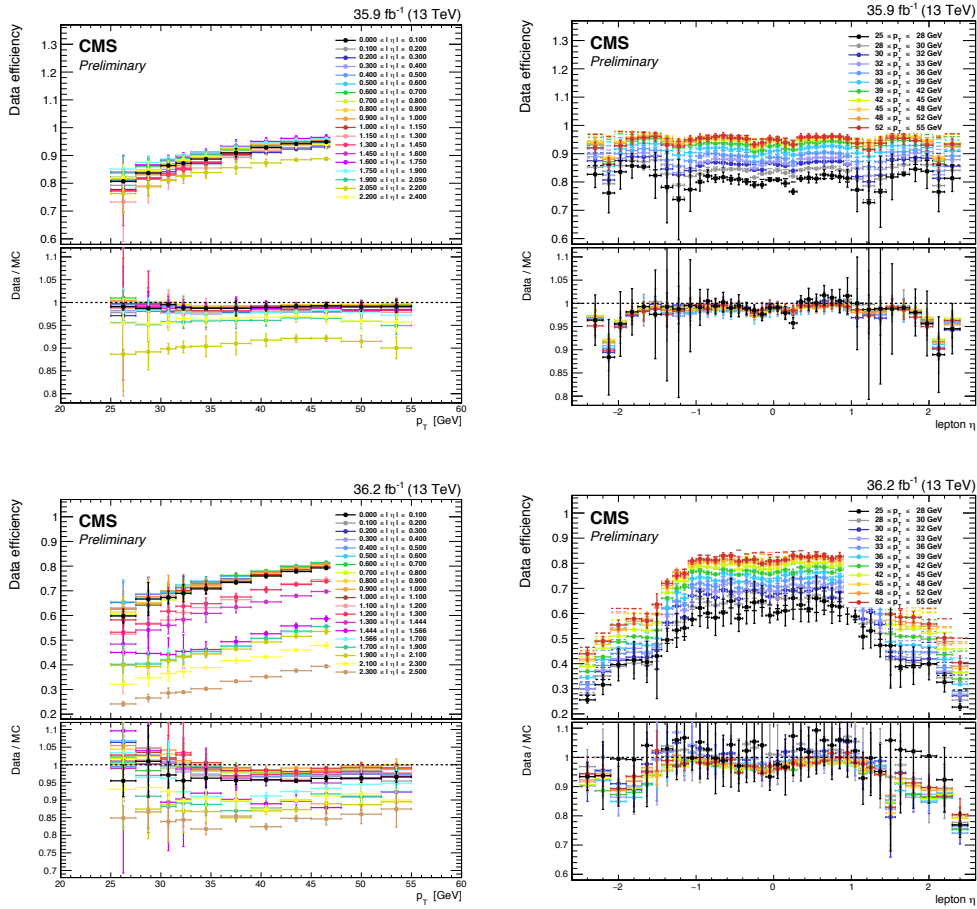


**Figure 4.11.** Selection efficiencies as a function of the muon (top) and electron (bottom)  $\eta$  and  $p_T$  in data. The lower panel shows the data/MC scale factors.

function of  $\eta$  on top of the aforementioned scale factors. It consists in splitting each original  $\eta$  bin in three segments: the scale factor in the central segment is left unchanged, while the one relative to the segment on each side is filled according to the linear interpolation of the scale factors between the central segment of that bin and the central segment of the neighboring one.

The scale factors for the trigger and selection efficiencies obtained after applying the procedure described above are shown in Fig.4.14 for both electrons and muons.

### Level-1 trigger pre-firing corrections

The scale factors derived for the analysis successfully cure most of the discrepancies between data and MC. However, a disagreement of up to 15% is still observed for the electron channel in the EE for  $|\eta| > 2.2$ , where the data/MC ratio is significantly lower than unity. This occurrence points to an additional source of inefficiency in data.

The origin of the inefficiency has been traced back to an issue affecting the trigger. In short, due to radiation damage, a time drift in the relative phase between the ECAL readout system and the Level-1 EG trigger was introduced. The effect turned out to induce

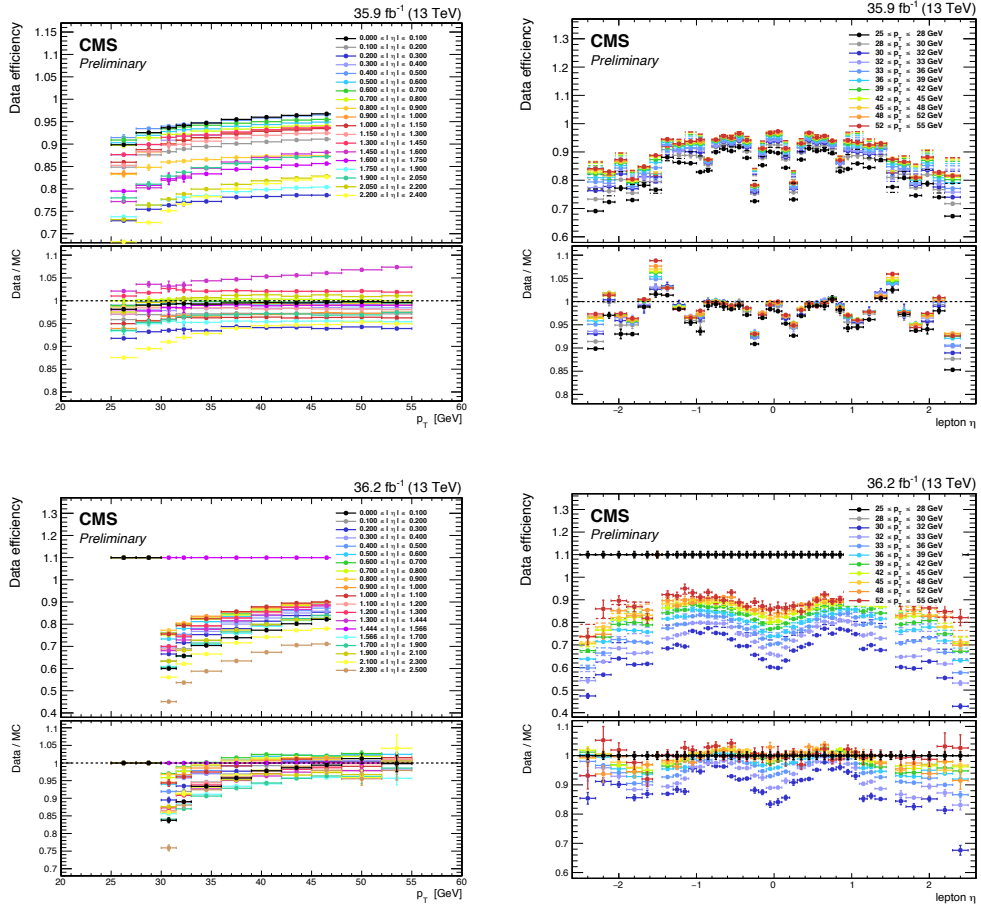


**Figure 4.12.** Trigger efficiencies as a function of the muon (top) and electron (bottom)  $\eta$  and  $p_T$  in data. The lower panel shows the data/MC scale factors.

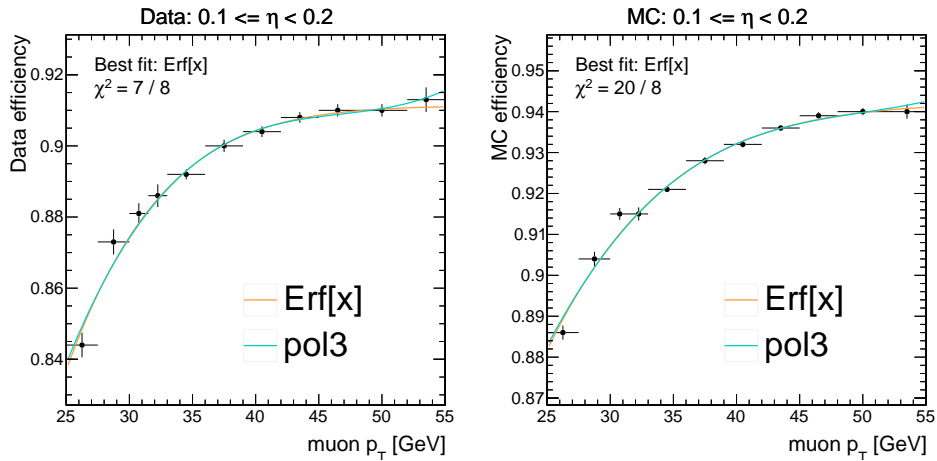


**Figure 4.13.** Trigger efficiencies for data (left) and MC (right) of the probe lepton for  $\eta$  between 0.1 and 0.2. The black points are the measured efficiencies, while the orange and turquoise lines represent fits to these points with an error function or a third order polynomial.

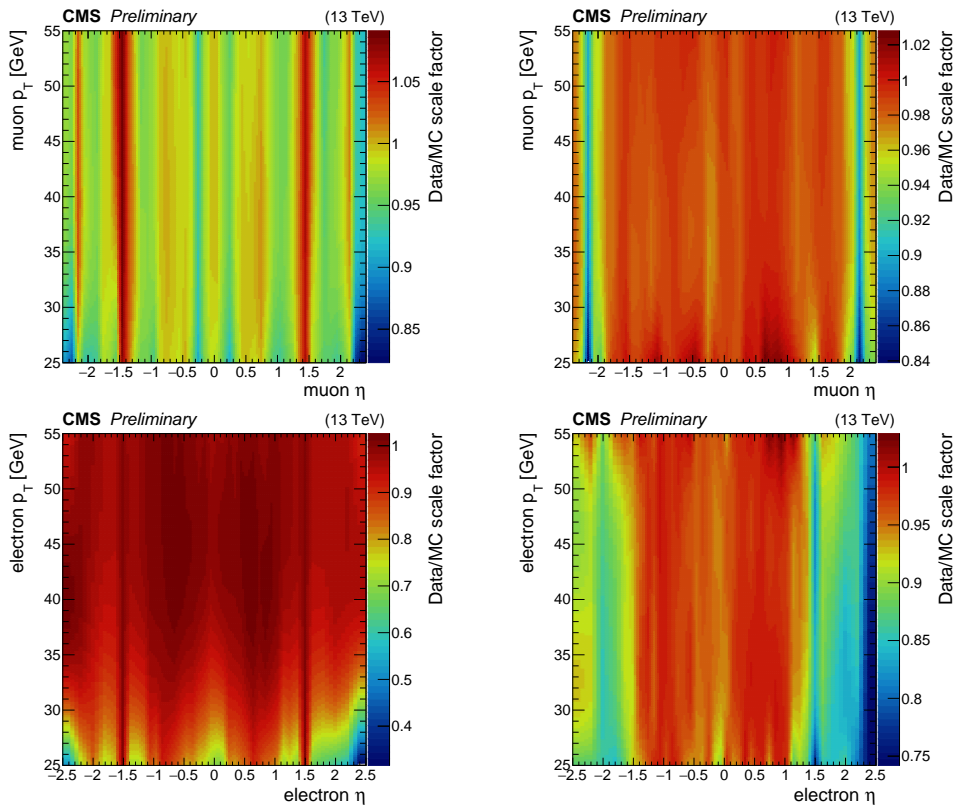


**Figure 4.14.** Scale factors for trigger (left) and selection (right) efficiency in the muon (top) and electron channel (bottom). These are obtained from the ratio of the smooth efficiencies in data and MC.

a significant level of “pre-firing”, causing the assignment of the event to the wrong bunch crossing (BX), typically to  $BX = -1$  ( $BX = 0$  refers to the in-time bunch crossing). Due to the trigger rules, whenever a given bunch crossing produces some activity that triggers the Level-1 decision, the two consecutive bunch crossings coming right afterwards are automatically vetoed. This implies that any time the L1 fires in  $BX = -1$  or  $-2$ ,  $BX = 0$  is rejected by the trigger decision, leading to a loss of efficiency in data.

This inefficiency is not accounted for by the TnP method in the derivation of the other efficiencies in data because pre-fired events are completely missing, both in the numerator and denominator. However, a similar TnP technique can be adopted to measure the pre-firing rate. Firstly, the trigger rules are exploited to select a set of un-preferable events in data where  $BX = -3$  has triggered the L1 decision, thus vetoing  $BX = -2$  and  $-1$  and preventing them from vetoing  $BX = 0$ . The size of this sample is about 0.2% of the total dataset. Then, using this data sample, events with a lepton pair from a Z-boson are selected, for which the tag lepton is required to pass tight selection criteria and be matched with an HLT electron candidate, and the probe is defined as an L1 EG candidate. Eventually, the pre-firing probability is defined as the fraction of probes matching  $BX = -1$ .

The pre-firing probability is measured as a function of the electron  $\eta$ . However, the small size of the sample of un-preferable events prevents the measurement in fine bins of  $\eta$  or differentially in  $p_T$ . Examples of fits in EE are shown in Fig. 4.15, while the measured

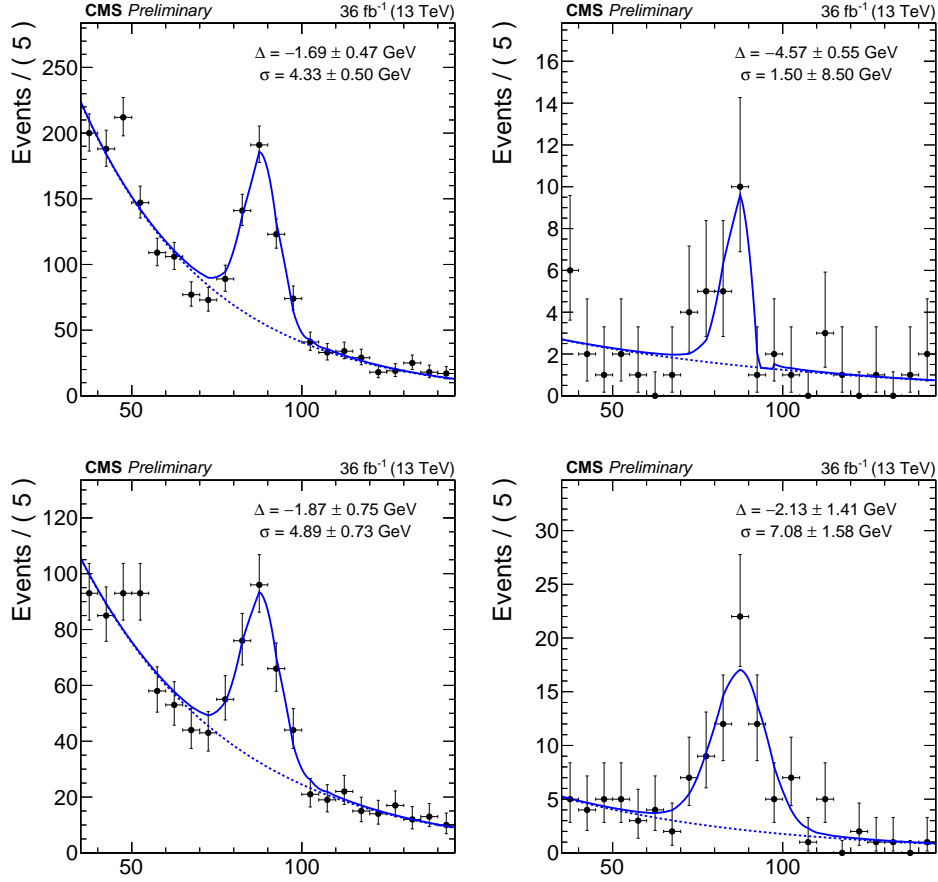


**Figure 4.15.** Invariant mass distribution for an electron pair composed of an offline-electron and a  $L1$  EG candidate, reconstructed in un-preferable events in the SingleElectron dataset. Left (right): probes associated to  $BX=0$  ( $BX=-1$ ). Top (bottom): probes in  $2.2 < \eta < 2.35$  ( $2.35 < \eta < 2.5$ ).

pre-firing probability is shown in Fig. 4.16. It can be observed that it is negligible in EB and becomes as large as 80% for  $\eta > 2.5$ .

As far as the  $Y_W$  measurement is concerned, it should be noted that the effect is relevant not only for signal electrons from  $W$  bosons, which are reconstructed up to  $|\eta| = 2.5$ , but also for the background made of events with  $Z \rightarrow ee$  for which one of the two electrons is lost in the endcap region with  $2.5 < |\eta| < 3.0$ , which is also the most affected region.

### 4.6.3 Validation of the corrections

The goodness of the efficiency corrections discussed before is assessed through a closure test in a sample of  $Z \rightarrow \ell\ell$  events, applying the same corrections and considering the 1-dimensional distributions of lepton  $p_T$  and  $\eta$ . Since the scale factors have to be used on both leptons, the distributions are filled using both the leading and the trailing lepton  $p_T$  and  $\eta$ . The results are shown in Fig. 4.17 and 4.18 for the muon and electron channel, respectively. The trigger scale factors are not applied in the bottom plots of Fig. 4.17, because of the ambiguity due to the fact that in almost all the events both muons from the  $Z$  bosons satisfy the SingleMuon trigger. This is the origin of the residual discrepancy between data and MC



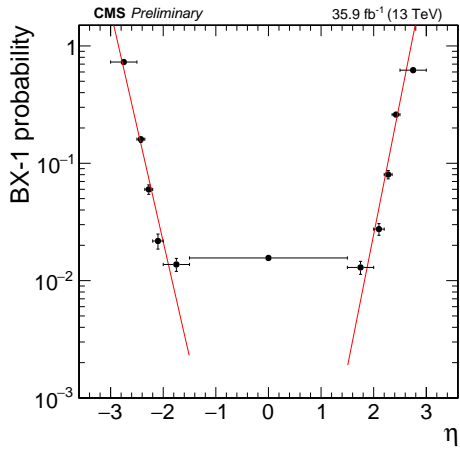


Figure 4.16. L1 EG pre-firing probability measured in data as a function of the electron supercluster  $\eta$  using the 2016 SingleElectron dataset. The red curve is the result of a fit with an exponential function used to smooth the efficiency.

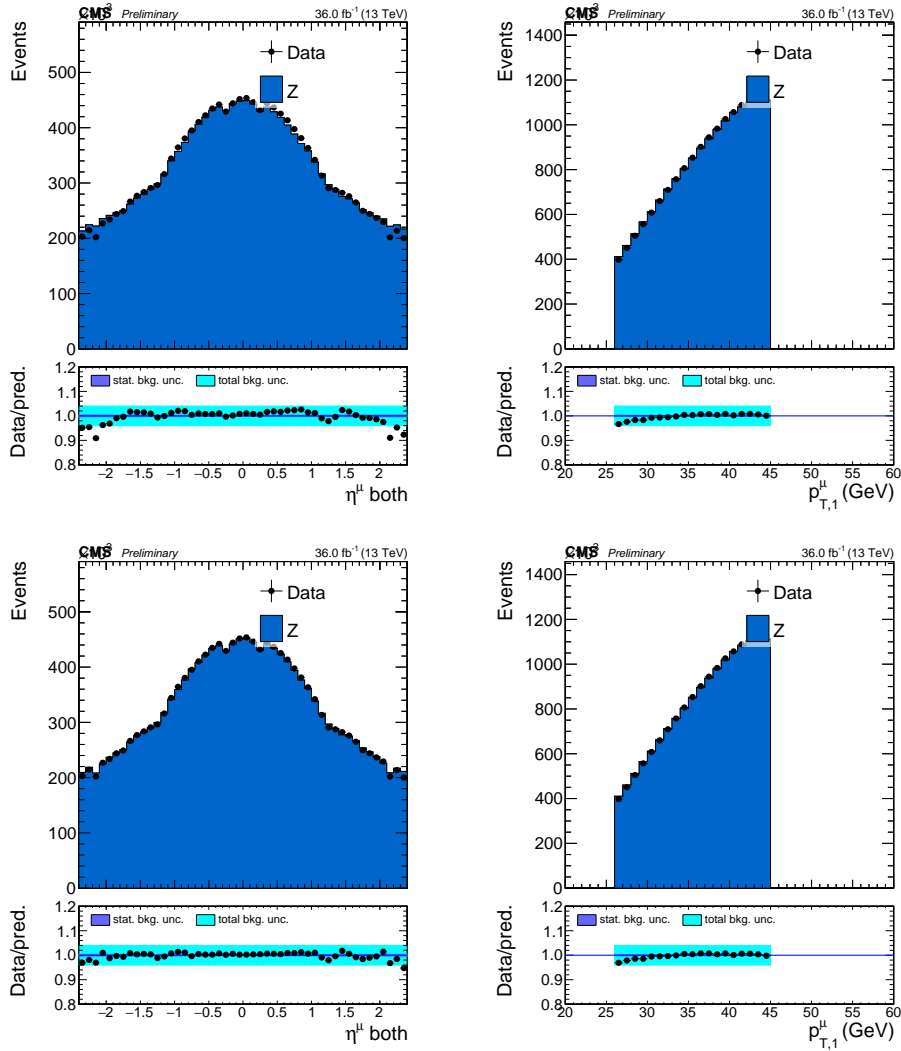
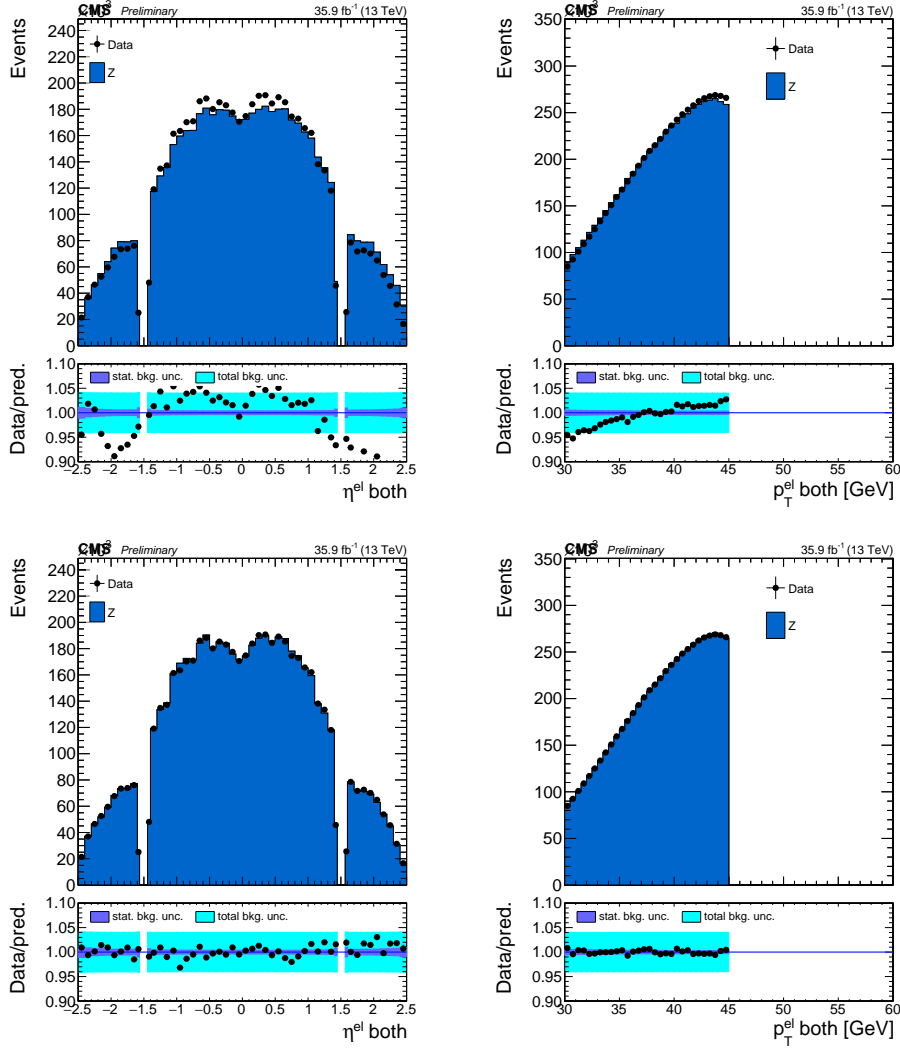


Figure 4.17. Closure test of efficiency scale factors in  $Z \rightarrow \mu\mu$  events:  $\eta$  and  $p_T$  distributions for muons before (top row) and after (bottom row) application of the selection scale factors. The light blue band represents the uncertainty in the cross section for simulated DY events (3.8%).



**Figure 4.18.** Closure test of efficiency scale factors in  $Z \rightarrow ee$  events:  $\eta$  and  $p_T$  distributions for electrons before application of any scale factor (top row), and after application of all data-MC scale factors (bottom row). The light blue band represents the uncertainty in the cross section for simulated DY events (3.8%).

for  $p_T < 30$  GeV, which is attributed to the uncorrected trigger turn-on.

The initial agreement between data and MC is already quite good for muons, but the usage of the efficiency scale factors significantly improves upon the baseline, especially at high  $\eta$ . On the other hand, the situation for electron looks much worse before applying the efficiency scale factors, especially without the trigger ones, while good closure is seen after using them. The level of agreement between data and MC after applying the corrections for the efficiency is generally below 3% and is roughly the same for both channels. It should also be observed that the corrections restore the symmetry along  $\eta$  in the ratio between data and MC yields. The symmetry is relevant for the helicity measurement, which is based on the fit to the  $p_T$ - $\eta$  template in data with simulated signal templates.

**Table 4.5.** *Uncertainty on the lepton efficiency scale factors (SF). The uncertainty due to the L1 pre-firing in the electron channel varies from 1 to 5% for  $|\eta| > 2$ .*

flavor	$ \eta $ region	SF uncertainty [%]
electrons	$ \eta  < 1$	0.6
	$ \eta  < 1.479$	0.8
	$ \eta  < 2$	1.3
	$ \eta  < 2.2$	$1.6 \oplus 1.0$
	$ \eta  < 2.5$	$4.0 \oplus 5.0$
muons	$ \eta  < 1$	0.2
	$ \eta  < 1.5$	0.4
	$ \eta  < 2.4$	1.4

#### 4.6.4 Systematic uncertainties

One source of uncertainty in the scale factors arises from the modeling of the Z-boson mass distribution in the derivation of the efficiency in data. The associated systematic uncertainty is estimated from the difference in the measured efficiencies observed after using alternative signal and background models in the fit, and is propagated to the scale factors. The origin of this uncertainty is the same for all  $\eta$  bins and therefore it is correlated among them. The magnitude of these uncertainties is summarized in Table 4.5. The alternative signal model consists in a template obtained from MC with a gaussian smearing, thus allowing the peak and the width to float freely in the fit. The background model in the sample of probes that pass the selection is a falling exponential, while in the samples of failing probes an exponential convoluted with an error function is used. The alternative background model is obtained using a polynomial. An example of a TnP fit in data in the electron channel is shown in Fig. 4.19 for one  $p_T$  bin in EB. The invariant mass distribution for the passing and failing probes is fitted using either the BW convoluted with the CB or a template obtained from MC as signal model. The effect of the L1 pre-firing is negligible for  $|\eta| < 2.0$  and only affects the electron channel. The corresponding uncertainty stems from the statistical uncertainty in the sample of un-preferable events: it varies between 1% and 5% for  $|\eta| > 2.0$  and is summed in quadrature to the other uncertainties mentioned above.

Another source of uncertainty is induced by the statistical uncertainty in the Z sample used to estimate the efficiency. This is considered as uncorrelated among different  $\eta$  bins. Indeed, the efficiencies are computed in bins of lepton  $p_T$ - $\eta$ , and therefore the subsamples of  $Z \rightarrow \ell\ell$  events used in each bin are statistically independent. The propagation of this uncertainty to the signal templates for the helicity measurement is implemented as three independent variations for each  $\eta$  bin, where the dependency on  $p_T$  in each bin is computed from the smoothing function in eq.(4.2) with a set of three decorrelated parameters of the fitted error function. This results in  $3 \times N_\eta$  varied templates for each signal category, where  $N_\eta$  is the number of  $\eta$  bins used to derive the efficiency scale factors. The variation of the efficiency due to this uncorrelated systematic uncertainty is shown in Fig. 4.20 for muons and electrons as a function of the lepton  $p_T$ - $\eta$ .

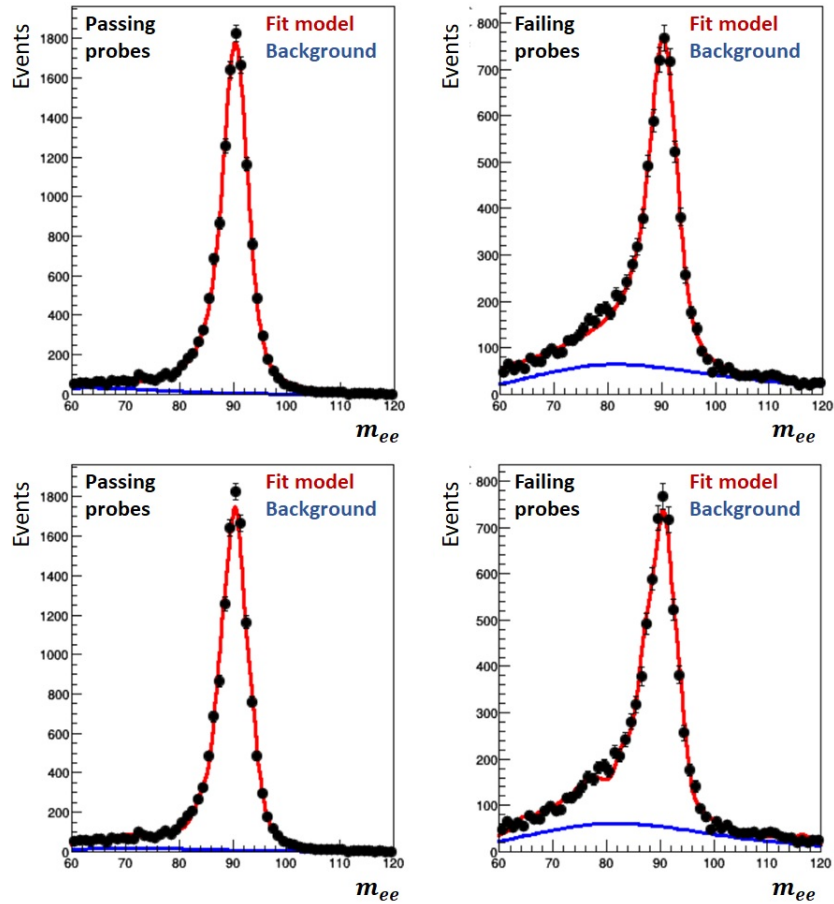


**Figure 4.19.** *TnP fits in data for the passing (left) and failing (right) probes. The top plots are made using a BW function convoluted with a CB as signal model, while in the bottom ones the signal is taken from a simulated template. To fill these distributions, the probes are selected with  $30 \text{ GeV} < p_T < 31.5 \text{ GeV}$  and  $0.7 < \eta < 0.8$ .*

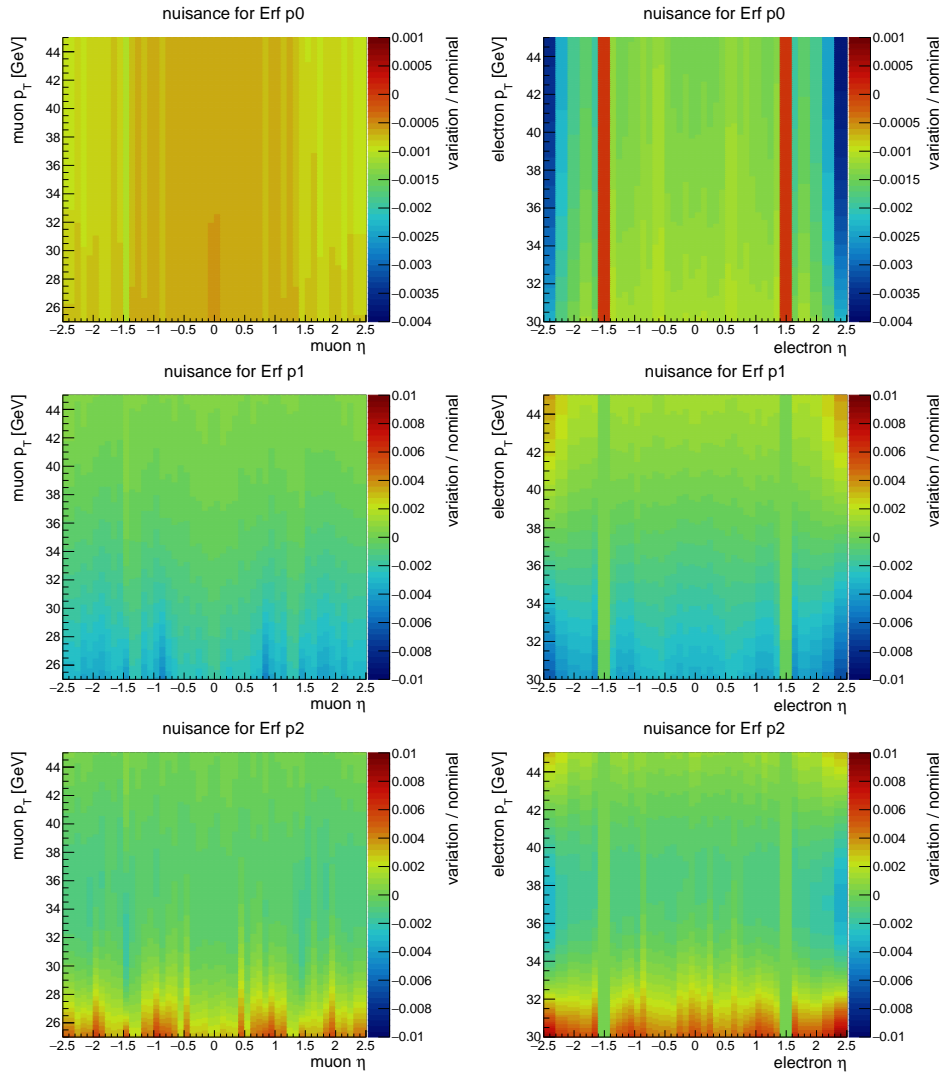


**Figure 4.20.** Muon (left) and electron (right) efficiency variations due to the decorrelated uncertainties from the 3 parameters of the error function used to model the efficiency as a function of the lepton  $p_T$  (see eq. (4.2)).



## Chapter 5

# Background estimation

The event selection described in chapter 4 is devised to enhance the signal purity and suppress the background component. However, the residual contribution from background processes to the final template in data is still not negligible and must be carefully evaluated to perform the measurement of the  $W$ -boson differential cross section. In this chapter, the techniques to estimate the backgrounds are presented.

It is possible to distinguish two typologies of background:

1. **prompt-lepton background:** it comprises electroweak (EWK) processes like  $DY$ ,  $W \rightarrow \tau\nu$ , and dibosons. The decays of these particles generate genuine isolated leptons that originate from the hard scattering vertex. For this reason, these are called prompt leptons. The production of top quarks, which immediately decay into a  $W$  boson and a  $b$ -quark, results both in prompt leptons from the  $W$  and leptons from the decay in flight of the  $b$ -quark, where the latter are more likely to appear less isolated and displaced from the primary vertex. For simplicity, all these processes are referred to as EWK backgrounds in the following;
2. **fake-lepton background:** it mainly consists of non-isolated leptons in the final state. This background is dominated by QCD multijet production, where the non-prompt lepton comes either from semileptonic decays of heavy-flavor mesons or a misidentified jet, usually from light quarks: the former is basically the only source of QCD background in the muon channel, while the latter dominates the background composition in the electron channel, along with electron pair production from photon conversions. This background is referred to as QCD or “fakes” and it is estimated from data.

The cross section for the EWK processes listed above is lower than the signal one, as reported in table 4.2. Moreover, these backgrounds are reduced to a small component after applying the signal selection. Since their kinematics is well reproduced by simulation and the theoretical cross sections are known with good precision, these backgrounds are estimated directly from simulation.

QCD represents the main background for the analysis. The associated cross section is several orders of magnitude larger than the one of the signal, which makes it unfeasible to simulate a number of events corresponding to the integrated luminosity in data. In addition, simulations do not accurately reproduce all the underlying processes. For example, a significant component of QCD background in the electron channel arises from charge

exchange processes in the calorimeter, or the matching of energy clusters from  $\pi^0$  in ECAL with random tracks. These are not well represented by simulations. On the other hand, other processes such as the production of leptons from decays of heavy-flavor quarks are relatively well described by MC. However, the small efficiency of the signal selection on QCD events and the large difference between the cross sections for signal and QCD makes simulations an unreliable tool to estimate the QCD background.

Hence, the QCD background must be estimated in a data driven way. In this analysis, the fake-rate (FR) method is used. The procedure is the same in both the muon and the electron channel and has the advantage of being able to predict both the normalization and the distribution of the QCD background, without relying on QCD simulations. The FR method is a common technique used at colliders to estimate QCD background. The following sections provide a general description of the method and the dedicated work that was performed in the context of the helicity measurement to predict the QCD background and assign a systematic uncertainty on the prediction.

## 5.1 Fake-rate method

Ideally, the procedure to estimate the QCD background would consist in measuring the probability that, given a QCD multijet event, a lepton is reconstructed which satisfies the selection criteria used in the analysis. In fact this is not feasible because the efficiency of the signal selection on a QCD sample is of the order of  $10^{-6}$ , which implies that the measurement of the QCD misidentification probability would be affected by a large relative uncertainty.

Therefore, it is actually more appropriate to perform this measurement in a phase space where a physics object, for instance a jet, has been already identified as a lepton with a loose set of selection criteria. This baseline selection defines the denominator for the computation of the misidentification probability. It must be loose enough to ensure that the selected sample in data is enriched in QCD events with respect to signal or other background processes. Then, the misidentification probability, denoted by fake-rate (FR), is measured as the fraction of these events for which the candidate lepton satisfies all the identification criteria of the analysis, that define the numerator. It should be noted that this definition of the FR is practically more suited for a physics analysis, for which selected events are already biased by the trigger selection. It should also be stressed that the FR is not a universal quantity, but strictly depends on the selection criteria defining the numerator and denominator.

In summary, the QCD background is estimated through the following two steps:

1. measure the probability that a physics object that was identified as a lepton based on a “loose” set of predefined identification criteria also passes the same “tight” identification selection as applied to leptons in signal events. This step is performed using a QCD-enriched sample of events in data;
2. use this probability (the FR) to reweight a subset of events in data that pass the “loose” but not the “tight” selection.

The terms “loose” and “tight” simply refer to the chosen selection applied at denominator and numerator when computing the fake-rate. The phase space of events failing the numerator selection is referred to as the FR application region.



Let  $N_{loose}^{QCD}$  be the number of QCD events passing the denominator selection, and  $N_{tight}^{QCD}$  the subset of these events that pass also the ‘‘tight’’ identification of the signal region, which one wants to estimate. Let  $f$  be the lepton FR. Then, the following relation can be written:

$$\begin{aligned} N_{tight}^{QCD} &= N_{loose}^{QCD} \cdot f \\ &= (N_{notTight}^{QCD} + N_{tight}^{QCD}) \cdot f \end{aligned} \quad (5.1)$$

from which

$$N_{tight}^{QCD} = \frac{f}{1-f} \cdot N_{notTight}^{QCD} \quad (5.2)$$

where  $N_{notTight}^{QCD}$  denotes the number of QCD events in the application region. If the application region is dominated by QCD,  $N_{notTight}^{QCD}$  can be obtained as the event yield in data ( $N_{notTight}^{QCD} \approx N_{notTight}^{data}$ ). The advantage of the reparametrization in eq. (5.2) with respect to the second member of eq. (5.1) is that  $N_{notTight}^{QCD}$  is an orthogonal set of events with respect to the signal region. Moreover, using only those events that fail the numerator selection ensures that the space of events to be reweighted is enriched in QCD, thus reducing the systematic uncertainty induced by the prompt-lepton contamination from electroweak processes. Indeed, the set of events passing the loose selection in data does not constitute a pure QCD region, because it also includes the signal.

The formula in eq.(5.2) is obtained under the assumption that the prompt-lepton rate ( $p$ ) tends to unity. The prompt rate (PR) is the efficiency that a real prompt lepton passing the loose selection also satisfies the tight one. If  $p \approx 1$ , the contamination of prompt leptons in the application region is negligible. Since the lepton efficiency is significantly different from unity, especially in the electron channel, the contamination of prompt leptons cannot be neglected and the following general expression has to be used to estimate the QCD component:

$$N_{tight}^{QCD} = \frac{f}{p-f} \cdot (p \cdot N_{notTight}^{data} - (1-p) \cdot N_{Tight}^{data}) \quad (5.3)$$

As  $p$  approaches unity, the second term on the right hand side of eq. (5.3) tends to zero, and the formula reduces to eq. 5.2. Otherwise, the second term represents a negative correction factor that takes into account the presence of non-QCD events in the data sample to which the method is applied.

In the analysis, the QCD background is estimated by means of the general formula in eq. (5.3). Each event in data is reweighted with the factor  $fp/(p-f)$  if it fails the numerator selection, and with the factor  $-f(1-p)/(p-f)$  otherwise. The event weight depends on both the FR and PR. These are computed differentially in the lepton  $p_T$  and  $\eta$ .

## 5.2 Fake-rate measurement

The FR is measured in events with dijet-like topology with one well identified high- $p_T$  jet and a loosely identified lepton, the ‘‘fakeable’’ object, that might be a jet mis-identified as a lepton. These events are selected from the same dataset as for the signal region, that is to say, the SingleElectron or the SingleMuon dataset for the electron and muon channel respectively.

The probability to pass the identification criteria is highly dependent on the lepton  $p_T$  and  $\eta$ . Taking advantage of the large available dataset, the FR is computed as a function of the lepton  $p_T$  in bins of  $\eta$  with width  $\Delta\eta = 0.1$ . Positive and negative  $\eta$  sides are considered separately to account for possible asymmetries in the detector.

The denominator is defined applying the following selection criteria, which define the ‘‘computation region’’:

- there is exactly one lepton that passes the preselection defined in section 4.4;
- there must be at least one jet with  $p_T > 30$  GeV and  $\Delta R(\text{lep}, \text{jet}) > 0.7$ ;
- $m_T < 40$  GeV.

The  $\Delta R$  requirement is meant to reject events where the lepton overlaps with the jet. The selection on  $m_T$  makes the computation region orthogonal to the signal region and ensures that the former is enriched in QCD multijet events. The selection defining the numerator has already been reported in section 4.4 for each lepton flavor.

In the muon channel, the isolation variable provides good discriminating power between the fake-lepton background and the prompt-lepton sample. Indeed, fake leptons in the muon channel originate mostly from decays in flight of heavy-flavor mesons and tend to be less isolated than prompt leptons. Instead, in the electron channel one has to require that either the isolation or the ID selection (or both) is not satisfied to define the application region, as the dominant source of fakes is jet misidentification: a jet can appear as an isolated electron if it has a large electromagnetic component, but it will most likely fail the other identification criteria.

The computation region is not a pure QCD sample. Therefore, the EWK contamination has to be removed to avoid a bias in the measured FR. Since the EWK component is well described by simulation, the expected number of EWK events in simulation is subtracted from data in both denominator and numerator. Therefore, the FR is defined as

$$f_{ij} = \frac{N_{ij}^{\text{tight}}(\text{data}) - N_{ij}^{\text{tight}}(\text{EWK})}{N_{ij}^{\text{loose}}(\text{data}) - N_{ij}^{\text{loose}}(\text{EWK})} \quad (5.4)$$

where  $i, j$  denote the specific bin of lepton  $p_T$  and  $\eta$ . The PR is obtained directly from MC as  $p_{ij} = N_{ij}^{\text{tight}}(\text{EWK})/N_{ij}^{\text{loose}}(\text{EWK})$ .

### 5.2.1 Electrons

The electron FR and PR measured in some bins of  $\eta$  are shown in Fig. 5.1. In order to reduce the associated statistical uncertainty, the PR is measured in an inclusive sample of events with a W or a Z boson, top quark(s) or dibosons, as no significant difference is found among the PR measured from each single EWK process.

The black (red) graph shows the FR in data before (after) the electron PR subtraction. At higher  $p_T$ , the two graphs tend to diverge due to the larger fraction of prompt leptons, mainly from decays of W and Z bosons. The blue graph represents the electron PR obtained from MC. The green graphs are obtained from data after subtracting the contributions from EWK processes scaled by  $\pm 1\sigma$  of their respective cross section uncertainty. The scaling of the EWK normalization induces a variation in the measured FR due to the subtraction in eq. (5.4). This variation increases at higher  $p_T$  and becomes significant in EB, where the

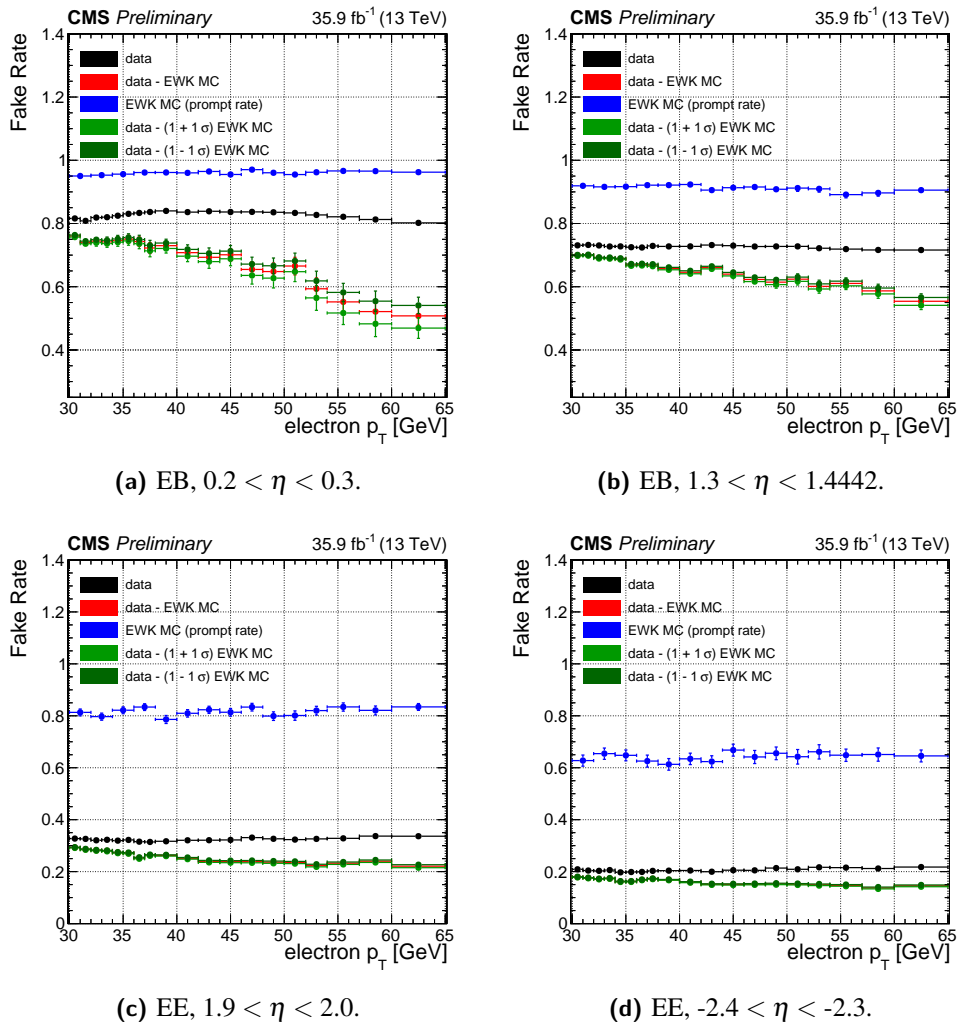


**Figure 5.1.** Electron fake-rate (FR) as a function of electron  $p_T$  is few bins of electron  $\eta$ . The black and red graphs show the FR in data before and after the electron prompt-rate (PR) subtraction respectively. The blue points show the electron PR obtained from simulated events with a W or Z boson, or top and dibosons production. The error bars represent the statistical uncertainty on the measured rate: it is larger at low  $\eta$  for the FR, while the opposite behaviour holds for the PR. The green graphs are obtained from data after subtracting the EWK component, scaled by  $\pm 1\sigma$  of its cross section uncertainty

EWK component is larger than in EE. However, it is generally small within the  $p_T$  range of the analysis. Both the FR and PR are significantly different between EB and EE due to non homogeneous lepton identification criteria adopted in the two partitions both in the numerator and denominator.

The  $p_T$ - $\eta$  template for the QCD background used in the W-boson rapidity measurement is built using events in data, reweighted according to eq. (5.3). In order to avoid spurious steps in the QCD background template due to the coarse  $p_T$  binning used to compute the FR, the measured FR is interpolated by fitting the graphs with a first order polynomial. The

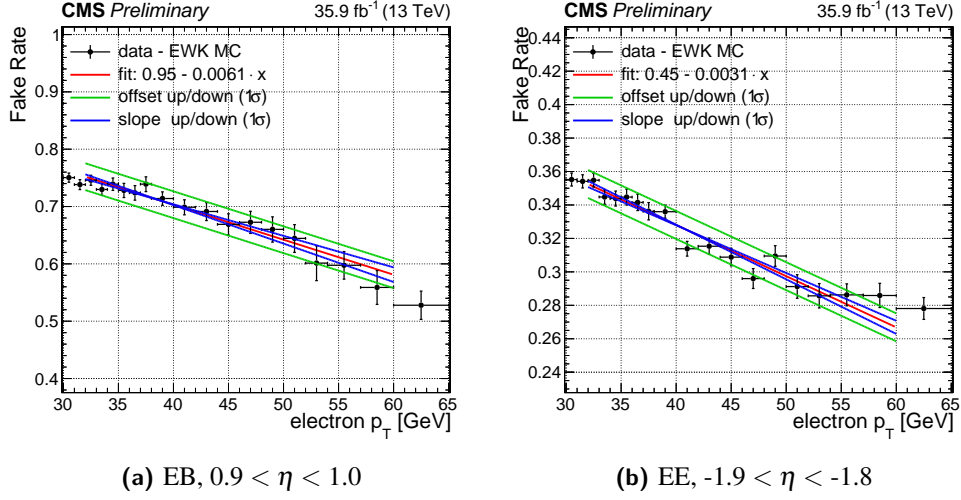


**Figure 5.2.** Fitted electron fake-rate (FR) in two bins of  $\eta$ , one in EB (left) and one in EE (right). The fit is performed with a straight line (in red) between 32 and 60 GeV. The green and blue lines are obtained scaling the fitted offset and slope by  $\pm 1\sigma$  of their uncertainty.

same procedure is applied for the PR, which is found to be well described by a straight line. Figure 5.2 shows the results of the fits in some  $\eta$  bins. Although the analysis acceptance is restricted to  $p_T < 45$  GeV, the interpolation is performed in a wider range to increase the lever arm in the fit.

The background due to Z bosons represents a large fraction of the events in the computation region. This background is made of  $Z \rightarrow ee$  events where the second electron is not vetoed by the selection and is reconstructed as a jet. A small discrepancy in the Z normalization can bias the FR measurement around 45 GeV where the Jacobian peak of the Z boson is expected. Therefore, in order to suppress the  $Z \rightarrow ee$  component, events are rejected if the reconstructed invariant mass computed with the electron and the jet lies within a window of 10 GeV around the observed mass peak.

A global summary of the smoothed fake and prompt-rate as a function of electron  $p_T$  and  $\eta$  is shown in Fig. 5.3. The goodness of the linear fit to describe the FR was assessed through a validation test in a QCD-enriched sideband of the signal region, as described in section 5.3.

### 5.2.2 Muons

The muon trigger is much looser than the offline selection and provides a larger sample enriched in jets for the loose to tight extrapolation. The procedure to measure the muon FR is very similar to the one in the electron channel, except in the way the EWK component is subtracted.

For each bin of muon  $\eta$ , the inclusive  $m_T$  distribution in data is fitted with the sum of the analogue distributions in simulated QCD multijet and EWK events, where the EWK component includes events with a W or a Z boson decaying into muons. The yields of the QCD and EWK components are left free to float independently in the fit. The fit has the purpose of extracting a normalization scale factor for the EWK component, allowing for

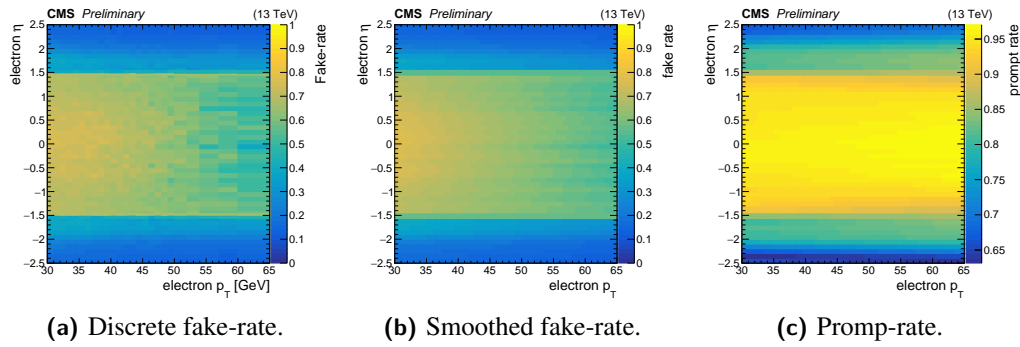


**Figure 5.3.** Electron FR before smoothing (left), after smoothing (middle) and PR (right) as a function of electron  $p_T$  and  $\eta$ . The FR is obtained from data after subtracting the yields of EWK processes. The PR is measured from MC using events with a  $W$  or a  $Z$  boson, top quark or dibosons.

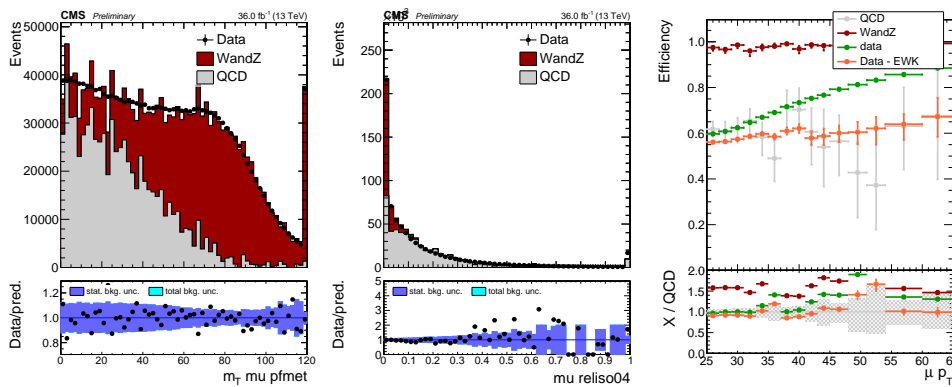


**Figure 5.4.** Example of muon fake-, and prompt-rate derivation in  $1.9 < \eta < 2.0$ .

the measurement of the FR with the best possible estimate of the EWK normalization. This method requires the usage of a QCD MC and therefore it is not feasible in the electron channel due to the much tighter trigger and the limited size of the simulated QCD sample.

The region where the FR is measured is defined as in the electron channel by requiring  $m_T < 40$  GeV. The previously measured scale factor is applied to the EWK yields in eq. (5.4) before subtracting them from data. Fig. 5.4 shows an example of this procedure for one  $\eta$  bin. The left panel shows the  $m_T$  distribution in which the scale factor for the EWK processes is derived. The central panel shows the isolation spectrum in the region with  $m_T < 40$  GeV in which the fake-rate is calculated. The rightmost panel finally shows the fake-rate and prompt-rate as a function of  $p_T$  for this particular  $\eta$  bin. After the subtraction of the EWK component from data, the measured FR (in orange) becomes consistent with the one expected from QCD MC (in gray).

### 5.3 Fake-rate validation

The QCD background estimation method is validated in a sideband of the signal region. The validation region is defined with the same selection criteria as the signal region except for

the transverse mass cut, which is substituted with the requirement  $m_T < 40(30)$  GeV for the muon (electron) channel. The inverted  $m_T$  cut has the purpose of enriching the validation region in QCD events. The inclusive  $p_T$  and  $\eta$  distributions are shown in Figure 5.5 for the electron and muon channel. All the corrections discussed in chapter 4 are applied to selected leptons. The agreement between data and the prediction is generally better than 4%, suggesting that the procedure adopted to estimate the QCD background provides a reliable description of this component. The dark colored band in the lower panel represents the statistical uncertainty on the background prediction, while the light band is obtained by summing the systematic uncertainty in quadrature. The systematic uncertainty in the light band only accounts for the normalization uncertainty on each component: 30% is assigned to the QCD background for illustration purpose only. The sources of systematic uncertainty that are considered for the QCD background estimate in the helicity measurement are described in Sect. 5.4.

## 5.4 Systematic uncertainties

In this section, the systematic uncertainties on the QCD background estimate are discussed. These uncertainties account for the modeling of the QCD through the FR, and affect the QCD template in the helicity measurement by changing both its global normalization and the shape as a function of  $p_T$ - $\eta$ .

The following sources of uncertainty are considered:

- modeling of the FR versus  $p_T$ : for each  $\eta$  bin, the FR is modeled as a straight line as a function of  $p_T$ . An alternative parametrization of the measured FR is obtained by varying the slope of the fitted line by  $\pm 1\sigma$  of its uncertainty, as shown in Fig. 5.2 (blue solid line);
- composition of the QCD event sample in data: the QCD background arises from different processes. The measured FR can vary depending on the relative fraction of each process in the event sample used to derive the FR. These fractions, that can be different in the computation and application region, depend mainly on the jet composition and are correlated with the  $p_T$  of the jet. Therefore, the FR and PR are derived again by increasing the jet  $p_T$  from 30 to 45 GeV. The ratio of the FR and PR for the two  $p_T$  thresholds as a function of the lepton  $p_T$  and  $\eta$  are shown in Fig. 5.6 and 5.7 for the electron and muon channel, respectively.

The muon channel is more affected than the electron one: a possible explanation is that the QCD background in the former is dominated by the production of non-isolated leptons from decays in flight of heavy quarks, and the isolation efficiency is highly correlated with the  $p_T$  of the jet; on the contrary, the QCD background in the electron channel originates primarily from jet misidentification, which is less dependent on the  $p_T$  of the jet within the kinematic acceptance of the analysis;

- normalization of the EWK component: the expected yields of the EWK processes are subtracted from data in both denominator and numerator in each bin of  $p_T$ - $\eta$  before measuring the FR. Since the relative fraction of EWK events in data is not negligible, especially in the electron channel, the uncertainty in the EWK normalization can lead to significant variations of the measured FR. To assess the magnitude of this effect,

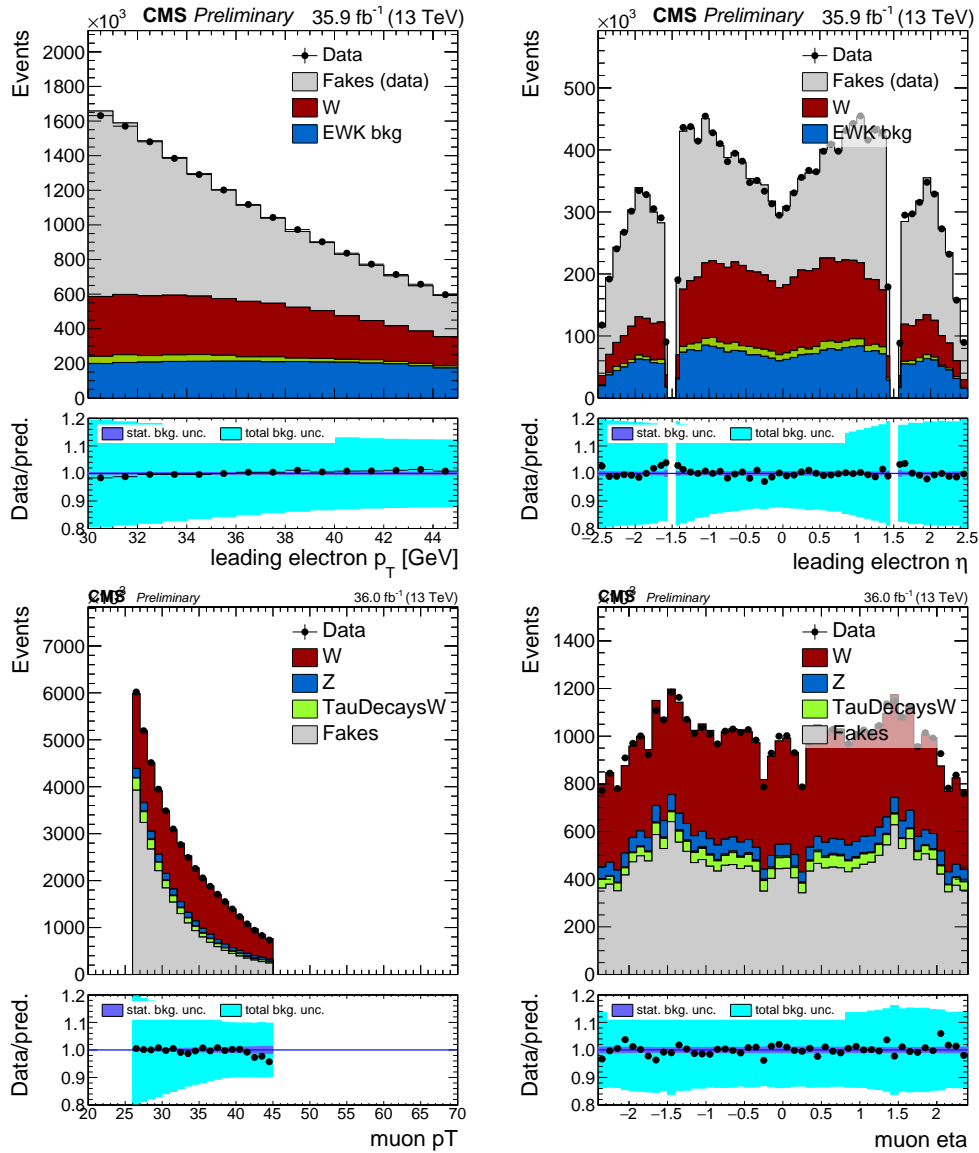


**Figure 5.5.** Distributions of electron and muon  $p_T$  and  $\eta$  in the FR validation region. The QCD component, denoted as “Fakes” in the plots, is estimated from data using the FR method. The normalization of the QCD process is floated to match the observed yield in data. The light green component in the stack is the contribution of the  $W \rightarrow \tau\nu_\tau$  background. The sum of Drell-Yan, Top and dibosons is shown in blue.

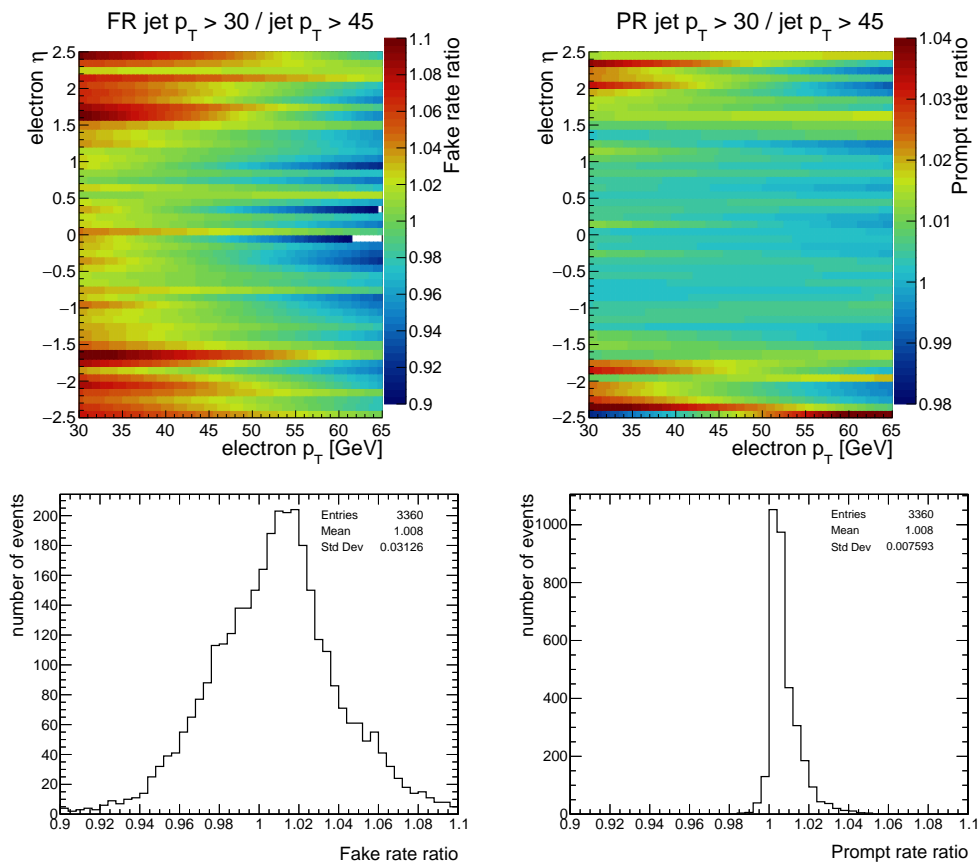


**Figure 5.6.** Ratio of the measured FR (left) and PR (right) in the electron channel, obtained selecting events with jet  $p_T > 30$  or  $45$  GeV. The top plots show the ratio as a function of the lepton  $p_T$ - $\eta$ , while the bottom ones show the distribution of the ratio.

the FR is computed by scaling up or down the global normalization on the EWK processes according to the uncertainty in their respective theoretical cross section. This procedure results in an alternative distribution for the FR as a function of  $p_T$ . The magnitude of the FR variation depends on  $p_T$ . In the electron channel, the effect is quite significant in central EB and negligible in outer EB and EE, as shown in Fig. 5.1 (dark and light green graphs).



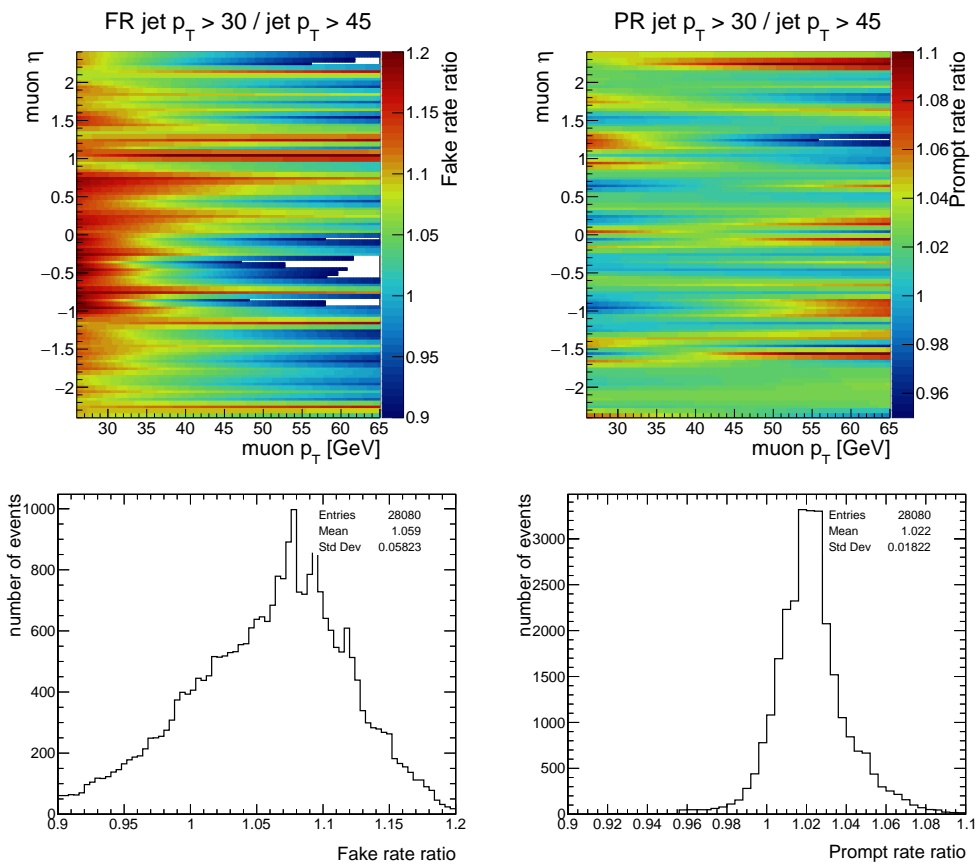


**Figure 5.7.** Ratio of the measured FR (left) and PR (right) in the muon channel, obtained selecting events with  $\text{jet } p_T > 30$  or  $45$  GeV. The top plots show the ratio as a function of the lepton  $p_T$ - $\eta$ , while the bottom ones show the distribution of the ratio.



## Chapter 6

# Maximum likelihood fit

The measurement of the W-boson rapidity relies on a fit to the 2-dimensional  $p_T$ - $\eta$  distribution of the charged lepton in data with binned templates for signal and background processes. The aim of the fit is to statistically subtract the backgrounds and unfold the generator-level W-boson differential cross section as a function of the rapidity and helicity state. The same approach can be followed to measure the W-boson charge asymmetry and double-differential cross section as a function of the generator-level lepton  $p_T$  and  $\eta$ .

The expression "generator-level", often used as a synonym for "stable-particle-level" in the following, refers to unfolded quantities evaluated before detector and resolution effects. Presenting the measurement in terms of generator-level cross section is very convenient, as it allows for direct comparison of data with theoretical predictions and analogue results from other experiments, without the need to pass generated events through a simulation of the CMS detector. Concerning the generator-level lepton, it is worth reminding that the pre-FSR definition of the lepton is considered, as already described in Sect. 2.3.

Signal templates are built using the NLO  $W + \text{jets}$  Monte Carlo sample: each template corresponds to a given bin in  $|Y_W|$ , helicity state, and charge. There are 16 bins in  $|Y_W|$ : 15 of them span the region  $0 < |Y_W| < 3.0$  with uniform width of 0.2, while the last one covers the region with  $3.0 < |Y_W| < 6.0$ . As discussed in chapter 2, the analysis starts losing sensitivity for  $|Y_W| \gtrsim 3.0$  because of detector acceptance, so that no attempt is made to probe large rapidity values with finer granularity. Each template comprises 912 (750)  $p_T$ - $\eta$  bins with 0.1 granularity in  $\eta$  and 1 GeV in  $p_T$ , corresponding to 19 (15)  $\times$  48 (50)  $p_T$ - $\eta$  bins in the muon (electron) channel.

$W + \text{jets}$  events are considered as signal if the charge of the reconstructed lepton matches the one of the generator-level lepton from the W-boson decay. Those events for which this condition is not fulfilled constitute the charge-flips background. One fit component, described by its own 2D template, is considered for each background process in Table 6.1. The QCD template is obtained from data through the fake-rate method, while the others are obtained directly from simulations.

About 105M (44M)  $W^+$  and 79M (35M)  $W^-$  events are expected in the muon (electron) final state. Table 6.1 reports the total expected signal and background yields in  $35.9 \text{ fb}^{-1}$  and the number of events observed in data after the selections.

The inclusive  $p_T$  and  $\eta$  distributions in the signal region after the full selection and with the QCD background predicted with the fake-rate method are shown in Fig. 6.1a and 6.2a for the electron and muon channel, respectively. The yields of each process in the electron

**Table 6.1.** *Expected and observed yields after the full event selection, split in lepton charge and flavor. The charge-flips background is considered only for electrons.*

Process/channel	$W^+ \rightarrow \mu^+ \nu_\mu$	$W^- \rightarrow \mu^- \bar{\nu}_\mu$	$W^+ \rightarrow e^+ \nu_e$	$W^- \rightarrow e^- \bar{\nu}_e$
$W_L$	66400000	38200000	26900000	16100000
$W_R$	33300000	36500000	14400000	16500000
$W_0$	5620000	4770000	2370000	2100000
QCD	4070000	4200000	3610000	3920000
Z	4150000	3680000	1570000	1500000
$W \rightarrow \tau \nu$	2600000	2150000	788000	661000
Top	404000	368000	187000	172000
dibosons	86700	81300	38000	35900
Charge-flips	N/A	N/A	15600	22200
data	113680384	88392044	50920954	42021006

channel are scaled through a  $\chi^2$  fit according to their cross-section uncertainty in order to match the total number of events in data. The lower panel in each plot shows the ratio of observed and predicted yields. The dark band represents the statistical uncertainty in the prediction, while the light band also includes the uncertainty in the cross section for each process (Table 6.2).

## 6.1 Extraction of the W-boson helicity

The signal cross section is extracted through an extended simultaneous maximum likelihood fit to the binned distributions of lepton  $p_T$  vs.  $\eta$  for both charges and lepton flavors. Systematic uncertainties are treated as nuisance parameters in the likelihood.

In the likelihood fit, each  $p_T$ - $\eta$  template is unrolled into a 1-dimensional distribution obtained by joining consecutive stripes of the original  $p_T$ - $\eta$  distribution at constant  $p_T$ . The unrolled template for the electron (muon) channel is shown in Fig. 6.1b ( 6.2b). The corresponding distribution of pulls, which are defined as the difference between the observed and predicted yields divided by the uncertainty on the prediction, is shown as well. The likelihood fit receives the unrolled template for each process as input.

The likelihood can be written as:

$$\mathcal{L}(\text{data} | \vec{\sigma}, \vec{n}_{\text{bkg}}, \vec{\theta}_S, \vec{\theta}_B) = \prod_{i=1}^{n_{\text{cat}}} \prod_{j=1}^{n_{\eta, p_T}} \left( \sum_{k=1}^{n_{Y_W}} \sum_{m=L, R, 0} \sigma_{\text{km}}(\vec{\theta}_S) \cdot S_{\text{km}}(\eta, p_T | \vec{\theta}_S) \cdot L_{\text{int}} + \sum_{l=1}^{n_{\text{bkg}}} n_l \cdot B_l(\eta, p_T | \vec{\theta}_B) \right)^{n_{\text{ev}}^{ij}} \cdot \text{Poisson} \left( n_{\text{ev}}^{ij} \middle| n_{\text{sig}}^{ij} + \sum_{l=1}^{n_{\text{bkg}}} n_l^{ij} \right) \cdot p(\vec{\theta}_S) \cdot \prod_{l=1}^{n_{\text{bkg}}} p_l(\vec{\theta}_B) \quad (6.1)$$

where

- $n_{\text{cat}} = 4$  is the number of analysis categories (2 charges times 2 lepton flavors),  $n_{Y_W}$  is

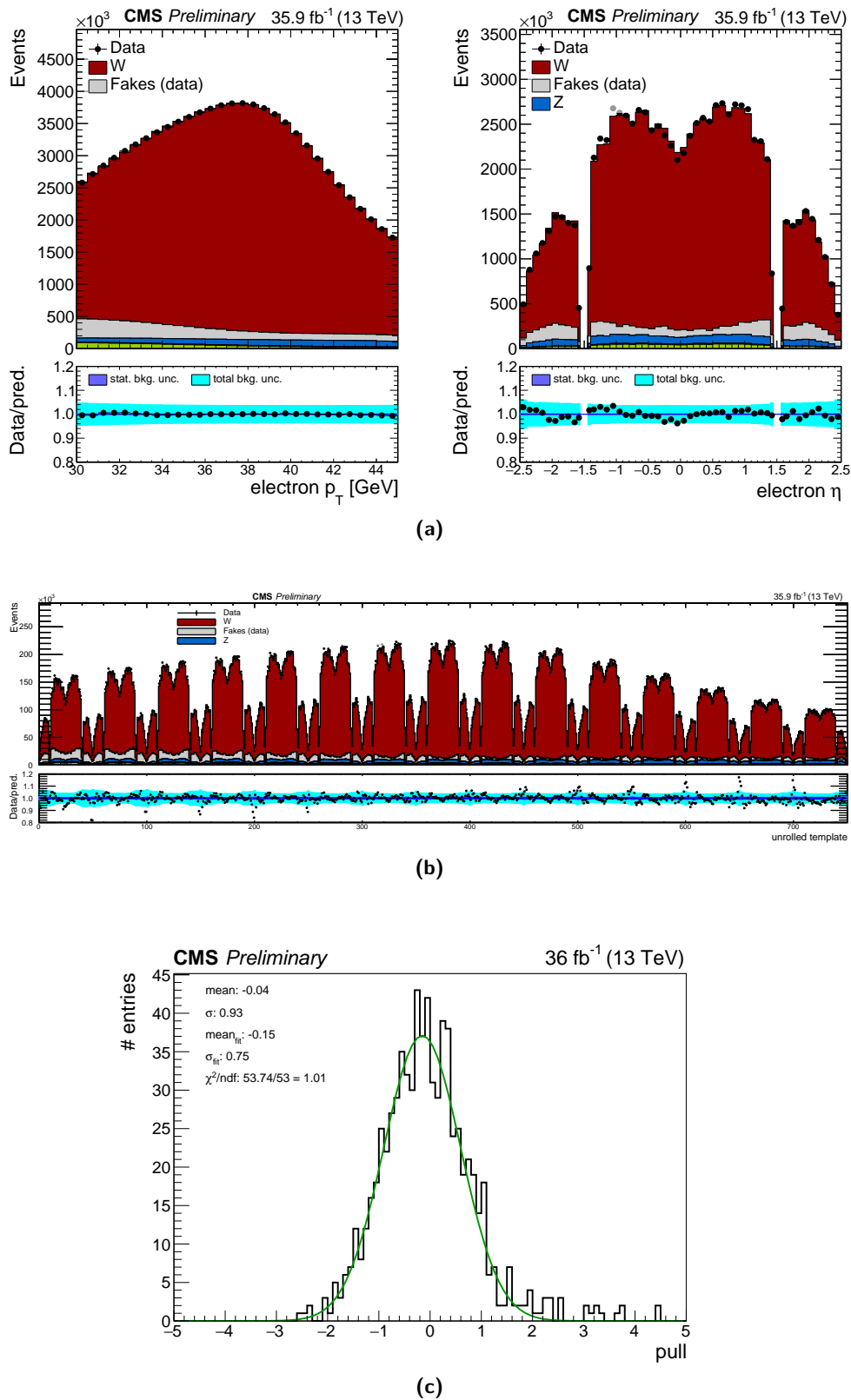


**Figure 6.1.** Inclusive distributions of electron  $p_T$  (top left) and  $\eta$  (top right), and unrolled  $p_T$ - $\eta$  distribution (middle) after the full signal selection. The yields of all the processes are scaled with a  $\chi^2$  fit to match the observed yield in data. The pulls for the unrolled distribution is also shown (bottom).

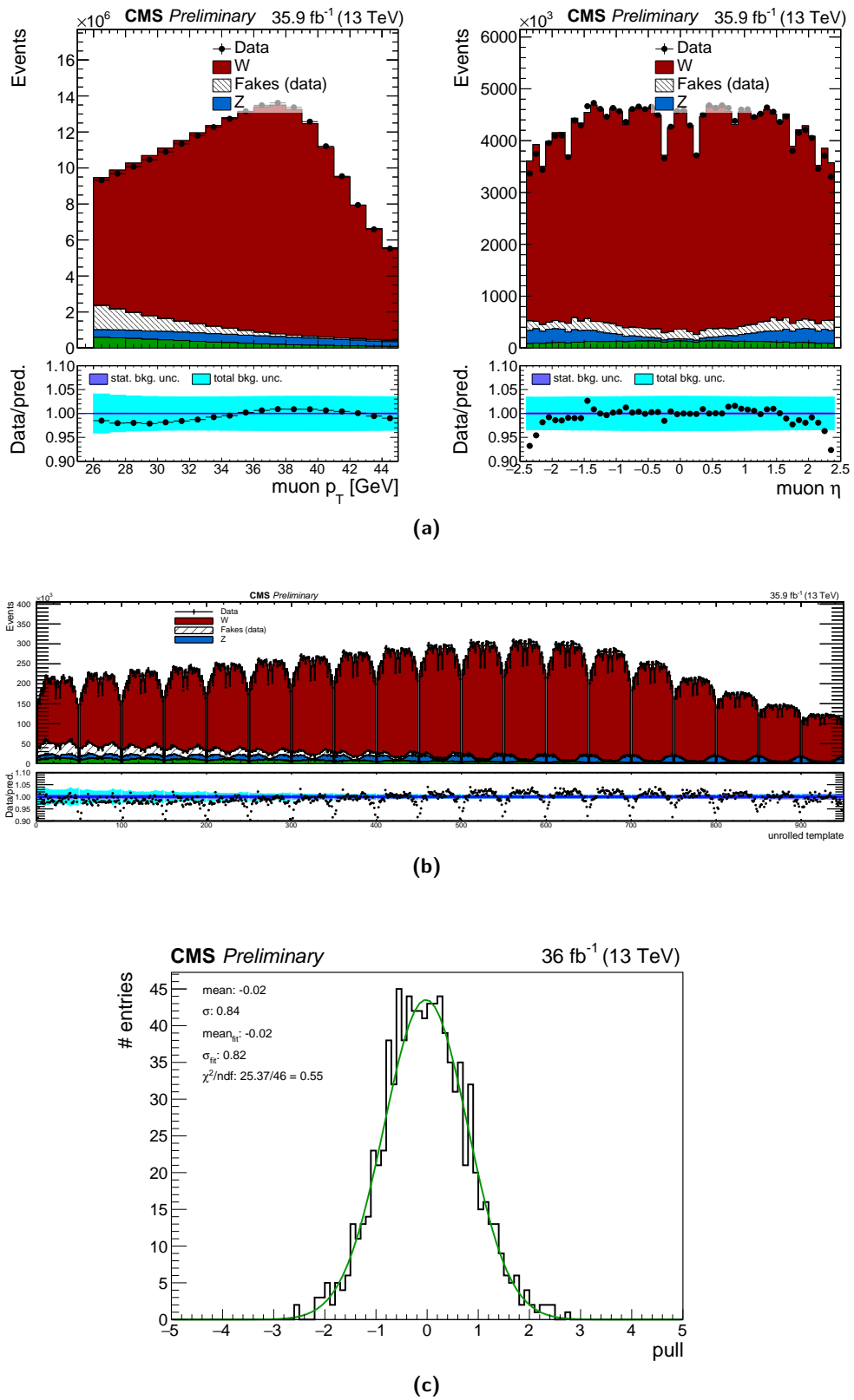


**Figure 6.2.** Inclusive distributions of muon  $p_T$  (top left) and  $\eta$  (top right), and unrolled  $p_T$ - $\eta$  distribution (middle) after the full signal selection. The pulls for the unrolled distribution is also shown (bottom).

the number of  $|Y_W|$  bins and  $n_{\eta, p_T}$  is the number of bins in the 2D lepton  $p_T$  vs.  $\eta$  distribution;

- $\vec{\sigma} = (\sigma_{1L}, \dots, \sigma_{n_{Y_W}0})$  is the vector of W-boson generator-level cross sections being measured for each rapidity bin and helicity state, multiplied by the branching fraction of the leptonic decay;
- the functions  $S_{km}$  (for the k-th rapidity bin and the m-th helicity state) and  $B$  are the signal and background 2D templates, normalized to unity;
- $L_{int}$  is the total integrated luminosity being analyzed;
- $n_{ev}^{ij}$ ,  $n_{sig}^{ij}$ ,  $n_{bkg}^{ij}$  are the number of observed, signal, and background events in the ij-th event category;
- the factors  $\vec{\theta}_S$  and  $\vec{\theta}_B$  are the nuisance parameters associated with the signal and background models;

The unfolding to particle-level cross sections is achieved by extracting the vector  $\vec{\sigma}$  directly from the likelihood fit. The cross section is measured for each flavor and charge through a simultaneous fit performed on both charges, which results in a reduced uncertainty due to the strong anti-correlation of the PDF uncertainties between the two charges, as explained in Sect. 2.2.

Assuming lepton flavor universality, the measured cross section is expected to be the same in both the electron and muon channel. In the fit, this is technically implemented by defining a single signal strength parameter for each  $|Y_W|$  bin, where the signal strength denotes the ratio of the observed over expected number of events in a specific category of the fit.

Calling the signal strength for a given bin as  $\mu$ , it holds:

$$\mu = \frac{N}{N_{exp}} = \frac{\sigma \cdot \varepsilon}{\sigma_{exp} \cdot \varepsilon_{exp}} \quad (6.2)$$

where common factors between numerator and denominator, such as the integrated luminosity, have been removed. The factor  $\varepsilon$  represents a global efficiency that connects the cross section to the number of observed events. The subscript “exp” refers to the expected pre-fit quantities.

It should be observed that both the cross section and the efficiency depend on the nuisance parameters included in the likelihood. For instance, the dependence can arise from the PDFs, which affect the kinematic distributions and also correlate different bins. This has the important consequence that the factors  $\varepsilon$  in eq. (6.2) do not trivially cancel out and therefore it is not possible to derive the post-fit cross section  $\sigma$  directly from the expected one as  $\sigma = \mu \cdot \sigma_{exp}$ . Instead, the correct evaluation of the cross section must take into account the effect of the nuisances on  $\varepsilon$  as well, as it is implemented in the output of the fit.

It should be pointed out that there is an intrinsic dependence of the measured cross section on the MC and PDF set used to derive the expected cross section and the helicity fractions. The analysis presented in this thesis is built on the aMC@NLO\_MadGraph5 MC with NNPDF3.0 PDF set. The comparison with other generators or different PDF sets has not been performed.

The uncertainties and the correlation matrices are obtained from the test statistics  $q(\vec{\sigma})$ , which is asymptotically distributed as a  $\chi^2$  [56]. The test statistics is defined as

$$q(\vec{\sigma}) = -2 \cdot \log \left( \frac{\mathcal{L}(\vec{\sigma}|\hat{\vec{\theta}})}{\mathcal{L}(\hat{\vec{\sigma}}|\hat{\vec{\theta}})} \right) \quad (6.3)$$

where  $\vec{\theta} = (n_{\text{bkg}}, \vec{\theta}_S, \vec{\theta}_B)$ . In eq. (6.3),  $\hat{\vec{\sigma}}$  and  $\hat{\vec{\theta}}$  are the values of the parameters that maximize the likelihood, while  $\hat{\vec{\theta}}$  are the values of the parameters that maximize the likelihood at fixed  $\vec{\sigma}$

The nuisance parameters are also minimized simultaneously with the  $\vec{\sigma}$  parameters. Regarding the PDF uncertainties, the fit can be performed in two different scenarios:

- fit for the cross sections  $\vec{\sigma}$ , floating the PDFs and the other nuisance parameters;
- fit performed fixing the  $\vec{\sigma}$  to the expected values.

As will be presented in chapter 7, the latter case allows to set a direct constraint on the PDFs, which is one of the main goals of the analysis.

For each charge and flavor, the likelihood has 48 signal templates (3 helicity  $\times$  16 rapidity bins) with roughly 250 nuisances associated to each of them, as discussed in next sections, plus another 5-6 background templates with additional related nuisances. Moreover, signal templates for neighbouring  $Y_W$  bins are statistically very anti-correlated due to the large overlap in the  $p_T$ - $\eta$  space. The level of complexity of the fit is also enhanced by the fact that each template is made of about one thousand  $p_T$ - $\eta$  bins.

The likelihood and minimization thereof are implemented in TensorFlow (TF) [54]. TF is an open source software library for high performance numerical computation, originally developed at Google for deep learning applications. Among the advantages provided by this tool, it is worth mentioning that it features modern minimization algorithms that are able to deal with non-convex regions in the likelihood. Non-convex regions result from the polynomial interpolation of asymmetric log-normal uncertainties (see Sect. 6.3.1) and induce numerical instabilities that standard minimization tools based on MINUIT [55] are not fully optimized to deal with.

## 6.2 Signal and background templates

Signal templates for the  $W^+ \rightarrow \mu^+ \nu_\mu$  channel are shown in Fig. 6.3 for a few  $|Y_W|$  bins and for the left, longitudinal and right polarization states. For a given polarization, the lepton populates different regions of the  $p_T$ - $\eta$  space depending on the rapidity of the parent W-boson. Conversely, at fixed  $Y_W$  the distributions are different depending on the helicity. These features are the key to extracting the signal strength of each signal category. Some templates for the  $W^- \rightarrow \mu^- \bar{\nu}_\mu$  channel are shown in Fig. 6.4. It can be observed that the ones for the opposite charge manifest different patterns.

The band at  $|\eta| \approx 1.5$  corresponds to the gap between EB and EE, which is excluded by the electron selection. There is no equivalent transition region in the muon channel. Neglecting differences in the selection, the templates in the muon and electron channels show essentially the same features.



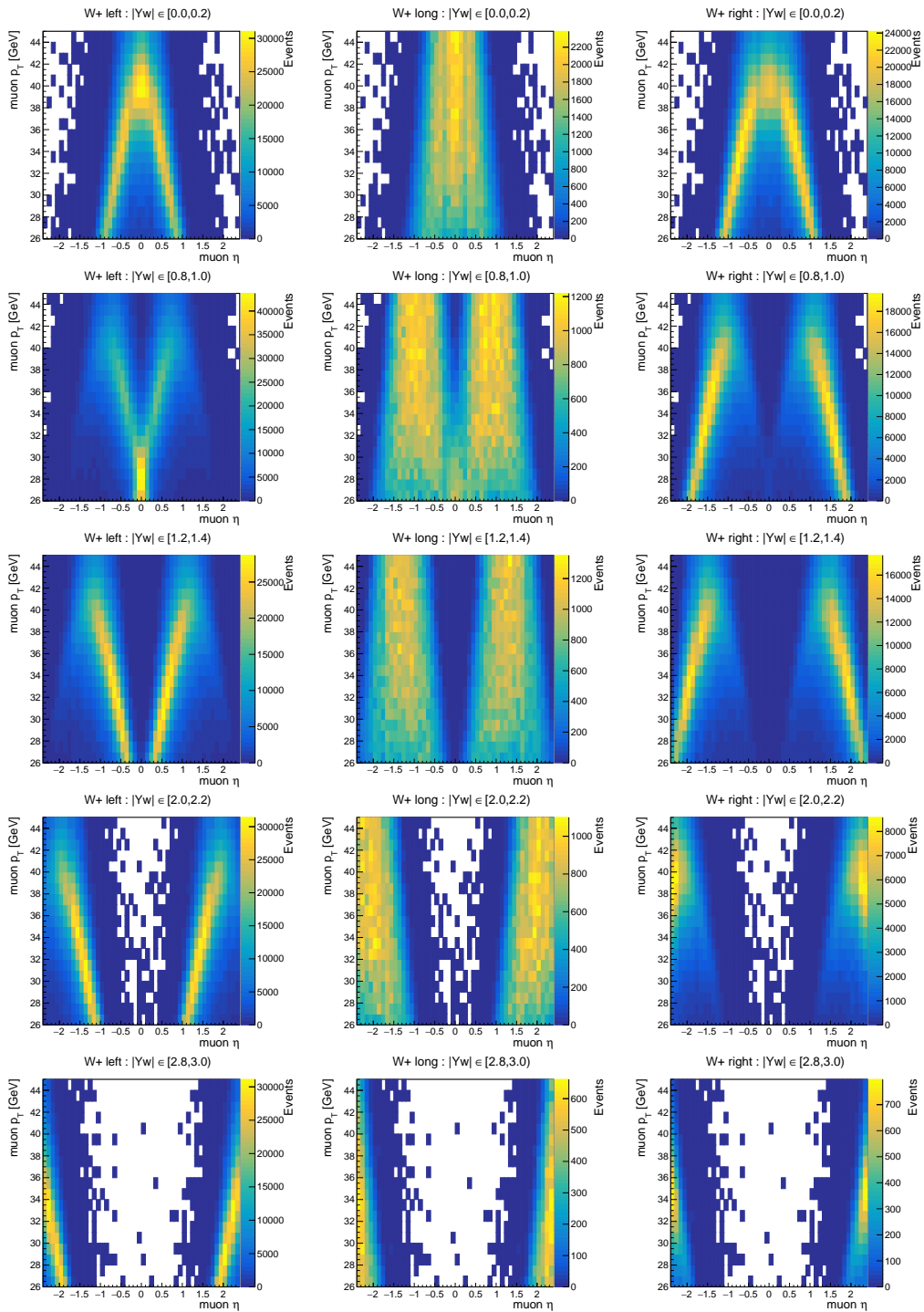


**Figure 6.3.** Some signal templates in the  $W^+ \rightarrow \mu^+ \nu_\mu$  channel for the left, longitudinal and right polarization states (from top to bottom).

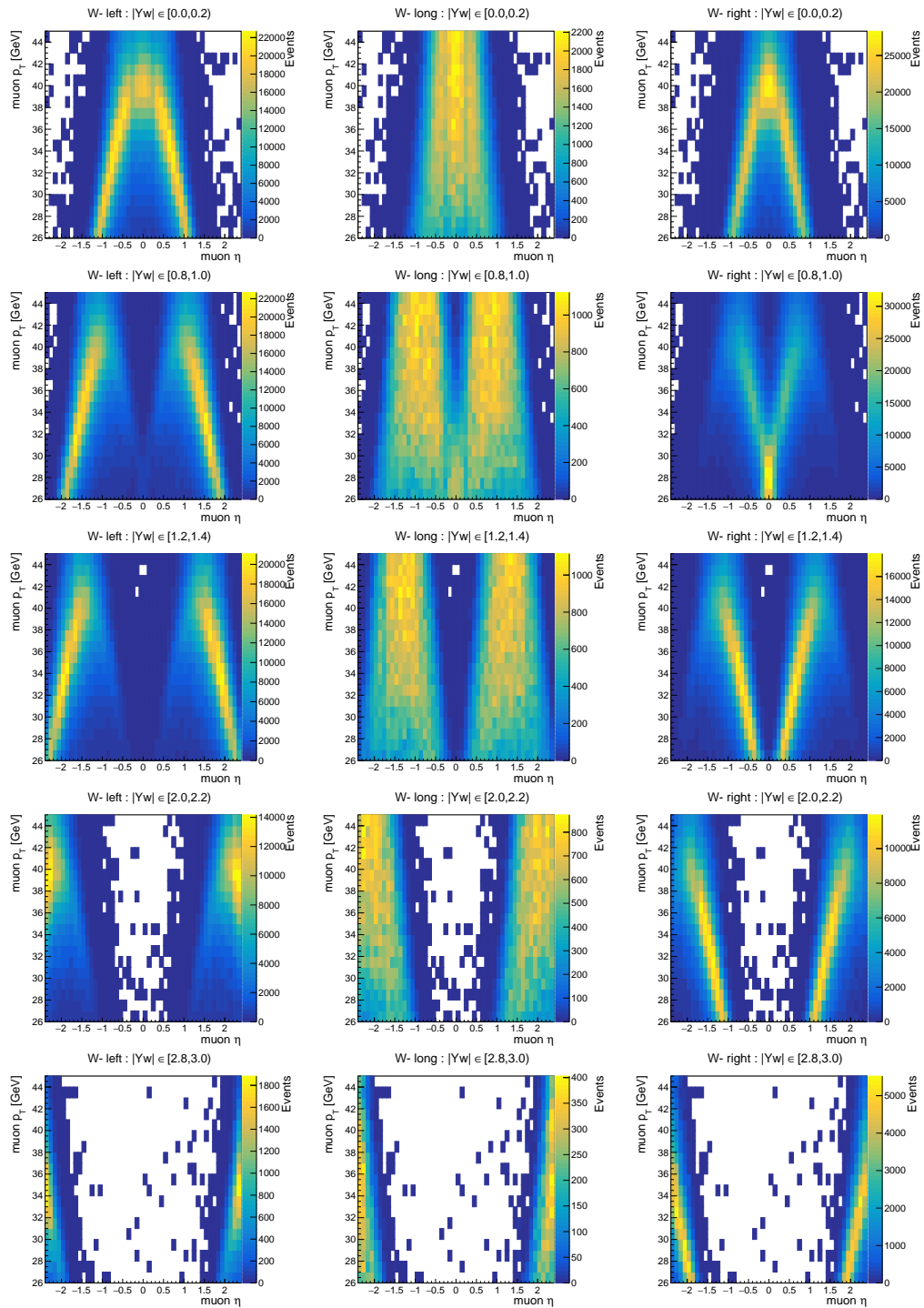


Figure 6.4. Some signal templates in the  $W^- \rightarrow \mu^- \bar{\nu}_\mu$  channel for the left, longitudinal and right polarization states (from top to bottom).

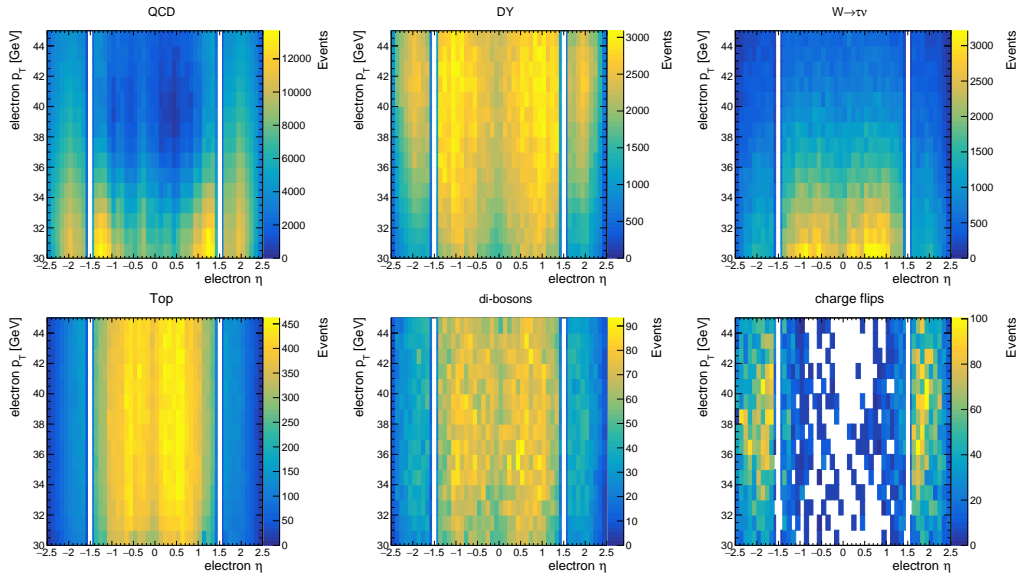


Figure 6.5. Background templates in the  $W^+ \rightarrow e^+ \nu_e$  channel.

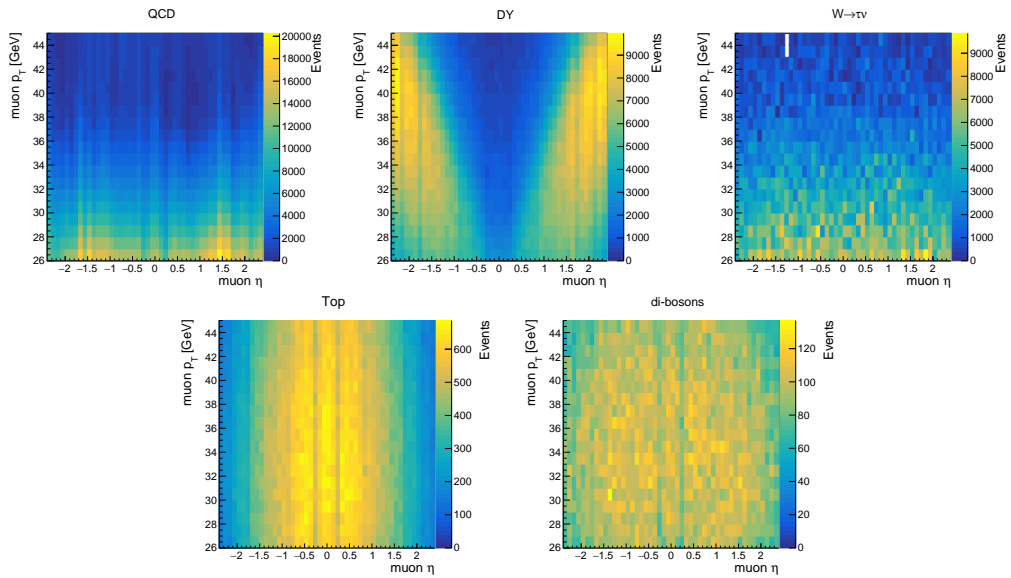


Figure 6.6. Background templates in the  $W^+ \rightarrow \mu^+ \nu_\mu$  channel.

**Table 6.2.** Normalization and shape uncertainties on signal and background templates. The cross section uncertainty for  $W \rightarrow \mu/e + \nu$  is not applied when fitting for the signal cross section. The uncertainty due to lepton efficiency on signal is applied as function of the lepton  $p_T$  and  $\eta$ , as explained in the text.

source/process	signal	Z	QCD	Top	$W \rightarrow \tau\nu$	dibosons	flips (e only)
normalization uncertainties							
luminosity	2.5%	2.5%	-	2.5%	2.5%	2.5%	2.5%
$\delta\sigma_Z$	-	3.8%	-	-	-	-	-
$\delta\sigma_{top}$	-	-	-	6%	-	-	-
$\delta\sigma_{VV}$	-	-	-	-	-	16%	-
fakes normalization (corr.)	-	-	30%	-	-	-	-
$W \rightarrow \tau\nu$ normalization	-	-	-	-	30%	-	-
flips normalization	-	-	-	-	-	-	30%
lepton efficiency	-	1%	-	1%	1%	1%	1%
lepton veto	-	3%/2% (e/ $\mu$ )	-	-	-	-	-
shape uncertainties							
lepton efficiency (corr.)	yes	-	-	-	-	-	-
$150 \times$ lepton efficiency (uncorr.)	yes	yes	-	-	-	-	-
pdfs	yes	yes	-	-	-	-	-
$\alpha_S$	yes	yes	-	-	-	-	-
$\mu_F$ (binned in $p_T^W$ )	yes	-	-	-	-	-	-
$\mu_R$ (binned in $p_T^W$ )	yes	-	-	-	-	-	-
$\mu_{F+R}$ (binned in $p_T^W$ )	yes	-	-	-	-	-	-
$m_W$	yes	-	-	-	-	-	-
$\mu_F$	-	yes	-	-	-	-	-
$\mu_R$	-	yes	-	-	-	-	-
$\mu_{F+R}$	-	yes	-	-	-	-	-
lepton momentum scale	yes	-	-	-	-	-	-
fakes shape vs. $p_T$ (correlated)	-	-	yes	-	-	-	-
fakes shape vs. $\eta$ (10 uncorr. bins)	-	-	yes	-	-	-	-

The background templates for the electron (muon) channel are shown in Fig. 6.5 (Fig. 6.6) for the positive charge case. Unlike the signal, the background yields are expected to be mostly symmetric with respect to the charge.

It should be noted that background templates manifest very different shapes with respect to each other, both as a function of  $p_T$  and  $\eta$ . At the same time, they present different patterns compared to signal templates. These features provide the fit with lever arm to distinguish the various components. The observed differences in the background templates between the electron and muon channel should be ascribed to the different selection and identification criteria applied to leptons, as well as to the reconstruction efficiency for each flavor. Regarding the electron channel, the event yields are not uniform between EB and EE due to the different identification and isolation requirements applied in the two detector region.

### 6.3 Systematic uncertainties

In this section the effect of systematic uncertainties on signal and background templates is described. Systematic uncertainties induce variations in the shape and normalization of the templates. Each uncertainty on a given template is treated in the fit as two alternative bounding templates covering the expected variations on the nominal one.

### 6.3.1 Normalization uncertainties

Nuisances affecting only the template normalization are treated using log-normal priors. If a random variable  $X$  has a log-normal probability density function, the variable  $Y = \log X$  follows a normal distribution. Therefore, the advantage of using log-normal priors in the likelihood fit lies in the fact that the minimization is typically made on  $\log \mathcal{L}$ , where  $\mathcal{L}$  denotes the likelihood defined in eq. (6.1).

A summary of the normalization systematic uncertainties is given in Table 6.2. The following sources are considered:

- **luminosity:** it affects all signal and background processes estimated from MC with a 2.5% uncertainty [43];
- **cross section:** it summarizes the uncertainty in the theoretical cross section in the MC samples. In the fit, 3.8% is assigned on  $Z$ , 6% on top, 16% on dibosons, and a conservative 30% uncertainty on  $W \rightarrow \tau\nu$  background to account for the kinematic acceptance due to the selection applied on the electron/muon in the decay chain of the  $\tau$ . The normalization for the  $W$  signal process is left freely floating when fitting for the cross section, while 3.8% is assigned on it when fitting for the PDFs;
- **lepton veto:** it arises from the second lepton veto selection that is used to suppress the  $Z$  background and amounts to 3% (2%) for  $Z \rightarrow ee$  ( $Z \rightarrow \mu\mu$ );
- **charge-flips normalization:** 10% uncertainty is applied to the charge-flips background (only in the electron channel) to cover the difference in the measured charge misidentification probability between data and MC (right plot in Fig. 4.4);
- **lepton efficiency:** 1% uncertainty due to the lepton efficiency scale factors is applied on background processes, while a different approach is adopted for signal, as explained later on.

### 6.3.2 Shape uncertainties

Other sources of uncertainty affect the measurement by varying the shape of the signal and background  $p_T$ - $\eta$  distributions and possibly also their normalization. They can be categorized into two groups: experimental and theoretical uncertainties. The sources of systematic uncertainties affecting the shape of the templates are summarized in Table 6.2.

Experimental uncertainties on the signal arise mainly from the derivation of the lepton corrections for the scale and efficiency. Additional sources of uncertainty are associated to the estimation of the QCD background using the fake-rate method. The theoretical uncertainties stem from the PDFs, the modeling of the  $W$ -boson  $p_T$  and the factorization and renormalization scales ( $\mu_F$  and  $\mu_R$ , respectively) in the QCD calculations of the cross section. The following sources of uncertainty are considered.

**Lepton energy/momentum scale:** this uncertainty derives from the computation of the lepton momentum scale corrections and is applied to signal templates as described in Sec. 4.5 to obtain one alternative signal template for each process.

**Lepton efficiency scale factors:** the scale factors are obtained using the Tag-and-probe

technique fitting the  $Z \rightarrow \ell\ell$  mass spectrum in bins of lepton  $p_T$  and  $\eta$ . The corresponding systematic uncertainty has been described in Sec. 4.6.4: it comprises one component which is fully correlated across different  $\eta$  bins in each signal template and results in one alternative template for each signal process, and another component which is uncorrelated among  $\eta$  bins and results in  $3 \times N_\eta$  additional templates for each signal process ( $N_\eta = 48$  (50) in the muon (electron) channel). The magnitude of the correlated uncertainties is summarized in Table 4.5. The uncorrelated systematic uncertainties on the efficiency were already shown for electrons and muons in Fig. 4.20. The uncorrelated nuisances for the lepton efficiency are also applied to the  $Z$  background, and are treated as fully correlated between signal and  $Z$ .

**QCD background estimation:** it originates from the modeling of the QCD background with the fake-rate (FR). The systematic uncertainties in the measured FR have been discussed in Sec. 5.4. They are used to provide an alternative parametrization of the FR as a function of the lepton  $p_T$  and  $\eta$ . Then, new QCD templates are defined by using the varied FR. The shape variation along  $p_T$  is correlated among different  $\eta$  bins of the QCD template.

Finally, in order to cover for  $\eta$ -dependent variations in the QCD normalization, alternative QCD templates are built by varying the normalization of the nominal one by 5% in 10 independent bins along  $\eta$ , with bin edges at  $|\eta| = [0, 0.5, 1.0, 1.6, 2.0, 2.4]$ .

**PDFs:** The  $W/Z + \text{jets}$  MC used in the analysis is produced with NNPDF3.0 PDF set, for which PDFs are delivered through the MC method in the form of 100 replicas (see Sec. 1.2.2). The MC2HESSIAN methodology described in [25] is applied to transform them into a basis of 60 Hessian eigenvalues, that provide a good approximation of the original Monte Carlo replicas. This procedure allows to treat them as 60 uncorrelated nuisance parameters in the likelihood. The Hessian eigenvalues are used to reweight signal events and produce 60 alternative templates for each signal process. The same procedure is also applied to the  $Z$  background, and the PDF uncertainties are treated as fully correlated between the  $W$  and  $Z$  processes.

The analysis sensitivity to the PDFs arises from the variation in both the normalization and shape of the signal templates. In particular, the largest discrimination power is obtained from the difference in the shape. Indeed, the variation in the normalization is generally lower than 1% and is thus hidden by the larger luminosity uncertainty, which is 2.5%. Figure 6.7 shows some examples of the relative event-yield variations between the PDF alternative template and the nominal one for four selected PDF eigenvalues. Examples are shown for different  $W$ -boson charge and helicity, summing all the rapidity bins for simplicity. For a given PDF eigenvalue, the distributions in Fig. 6.7 can be interpreted as the relative difference induced by the PDF uncertainties on the  $W$ -boson cross section in the  $p_T$ - $\eta$  space: some weights induce relatively large variations in both the shape and normalization of the templates and will be significantly constrained by the fit.

**QCD renormalization and factorization scales ( $\mu_R$  and  $\mu_F$ ):** variations of  $\mu_R$  and  $\mu_F$  by half or twice their nominal value are considered, resulting in 6 combinations: 4 of them are obtained by letting either  $\mu_R$  or  $\mu_F$  vary up or down while keeping the other one fixed to the nominal value; the remaining 2 arise from the simultaneous variation of  $\mu_R$  and  $\mu_F$  up or

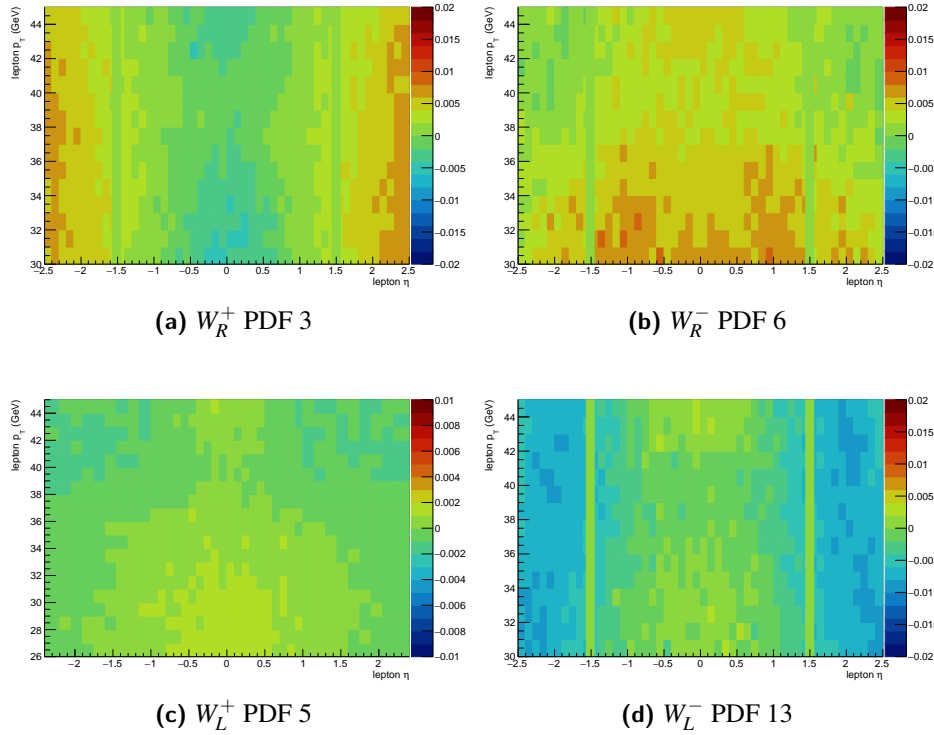


**Figure 6.7.** Relative difference in the event yields between the alternative  $p_T$ - $\eta$  template for few PDF Hessian weights and the nominal one. Four examples are shown for different W-boson charges and helicity states: for each of them, all bins in  $Y_W$  are summed up for simplicity.

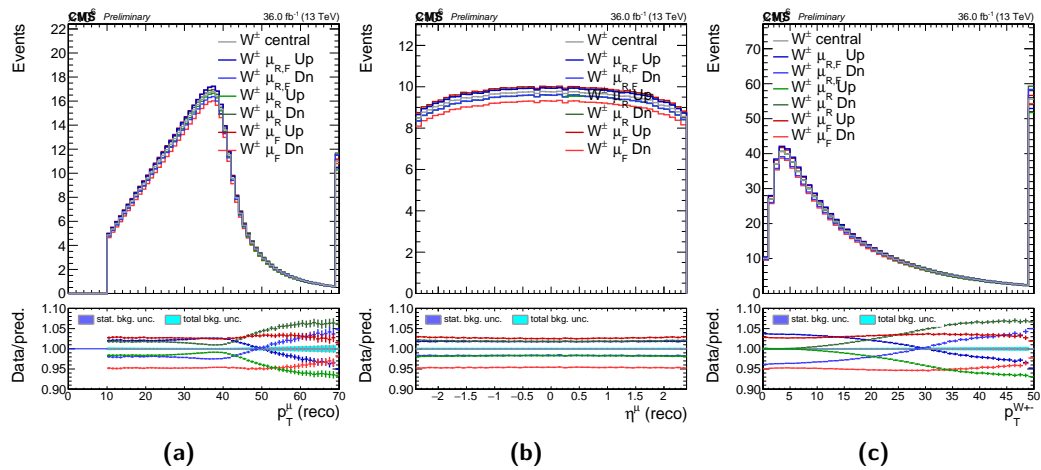


**Figure 6.8.** Effect of  $\mu_F$  and  $\mu_R$  variations on the lepton  $p_T$  and  $\eta$ , and on the W-boson  $p_T$ .

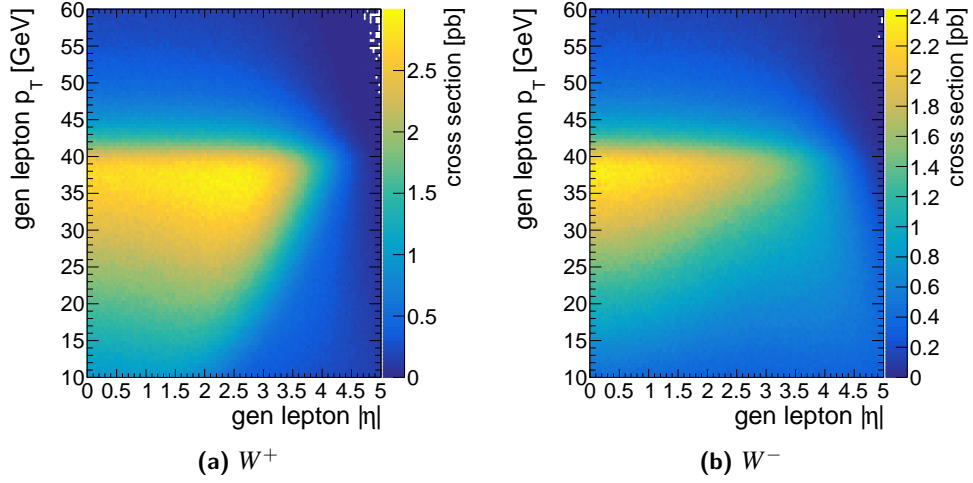


**Figure 6.9.** Generator level W-boson cross section in bins of the electron  $p_T$  and  $|\eta|$ . The cross section is shown for a  $W^+$  on the left and a  $W^-$  on the right. The granularity of the histograms is 0.05 along  $|\eta|$  and 0.5 GeV in  $p_T$ . The presented cross section is not divided by the bin area.

down. For signal, each combination is evaluated independently in 10 different bins of  $p_T^W$  with bin edges at  $p_T^W = [0.0, 2.9, 4.7, 6.7, 9.0, 11.8, 15.3, 20.1, 27.2, 40.2, 13000]$  GeV, for a total of 60 variations. This procedure makes the fit less dependent on the modeling of the underlying  $p_T^W$  distribution. The unbinned QCD scale nuisances are considered as well, but they are applied only to the Z background. The effect of the QCD scales on the lepton  $p_T$  and  $\eta$  for signal events is shown in Fig. 6.8.

$m_W$ : simulated signal events are generated assuming  $m_W = 80420$  MeV. In order to account for the dependence of the lepton kinematics on the underlying value of  $m_W$ , two additional signal templates are defined for each signal category by reweighting signal events to different values of  $m_W$  shifted by  $\pm 50$  MeV from the nominal one. The mass weight is calculated assuming a pure Breit-Wigner distribution of the invariant mass at generator level. The mass shift is expected to affect mainly the lepton  $p_T$ : the impact of  $m_W$  on the lepton  $p_T$  distribution was already shown in Fig. 1.5.

**strong coupling constant  $\alpha_S$** : two variations of  $\alpha_S$  are available in the MC. They are associated to the PDF set used in the analysis and correspond to  $\alpha_S = 0.117$  and  $0.119$  (the central value is  $0.118$ ). Similarly to the PDF Hessian weights, they are used to assign a systematic uncertainty on both signal and Drell-Yan.

## 6.4 W-boson double-differential cross section

This section describes the measurement of the W-boson double-differential cross section as a function of the unfolded lepton  $p_T$  and  $|\eta|$ . The cross section only depends on  $|\eta|$  in  $pp$  collisions due to the symmetry in the initial state.

All the experimental techniques already described for the differential helicity measurement are adopted for this measurement as well, and also the selected dataset is the same. The



signal extraction procedure is similar, as it is based on template fits to the observed  $p_T$ - $\eta$  distribution in data. The substantial difference is in the definition of the signal templates: in this measurement there is one template for each bin of  $p_T$ - $|\eta|$  of the generator-level lepton. This implies that each template is very sparse: indeed, due to the high resolution in  $p_T$  and  $\eta$ , only the bins with reconstructed  $p_T$ - $\eta$  close to the generator values are filled. The  $p_T$  resolution is approximately 1 GeV, so that the majority of events are contained in a band of about 2 GeV around the considered  $p_T$  bin. On the other hand, the resolution on  $\eta$  is practically infinite, such that there is a very small fraction of events falling outside the  $\eta$  boundaries of the considered generator-level bin.

The measurement is performed separately for the two charges, and inclusively in the W-boson helicity and rapidity. The input generator-level W-boson cross section times branching ratio as a function of the gen-level  $p_T$  and  $|\eta|$  of the charged lepton is shown in Fig. 6.9 for a  $W^+$  and  $W^-$ . These distributions are obtained without applying any kinematic selection and are independent on the lepton flavor.

In order to facilitate the combination of the measurements in the electron and muon channels, the generator-level categories are defined with the same range and granularity for both flavors. The  $p_T$ - $\eta$  binning for the signal and background templates is chosen to match the generator-level one, except for the fact that positive and negative  $\eta$ -sides are kept distinct in the former.

The granularity of the generator-level binning is optimized on the expected fit to ensure that the measured cross section in each bin is larger than zero by at least five times the corresponding uncertainty, so to avoid biases in the measurement. The optimization is tuned in the muon channel, that provides the better precision. However, given that the electron channel is characterized by overall larger uncertainties than the muon one, the choice is further optimized to allow the convergence of the fit in the electron channel as well. The optimization results in the following non-uniform binning:

- $p_T$ : 12 bins, 2 with 2 GeV granularity from 26 to 30 GeV, and 10 with 1.5 GeV granularity from 30 to 45 GeV;
- $|\eta|$ : 18 bins, 12 with 0.1 granularity from 0 to 1.2 and 6 with 0.2 granularity from 1.2 to 2.4.

For electrons, the bins with  $26 \text{ GeV} < p_T < 30 \text{ GeV}$  are almost unconstrained due to the acceptance of the analysis. For both channels, an inclusive “out-of-acceptance” signal template with either gen-level  $p_T < 26$ ,  $p_T > 45$ , or  $|\eta| > 2.4$  is considered as well. This additional category contributes to the measurement inside acceptance because of the finite detector resolution.

Examples of signal templates in the electron channel are shown in Fig. 6.10. The templates for background processes are exactly the same as those used for the rapidity measurement, but using the optimized binning.

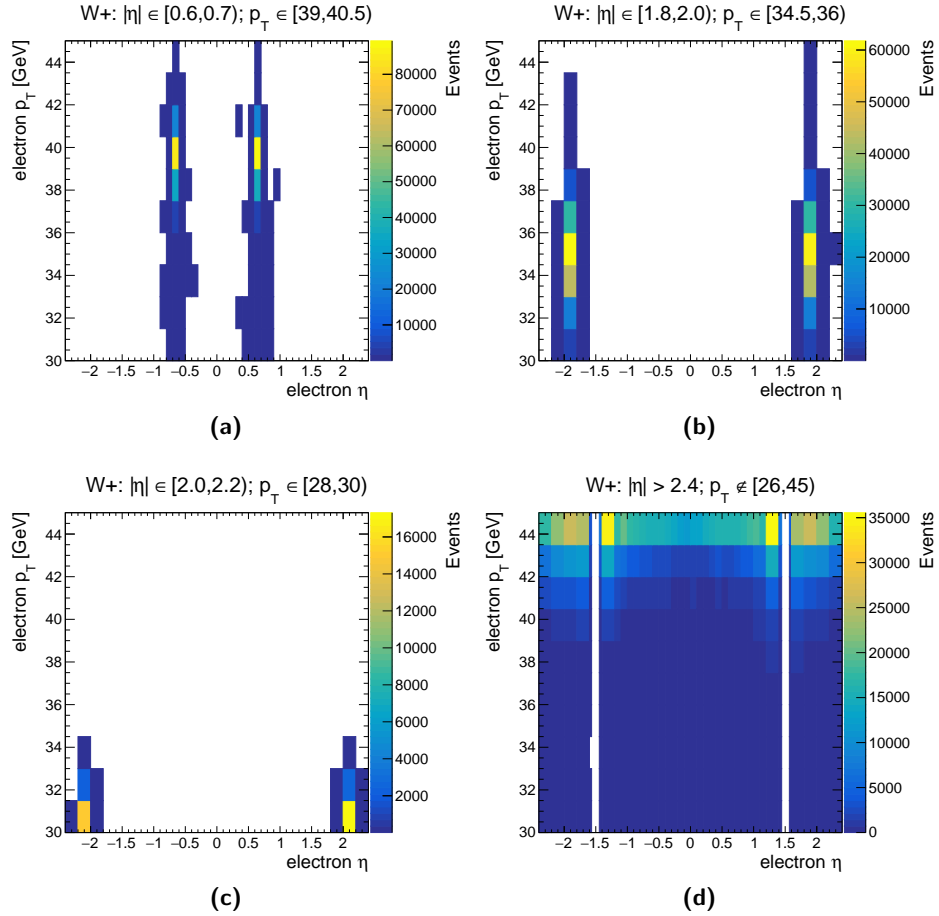


**Figure 6.10.** Example of signal templates for the differential cross section measurement in the  $W^+ \rightarrow \ell^+ \nu$  channel for a generator-level electron in EB (a) and EE (b). The case shown in (c) refers to gen-level electrons with  $p_T$  outside the acceptance, which contribute to the measurement inside acceptance due to the non-perfect  $p_T$  resolution. The inclusive signal template for gen-level electrons produced outside the reconstruction acceptance is shown in (d). Equivalent templates are obtained in the negative charge channel.

## Chapter 7

# Results and interpretation

In this chapter, the results concerning the  $Y_W$  measurement and the double-differential cross section  $d^2\sigma/dp_T d|\eta|$  are presented. The fitting procedure is validated by performing a computation of the expected uncertainties on the so-called Asimov dataset, defined by substituting data with the exact sum of the signal and all the backgrounds, without considering the Poissonian fluctuation in the expected rate. The expected fit is useful to assess whether the model is well-defined before fitting the data, for example by investigating the patterns in the covariance matrix of the full set of signal strengths and nuisance parameters.

A real fit validation is done through toy Monte Carlo experiments, allowing for Poissonian fluctuations of the event yields of the single components. Toys are a powerful tool to assess whether the measurement has a bias in the evaluation of one or more parameters. Indeed, if  $N$  toys are generated (and therefore  $N$  fits are performed), the bias can be evaluated by looking at the distribution of the residuals for a given parameter of interest (POI)  $r$  in the fit, i.e., at the distribution of

$$R_r = r_{fit} - r_{in} \quad (7.1)$$

where  $r_{fit}$  and  $r_{in}$  are the fitted and input values of the parameter being scrutinized. This distribution is expected to be a Gaussian centered at 0. Deviation of the observed mean from 0 indicates the presence of a bias.

In addition to that, it is useful to look at the pulls, which are the ratios of the residuals and the uncertainty on  $r_{fit}$ . In this case, the expected distribution becomes a Gaussian with standard deviation equal to unity. An observed standard deviation lower than unity indicates that the corresponding parameter is being constrained by the fit. This would generally happen if the measurement is sensitive to that parameter, which would result in an output uncertainty lower than the input one. Nevertheless, it might also suggest that the likelihood is ill-defined or that some uncertainties on one or more other parameters are not being taken into account.

The results shown in the following are obtained from fits to  $N = 10^4$  toy experiments. Toys allow to perform the correct propagation of the uncertainties on variables which are functions of the fitted POIs. For instance, if  $f_j(x_1, \dots, x_n)$  is a function of  $n$  POIs named  $x_i$ , evaluated for a given toy  $j$ , the expected value and uncertainty on  $f$  can be estimated as the mean and RMS of the distribution of  $f_j$  in a set of toys. This method is used in the following to obtain the cross section normalized to the total one. In this case, it is  $f_j = f_j(\sigma_i, \sigma_{tot}) \equiv \sigma_i / \sigma_{tot}$ , where  $\sigma_i$  is the cross section measured in the  $i$ -th bin (which might be a given bin of  $Y_W$  for a specific helicity) and  $\sigma_{tot} = \sum_i \sigma_i$ .

The normalized cross section has the advantage of a partial cancellation of some experimental and theoretical uncertainties that are correlated between numerator and denominator. For instance, the relative uncertainty on the measured absolute cross section cannot be lower than 2.5%, that is the boundary provided by the luminosity uncertainty. However, the luminosity uncertainty is fully correlated between the partial and total cross sections. Hence, it cancels out in the normalized cross section.

An important source of uncertainty to be considered in the analysis is the statistical uncertainty in the signal MC sample. It cannot be neglected because the equivalent integrated luminosity of the  $W$ + jets MC sample is roughly 1/2 of the one in data. The corresponding uncertainty is implemented in the fit using the Barlow and Beeston method [57] by modeling the number of events in each bin of the  $p_T$ - $\eta$  templates as Poisson values whose means are treated as nuisance parameters, uncorrelated between different bins. The uncertainty also includes the contribution from background processes, although the main effect is due to the signal component.

In the following, the statistical uncertainty in the MC samples is referred to as *bin-by-bin* (BBB) uncertainty. Since the BBB uncertainty is expected to be reduced by using a larger sample of simulated signal events, the results for the expected fits will be shown without including it, unless differently specified. It should be noted that the BBB uncertainty does not coincide with the statistical uncertainty of the fit: the latter is defined as the uncertainty obtained by freezing all the nuisance parameters in the fit.

## 7.1 Helicity and rapidity

In this section the results regarding the  $W$ -boson differential cross section as a function of its rapidity and helicity are presented. Given the large number of expected events, the analysis is sensitive to all the three helicity states, including the longitudinal polarization that only accounts for about 5% of the total sample. The muon channel is characterized by better sensitivity than the electron one due to the larger size of the selected event sample, lesser amount of background and generally lower systematic uncertainties.

The absolute cross section obtained from MC toys is shown in Fig. 7.1 (Fig. 7.2) for the muon (electron) final state. The measurement is carried out by performing a simultaneous fit in the two charge categories, so to take advantage of the anti-correlated effect of the PDFs on the signal yields. The result of the measurement is compared to the rapidity distribution predicted by the `aMC@NLO_MadGraph5` MC with `NNPDF3.0` PDF set, whose uncertainty is obtained from the quadrature sum of the 60 Hessian variations of the `NNPDF3.0` set. The relative uncertainty in the measured signal cross section is always larger than 2.5% because of the luminosity uncertainty. However, this uncertainty does not affect the normalized cross section, as can be seen from Figs. 7.3 and 7.4 for the muon and electron final state, respectively.

It should be noted that:

- the central value represents the unfolded  $W$ -boson production cross-section at generator level, as obtained directly from the fit;
- the muon channel provides lower uncertainties than the electron one in the entire acceptance region;
- the statistical uncertainty grows up at higher  $Y_W$ ;

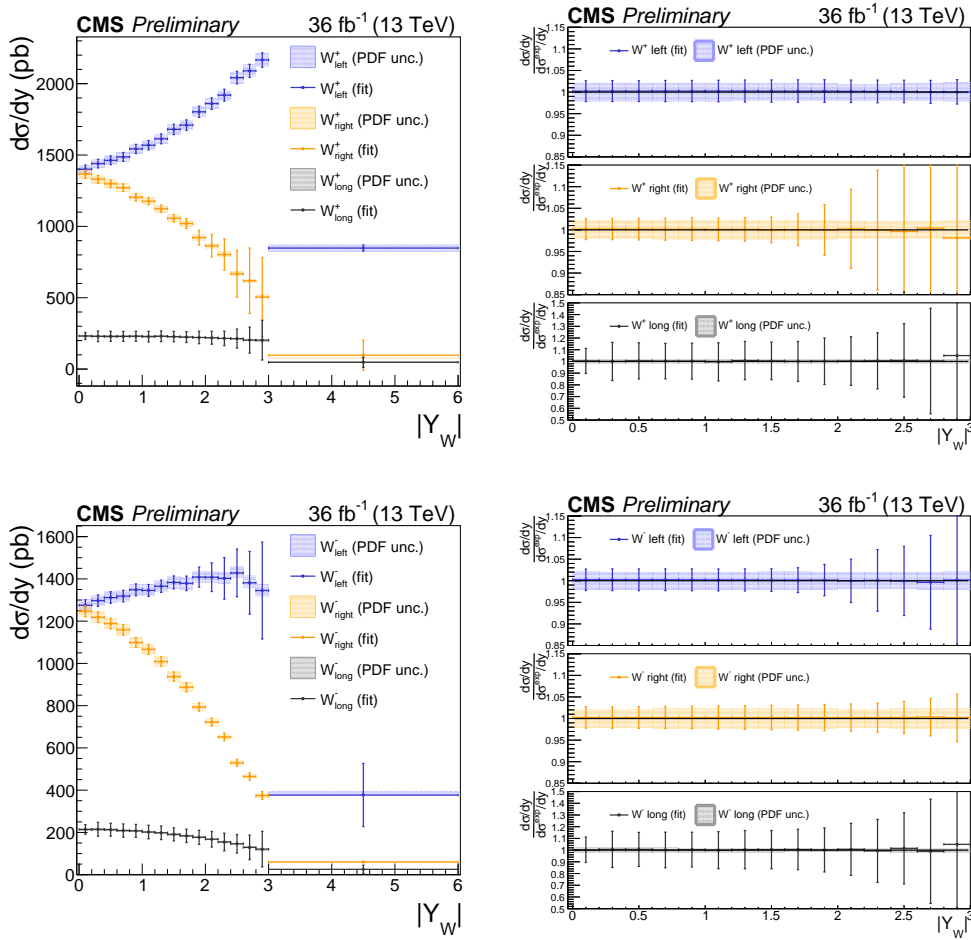


**Figure 7.1.** Fitted cross section (left) for the three helicity states in the muon final state for  $W^+$  (top) and  $W^-$  (bottom). The plot on the right shows the measured cross section divided by the expected one. In both plots, the light-filled band corresponds to the expected rate uncertainty from the PDFs, obtained from the quadrature sum of the 60 Hessian variations of the NNPDF3.0 set in the `aMC@NLO_MadGraph5` MC. Results are obtained using toy Monte Carlo experiments.

- the ratio of the fitted and the expected cross section is compatible with unity, showing that the bias in the signal extraction procedure is negligible;
- in most of the  $Y_W$  bins for left and right polarizations the fit uncertainty is smaller than the expected variations induced by the current PDF uncertainties.

The last item means that the measurement has the power to constrain the uncertainty originating from the PDFs. This topic is further developed in Sect 7.3. It was already shown in Fig. 6.7 that the analysis sensitivity to the PDFs originates mainly from the shape variation in the signal templates induced by the PDF Hessian weights. When considering the normalized cross section, the flat luminosity uncertainty is removed in the ratio and the variation of the template's normalization due to the PDFs becomes important as well.

The cross sections reported from Fig. 7.1 to Fig. 7.4 are obtained without including the statistical uncertainty of the MC samples. The effect of this additional source of uncertainty on the total one is visible in Fig. 7.5: it shows the relative uncertainty in the normalized

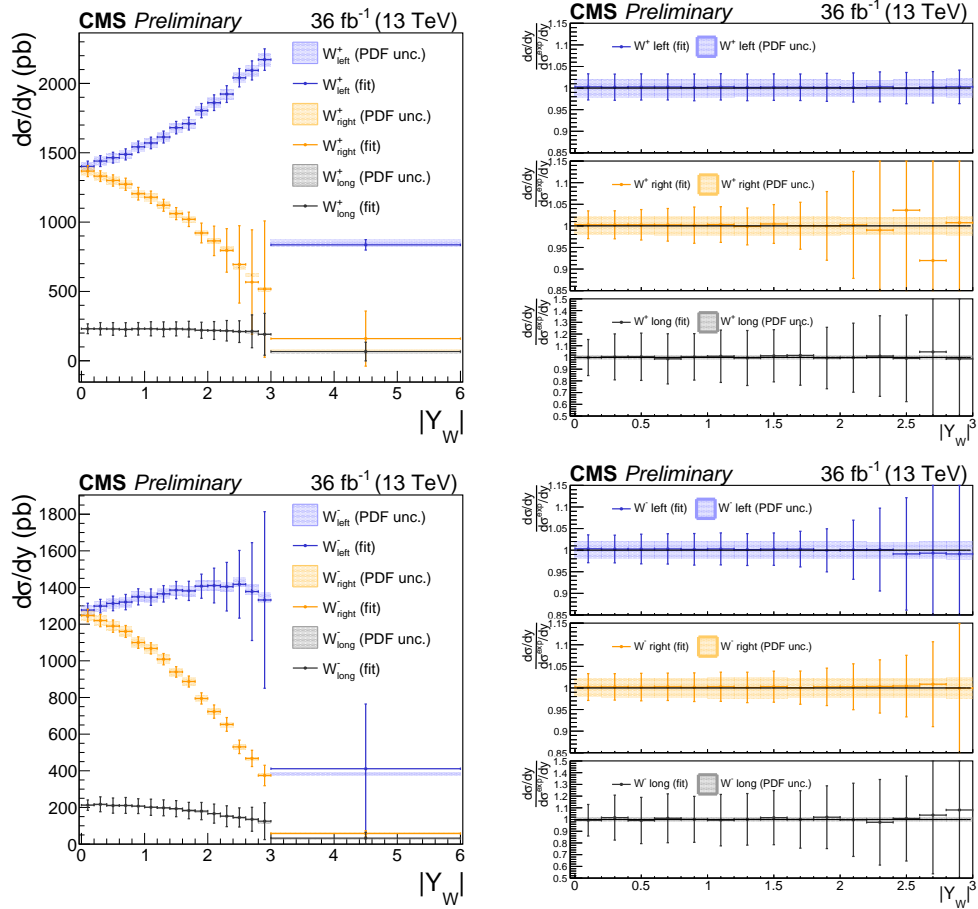


**Figure 7.2.** Fitted cross section (left) for the three helicity states in the electron final state for  $W^+$  (top) and  $W^-$  (bottom). The plot on the right shows the measured cross section divided by the expected one. In both plots, the light-filled band corresponds to the expected rate uncertainty from the PDFs, obtained from the quadrature sum of the 60 Hessian variations of the NNPDF3.0 set in the `aMC@NLO_MadGraph5` MC. Results are obtained using toy Monte Carlo experiments.

cross sections computed from the Asimov dataset, for both charges in the muon and electron channels, comparing it to the expected uncertainty from the PDFs. The total uncertainty on the fitted cross section grows significantly in the majority of the rapidity bins, especially at high  $|Y_W|$  and for the longitudinal polarization.

Since there is a high correlation among several POIs and nuisance parameters, it is important to provide the results both in terms of central values and Hessian uncertainties (as in Fig. 7.3 and 7.4), and their full covariance matrix. A subset of the correlation matrix, showing the correlation among signal strength parameters in the case of  $W^+ \rightarrow e^+ \nu$  is shown in Fig. 7.6 for the three polarizations (Figs. 7.6a, 7.6b and 7.6c for left, right and longitudinal polarization). Each of these matrices has 16 rows and columns corresponding to the number of rapidity bins, enumerated from 0 to 15 from the lowest to the highest rapidity bin.

Consecutive rapidity bins are expected to be statistically anti-correlated: indeed, the corresponding templates overlap and an upward statistical fluctuation in one bin implies a

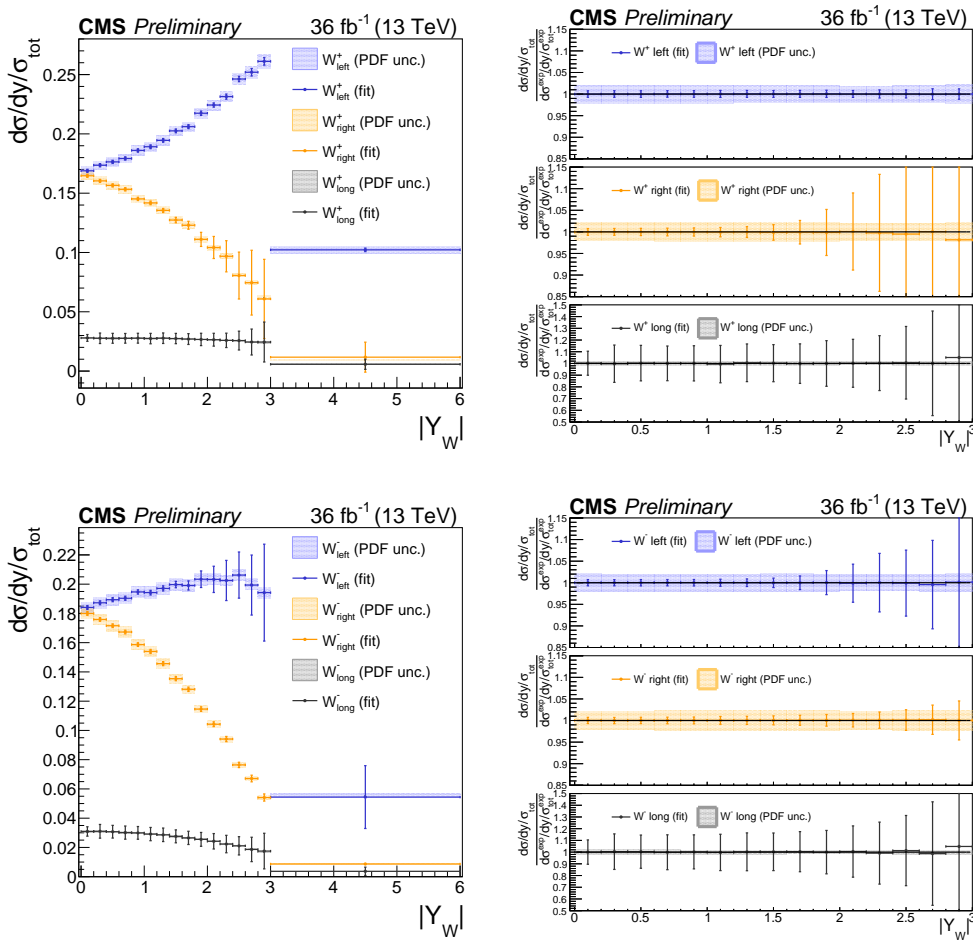


**Figure 7.3.** Fitted cross section normalized to the total one (left), for the three helicity states in the muon final state for  $W^+$  (top) and  $W^-$  (bottom). The plot on the right shows the measured cross section divided by the expected one. In both plots, the light-filled band correspond to the expected rate uncertainty from the PDFs, obtained from the quadrature sum of the 60 Hessian variations of the NNPDF3.0 set in the `aMC@NLO_MadGraph5` MC. Results are obtained using toy Monte Carlo experiments.

reduction in the observed number of events in the neighboring ones. However, the presence of nuisance parameters modifies this simple picture by introducing additional correlations.

In particular, the luminosity uncertainty correlates all the rapidity bins for which it is not negligible. This is what happens for the left polarization (Fig. 7.6a) and also for the right one (Fig. 7.6b) in the first rapidity bins. As the statistical uncertainty becomes dominant, the anti-correlation between consecutive bin shows up again. This is evident from Fig. 7.6c for the longitudinal polarization, and also from Fig. 7.6b, where it can be seen that the expected anti-correlation pattern is restored only at higher values of  $|Y_W|$ .

Figure. 7.6d shows the correlation among some selected signal bins for left and right polarizations and both charges. Finally, the correlation among signal bins with different helicity but same charge is shown in Fig. 7.6e and 7.6e for positive and negative charge, respectively.

All the correlation matrices in Fig. 7.6 are derived from the Asimov dataset considering

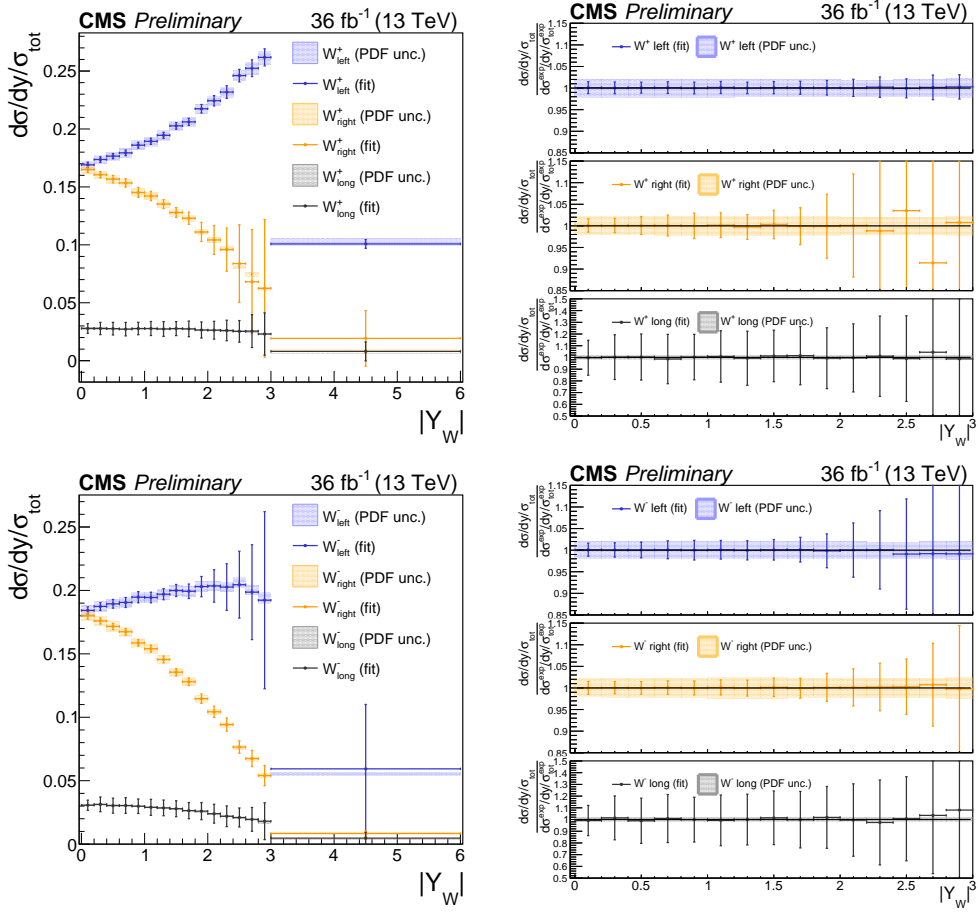


**Figure 7.4.** Fitted cross section normalized to the total one (left), for the three helicity states in the electron final state for  $W^+$  (top) and  $W^-$  (bottom). The plot on the right shows the measured cross section divided by the expected one. In both plots, the light-filled band corresponds to the expected rate uncertainty from the PDFs, obtained from the quadrature sum of the 60 Hessian variations of the NNPDF3.0 set in the `aMC@NLO_MadGraph5` MC. Results are obtained using toy Monte Carlo experiments.

all the systematic uncertainties implemented in the analysis, including the BBB uncertainty.

## 7.2 Charge asymmetry

The differential W-boson charge asymmetry as a function of the W-boson rapidity and helicity is defined as

$$\mathcal{A}^{pol}(Y_W) = \frac{\frac{d\sigma^{pol}}{dY_W}(W^+ \rightarrow \ell^+ \nu) - \frac{d\sigma^{pol}}{dY_W}(W^- \rightarrow \ell^- \bar{\nu})}{\frac{d\sigma^{pol}}{dY_W}(W^+ \rightarrow \ell^+ \nu) + \frac{d\sigma^{pol}}{dY_W}(W^- \rightarrow \ell^- \bar{\nu})} \quad (7.2)$$

where *pol* represents the W-boson polarization state. The expression can be evaluated for each bin of  $Y_W$  and polarization from the set of toys to extract the measurement of  $\mathcal{A}^{pol}(Y_W)$  from the mean and RMS of the corresponding distribution. It is important to observe that the



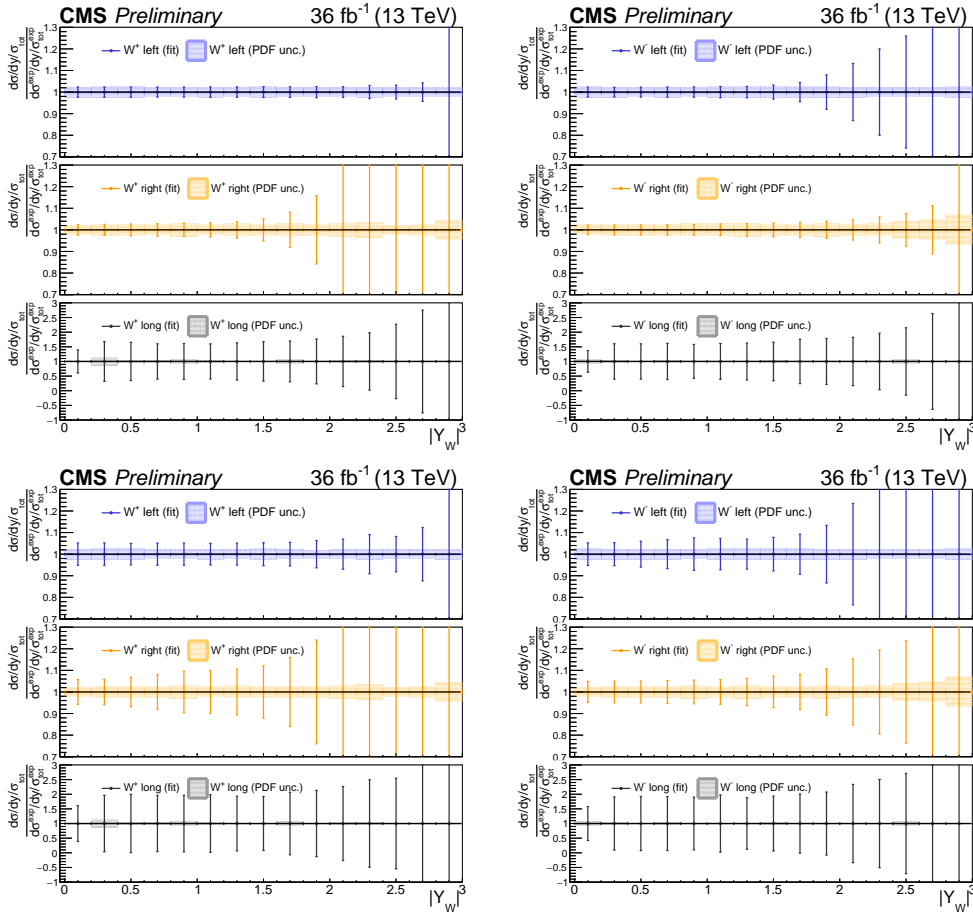


**Figure 7.5.** Relative uncertainty in the fitted cross section normalized to the total one for the three helicity states in the muon (top) and electron (bottom) final state, for  $W^+$  (left) and  $W^-$  (right). The uncertainty is evaluated on the Asimov dataset including the statistical uncertainty in the MC samples. The light-filled band corresponds to the expected rate uncertainty from the PDFs, obtained from the quadrature sum of the 60 Hessian variations of the NNPDF3.0 set in the  $aMC@NLO\_MadGraph5$  MC. Note the different scale on the y axis with respect to the one in Figs. 7.3 and 7.4.

POIs entering in eq. (7.2) are obtained from the simultaneous fit on both charges. Therefore, all the correlations between parameters are properly taken into account when extracting the asymmetry. The results are shown in Fig. 7.7.

It should be stressed that the measurement of the W-boson charge asymmetry as a function of  $Y_W$  and split in the three helicity states has never been performed before in the kinematic range that is relevant for the W-boson mass measurement, which is characterized by low  $p_T^W$ .

### 7.3 Constraint on PDFs

It was shown in Sec. 7.1 that the helicity measurement is able to constrain the uncertainty stemming from the PDFs. The maximum sensitivity to PDFs is obtained by performing

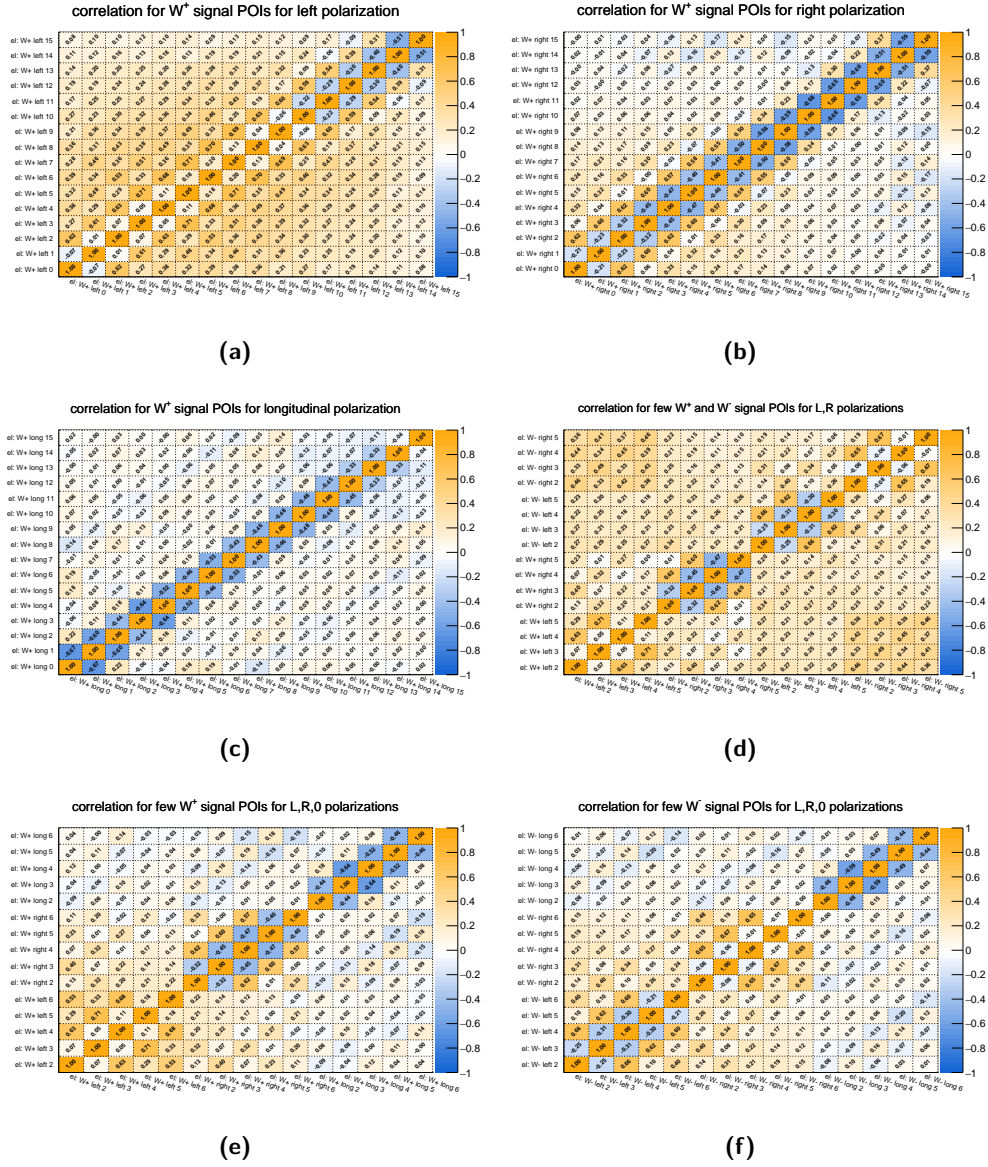


**Figure 7.6.** Correlation matrices for some of the fitted parameters in the electron final state. The correlation among signal strength parameters is shown for the left (a), right (b) and longitudinal (c) polarization. Other matrices show the correlation among few central rapidity bins, for different charges and/or helicities. These matrices are obtained from the Asimov dataset including the BBB uncertainty as well.

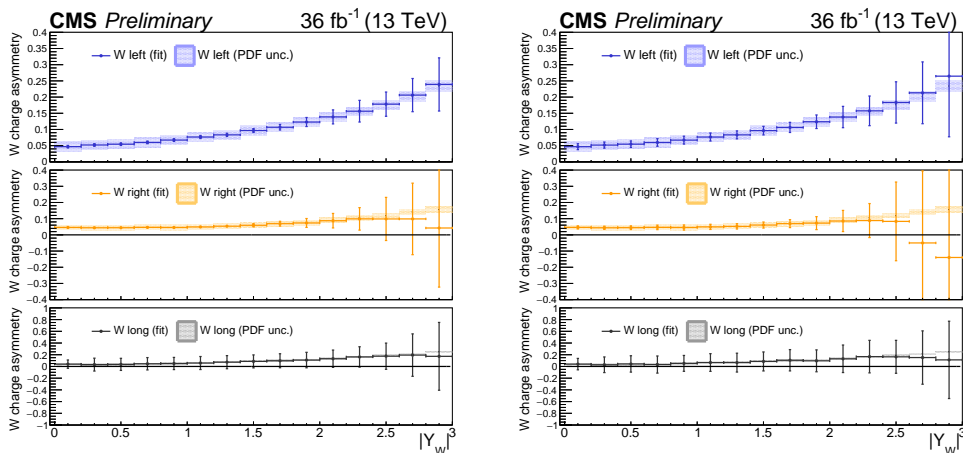


**Figure 7.7.** Fitted  $W$ -boson charge asymmetry for the three helicity states as a function of the  $Y_W$  in the muon (left) and electron (right) final states. Results are obtained from toy Monte Carlo experiments. The light-filled band correspond to the expected rate uncertainty from the PDF variations, obtained from the quadrature sum of the 60 Hessian variations of the NNPDF3.0 set (correlations are ignored in the expected PDF systematics and summed up in quadrature, which is not fully correct).

the fit with the signal POIs fixed to their expected value. In this case, an uncertainty of 3.8%, equivalent to the current knowledge of the theoretical  $W$ -boson inclusive cross section (including PDF variations), is assigned to the signal yields as additional nuisance parameter.

The pulls of the 60 PDF nuisance parameters, evaluated from the output of the fit performed with fixed signal POIs, are shown in Fig. 7.8. Most of the PDF Hessian variations are constrained to 80% of the initial value on average, whereas some of them are constrained up to 50%. Some of these highly constrained PDF parameters correspond to the template variations shown in Fig. 6.7, from which it can be seen that both the shape and the normalization of the nominal template are notably modified.

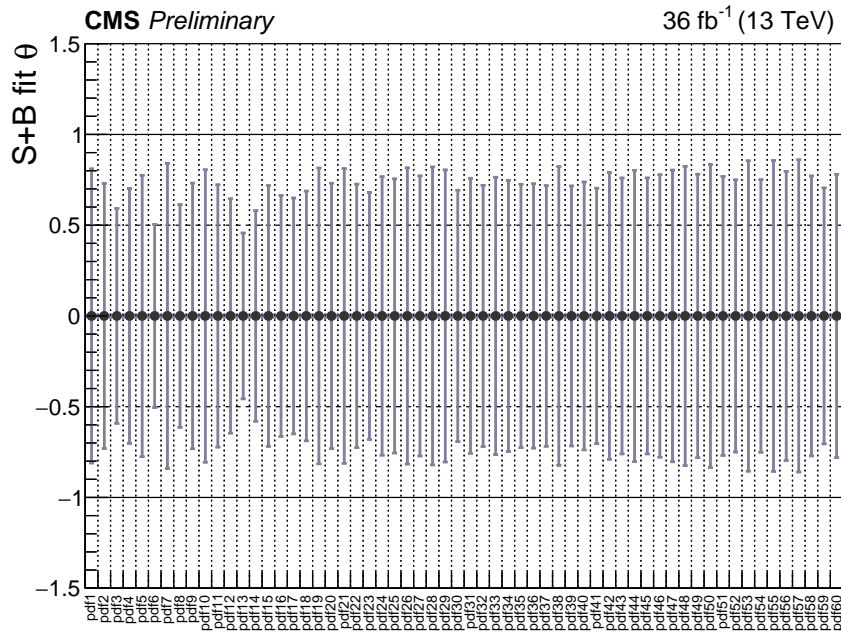
The plots in Fig. 7.8 also demonstrates that the electron channel is competitive with the muon one concerning the PDF constraints. Therefore, it is expected that the sensitivity to PDFs will be improved by performing a simultaneous fit combining both lepton flavors.

The previous plots are obtained without including the MC statistical uncertainty in the fit. When this uncertainty is added in the fit, the constraint on the PDFs is significantly reduced, as can be seen for the electron channel in Fig. 7.9.

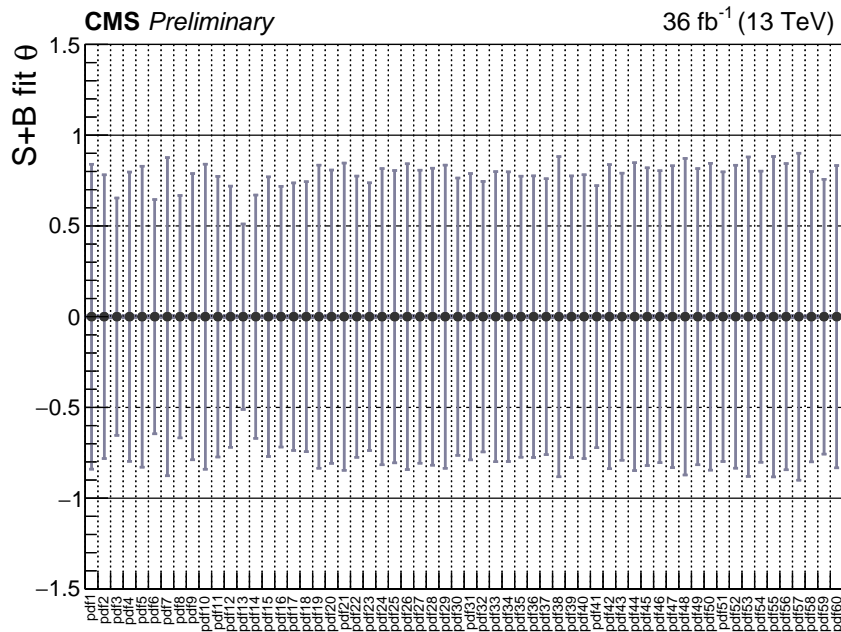
## 7.4 Double-differential cross section

In this section, the measurement of the  $W$ -boson double-differential cross section in the gen-level lepton  $p_T$  and  $|\eta|$  ( $d^2\sigma/dp_T d|\eta|$ ) is presented. The binning for the measurement is defined in Sec. 6.4. Results are obtained from the expected fit in toy Monte Carlo experiments, including the effect of the BBB uncertainty. The corresponding double-differential charge asymmetry is defined as

$$\mathcal{A}(p_T, |\eta|) = \frac{\frac{d^2\sigma}{dp_T d|\eta|}(W^+ \rightarrow \ell^+ \nu) - \frac{d^2\sigma}{dp_T d|\eta|}(W^- \rightarrow \ell^- \bar{\nu})}{\frac{d^2\sigma}{dp_T d|\eta|}(W^+ \rightarrow \ell^+ \nu) + \frac{d^2\sigma}{dp_T d|\eta|}(W^- \rightarrow \ell^- \bar{\nu})} \quad (7.3)$$

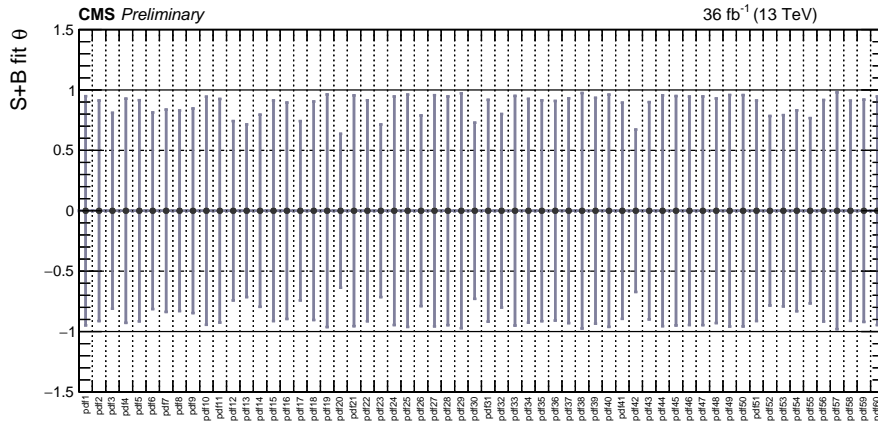


(a)



(b)

**Figure 7.8.** Post-fit pulls of the 60 Hessian variations of the NNPDF3.0 PDF set, on the Asimov dataset for the muon (top) and electron (bottom) channel. Each fit is done on the combination of both charges, fixing the signal rates to the expected yields as well. The BBB uncertainty is not considered in this fit.



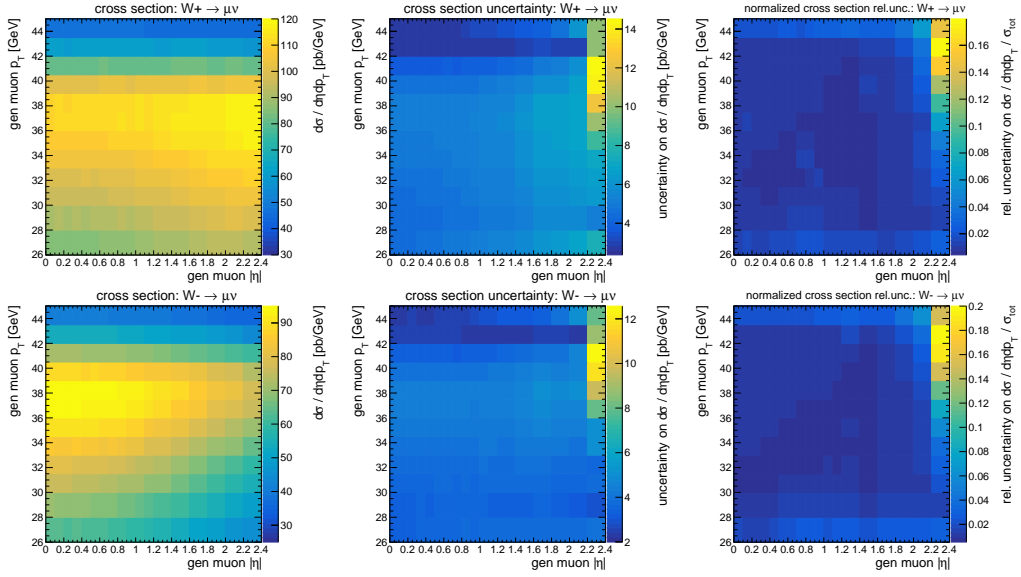
**Figure 7.9.** Post-fit pulls of the 60 Hessian variations of the NNPDF3.0 PDF set, on the Asimov dataset for the electron channel. The fit is done on the combination of both charges, fixing the signal rates to the expected yields as well. The BBB uncertainty is included in the fit.

Figure 7.10 shows the differential cross section in the muon channel for both charges. The charge asymmetry obtained from the combined fit in the two charges is shown in Fig. 7.11. The method that is used to derive the charge asymmetry represents an innovation with respect to previous Run 1 measurements [58,59], where the W-boson charge asymmetry was estimated only as a function of the  $\eta$  of the reconstructed lepton. Moreover, the approach discussed in this thesis allows to unfold the charge asymmetry directly as a function of the stable-particle-level quantities. Unlike the traditional unfolding technique, that is performed as a separate step after the fit, this method allows for both the proper treatment of correlations and the correct propagation of all the experimental uncertainties.

Finally, Fig. 7.12 shows the differential cross section obtained from toys in the muon channel unrolled into a 1-dimensional histogram. The plot provides a visual representation of different slices of the double-differential cross section as a function of the muon  $p_T$  for consecutive bins in  $|\eta|$ . It can be observed from the relative uncertainty in the lower panel that the precision is always limited by the uncertainty in the luminosity except at very high  $p_T$  and at large  $|\eta|$ , where the statistical uncertainty and other systematic uncertainties are not negligible with respect to the luminosity uncertainty. The normalized cross section, not affected by the uncertainty in the luminosity, is shown in Fig. 7.13.

## 7.5 Results on data

In this section the results of the fit performed on data are presented. They are not approved by CMS yet, and therefore should be considered as private results. The uncertainty on the measured quantities are obtained propagating all the uncertainties discussed in previous sections for the expected fits. The statistical uncertainty in the signal MC sample is included as well and is treated as uncorrelated among signal bins.



**Figure 7.10.** Differential cross section in the muon channel as a function of the muon  $p_T$  and  $|\eta|$ , obtained from toy MC experiments. The top (bottom) row shows the results for the positive (negative) charge. The plots on the left show the absolute cross section. The plots in the middle are the uncertainty on the absolute cross section. The plots on the right show the relative uncertainty on the normalized cross section. The absolute cross section and the corresponding uncertainty are normalized to the bin area.

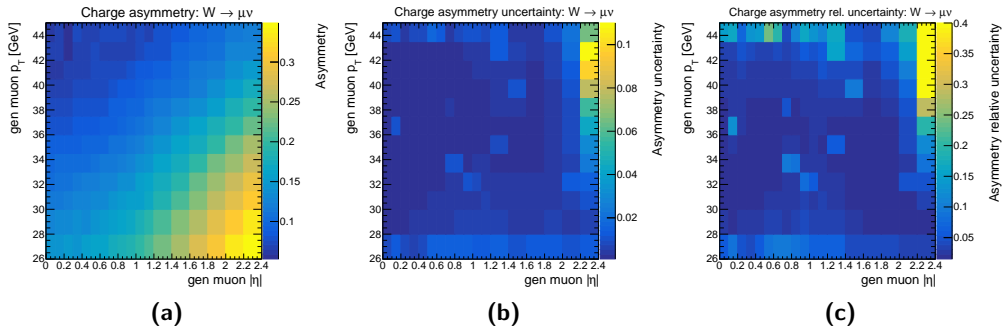
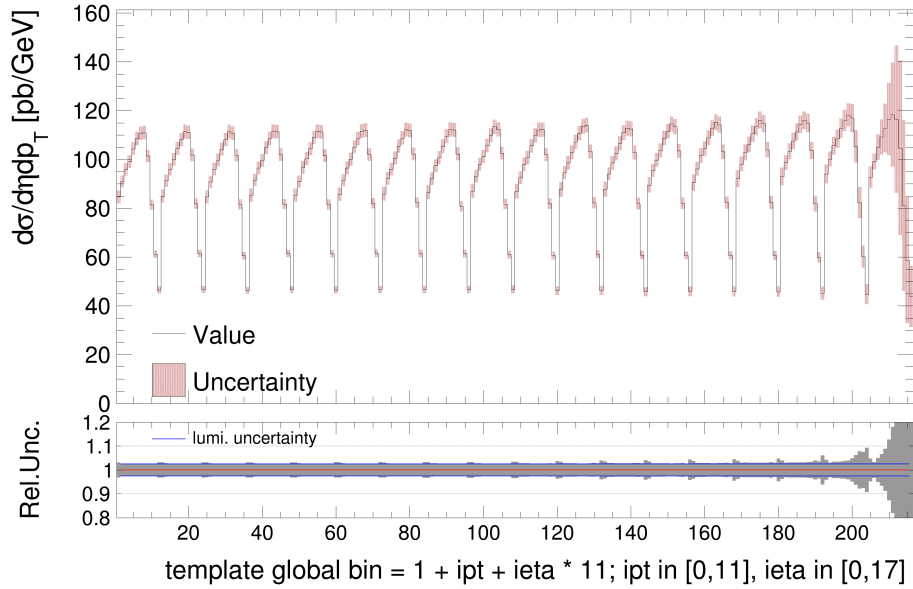
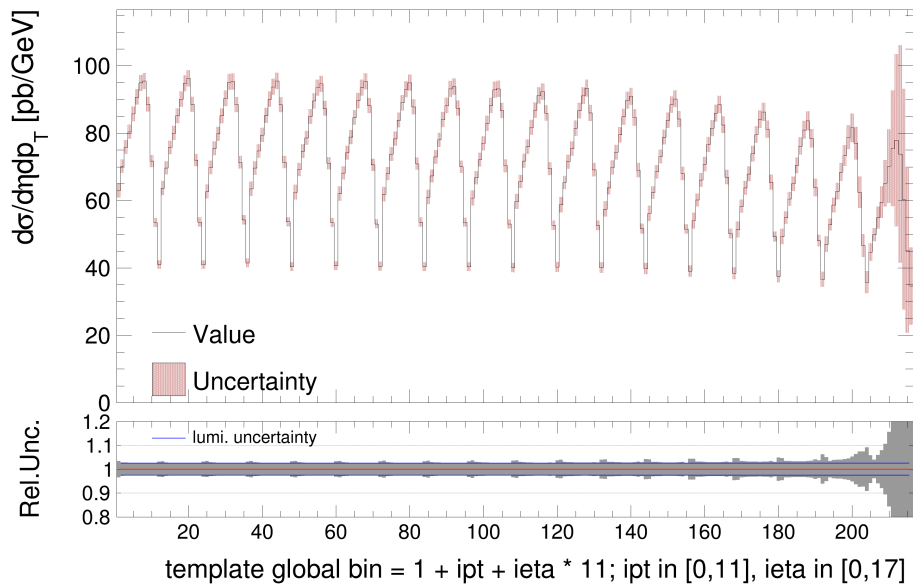


**Figure 7.11.** (a): charge asymmetry in the muon channel as a function of the muon  $p_T$  and  $|\eta|$ , as obtained from toys. (b): uncertainty on the charge asymmetry. (c): relative uncertainty on the charge asymmetry.

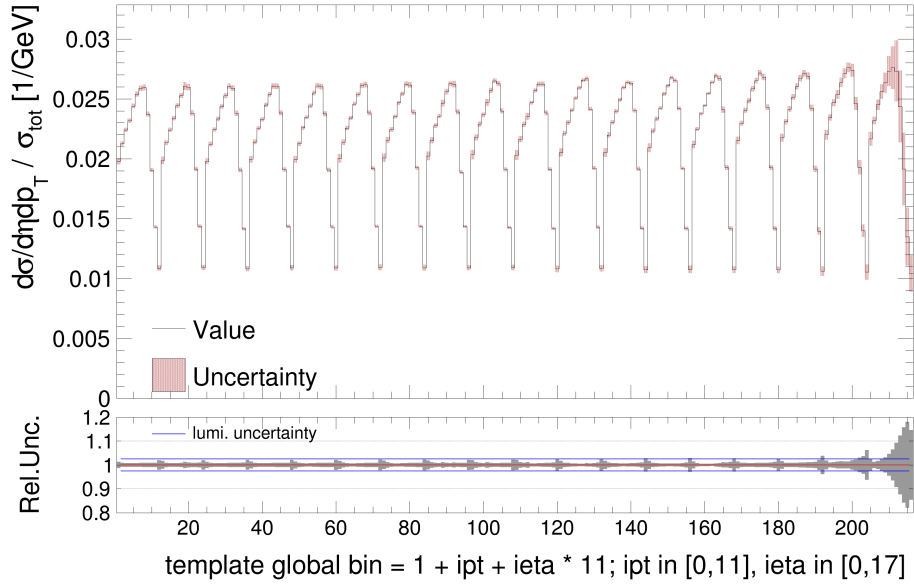


(a)

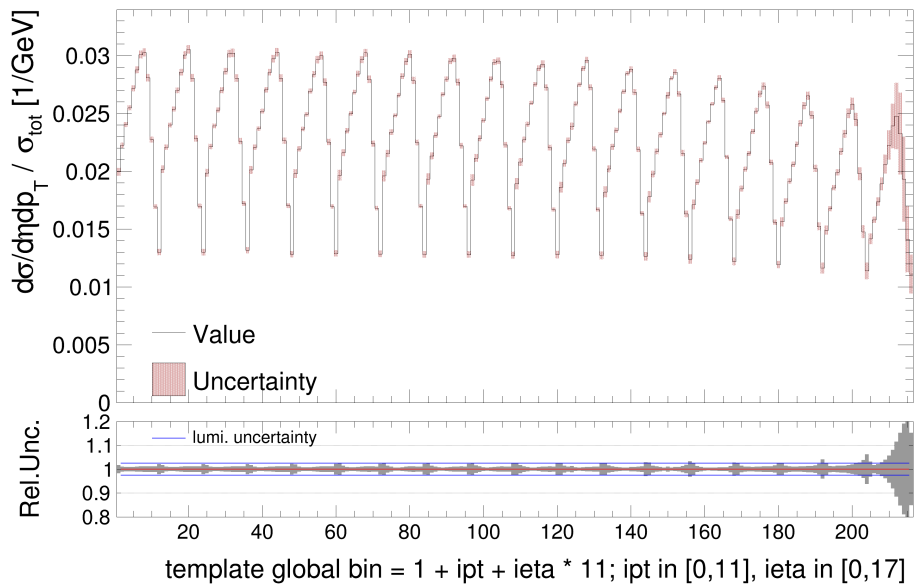


(b)

**Figure 7.12.** Expected double-differential cross section as a function of the muon  $p_T$  and  $|\eta|$ , unrolled in a 1D histogram for the positive (negative) charge on top (bottom). The lower panel shows the relative uncertainty, which is limited by the luminosity uncertainty in all the acceptance region except for the high  $p_T$  or  $|\eta|$  region.



(a)



(b)

**Figure 7.13.** Expected double-differential cross section as a function of the muon  $p_T$  and  $|\eta|$ , normalized to the total one and unrolled in a 1D histogram for the positive (negative) charge on top (bottom). The lower panel shows the relative uncertainty. The uncertainty in the luminosity (blue line) does not affect the normalized cross section and is reported as a reference.



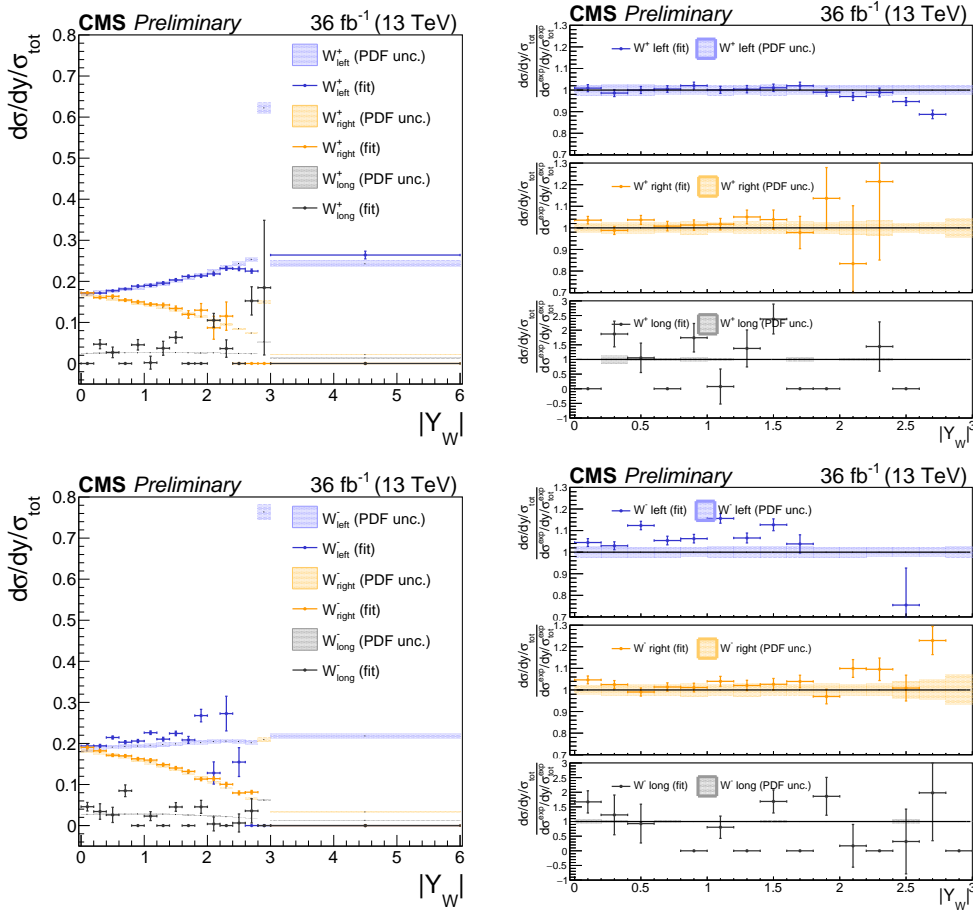


**Figure 7.14.** Measured cross section normalized to the total one (left), for the three helicity states in the muon final state for  $W^+$  (top) and  $W^-$  (bottom). The plot on the right shows the measured cross section divided by the expected one. In both plots, the light-filled band correspond to the expected rate uncertainty from the PDFs, obtained from the quadrature sum of the 60 Hessian variations of the NNPDF3.0 set. The total cross section used in the normalization does not include the last two rapidity bins. Last two bins are normalized to the sum of their cross section. *preliminary and private.*

### 7.5.1 Helicity and rapidity

Figure 7.14 shows the measured normalized differential cross section as a function of the W-boson rapidity in each helicity state in the muon channel. The total cross section used in the normalization does not include the last two rapidity bins, which are characterized by a large uncertainty. The last two bins are normalized to their total cross section. The plot on the left shows the observed spectrum in data, whereas the one on the right shows the ratio of the measured and expected spectra. The colored band represents the PDF uncertainty on the expected cross section. Results obtained in the electron channel are shown in Fig. 7.15. In both channels, the longitudinal polarization is poorly constrained by the fit due to the lower number of selected events compared to the other two helicity states. The largest uncertainty in the measurement of the longitudinal polarization is given by the BBB uncertainty.

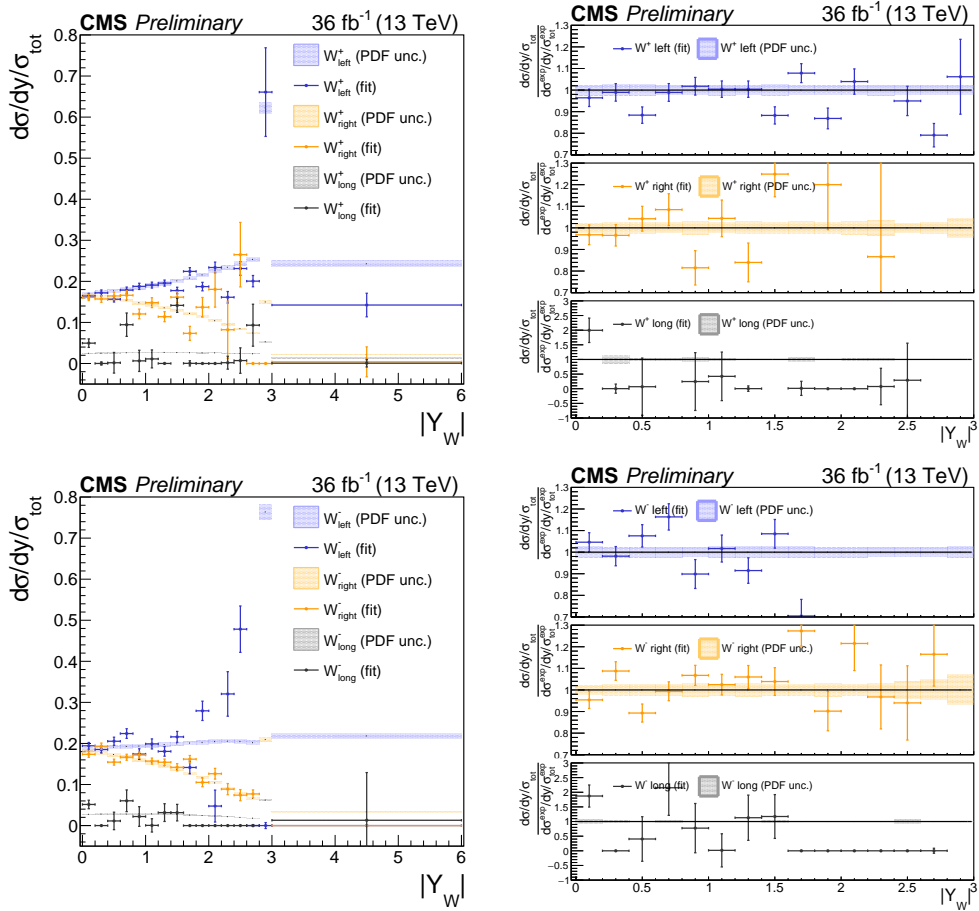


**Figure 7.15.** Measured cross section normalized to the total one (left), for the three helicity states in the electron final state for  $W^+$  (top) and  $W^-$  (bottom). The plot on the right shows the measured cross section divided by the expected one. In both plots, the light-filled band correspond to the expected rate uncertainty from the PDFs, obtained from the quadrature sum of the 60 Hessian variations of the NNPDF3.0 set. The total cross section used in the normalization does not include the last two rapidity bins. Last two bins are normalized to the sum of their cross section. *preliminary and private.*

### 7.5.2 Double-differential cross section

The double-differential cross section measured in the muon channel is shown in Fig. 7.16 for both charges. The measured absolute cross section and its uncertainty are shown in the left and middle column, respectively. The right column presents the relative uncertainty on the measured cross section normalized to the total one inside acceptance. It should be remarked that the cross section is measured as a function of the kinematic quantities of the stable-particle muon, where the unfolding to generator level is performed directly in the fit. The uncertainty on the absolute cross section stays relatively flat as a function of  $|\eta|$  due to the non-uniform binning: it ranges between 2.5% and 4%, dominated by the luminosity uncertainty up to  $|\eta| < 2.0$ . For  $|\eta| > 2.0$ , the uncertainty grows up to about 20%.

The cross section measured in the muon channel and unrolled into a 1-dimensional distribution is reported in Fig 7.17 and is compared to the expected one. The agreement

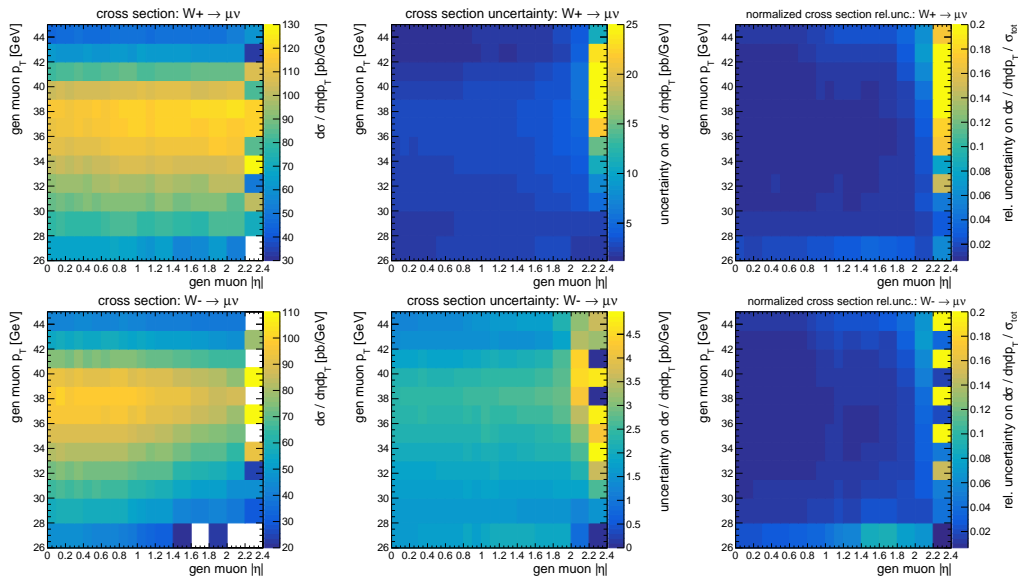


**Figure 7.16.** Measured differential cross section in the muon channel as a function of the muon  $p_T$  and  $|\eta|$ , unfolded to stable-particle level. The top (bottom) row shows the results for the positive (negative) charge. The plots on the left show the absolute cross section. The plots in the middle are the uncertainty on the absolute cross section. The plots on the right show the relative uncertainty on the cross section normalized to the total one in acceptance. The absolute cross section and the corresponding uncertainty are normalized to the bin area. **preliminary and private.**

between data and the prediction is generally within 5% around the bulk of the  $p_T$  distribution in each bin of  $|\eta|$ . However, there seems to be a difference in the shape of the  $p_T$  distribution between data and the prediction, which needs to be further investigated. The associated W-boson charge asymmetry measured in the muon channel is shown in Fig. 7.18.

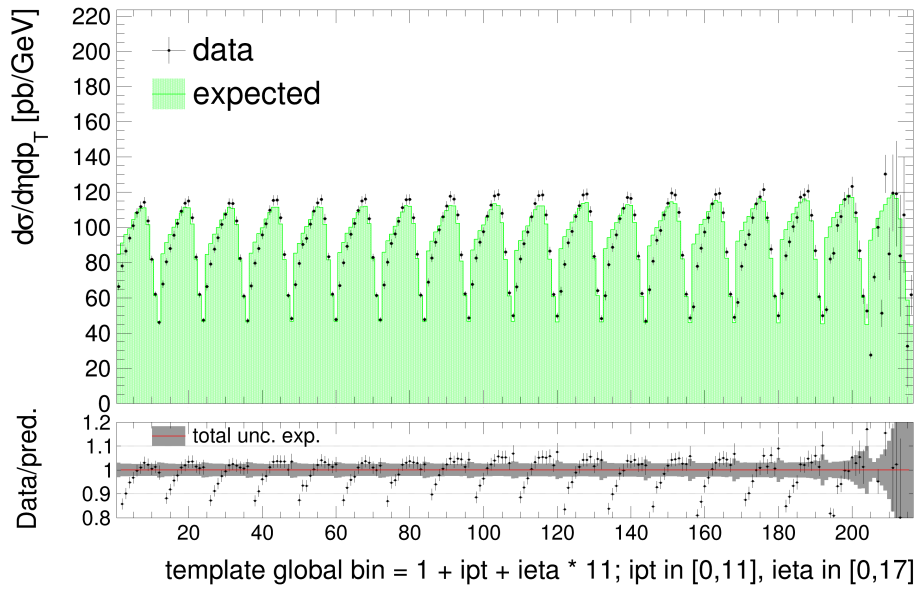
Figure 7.19 shows the unrolled cross section measured in the electron channel. The empty bins correspond to the signal categories with  $p_T < 30$  GeV and  $1.4 < |\eta| < 1.6$ . These are considered as background processes in the fit, since they are less constrained due to the acceptance. This makes the fit more stable and also leads to a slight reduction of the uncertainty in the neighboring bins.

The measurement and the prediction agree within 5% for  $|\eta| < 1.0$ . At higher values of electron pseudorapidity, the agreement stays within 20%. The uncertainty on the measured cross section ranges between 2.5% and 10% in EB, and is lower than 5% for  $|\eta| < 1.1$ . The uncertainty in EE fluctuates between 10% and 20%.

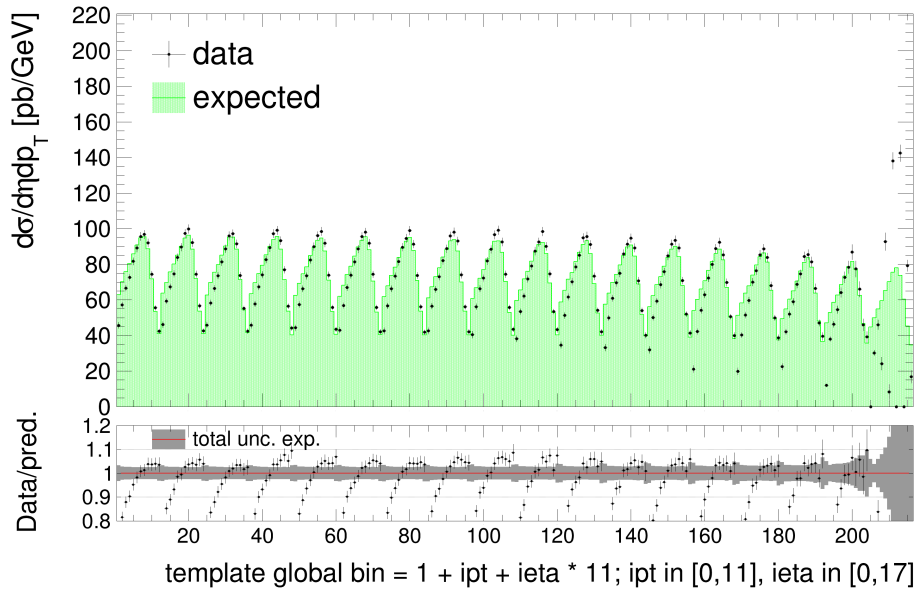
### 7.5.3 Impacts of systematic uncertainties

Each POI can be affected in different ways by the several sources of systematic uncertainty described in previous sections, depending on the correlation between each POI and the nuisance parameters.

The impact of a nuisance parameter  $\theta$  on a POI, either the signal strength  $\mu_i$  or the cross section  $\sigma_i$  in the  $i$ -th bin, is defined as the absolute shift that is induced on the fitted POI as  $\theta$  is fixed and brought to its  $+1\sigma$  or  $-1\sigma$  post-fit values, with all other parameters being profiled.



(a)



(b)

**Figure 7.17.** Double-differential cross section measured in data as a function of the muon  $p_T$  and  $|\eta|$ , unfolded to stable-particle level and unrolled in a 1D histogram for the positive (negative) charge on top (bottom). The green histogram represents the expectation, and the lower panel shows the ratio of the measured and predicted cross section. The gray band in the ratio represents the total uncertainty in the prediction. *preliminary and private.*

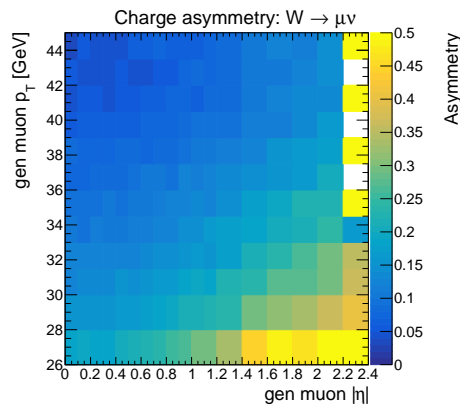


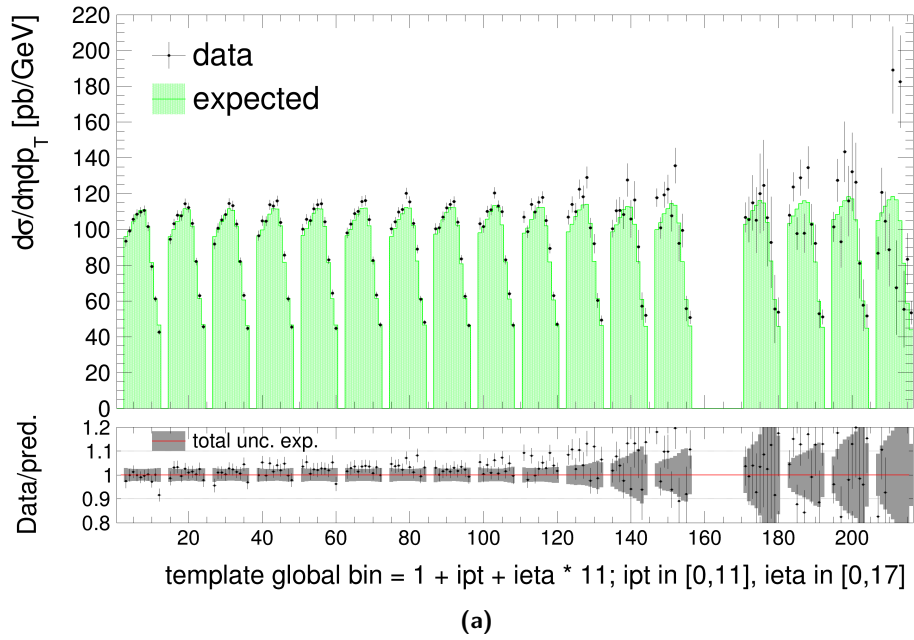
**Figure 7.18.** Measured  $W$ -boson charge asymmetry in the muon channel as a function of the muon  $p_T$  and  $|\eta|$ , unfolded to stable-particle level. *preliminary and private.*

Given the large number of nuisance parameters considered in the analysis, the impacts of theoretical and experimental systematic uncertainties are presented as a matrix of groups of nuisances on the set of POIs. The impact for a given group is the effect of the simultaneous variation of all the parameters present in the group with the covariance matrix of the fit. Groups are defined for:

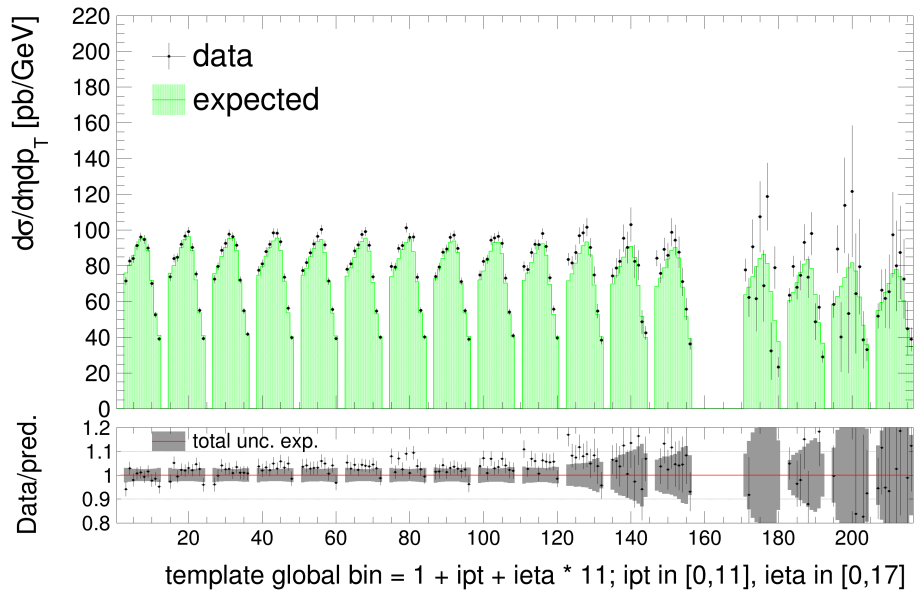
- bin-by-bin template MC statistical uncertainty (binByBinStat);
- pure statistical uncertainty (stat);
- uncorrelated part of the lepton efficiency systematic uncertainties (EffStat);
- PDFs (pdfs);
- QCD scales (scales);
- $m_W$  modeling (wmodel);
- $\alpha_S$  (alphaS);

For simplicity, impacts are shown only for some selected signal strength parameters in the electron channel. Impacts on these parameters related to the helicity measurement are shown in Fig. 7.20 for all the 16 rapidity bins, numbered from 0 to 15. The magnitude of the impact of each group of nuisances depends on the helicity and the rapidity bin. It can be observed that the largest impacts are provided by the BBB uncertainty, followed by the theoretical uncertainties in the PDFs and the lepton efficiency.

In a similar way, impacts of groups of systematic uncertainties are also shown for the signal strength parameters of the double-differential cross section measurement. Given the large number of signal POIs ( $216 p_T \times |\eta|$  bins), the impacts are shown for some selected strips at constant  $p_T$  or  $|\eta|$  (the bin edges are defined in Sec. 6.4). They are shown in Fig. 7.21 for the outer bins in  $|\eta|$  and  $p_T$ , as well as for some central bins in both variables. The largest impacts are provided by the BBB uncertainty, followed by the theoretical uncertainties on the PDFs and the QCD scales.



(a)



(b)

**Figure 7.19.** Double-differential cross section measured in data as a function of the electron  $p_T$  and  $|\eta|$ , unfolded to stable-particle level and unrolled in a 1D histogram for the positive (negative) charge on top (bottom). Empty bins correspond to signal categories treated as background processes (see text). The green histogram represents the expectation, and the lower panel shows the ratio of the measured and predicted cross section. The gray band in the ratio represents the total uncertainty in the prediction. **preliminary and private.**

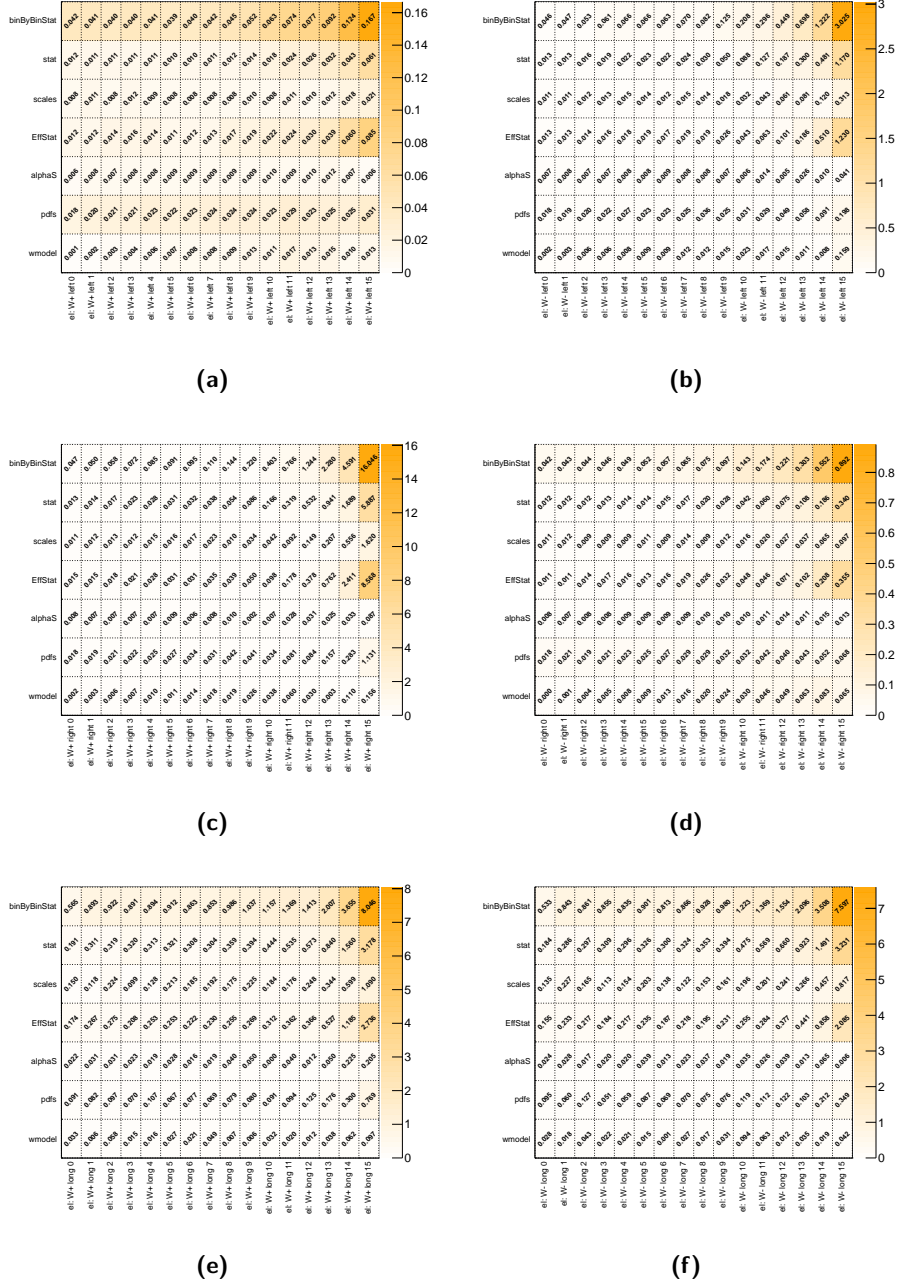


**Figure 7.20.** Impacts of some groups of systematic uncertainties on some signal strength parameters,  $\mu$ , for the helicity measurement in the electron channel. The left column shows the impacts on all the 16 rapidity bins in the positive charge channel for the left, right, and longitudinal polarization from top to bottom, respectively. The right column shows the impacts for the negative charge.

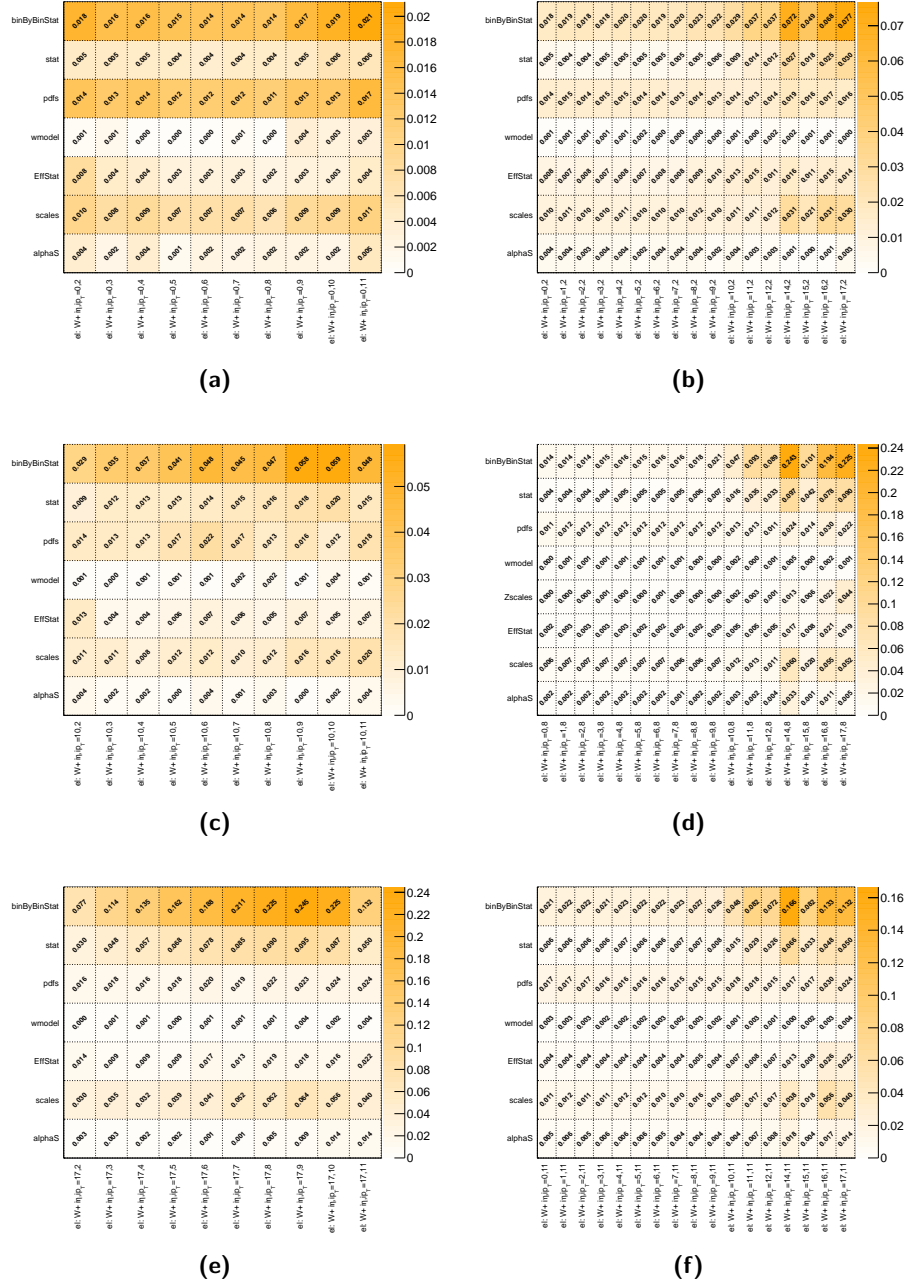


**Figure 7.21.** Impact of some groups of systematic uncertainties on some signal strength parameters,  $\mu$ , for the differential cross section as a function of the electron  $p_T$  and  $|\eta|$ . The left column shows the impacts for all bins at constant  $|\eta|$  for  $i_T = 0, 10, 17$  from top to bottom respectively. The right column shows the impacts for all bins at constant  $p_T$  for  $i_T = 2, 8, 11$  from top to bottom respectively.



## Chapter 8

# Conclusions and perspectives

In this thesis, the measurement of the W-boson helicity and rapidity distribution has been presented. The results are complemented by the measurement of the W-boson double-differential cross section as a function of the stable-particle-level lepton  $p_T$ - $\eta$ . The measurements are carried out using  $W \rightarrow e\nu$  and  $W \rightarrow \mu\nu$  events in a data sample of  $35.9 \text{ fb}^{-1}$  collected by CMS at  $\sqrt{s} = 13 \text{ TeV}$  during 2016, and employ a binned maximum likelihood fit to the 2-dimensional charged lepton  $p_T$ - $\eta$  distribution in data with simulated signal and background templates.

The analysis uses W bosons with positive and negative charge, and the simultaneous measurement performed using both channels is translated into the measurement of the W-boson charge asymmetry, carried out double-differentially in either the W-boson helicity and rapidity or the stable-particle-level lepton  $p_T$  and  $\eta$ .

The uncertainty in the measured absolute cross sections is currently limited by the uncertainty in the integrated luminosity, that amounts to 2.5%. For the measurement of the normalized cross sections, which are not affected by the luminosity uncertainty, an important contribution on the total uncertainty is represented by the statistical uncertainty in the signal MC sample in most of the considered phase space. However, the corresponding uncertainty is expected to be reduced by exploiting a larger sample of simulated events.

Both measurements represent innovative results in terms of experimental techniques and physics reach. The charge asymmetry has never been measured as a function of the W-boson helicity and rapidity in the kinematic range characterized by  $p_T^W \lesssim 30 \text{ GeV}$ . Moreover, the method discussed in this thesis allows to unfold the double-differential cross section and charge asymmetry directly as a function of the stable-particle lepton  $p_T$ - $\eta$ , thus representing an innovation with respect to the standard technique used for Run 1 measurements.

The fit to the W-boson helicity is also performed fixing the W-boson cross section to the expected value. This configuration maximizes the analysis sensitivity to the PDFs and leads to a reduction of the PDF uncertainties by more than 20% on average, demonstrating the statistical power of an in-situ constraint on them. This result is of vital importance to reduce the main systematic uncertainty on the W-boson mass ( $m_W$ ) measurement. A paper featuring the aforementioned results will be submitted for publication by Winter 2019.

The precise measurement of the W-boson mass represents a powerful tool to test the Standard Model and probe the possible existence of new physics. A global fit to Standard Model electroweak parameters predicts  $m_W$  with an uncertainty of 7 MeV. Reaching this accuracy in a direct measurement of  $m_W$  is a formidable challenge and requires an outstanding

control of all the experimental and theoretical systematic uncertainties.

The measurements discussed in this thesis represent an important benchmark towards the precision measurement of  $m_W$  with CMS data. Indeed, the analysis framework and the experimental techniques developed to perform the helicity measurement are going to be adapted to carry out the first CMS measurement of  $m_W$ . This target foresees in-situ constraints of the PDFs and the W-boson production kinematics based on the fit to the 2-dimensional  $p_T$ - $\eta$  distribution, with the possible extension to a 3-dimensional space by including the information based on the hadronic recoil. This innovative approach to measure  $m_W$  aims at reducing the large theoretical uncertainties that currently limit the precision of the  $m_W$  measurement at the LHC.

The next developments for the coming years will target the measurement of the full 5-dimensional W-boson cross section  $d^5\sigma/dp_T^2 dY dm d\cos\theta d\phi$  and will require the extension of the analysis to the full 13 TeV dataset collected by CMS during Run 2, which comprises about  $150 \text{ fb}^{-1}$ . This result will constitute an important milestone for the CMS Standard Model physics program.

## **Appendices**



## Appendix A

# ECAL inter-calibration with $\pi^0 \rightarrow \gamma\gamma$

This chapter illustrates the inter-calibration of the CMS electromagnetic calorimeter (ECAL) [61]. A more detailed description of ECAL and the reconstruction of electrons and photons, is provided as well, expanding the one reported in Sect. 3.2.3. All the procedures and techniques adopted by CMS for the calibration of the calorimeter are briefly discussed, giving larger emphasis on one specific method which exploits photon pairs from decays of  $\pi^0$  particles produced in proton-proton collisions during LHC operations.

The excellent performance in the reconstruction and identification of high energy photons and electrons has played a key role in the observation of the Higgs boson and the study of its properties [62, 63] during the LHC Run I. Maintaining and improving the excellent ECAL performance during Run I in the harsher environment of the LHC Run II and beyond is vital for all the physics analyses that include photons or electrons in their final state. Achieving this goal requires a continuous effort in the operation, monitoring and calibration, and simulation of the calorimeter.

Despite the fact that the analysis presented in this thesis is based on the dataset collected by CMS during 2016, most of the material presented in this chapter about the inter-calibration (IC) campaign with  $\pi^0$ 's comes from data collected in 2017. Indeed, the continuous increase of the instantaneous luminosity provided by LHC since the beginning of Run II in 2015 entailed harsher conditions of data taking, such as higher pileup, more intense radiation damage and the subsequent increase in the measured noise in the calorimeter. As explained with more details in next sections, several improvements and changes in the CMS software were deployed in order to cope with these effects: for instance, the energy thresholds in the ECAL readout system were optimized every year to comply with the limits in the CMS readout bandwidth and storage space. However, this led to the increase of the energy thresholds, resulting in undesired patterns in the IC constants produced using  $\pi^0$ 's, which were fully understood only by early 2018.

Moreover, taking advantage of the understanding of many systematic effects and the larger dataset collected by CMS during 2017, a new set of inter-calibration constants was derived in early 2018 using all the available methods. Therefore, the choice to present results based on 2017 data is mainly motivated by the quest for consistency with the historical evolution of the ECAL calibration campaign. Nonetheless, the techniques that will be described later have a general validity and will also be used to derive new ECAL inter-calibration constants for all the years of data taking during Run II.

## A.1 ECAL detector

CMS features a high-resolution, homogeneous electromagnetic calorimeter comprising 61200 crystals of lead tungstate ( $\text{PbWO}_4$ ) in the central barrel detector (EB), complemented by 7324 crystals in each of the two endcaps (EE). In the following, since each crystal represents a single readout channel, the terms crystal and channel will often be used as synonyms. Thanks to the properties of  $\text{PbWO}_4$  (Molière radius of 2.19 cm and a radiation length  $X_0 = 0.85$  cm), ECAL is characterized by high granularity and excellent longitudinal containment of the electromagnetic shower of electrons and photons with energies up to the TeV scale. In addition, the decay time of the scintillation light is about 25 ns, which guarantees a fast detector response. The timing resolution of ECAL is measured from data using  $Z \rightarrow ee$  events: by comparing the time difference between the energy deposits of the two electrons, the estimated single channel timing resolution is 190 ps in EB and 280 ps in EE. The scintillation light is detected by avalanche photodiodes (APDs) in EB and by vacuum phototriodes (VPTs) in EE, resulting in an average of 4.5 photoelectrons per MeV deposited in the crystals. The relatively low light yield of  $\text{PbWO}_4$  demands for an amplification of the input signal.

The barrel covers the region within  $|\eta| = 1.479$ , while the endcaps extend the coverage up to  $|\eta| < 3.0$ . A preshower detector (ES), based on lead absorbers equipped with silicon strip sensors, is placed in front of EE. It covers the region  $1.65 < |\eta| < 2.6$  and helps resolve the signals of high-energy photons from the decays of neutral pions into two close photons, improving also the measurement of the position of the electromagnetic deposit in EE.

## A.2 ECAL geometry

EB uses 23 cm long crystals with a truncated pyramidal shape and front face cross-sections of around  $2.2 \text{ cm} \times 2.2 \text{ cm}$ , while EE comprises 22 cm long crystals with front face cross-sections of  $2.9 \text{ cm} \times 2.9 \text{ cm}$ . Therefore, ECAL provides about  $25 X_0$  thickness to the passage of electromagnetic particles.

Crystals in EB are organized in 36 supermodules, 18 on each side on the detector. In turn, each supermodule is divided in 4 modules along the  $\eta$  direction. Each supermodule hosts 1700 crystals arranged in a  $20 \times 85$  matrix in the  $\phi$ - $\eta$  coordinates: along  $\eta$ , 25 arrays of 20 crystals for each are located in the first module ( $25 \times 20$  crystals in total), while each of the remaining three modules has 20 arrays of crystals ( $20 \times 20$  channels). In summary, EB provides a 360-fold granularity along the  $\phi$  angle and  $(2 \times 85)$ -fold granularity along  $\eta$ . In the following, the discrete coordinates  $i\phi \in [1, 360]$  and  $i\eta \in [-85, 85]$  with  $i\eta \neq 0$  will often be used to identify an ECAL crystal in EB.

Crystals in EE are arranged in an X-Y grid to form an approximately circular shape with a diameter of 100 crystals, and are identified by their  $iX$  and  $iY$  coordinates ranging from 1 to 100. They are grouped in bunches of 25 crystals ( $5 \times 5$ ) known as supercrystals. Crystal in EE are virtually grouped into 39  $\eta$ -rings which collect channels located approximately at the same  $\eta$ .

Crystals in EB and EE are arranged pointing slightly off the nominal interaction vertex in the center of CMS (about  $3^\circ$ ), so to prevent particles from traversing the gaps between neighboring crystals. A sketch of the ECAL detector is shown in Fig. A.1. Figure A.2 illustrates the relation between the  $\eta$  and the  $\eta$ -ring coordinates in EE.

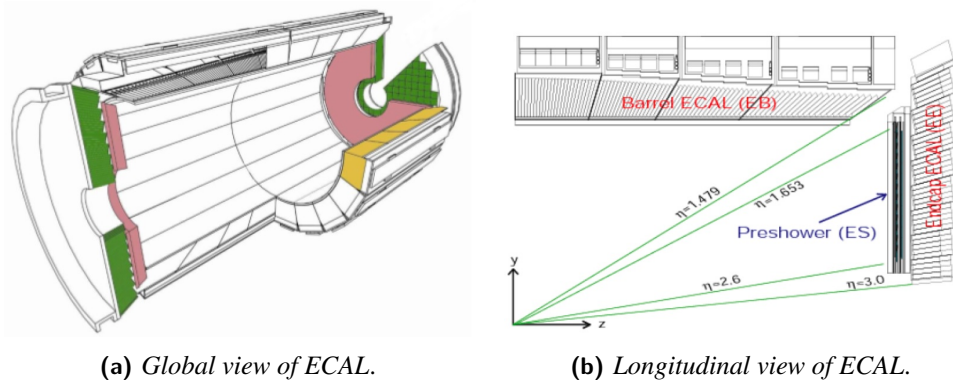


**Figure A.1.** ECAL geometry. A global view is shown on the left, with one EB supermodule in yellow (divided in 4 modules), EE in green and ES in pink. On the right, a longitudinal view of ECAL is presented: it is possible to distinguish the arrays of crystals arranged in 4 modules in EB and the coverage of each subdetector along  $\eta$ .

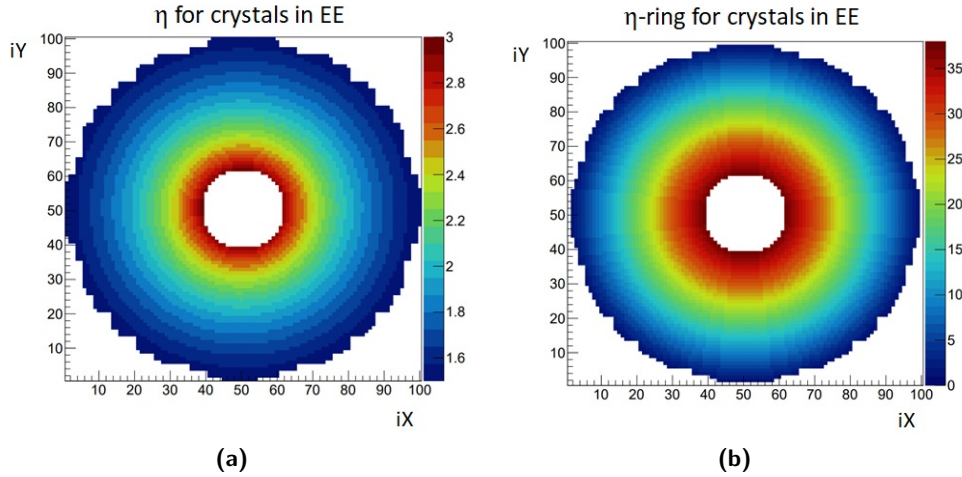


**Figure A.2.** Maps of  $\eta$  (a) and  $\eta$ -ring (b) coordinate in EE.

### A.3 ECAL energy reconstruction

The electrical signal from the photodetectors is amplified and shaped by a multi-gain preamplifier (MGPA), which uses three parallel amplification stages (with gains 1, 6 or 12) followed by three integrated sampling Analog to Digital Converters (ADC) working at the LHC frequency (40 MHz). The non-saturated ADC output with the highest gain is read out and stored, waiting for the decision of the L1 trigger system (see 3.2.7). The signal amplitude is reconstructed from a series of 10 consecutive samples recorded by the ADC, one every 25 ns.

During the LHC Run I, a digital filtering algorithm was used [64] to estimate the signal amplitude  $A$ , which is obtained as a linear combination of the 10 samples  $S_i$ :

$$A = \sum_{i=1}^{N=10} w_i \times S_i \quad (\text{A.1})$$

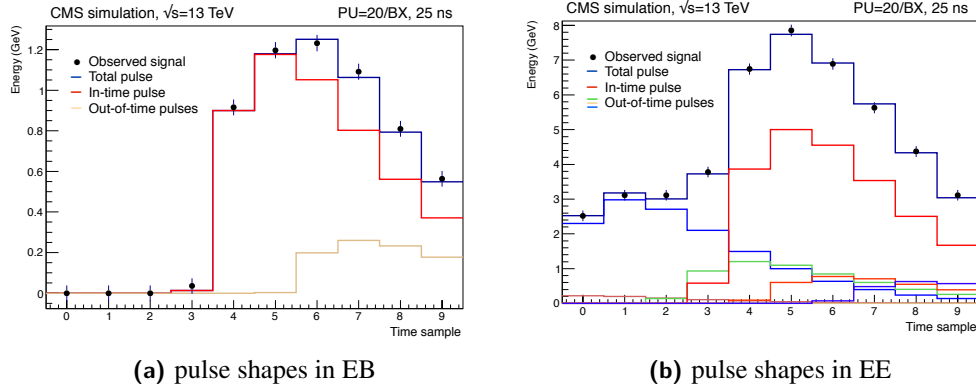


**Figure A.3.** Fitted pulse shapes in (a) EB and (b) EE for simulated events. The total pulse (blue line), overlaid with the observed signal (black dots), is obtained as the sum of the fitted pulses (other colored lines). The in-time pulse (red line) peaks at the sixth time sample corresponding to the in-time bunch crossing. The distortion induced by out-of-time pileup is larger in EE than in EB.

where the weights  $w_i$  are calculated from the minimization of the variance of  $A$ . However, the observed pulse shape is distorted by the energy deposited by particles originating from simultaneous proton collisions (pileup) and the estimated signal amplitude is then biased. Moreover, the time spacing between colliding proton bunches was reduced from 50 to 25 ns during Run II, enhancing the contribution of out-of-time pileup (OOT).

In order to mitigate the impact of OOT on the measured amplitude, an improved algorithm, named multifit, was developed during Run II [65]. The multifit models the observed pulse shape as the sum of one in-time and up to 9 out-of-time pulse amplitudes. The in-time signal amplitude is then extracted through the minimization of a  $\chi^2$  variable defined as

$$\chi^2 = \sum_{i=1}^{N=10} \frac{(\sum_{j=1}^{M=10} A_j p_{ij} - S_i)^2}{\sigma_{S_i}^2} \quad (\text{A.2})$$

where  $A_i$  are the amplitudes of up to  $M = 10$  interactions. The index  $j$  refers to a given bunch crossing, in which a specific pulse shape is generated. Instead, the index  $i$  refers to the given time sample out of the total 10 recorded by the ADC. All the pulse templates  $\vec{p}_j$  for each bunch crossing  $j$  have the same shape and only differ by a 25 ns shift on the horizontal axis. The total electronic noise  $S_i$  and its associated covariance matrix,  $\sigma_{S_i}$ , are measured from dedicated pedestal runs, which measure the noise in all the three gains of the MGPA in the absence of signal pulses.

An example of a fit in EB and EE for simulated events is shown in Fig. A.3. The total pulse, overlaid with the observed signal, is obtained as the sum of the fitted pulses. The in-time pulse peaks at the sixth time sample corresponding to the in-time bunch crossing. The other out-of-time pulses peak at different time samples and represent the energy contribution from OOT.

Electrons and photons deposit their energy in several ECAL crystals and are reconstructed through a clustering algorithm. The magnetic field bends the trajectory of electrons along the  $\phi$  angle direction. Therefore, basic clusters are extended along  $\phi$  to form super-clusters (SC) and recover additional energy deposits produced by electron bremsstrahlung



or photon conversions in the tracker. The SC energy is estimated as

$$E_{e,\gamma} = F_{e,\gamma} \cdot G \cdot \sum_i (S_i(t) \cdot C_i \cdot A_i) \quad (\text{A.3})$$

where  $F_{e,\gamma}$  includes corrections to the clustered energy and  $G$  is an ADC to GeV conversion factor. The sum runs over the channels in the cluster:  $A_i$  is the amplitude measured in the  $i$ -th channel;  $S_i(t)$  is a time-dependent correction for variations of channel response due to changes in crystal transparency;  $C_i$  is a relative calibration constant accounting for differences in the light yield and photodetector response of each channel.

### A.3.1 Corrections to clustered energy

The energy of an SC is corrected using a multivariate analysis technique (MVA) trained on simulations. The MVA receives as input, among other variables, the coordinates of the crystals, the shower shapes and the vertex multiplicity (to account for in-time PU). The MVA addresses the energy containment inside the SC and corrects for several effects, such as:

- the energy loss due to interactions with material in front of ECAL (the tracker detector, cables or other services);
- the energy leakage in gaps between crystals: this item is particularly relevant in EB, due to the borders between modules and supermodules;
- the contribution from spurious energy deposits due to in-time pileup events.

The output correction factor  $F_{e,\gamma}$  in eq. (A.3) is tuned separately on electrons and photons to account for differences due to photon conversions in the material upstream of ECAL or electron bremsstrahlung. A cluster shape parameter  $R_9$  is introduced to quantify the spread of the electromagnetic shower: it is defined as the ratio of the energy contained in a  $3 \times 3$  matrix of crystals centered on the SC crystal with the highest energy (called as the *seed*) and the total SC energy. This variable helps distinguish photons converting before arriving to ECAL from unconverted photons. It also discriminates electrons with high bremsstrahlung in the material in front of ECAL from those with low bremsstrahlung. Generally, the chosen  $R_9$  threshold to distinguish the two cases is set to 0.94, such that larger values of  $R_9$  correspond to lower bremsstrahlung.

Finally, the absolute energy scale  $G$  is set such that the invariant mass of Z bosons in  $Z \rightarrow ee$  events measured in a reference region matches the invariant mass from simulated events. The central part of the first module for each supermodule is used as the reference region: this choice is mainly motivated by the lesser material budget in front of ECAL.

### A.3.2 Crystals response monitoring

ECAL crystals undergo a change of transparency due to radiation damage during periods of LHC operation. This effect induces a change in the energy response of each channel, which is constantly monitored and corrected for by a dedicated laser system. Figure A.4 shows the relative response of ECAL crystals to laser light as a function of time, for different regions of  $\eta$ . The loss of transparency is larger at higher  $\eta$  due to heavier radiation damage, and is partially recovered during periods with no collisions.

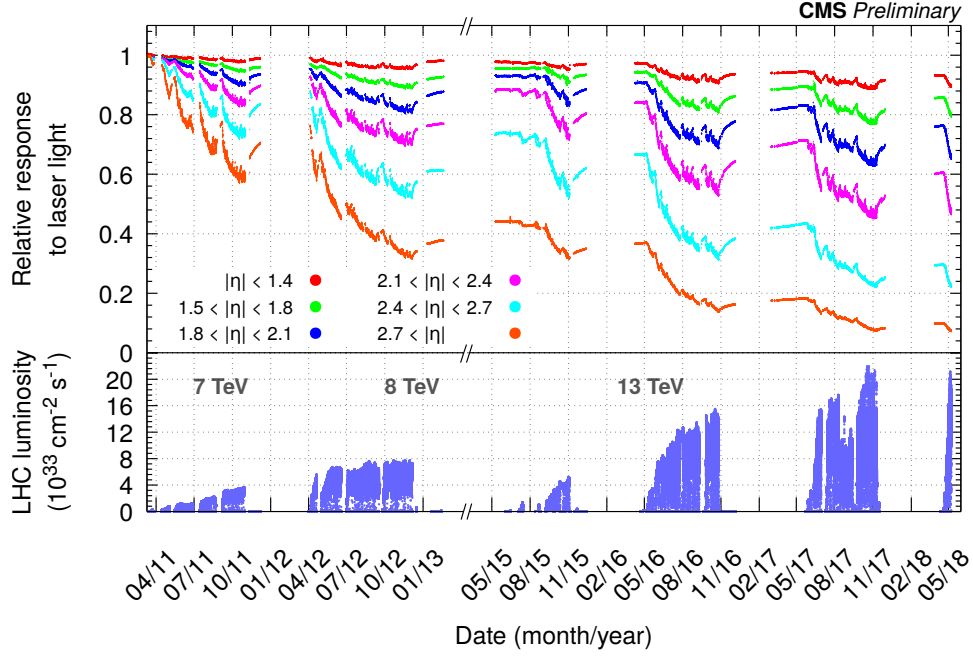


**Figure A.4.** ECAL crystals relative response to laser light as a function of time, for different regions of pseudorapidity. The lower panel shows the instantaneous luminosity reached by LHC during operation. A partial recovery of crystal transparency is observed during periods without collisions.

The stability of the energy scale is monitored using the diphoton invariant mass distribution in events with  $\pi^0 \rightarrow \gamma\gamma$  decays [67]. Electrons from decays of Z and W bosons are used as well, exploiting the  $Z \rightarrow ee$  invariant mass or the ratio of the electron energy measured with ECAL and its momentum measured with the tracker [66].

As shown in fig. A.5, the time-dependent drift in these observables is removed after applying the laser monitoring correction, thus validating the goodness of such correction. Each point in the  $\pi^0$  monitoring history is obtained from a fit to about  $5 \times 10^5$   $\pi^0$ 's collected every 5 minutes of data taking by a special data stream (the same one that collects the dataset used for the calibration with  $\pi^0$ 's). Z and W bosons are selected with much lower rate, but generate electrons whose energy is closer to physics events. The measured energy scale was generally found to be stable within 0.1% (0.2%) in EB (EE) during Run II.

### A.3.3 Crystals inter-calibration

The energy resolution of a calorimeter is expressed by the following relation:

$$\frac{\sigma(E)}{E} = \frac{a}{\sqrt{E}} \oplus \frac{b}{E} \oplus c \quad (\text{A.4})$$

where the symbol  $\oplus$  denotes the sum in quadrature (a global square root is assumed on the right-hand-side of (A.4)) and  $E$  is the energy released by a physics object in the calorimeter. The coefficients  $a$ ,  $b$ , and  $c$  represent the stochastic term, the noise term, and the so-called constant term. The ECAL EB energy resolution for electrons has been measured in beam tests, yielding  $a = 2.8\% \text{ GeV}^{-1}$ ,  $b = 0.124 \text{ GeV}$  and  $c = 0.3\%$  (for  $E$  measured in GeV). The

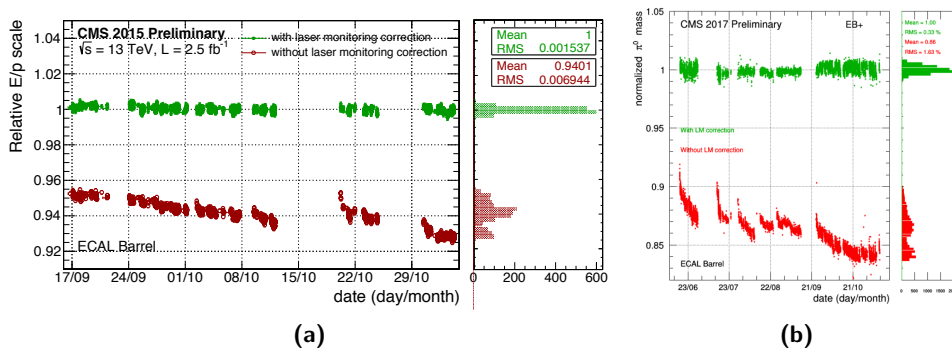


**Figure A.5.** (a) Validation of the crystals response corrections using electrons from decays of  $W$  and  $Z$  bosons in 2015. The parameter of interest is the ratio of the electron energy measured with ECAL and its momentum measured with the tracker, which is used as a reference. (b) Validation of the crystals response corrections using the invariant mass of photon pairs in  $\pi^0 \rightarrow \gamma\gamma$  decays in 2017. The measured mass is normalized to the PDG value [12]  $m_{\pi^0} = 0.1349 \text{ GeV}$ . For both figures: the panel on the left shows time-dependent behaviour of the chosen observable before (red points) and after (green points) applying the laser corrections to ECAL crystals; the right panel shows the projection of these observables on the y-axis.

measured noise term corresponds to a single crystal noise of about 40 MeV, giving 124 MeV in a matrix of  $3 \times 3$  crystals, obtained summing in quadrature the noise contribution of the involved crystals. The noise per crystal has increased during the years of LHC operation due to several effects such as radiation damage, which have an impact on both the readout electronics and the crystals' molecular structure. Nonetheless, it is evident from eq. (A.4) that the resolution for high energy electron and photon showers is dominated by the constant term for energies approximately above 100 GeV. Therefore, it is extremely important to keep this term as low as possible not to degrade the resolution.

There are several effects contributing to the constant term:

- the non-uniformity of the longitudinal light collection;
- the possible energy leakage from the back of the calorimeter;
- instabilities;
- the accuracy of the inter-calibration (IC) constants.

According to studies performed at beam tests, the last item provides the leading contribution. The resolution measured in-situ during operation is expected to be larger than the one obtained in beam tests due to the presence of material upstream of ECAL, which leads to energy losses through electron bremsstrahlung or photon conversions in the tracker. However, the target resolution is set to be of the order of 1%: meeting this target requires to keep the contribution to the constant term from the IC precision as low as 0.5%.

The IC procedure aims at equalizing the variations of the measured energy among different ECAL channels. Several methods based on physics processes are used to provide an IC constant for each channel [68]. Each method compares a given observable, measured using only ECAL information, with a physics reference. They are:

- $\pi^0 \rightarrow \gamma\gamma$ : it exploits the position of the peak in the invariant mass distribution of unconverted photon pairs;
- $Z \rightarrow ee$ : this method is similar to the  $\pi^0$  one, but relies on the invariant mass of the Z resonance;
- $E/p$ : it uses prompt electrons from decays of W and Z bosons and is based on the comparison of the electron energy measured with ECAL ( $E$ ) and the electron momentum measured with the tracker ( $p$ );
- $\phi$ -symmetry: this method is based on the azimuthal symmetry in the energy distribution of minimum bias events<sup>1</sup>.

The  $\phi$ -symmetry provides lower precision compared to other methods: it was used up to 2016 to track the evolution of the IC constants computed since Run I, as at that time the available event sample collected at 13 TeV was not large enough to derive a complete set of new IC constants with other methods<sup>2</sup>. On the other hand, the  $\phi$ -symmetry was not used for the calibration campaign of 2017 due to the availability of a larger dataset that allowed to better exploit the other more reliable methods.

All these methods are used to inter-calibrate channels at the same pseudorapidity. The methods using electrons are also exploited to derive the relative response of the various rings at different  $\eta$ . Events used for the calibration with W and Z bosons are collected using standard CMS triggers requiring the presence of 1 or 2 electrons satisfying some predefined selection criteria. These triggers have a rate of some tens of Hz. On the other hand,  $\pi^0$ 's which are used for the calibration are selected by a dedicated trigger system described in section A.4, which allows to collect candidate  $\pi^0$ 's with a rate of several kHz. Thanks to the high rate of collected events, the  $\pi^0$  method can potentially provide a set of IC constants every month of data taking (less than  $10 \text{ fb}^{-1}$  are enough to guarantee that the statistical uncertainty is negligible in EB), while the other methods based on prompt electrons require some tens of  $\text{fb}^{-1}$  to minimize the impact of the statistical uncertainty on the calibration precision.

### A.3.4 ECAL selective readout algorithm

In order to comply with the limit in the CMS readout bandwidth and storage space, it is not possible to save the information from all ECAL crystals for each event accepted by the L1 trigger<sup>3</sup>. Therefore, in the data acquisition (DAQ) path, the crystal data that is read out

<sup>1</sup>Physics events collected by CMS are selected by dedicated triggers requiring the presence of specific objects with well defined kinematic properties and identification criteria (for example, an isolated electron with  $p_T$  above a certain threshold). By definition, this induces a bias in the collected dataset. Minimum-bias triggers are devised to avoid any possible bias and are based on very loose criteria, such as the presence of at least one hard scattering vertex or some hadronic activity in the forward calorimeter (HF). One can also define so-called Zero-bias triggers which are just based on the presence of beams within CMS without necessarily requiring collisions. In case of high pileup ( $\gtrsim 10$ ) there is no real difference between Zero-bias or Minimum-bias events.

<sup>2</sup>Actually, the  $\pi^0$  method was used as well to provide IC constants, but at that time they were exhibiting some features that were preventing a combination with those obtained with the  $\phi$ -symmetry. These features were eventually understood during 2017.

<sup>3</sup>The intrinsic payload limit amounts to 2 kB/event/DCC (DCC stands for Data Concentrator Card). In the data acquisition path, a DCC receives the crystal data that is read out by the on-detector Front-End boards and performs the filtering of the data based on the decision made by the L1 trigger and the Selective Readout

**Table A.1.** *Thresholds used by the ECAL Zero-Suppression (ZS) and Selective Readout (SR) algorithm during Run II. An ADC count corresponds to 40 (60) MeV in EB (EE). The SR thresholds are applied on the transverse energy and are the same for both EB and EE (clearly, the corresponding absolute energy is larger in EE), while the ZS thresholds are larger in EE to account for higher noise.*

Year	ZS threshold [ADC]		SR threshold [GeV]	
	EB	EE	Medium Interest	High Interest
2016	4.5	6.5	1.5	2.5
2017	4.5	6.5	2.5	4.5
2018	5.5	6.0	2.0	4.0

by the on-detector Front-End boards is processed by a Selective Readout Processor (SRP). The SRP applies some filters based on the energy measured in each crystal and some local topological criteria meant to keep energy deposits from interesting physics processes while rejecting those compatible with noise.

The Selective Readout (SR) algorithm always reads the crystal data in Zero-Suppression mode (ZS): the crystal is read out only if the corresponding pulse in ADC counts is above the ZS threshold. An ADC count corresponds to 40 (60) MeV in EB (EE). However, electrons and photons deposits their energy is several crystals, and those which are far from the seed of the SC generally receive only a small fraction of the total SC energy. Reading them in ZS mode might lead to a significant loss of information, degrading the energy resolution or inducing other biases in the measured energy. To avoid this situation, the SR algorithm defines additional thresholds on the total transverse energy  $E_T$  measured in a group of crystals forming a so-called trigger tower (TT). In EB, a TT corresponds to a matrix of  $5 \times 5$  crystals<sup>4</sup>, while in EE a TT doesn't have a fixed geometrical shape in terms of number of crystals. The SR thresholds define a medium and a high interest region such that all the crystals belonging to any of these regions are read in Full-Readout mode, bypassing the ZS regardless their pulse amplitude and according to the following rules:

- Medium Interest (MI) region: if a TT has a total  $E_T$  above the MI threshold, that TT is read in Full-Readout;
- High Interest (MI) region: if a TT has a total  $E_T$  above the HI threshold, that TT and all the other surrounding 8 TT's are read in Full-Readout if the TT is in EB, while in EE all the supercrystals (groups of  $5 \times 5$  crystals) contributing to that TT are read out.

These thresholds were raised every year to cope with changes in noise and pileup. A summary of the ZS and SR thresholds applied since 2016 is reported in table A.1, while Fig. A.6 illustrates the logic of the SR algorithm.

### A.3.5 Data formats in the ECAL software

The data read from ECAL, as well as simulated data, are both stored in 4 layers, or tiers, within the ECAL software: each of them represents a different step in the hierarchy of the

Processor [69]. In EB, there is a DCC associated to each supermodule, while each of the two endcaps is divided in 9 sectors corresponding to a DCC. Therefore, there are 54 DCC's in total.

<sup>4</sup>From what was shown in section A.2, each supermodule in EB is divided in  $4 \times 17$  TT in the  $\phi - \eta$  plane.

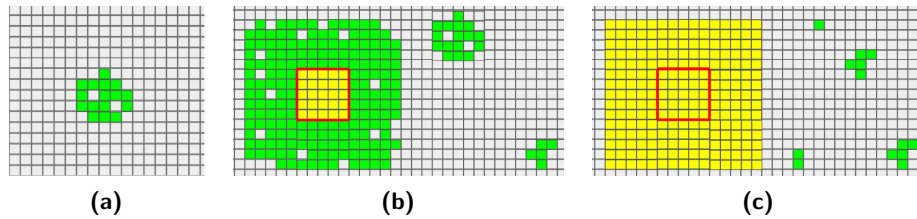


**Figure A.6.** Illustration of the ECAL Zero-Suppression (ZS) and Selective-Readout (SR) algorithm. In Fig. A.6a, a particle has deposited its energy in some crystals. The total energy observed in any trigger tower (TT) hit by the particle is below the SR Medium Interest (MI) threshold. Therefore, the information is read in ZS mode and only the green crystals are actually read out. In Fig. A.6b, the energy measured in a TT (red square) is above the MI threshold but below the High Interest (HI) one: the crystals inside the tower (in yellow) are read in Full-Readout mode, while the others are read in ZS mode if they pass the corresponding threshold (green crystals). Finally, in Fig. A.6c a TT (red square) has an energy above the HI threshold: that tower and the surrounding 8 ones are read in Full-Readout mode (yellow crystals). Other possible crystals outside this region might still be read in ZS or Full-Readout mode if they belong to an appropriate region.

reconstruction.

- **RAW data:** this is the data as it is read out from the detector front-end electronics. RAW data can be seen as an array of formatted 64-bit unsigned integers saved by the data acquisition (DAQ) system;
- **SimHits:** MC simulations consist in an event generator and the subsequent passage of the generated particles into a detector simulation based on GEANT. The SimHits data format represents the simulated energy deposits and is the equivalent of RAW data in simulation;
- **Digis:** these are the data from each detector channel. They are the sets of 10 samples for a given event recorded by the ADC, as described in the beginning of section A.3. Digis show the pulse shape of the detector and are used to reconstruct the energy and time of the hit in the calorimeter;
- **UncalibratedRecHit:** this data format stores some quantities obtained from the Digis, such as the amplitude (the peak of the pulse shape) and the time when the maximum of the pulse shape occurs;
- **RecHits:** they are obtained from the UncalibratedRecHit after applying the conversion factor from ADC to GeV and the available calibration constants. The RecHits are the basic ingredients used in the ECAL software to build clusters.

#### A.4 ECAL inter-calibration with the $\pi^0$ method

The calibration with  $\pi^0 \rightarrow \gamma\gamma$  exploits the invariant mass distribution of photon pairs to assign an IC constant to each channel. The basic idea consists in deriving a mass distribution for each channel, extracting the position of the peak with a fit and obtaining a response correction equalizing the measured mass in each channel to the known  $\pi^0$  mass.

### A.4.1 The $\pi^0$ trigger stream

The dataset used for the calibration with  $\pi^0$ 's is selected by a special HLT stream which saves only limited ECAL information in the vicinity of the selected photon candidates. This feature minimizes the usage of the CMS readout bandwidth and storage space, allowing the stream to run with a high rate of several kHz in EB and EE. The stream rate during 2017 was about 7 kHz for events in EB, and about 2 kHz in EE. At the same time, the event size for each event selected by the stream is about 2 kB, roughly a thousand times smaller than the typical CMS physics event size. The lower rate in EE comes from the tighter kinematic selections deployed to reduce the contribution from noise and guarantee a high enough signal purity. In 2016, before the optimization of the selection, the rate was 7 kHz in EE as well.

The stream takes as input the events selected by the CMS L1 trigger: different L1 algorithms are used, requiring the presence of at least one electromagnetic object or one or more hadronic jets. Several L1 algorithm, characterized by different energy thresholds for each type of L1 objects, are used to feed the stream through a logical OR: this feature guarantees a stable rate through the year, making the stream basically immune to the frequent changes in the L1 menu during data taking, which might affect the prescales of the L1 bits.

It is important to observe that, in a hadronic collider,  $\pi^0$  are copiously produced from the decay chain of hadrons originating from both the hard scattering process and the underlying event. For this reason, the  $\pi^0$  candidates are not necessarily built from energy deposits in the vicinity of the L1 objects: the L1 input is just meant to provide a set of events which might potentially contain  $\pi^0$  particles. For instance, a physics event triggered by a L1\_DoubleEG\_24\_17 L1 bit is characterized by the presence of at least two large energy deposits in ECAL. Their source might be a Z boson decaying into a pair of electrons and it wouldn't make much sense to look for a  $\pi^0 \rightarrow \gamma\gamma$  in those energy clusters. However, a Z boson is often produced in association with one or more jets that balance its transverse momentum: these jets can be a source of  $\pi^0$ . In addition to that,  $\pi^0$ 's can also be produced from decays of other low- $p_T$  particles originating from pileup events.

The stream employs two independent HLT paths, one for EB and one for EE, which are both seeded by the same L1 inputs.  $\pi^0$  candidates in EB or EE are obtained from photon clusters in the same ECAL partition (that is to say, they both belongs to either EB or EE). It actually manages other two analogue paths devised to select events with  $\eta \rightarrow \gamma\gamma$ . The  $\pi^0$  and  $\eta$  paths share the same clustering algorithm with different kinematic selections to take into account the different masses of the mesons. Since  $\eta$  particles were not used for calibration during Run II (at least at the time of writing this thesis), they will not be considered further in the following.

The output saved by the stream is a set of collections of ECAL Digis for all the crystals belonging to identified  $\pi^0$ 's. Technically, the stream builds  $\pi^0$  candidates using RecHits, but eventually converts them back to the original Digis, which allows for more versatility for offline analysis. The Digis contain all the relevant information (i.e. the pulse shapes) from ECAL channels that is needed to reconstruct the event. They do not contain other correction factors related to the conditions of data taking (for instance, crystal transparency or calibration constants), which can be changed during offline calibration according to one's need. In addition, the stream output contains the information from the ES detector and, since 2017, a list of flags reporting the decision of the SR algorithm for each crystal, i.e., whether the crystal was read in ZS or Full-Readout mode.

### A.4.2 Clustering algorithm

The stream employs a dedicated clustering algorithm that identifies photons as  $3 \times 3$  crystal matrices centered on crystals with the local highest energy deposit. Matrices passing some kinematic selection criteria are used to form  $\pi^0$  candidates and the corresponding crystal data are then saved for offline analysis.

The usage of such a small cluster to identify photons mainly aims at reducing the contribution of detector noise to the measured energy. The noise induces about 1 ADC count per crystal on average: the total noise in a cluster is given by the sum in quadrature of the single contributions for each crystal in the cluster, which results in more than 100 MeV. The ZS thresholds are tuned to be about 5 times the expected crystal noise value (see table A.1).

The transverse energy distribution of selected photons used for the  $\pi^0$  calibration method peaks between 1 and 2 GeV for the leading photon in the  $\gamma\gamma$  pair, with an exponentially decreasing tail extending above 10 GeV. While this observation confirms that the  $3 \times 3$  matrix is adequate to contain the energy from such photons, it is also clear that detector noise can potentially bias the measured energy or create spurious clusters. In addition, it is evident that the ZS and SR thresholds might potentially lead to significant loss of information in the reconstruction of  $\pi^0$ 's and bias the IC constants. This effect has actually been observed and was taken into account and corrected for with ad-hoc techniques that will be explained later. Finally, one should note that a fraction of the photon's energy is still expected to leak outside the cluster or be lost if the cluster is formed in the vicinity of detector gaps or dead channels: these losses are corrected for using a dedicated set of containment corrections obtained from simulations. The effect of gaps is particularly relevant in EB due to the boundaries between modules and supermodules.

The algorithm to select  $\pi^0$  particles can be divided in three main steps: seeding, clustering and pairing of photon candidates.

- **Seeding:**

1. a list of channels, denoted as seeds, is formed from crystals whose measured absolute energy is above 0.5 (1.0) GeV in EB (EE);
2. the seeds are ordered by energy and a loop on them is made, starting from the one with the highest energy: each seed will be passed to the next step to start the building of photon clusters.

- **Clustering:**

1. given a seed, a matrix of  $3 \times 3$  crystals is opened (such that the seed lays in the center) and a list of RecHits within the matrix is created. In principle the number of RecHits can be lower than 9 due to the SR or because they were already used to form a previous matrix. Indeed, a crystal can only be associated to a single matrix, there is no attempt to share its energy among more matrices. The same logic apply to seeds: a seed that was already embedded in another matrix is not used to form a new matrix. As a consequence, the seeds of two different matrices cannot be adjacent;
2. each RecHit in the  $3 \times 3$  matrix is required to be a good channel, i.e., it must not be flagged as a noisy, dead or problematic crystal for which the deposited energy is not measurable. If this condition is not fulfilled, the matrix is discarded



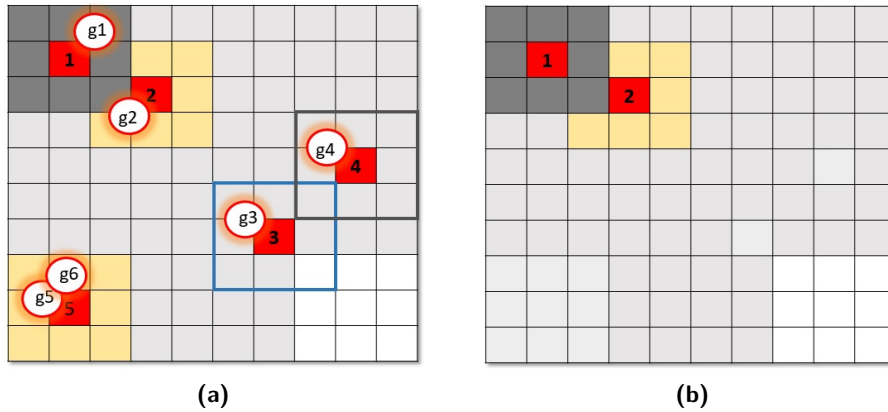


**Figure A.7.** Simplified scheme of the  $\pi^0$  clustering algorithm. Let's assume a  $\pi^0$  has generated two photons  $g_1$  and  $g_2$  hitting ECAL in crystals 1 and 2, a second  $\pi^0$  has decayed into photons  $g_3$  and  $g_4$  depositing their energies around crystals 3 and 4 and a third very energetic  $\pi^0$  has decaying into two close photons  $g_5$  and  $g_6$ . Starting from a list of seeds ordered by energy (red squares), a  $3 \times 3$  matrix centered on them is evaluated and all the available RecHits are used to form a cluster  $c_i$  centered on crystal  $i$ . Cluster  $c_1$  (in dark grey) has 9 RecHits, while cluster  $c_2$  (light brown) has only 7, since two are already taken by the first one. The clustering continues with  $c_3$ , which would have 9 RecHits as well. However, one of them belongs to a dead region (white area) and has a bad channel status, causing the cluster to be rejected. The algorithm continues with the remaining seeds. At the end,  $c_1$  and  $c_2$  are successfully paired into a  $\pi^0$  candidate.  $c_4$  should have been paired with  $c_3$ , but the latter was discarded: the parent  $\pi^0$  is lost as  $c_4$  could not be paired with other clusters (it might have been incorrectly paired with  $c_5$ , but this pair would probably fail the isolation, since  $c_2$  is very close to  $c_4$ ). At the same time, it was not possible to distinguish two photons inside  $c_5$ , so the corresponding  $\pi^0$  is lost as well. Eventually, only a single  $\pi^0$  was reconstructed: its mass will contribute to the mass distributions for all crystals in  $c_1$  and  $c_2$ , as detailed in section A.4.4.

and its crystals are freed and made available again to form other matrices. This condition prevents seeds from being adjacent to a problematic region;

3. once a cluster is formed with the available RecHits, it is required to pass some kinematic selection criteria, which are detailed in section A.4.3;
4. A cluster that fulfills all the selections is saved for the next phase to form  $\pi^0$  candidates. Its RecHits will not be available anymore to form another cluster. It is worth pointing out that the cluster might have less than 9 RecHits and therefore be made of less than 9 crystals.

• **Pairing of photon candidates into  $\pi^0$ :**

1. a double loop is performed on the available clusters (according to the previous steps, they are sorted by the energy of the seed);
2. each pair of clusters must fulfill additional selection criteria (see section A.4.3);
3. a pair satisfying all the selections makes a  $\pi^0$  candidate: the corresponding clusters are removed from the list and cannot be used again to form other  $\pi^0$ 's. One should observe that a priori the wrong pair might be chosen in case there are many close candidate clusters (for instance, because of a high number of

pileup interactions). The probability to make an incorrect match is reduced by applying an isolation criterium on the considered clusters.

A visual representation of the clustering algorithm is presented in Fig. A.7. For  $\pi^0$  in EE, the information from the preshower detector is used to improve the measurement of the energy and position of the two photons. As a matter of fact, the  $m_{\gamma\gamma}$  distribution of  $\pi^0$ 's in the fiducial region covered by the preshower is characterized by a better resolution.

#### A.4.3 Selection criteria

Some kinematic selection criteria are applied on photon and  $\pi^0$  candidates to improve the signal over background ratio and possibly ensure that the background component in the invariant mass distribution is as much flat as possible. This is particularly important for the fit to the invariant mass distribution, from which the IC constants are derived: indeed, a non-flat background component (or even worse, that resonates below the signal peak originating from real  $\pi^0$ 's) would bias the measured mass and therefore the IC constants. It is important to observe two things:

- the signal is made of very soft particles with energies at the GeV scale;
- the background does not arise from specific physics processes, but originates mainly from combinatorics: spurious energy deposits from noise, incorrect association of genuine photons from different  $\pi^0$ 's and other similar sources of low- $p_T$  photon candidates.

This makes it quite hard to define good discriminating variables, as many kinematic distributions for signal and background have almost the same shape.

The selections applied on each individual photon use the same thresholds for both photons. Photons are required to have  $p_T$  and  $S_4/S_9$  above a given threshold, where  $p_T$  is estimated from the sum of the RecHit transverse energy. The  $S_4/S_9$  variable is defined as the ratio of the  $S_4$  and  $S_9$  quantities: the former is the highest energy value deposited in the four possible combinations of  $2 \times 2$  crystal matrices containing the seed crystal inside the cluster, while the latter is the total energy in the cluster. Photons are required to have a minimum number of RecHits inside their cluster: this selection was added into the stream software and in the offline selection in 2017 to reject those photon candidates with several missing RecHits due to the SR.

A pair of clusters must be isolated from other energy deposits in the nearby. The isolation is defined as the ratio of the scalar sum of  $p_T$  from all clusters (excluded those forming the  $\pi^0$ ) found within a cone of radius  $\Delta R = 0.2$  centered on the  $\pi^0$  candidate and the  $p_T$  of the diphoton pair itself. The isolation cone is further restricted to a band along  $\eta$  with a width of  $\delta\eta = 0.03$  (roughly equal to 2 ECAL crystals). This ratio must be lower than 0.5. In other words, the energy spread around the  $\pi^0$  must be less than half the energy of the candidate. The previous definition of isolation is implemented in the stream software. In the offline calibration, a similar but tighter criterium is applied on top: there must be no other clusters within a cone of radius  $\Delta R = 0.2$  centered on each photon forming the  $\pi^0$  candidate. For both definitions of the isolation, only those clusters with  $p_T > 0.5$  GeV are considered. A graphical illustration of the isolation is shown in Fig. A.8. Finally the invariant mass of the diphoton system,  $m_{\gamma\gamma}$ , must lie within 60 and 250 MeV: the thresholds are designed to fully

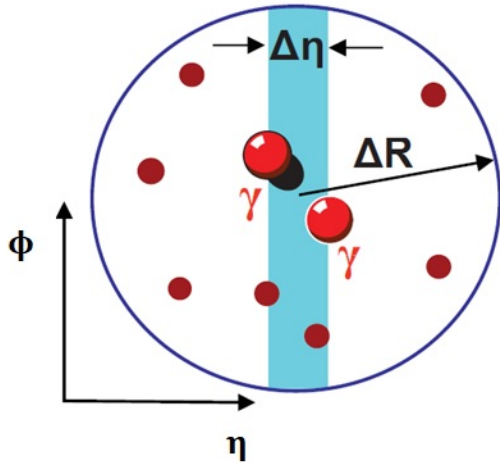


**Figure A.8.** Definition of isolation.

At HLT level, a cone with radius  $\Delta R = \sqrt{(\Delta\phi)^2 + (\Delta\eta)^2} = 0.2$  is opened around the  $\pi^0$  candidate. Then, the sum of  $p_T$  of all clusters inside this region and within a narrower band in  $\eta$  is evaluated (using only clusters with  $p_T > 0.5$  GeV). The ratio of this quantity and the  $p_T$  of the  $\pi^0$  is required to be less than 0.5.

For the offline calibration, a tighter criterium is used, which reject the pair if there is at least one cluster with  $p_T > 0.5$  GeV inside the cone.

**Table A.2.** Summary of kinematic cuts to select  $\pi^0$ 's. A  $\pi^0$  is reconstructed imposing that the following quantities are bigger than or equal to the thresholds in the table. Those selections regarding photons are applied on both photons with the same threshold. In addition to the requirements reported here, the measured invariant mass must be within 60 and 250 GeV and the isolation must be lower than 0.5 (see text for the definition the isolation).

Region	Seed energy [GeV]	$p_T$ ( $\gamma$ ) [GeV]	$S_4/S_9$ ( $\gamma$ )	$N_{RecHits}$	$p_T$ ( $\pi^0$ ) [GeV]
EB: $ \eta  < 1.0$	0.5	0.65	0.88	7	2.0
EB: $ \eta  > 1.0$	0.5	0.65	0.9	7	1.75
EE: $ \eta  < 1.8$	1.0	1.1	0.85	6	3.75
EE: $ \eta  > 1.8$	1.0	0.95	0.92	6	2.0

contain the mass peak while still guaranteeing enough leverage to model the background component.

The thresholds adopted for the selection are tuned independently for EB and EE, which are characterized by different levels of noise (and different dimensions of the crystals). Moreover, the selection is  $\eta$  dependent: two regions are defined in EB with the border at  $\eta = 1.0$ , and 3 regions are defined in EE with borders at  $\eta = 1.8$  and  $\eta = 2.0$  (although the current selection is actually the same for the two regions with  $\eta > 1.8$ ). The full selection is summarized in table A.2.

#### A.4.4 Derivation of the inter-calibration constants

The derivation of the IC constants is based on the peak exhibited by the invariant mass distribution of  $\pi^0$ 's, which is used as a reference to equalize the energy response among ECAL channels. As it was already discussed, the photons from decays of  $\pi^0$ 's deposit their energy in several crystals. Therefore, the single channel invariant mass distribution is obtained in the following way:

- for each  $\pi^0$ , the reconstructed invariant mass ( $m_{\gamma\gamma}$ ) is used to fill the distribution of all channels contributing with a RecHits to the clusters of the two photons from the decay.

- for each involved channel in each of the two clusters, the corresponding distribution is filled with a weight computed as the fraction of the cluster's energy that is deposited in that specific channel. By definition, the sum of weight amounts to 1 for each cluster.

The aforementioned procedure allows to obtain an IC constant also for those crystals which are adjacent to dead regions in the detector: if the mass of the  $\pi^0$  were associated only to the seed crystal (which cannot be adjacent to dead regions in the algorithm), those crystals would not be calibrated.

Finally, a binned maximum likelihood fit is performed of the  $m_{\gamma\gamma}$  distribution obtained for each channel. Data are fit with the sum of a signal and background components modeled as a Gaussian function and a second order Chebychev polynomial, respectively. The parameter of interest of the fit is the position of the peak of the  $m_{\gamma\gamma}$  distribution. Eventually, the IC constant ( $C$ ) is computed as:

$$C = \frac{1}{1+r} \quad \text{with} \quad r = \frac{1}{2} \left[ \left( \frac{m_{\pi^0}^{meas}}{m_{\pi^0}^{true}} \right) - 1 \right], \quad (\text{A.5})$$

where  $m_{\pi^0}^{true} = 0.1349 \text{ GeV}$  is the known mass of the  $\pi^0$  [12], while  $m_{\pi^0}^{meas}$  is the value measured from the fit. If the measured mass is lower than the expected one, the  $r$  factor is negative and  $C > 1$ . The formula in (A.5) originates from a Taylor expansion of the reconstructed invariant mass expression divided by the true mass, neglecting second order terms.

Figure A.9 shows two typical fits, one in EB and one in EE. These distributions were obtained using  $9.8 \text{ fb}^{-1}$  collected in 2017, applying the selection criteria described in section A.4.3. The fit is performed in a narrower range (from 80 to 210 MeV) than the selected mass window, so to avoid instabilities in the modeling of the background far from the peak.

The larger  $p_T$  thresholds applied on photons and  $\pi^0$ 's in EE produce a steeper shape for the background component. The effect is also correlated with the presence of the preshower, where a large fraction of the incoming  $\pi^0$  is deposited: this reflects into a lesser energy deposited in EE and therefore to a lower number of RecHits in the photon cluster on average. As a consequence, low energy photons are suppressed by the  $N_{RecHits}$  selection. On the other hand, the clustering algorithm is not able to correctly distinguish two photons if they have very high  $p_T$ , since the associated clusters would largely overlap. The convolution of these effects is the source of the significantly lower size of the collected dataset in EE with respect to EB.

#### A.4.5 Convergence of inter-calibration constants

As mentioned above, the formula in (A.5) is an approximation at first order. Therefore, the procedure adopted to derive the IC constants has to be iterated until the measured constants converge. For each iteration  $i$ , a new set of constants is obtained using the same method but correcting the energy in each ECAL channel by the product of the IC constants derived in the previous iterations. The converge is evaluated through the following steps:

- take the map of IC constant for each pair of consecutive iterations;
- for each crystal of the two maps, take the difference of IC constants and fill a histogram;

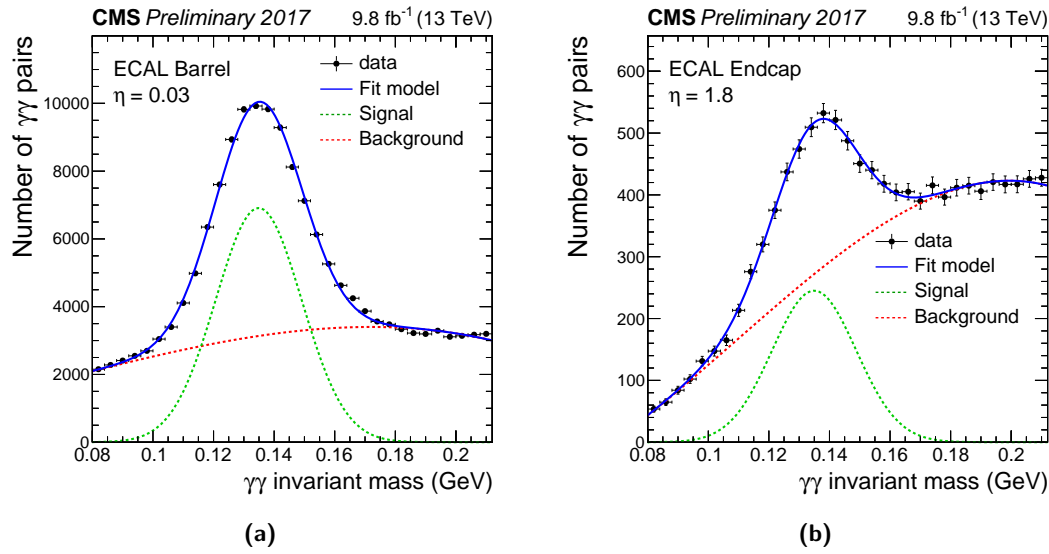


**Figure A.9.** Fits to the invariant mass distributions in two ECAL crystals, one in central EB (left) and one in EE (right). Data (black points) are fitted with the sum (solid blue line) of a signal and background components (dashed green and red lines) modeled as a Gaussian function and a second order Chebychev polynomial, respectively. Note the different size of the selected samples due to the lower signal purity and selection efficiency in EE. The difference in the shape of the background component is mainly induced by the larger  $p_T$  thresholds applied in EE.

- evaluate the RMS of the aforementioned histogram and use this value to fill a graph;
- convergence is obtained once the graph of RMS reaches a plateau.

The procedure described above is performed after splitting crystals in four groups based on their location along  $\eta$ . Indeed, the convergence will be slower at higher  $\eta$  due to larger systematic and statistical uncertainty. In the case of EB, each group represents a module, while for EE there is no specific topological structure to guide the division and the 39  $\eta$ -rings are splitted in 4 groups with 10 rings in each (9 in the fourth one).

The evaluation of the convergence is also useful to check for possible problems in the IC derivation procedure at a given step. For example, a problem in the processing of data during one iteration will result in loss of data and a subsequent larger statistical uncertainty on the corresponding IC constants. This occurrence will reflect in a larger RMS and would show up as a bump in the convergence graph, which would otherwise be a monotonically decreasing function.

It was observed that about 14 iterations are sufficient to reach a good level of convergence. The residual non-convergence could be considered as an additional systematic uncertainty on the IC constant. However, it is generally below 0.1% and is therefore negligible with respect to the statistical uncertainty and other systematic uncertainties,

Figure A.10 shows the achieved convergence in each EB module. These results were obtained on a dataset of  $9.8 \text{ fb}^{-1}$  collected in 2017, which was used to derive a set of IC constants, as described in section A.5.

As the IC constants converge, the measured mass for each channel converge to the same value, which indeed is the purpose of the IC procedure. In addition to that, the energy

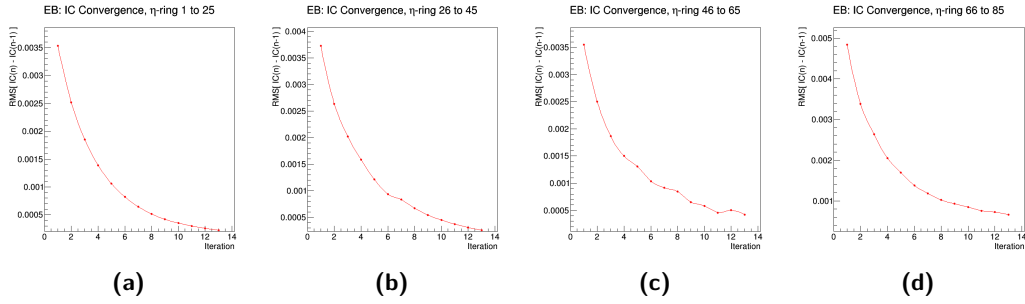


**Figure A.10.** Convergence of IC constants in the four EB modules obtained using  $9.8 \text{ fb}^{-1}$  collected in 2017. The residual spread after convergence is reached represents a source of systematic uncertainty. This spread is larger at higher  $\eta$ .

resolution improves (the resolution is estimated as the width of the gaussian component in the fit to  $m_{\gamma\gamma}$ ). This is shown in Fig. A.11 for EB. One can observe that the energy resolution is better at larger  $\eta$ : this occurrence is explained by the fact that events are selected cutting on the transverse energy, which implies a larger absolute energy at high  $\eta$ . Based on eq.(A.4), this entails a better energy resolution. In other words, the energy distribution of selected photons has a larger mean for photons produced at larger pseudorapidity, as it is shown in Fig. A.12.

#### A.4.6 Statistical uncertainty

The statistical uncertainty on the measured IC constants for a given iteration can be assessed as a function of  $\eta$  by splitting the dataset into two subsamples composed of even and odd events and eventually deriving the constants for each of them. Then, the following procedure is used:

- for each  $i\eta$  in EB ( $\eta$ -ring in EE), fill a histogram with the difference of IC constants for each pair of crystals in the two sets located at the same coordinate (for instance, this amounts to  $2 \times 85$  differences in EB);
- evaluate the RMS of the previous histograms;
- get the statistical uncertainty at each pseudorapidity region as the corresponding  $\text{RMS}/\sqrt{2}$ .

The underlying assumption of this procedure is that the two dataset have correlated systematic uncertainties, but are statistically independent. Therefore, when considering the difference, the systematic component of the uncertainty cancels out. In other words, the IC constants for the two sets are expected to differ only because of their statistical fluctuations.

Given the symmetry of the detector along  $\phi$ , the statistical uncertainty can safely be assumed to be the same for each crystal at the same  $i\eta$ . Actually, this is not completely true, as the crystals close to gaps between supermodules have less statistics due to lower selection efficiency. Therefore, the statistical uncertainty obtained from the procedure described above is an average. However, the crystals at borders are only 10% (2 every 20) of the total number, which support the validity of the approximation. Moreover, the statistical uncertainty is

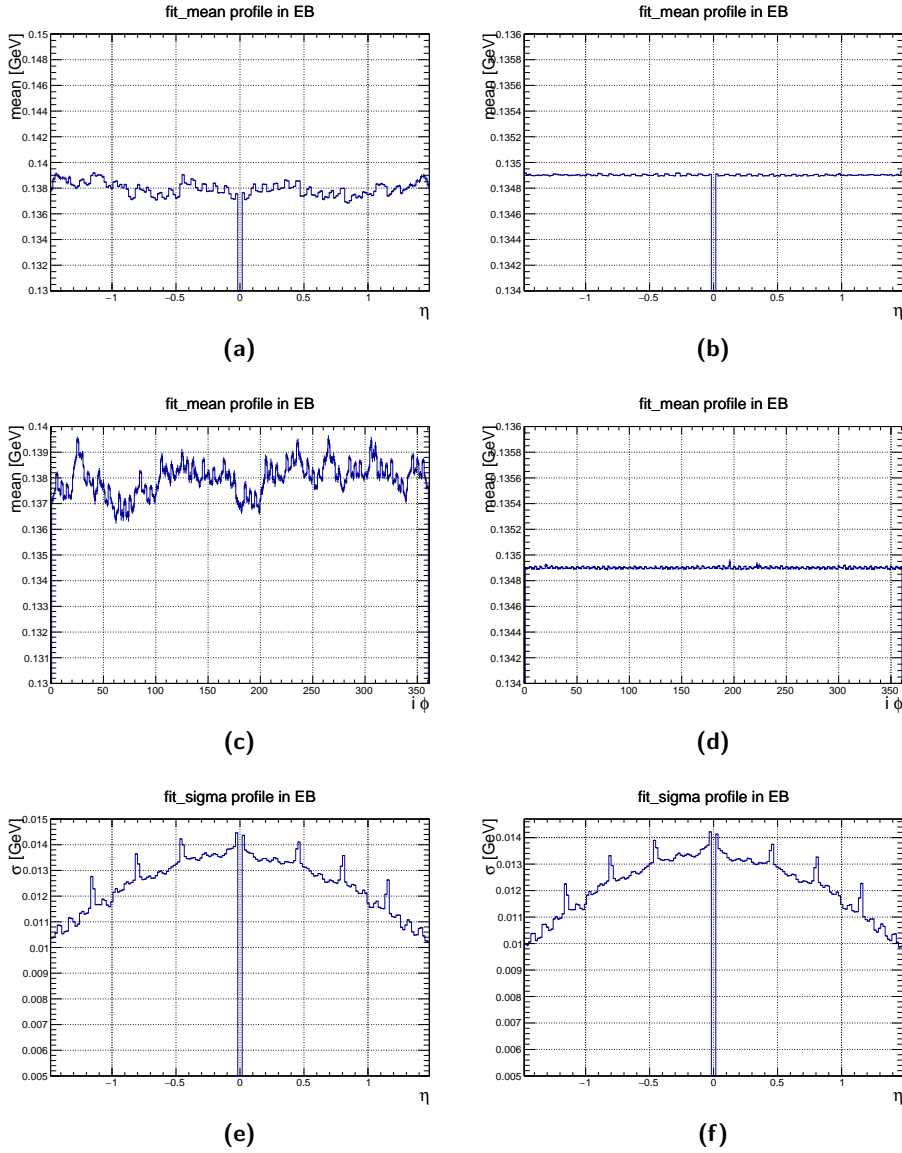
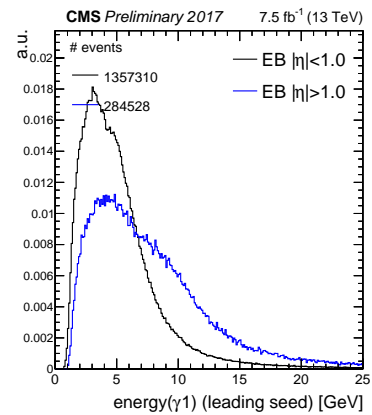


**Figure A.11.** Comparison of some relevant distributions in EB from the IC procedure after the first (left) and the 14-th iteration. (Top) measured  $\pi^0$  mass profiled along  $i\eta$ . (Middle) measured  $\pi^0$  mass profiled along  $i\phi$ . (Bottom) measured mass resolution profiled along  $i\eta$ . The measured mass and resolution are defined as the position and width of the  $\pi^0$  peak obtained from the fit to the  $m_{\gamma\gamma}$  distribution. The reason why the initial measured mass is above the expected value is due to an over-correction in the absolute scale originating from the containment corrections (see section A.4.7). Note that, by definition, the absolute value of  $i\eta$  is always positive ( $i\eta \neq 0$ ). The reader is also invited to observe the different spread of the measured mass between the first and the last iteration (the axis range is also narrower in the latter case).

**Figure A.12.** Comparison of the energy of the leading photon between inner and outer EB. It can be observed that photons reconstructed at  $|\eta| > 1.0$  are characterized by a harder energy spectrum than those with  $|\eta| < 1.0$ . The reason is that the selection criteria are based on transverse quantities and use the same thresholds, which entails higher energy at larger  $\eta$  on average.



negligible with respect to the systematic uncertainty, provided that the used dataset consists of more than  $10 \text{ fb}^{-1}$ .

A simpler method to estimate the statistical uncertainty relies on the relative uncertainty on the position of the peak in the  $m_{\gamma\gamma}$  distribution, as obtained from the fit. In this case, the statistical uncertainty is taken directly as the relative uncertainty on the measured mass. The two methods were found to provide the same uncertainty, but the latter has the advantage of being able to provide an uncertainty for each crystal (as a mass distribution is available for any of them) and does not require to process the dataset twice. However, it relies on the fact that the fit has converged successfully and that the signal-over-background ratio is high enough so to avoid biases in the fitted peak. This is always the case in EB, while in EE the fits are reliable only up to  $\eta \approx 2.2$  (above this value the reconstruction of  $\pi^0$ 's becomes nearly impossible since the mass peak is hidden in the large background component, making the fit fails).

The statistical uncertainty obtained from  $9.8 \text{ fb}^{-1}$  using the second method is shown in Fig. A.13. It was obtained at the 14-th iteration of the IC procedure. The statistical uncertainty in EB is larger for crystals close to the gaps, and globally larger in the 4-th module due to the lower efficiency to reconstruct a  $\pi^0$  at larger  $\eta$ . In EE, the IC constants are ill-defined for  $\eta > 2.2$  and should not be considered further. Using less than  $10 \text{ fb}^{-1}$ , the statistical uncertainty in EB is always lower than 0.4% (about 0.1% excluding the fourth module), while the statistical uncertainty in EE is generally of the order of 1% (excluding the outer part of EE at lower  $\eta$ ). In order to keep the impact of the uncertainty of the IC constants on the constant term in the calorimeter resolution below 0.5%, the statistical uncertainty should be kept below 0.3%. The used dataset is large enough to meet this target in EB, while more data have to be used in EE.

#### A.4.7 Containment corrections

The IC constants computed with  $\pi^0$ 's are used to equalize the energy response of different channels. Hence, it is extremely important that these constants do not correct for other effects beyond the scope of the inter-calibration. It has been already mentioned that the  $3 \times 3$  matrix used in the clustering algorithm does not fully contain the energy of the photon. Moreover, if the photon cluster crosses the boundaries between modules and supermodules in EB, part of its energy will be lost in the gaps between these structures. In principle, one could absorb these losses into the IC constants, such that they automatically compensate for these



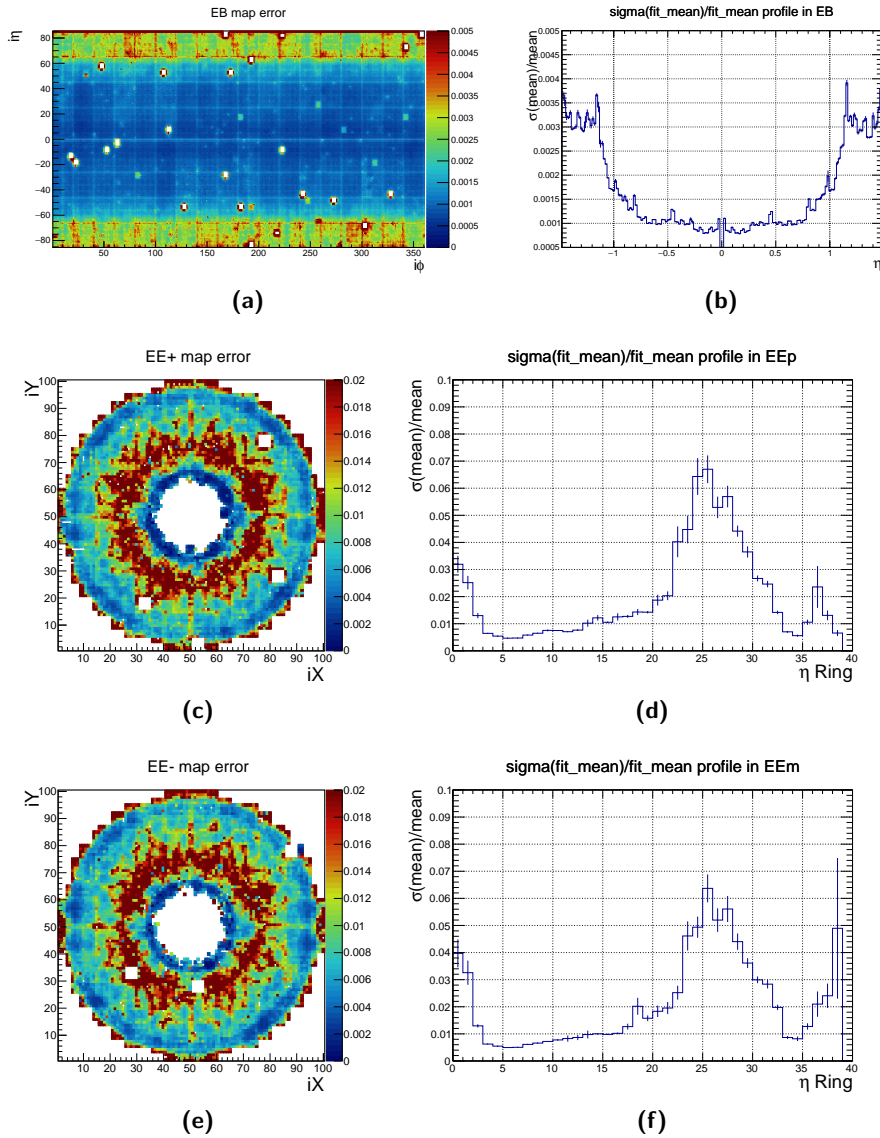


**Figure A.13.** Statistical uncertainty on the IC constants in EB (top), positive EE (middle) and negative EE (bottom). The uncertainty is estimated from the relative uncertainty on the measured  $\pi^0$  mass in each crystal, as obtained from the fit. They are obtained from a dataset of  $9.8 \text{ fb}^{-1}$  collected in 2017 at the 14-th iteration of the IC procedure. The plots on the left show the uncertainty in each crystal, while those on the right show the average at constant  $\eta$ . The error bars in the plots on the right represent the spread of the uncertainties used to compute the average. The statistical uncertainty in EB is larger for crystals close to the gaps, and globally larger in the 4-th module due to the lower efficiency to reconstruct a  $\pi^0$  at larger  $\eta$ . In EE, the IC constants are ill-defined for  $\eta > 2.2$  (see text): the uncertainty obtained for those crystals is an artifact of the failed fits and should not be considered further. Instead, the larger uncertainty on crystals with  $\eta$ -ring number below 5 stems from the lower selection efficiency.

effects by providing larger corrections next to borders or similar structures. However, the official clustering algorithm used in the CMS software to reconstruct electrons and photons is optimized for high energy particles, and the impact of gaps and energy containment on the corresponding clusters is significantly different than the one on low- $p_T$   $\pi^0$ 's. For this reason, one has to disentangle these effects from the IC constants by computing an appropriate set of dedicated containment corrections (CC).

These CC were computed using simulations and exploiting the so-called  $E/E_{true}$  method, where  $E$  represents the measured energy for a photon cluster and  $E_{true}$  is the true energy of the photon. This method uses the peak in the distribution of  $E/E_{true}$  from unconverted photons as a reference to derive the correction as  $1/E_{peak}$ , where  $E_{peak}$  is the value of the energy where the  $E/E_{true}$  distribution reaches its maximum. Since  $E_{peak}$  is the mode of such distribution, this correction is defined in such a way to move the most probable value of the measured energy towards the true one. The same target is adopted by the MVA that provide the corrections of the energy of superclusters for high energy electron and photons in the standard CMS algorithm, although a simpler strategy and less input information is used to derive the corrections for  $\pi^0$ 's. One might think of using the mean of the distribution instead of the mode. However, the distribution of  $E/E_{true}$  is largely asymmetric: as shown in previous studies on the optimization of the aforementioned MVA, using the mean would actually generate a bias in the computed CC, over-correcting the energy of the clusters.

The CC are derived for each crystal using an algorithm which is very similar to the one described for the calibration with  $\pi^0$ 's. The main difference is that one also exploits the generator-level information (the so called *Monte Carlo (MC) truth*) to match the reconstructed cluster to the parent photon. Taking the visual scheme presented in Fig. A.7a as a reference, the algorithm starts from the clustering to define potential photon candidates. Once a list of clusters is formed, the matching of clusters to the gen-level photons is made and the matched pairs are used to fill the  $E/E_{true}$  distribution. This step has no counterpart in the calibration procedure based on data, since in that case the MC truth is not available. The matching consists in the following passages:

- for each event, a loop is performed on the generator-level  $\pi^0$ 's (simulations might generate more particles per event)
- for each generator-level  $\pi^0$ , the  $\Delta R$  between its decay photons is evaluated and the pair is discarded if  $\Delta R < 0.025$ . This requirement rejects boosted  $\pi^0$ 's whose decay photons would largely overlap: indeed, 0.025 is roughly equal to the diagonal of a crystal's front face, ensuring that the seed crystals of the reconstructed cluster will likely not be adjacent (the clustering would discard these cases);
- for each pair satisfying the previous step, the generator-level photon with the largest energy is evaluated to find a cluster with  $\Delta R < 0.1$  between the cluster and the photon. The energy weighted barycenter of the cluster is used to compute  $\Delta R$  and, in case multiple clusters satisfy the requirement, the closer one is selected;
- if the first photon is successfully matched, the same procedure is repeated for the second photon as well;
- any time a pair of clusters is matched to the photons from a given  $\pi^0$ , those clusters are removed from the list and cannot be associated to other photons;

- the procedure is over when all  $\pi^0$  in the events have been evaluated: at this point, all the pairs which were successfully matched to reconstructed clusters are used to fill the  $E/E_{true}$  distribution.

The CC corrections are used to correct the energy of both photons from the decays of  $\pi^0$ 's. They must be obtained independently for the leading and trailing photons because their energy distributions are different due to the clustering algorithm, which intrinsically distinguishes the photons based on their  $p_T$  and does not allow the energy sharing between partially overlapped clusters.

For each cluster matched to a generator-level photon, the associated value of  $E/E_{true}$  is used to fill the distribution corresponding to each of the crystals forming the cluster, with a weight given by the fraction of the cluster's energy contained in that crystal. Figure A.14 shows the  $E/E_{true}$  distributions for the leading and trailing photons for some crystals in EB. One can observe that the distribution presents a pronounced peak at  $E/E_{true} < 1$ , with a tail on the left originating from the energy losses due to non perfect containment or the presence of gaps in the vicinity of the cluster.

The distribution associated to the second photon is characterized by a lower resolution and a bigger tail at low energy. This is a consequence of the absence of energy sharing between clusters: indeed, this feature penalizes the trailing photon, whose energy is absorbed by the cluster of the leading one.

The fit is performed using a Crystal Ball function with two tails, hereafter denoted as Double Crystal Ball (DCB). The DCB is defined as the convolution of a gaussian core and two exponential functions to better model the left and right tails. The mean of the gaussian component is used to measure the position of the peak. One might also exploit a gaussian function to fit the  $E/E_{true}$  distribution in a limited range around the peak. However, the DCB has more degrees of freedom to model the left and right side of the distribution, allowing for higher reliability and stability of the fit.

Events used to derive the CC are selected requiring the same criteria as in the calibration with data to ensure the consistency between the phase space where the CC are computed and the one on which they are applied. Due to the limited size of the simulated dataset after the selection, it was not possible to derive a correction for each crystal in EB. To overcome this limitation, the 36 EB supermodules were folded into a single one. This procedure relies on the fact the CC are mainly supposed to correct for geometrical effects (the presence of gaps between EB modular structures), which are invariant under translation of one supermodules into another. This approach results in a multiplication of the effective number of events available for each crystal by a factor 36. The distributions shown in A.14 are already derived after folding the supermodules.<sup>5</sup>

The CC folded in a single supermodules and their profile along the  $i\phi$  and  $i\eta$  for leading and trailing photons are shown in Fig. A.15. The measured CC are larger on crystals at the borders of the 4 modules, while they are nearly flat inside them. The fraction of lost energy is expected to be higher for the second photon and indeed the corresponding CC are larger. One should note that the CC also take into account the possible energy losses

<sup>5</sup>The folding is performed translating the supermodules belonging to the same sides of EB into a single supermodule, thus overlaying crystals with same  $i\eta$  and  $(i\phi - 1)\%20 + 1$ . On the other hand, supermodules belonging to different side of EB (EB+ and EB-) are superposed in such a way to overlay  $i\phi=1$  of one supermodules in EB+ to  $i\phi=20$  of a supermodule in EB- at constant  $|i\eta|$ , thus overlaying crystals with same  $(i\phi - 1)\%20 + 1$  in EB+ to those with  $(20 - i\phi)\%20 + 1$  in EB-. This arrangement complies with the topological structure of crystals arranged in EB+ and EB-, which are slightly tilted in opposite directions.

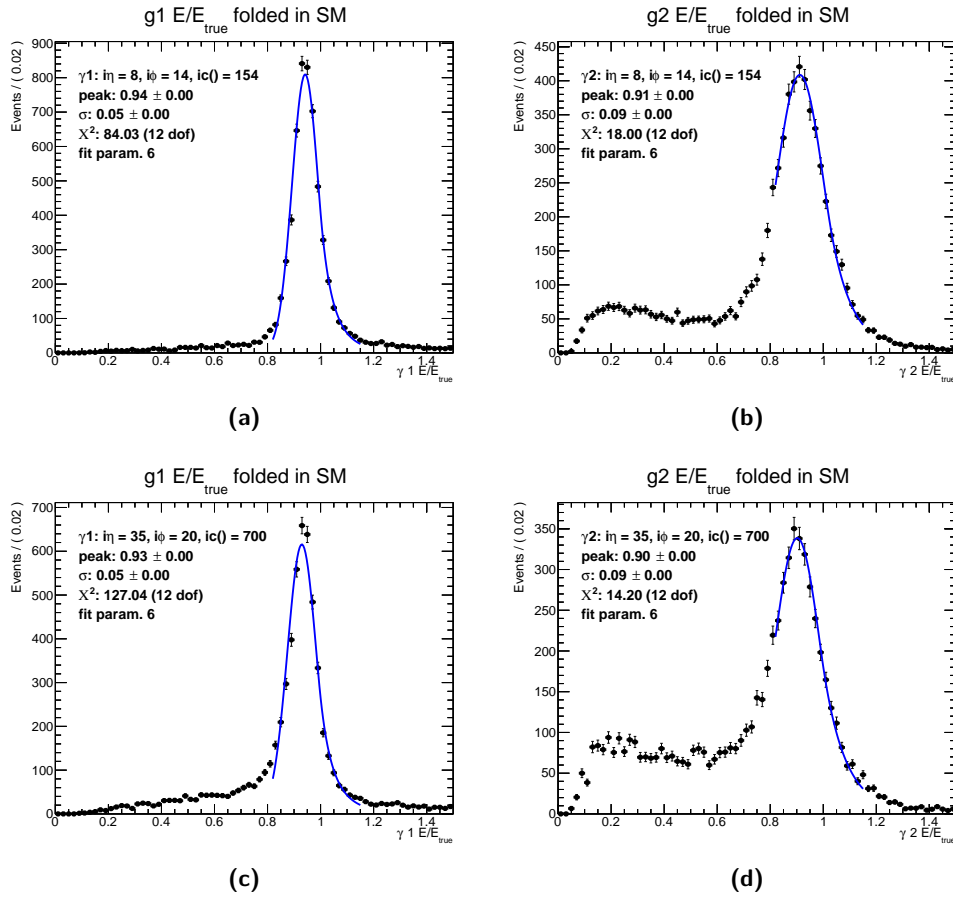


**Figure A.14.** Fits to the  $E/E_{true}$  distributions in two ECAL crystals, one in the first module of EB (top) at  $i\eta = 8$  and  $i\phi = 14$  (far from the borders of the module) and one in the second module (bottom) at  $i\phi = 35$  and  $i\eta = 20$  (at the border of the module). The plots on the left refers to the leading photons, those on the right are for the trailing photon. The fit is performed using a Crystal Ball function with two tails.

due to the ECAL ZS and SR algorithms, but the main purpose of these corrections is to compensate the losses in the gaps between modules. Moreover, the CC are not supposed to correct for the photon absolute energy scale: even though these corrections reflect into a better agreement on the measured and expected mass of a  $\pi^0$ , the IC made with  $\pi^0$ 's will not be used to correct the absolute ECAL energy scale. The ultimate goal of CC is to correct for the relative differences in the measured energy due to the geometry of the detector. The maps in Fig. A.15 demonstrates that this target is being met.

By definition, the  $E/E_{true}$  distributions obtained from a sample of events where the CC are already applied should have the mode at  $E = E_{true}$ . However, the photon energy is measured using the information from several crystals. Therefore, the  $E/E_{true}$  value that is used to fill the distribution for a specific crystal receives contributions from the surrounding crystals as well. This correlation reflects in the fact that a residual correction should be applied to make the mode of  $E = E_{true}$  really approach unity. Fig. A.16 presents the maps of CC at the second iteration, obtained after correcting the energy of crystals by the CC shown

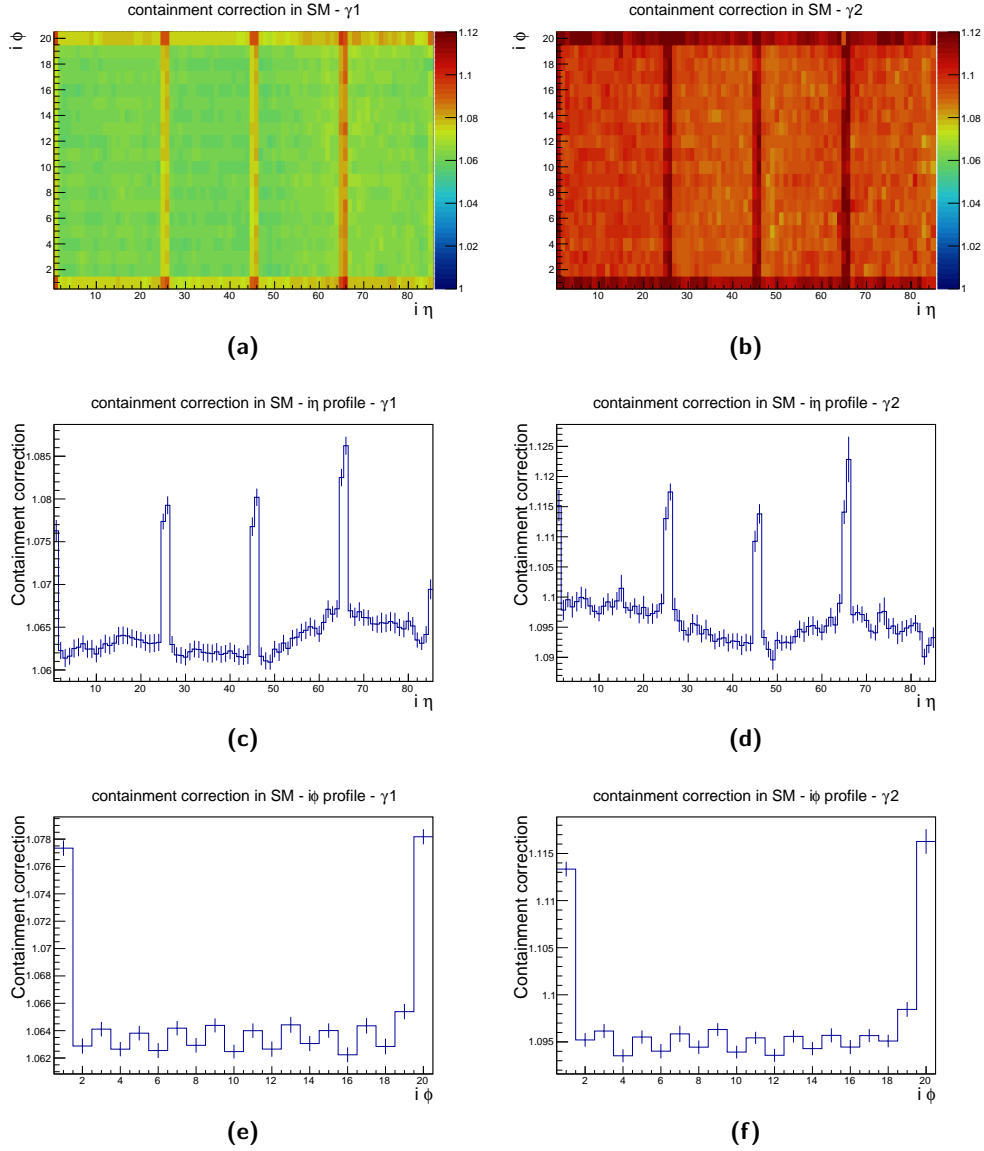


**Figure A.15.** Maps of containment corrections (CC) in EB, folded into a single supermodule for leading (left) and trailing (right) photons from decays of  $\pi^0$ 's in simulated events. The upper row shows the 2-dimensional maps with the CC as a function of  $i\eta$  and  $i\phi$ ; the central row shows the profile of the CC along  $i\eta$ ; the bottom row shows the profile of the CC along  $i\phi$ . The error bars in the profile plots represent the spread of the profiled CC along that corresponding direction. The measured CC are larger on crystals at the borders of the 4 modules, while they are nearly flat inside them. Note that CC are larger for the second photon, for which the fraction of lost energy is expected to be higher.

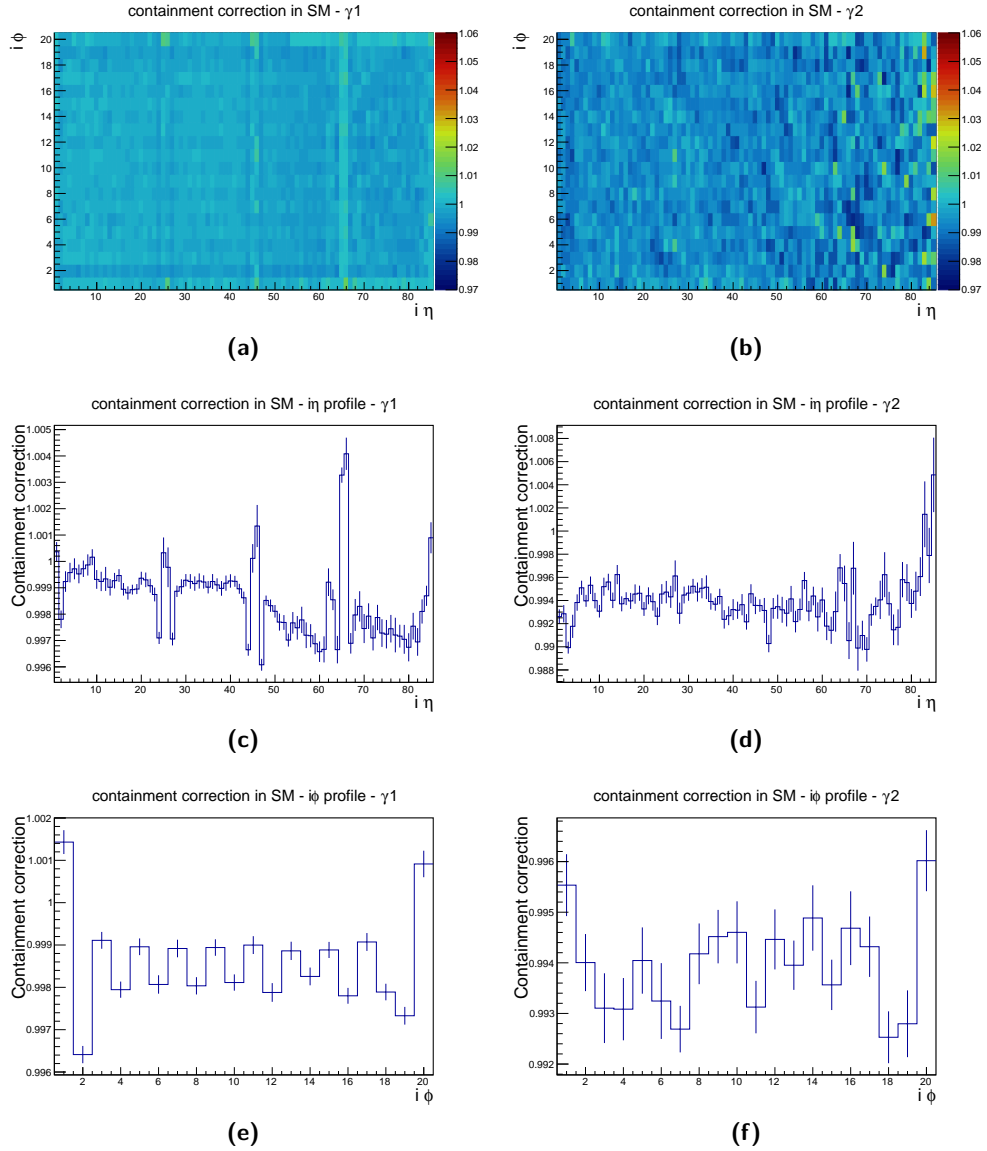


**Figure A.16.** Maps of containment corrections (CC) in EB, folded into a single supermodule for leading (left) and trailing (right) photons from decays of  $\pi^0$ 's in simulated events, computed on top of the CC shown in Fig. A.15. The upper row shows the 2-dimensional maps with the CC as a function of  $i\eta$  and  $i\phi$ ; the central row shows the profile of the CC along  $i\eta$ ; the bottom row shows the profile of the CC along  $i\phi$ . The error bars in the profile plots represent the spread of the profiled CC along that corresponding direction. The structures corresponding to the borders of modules are either removed or significantly reduced with respect to those in Fig. A.15.

in Fig. A.15. Regarding them, there are two consequences to be pointed out:

- the structures corresponding to the borders of modules are either removed or significantly reduced with respect to those in Fig. A.15
- there is still a global residual bias, which is generally below 0.5% and can be eliminated by computing further iterations of CC on top of this one.

Nonetheless, the residual bias in the CC was found to have no significant effect on the IC obtained in data. Indeed, a global scale in the IC constants is irrelevant for calibration, as they are eventually normalized to unity in each  $\eta$ -ring. In addition to that, the magnitude of the non-closure (i.e. the residual displacement from unity of the mode of the  $E = E_{true}$  distribution) is larger than the expected total uncertainty on the IC constants, which implies that the residual bias can safely be absorbed in the measured IC constants without the stringent need for further tuning of the CC.

Although the CC were successful in removing the bias of the borders in the final IC constants (as it will be shown in next section), it is worth pointing out that this approach has some limitations and drawbacks that are summarized as follows:

- a huge sample of simulated events is required in order to get a reliable correction for each crystal (even though the folding in supermodules already provides a multiplication factor of 36);
- simulations do not generally provide an exact representation of the dataset on which the CC will be applied: for example, the photon's kinematics, pileup distribution, SR thresholds or other time-dependent effects on the channels' response might be different between data and MC.

The second point can be partially mitigated by applying adequate reweighting of simulations in order to match the observed kinematic distributions in data. In spite of that, the correct treatment of other effects would still require an ad-hoc MC sample for each dataset on which the CC are supposed to be used (for example, to cope with the changes in the SR thresholds over different years of data taking). Nevertheless, the main effect to be corrected for originates from the geometrical structure of ECAL, which is well represented by simulation and is clearly not time-dependent.

#### A.4.8 Residual corrections

A set of IC constants was derived using the  $\pi^0$  method on a dataset of  $9.8 \text{ fb}^{-1}$  collected in 2017. This section is focused on EB, since the calibration of EE would require more data to minimize the impact of the statistical uncertainty<sup>6</sup>.

As already stated, CC were computed and applied to each channel to correct for the energy loss in the borders between modules. The IC constants obtained in this way were eventually normalized to unity in each  $\eta$ -ring. The corresponding IC map is shown in Fig. A.17a ( A.17b) before (after) the normalization to unity. The absolute IC constants in

<sup>6</sup>At the time of producing the IC constants for the calibration campaign on 2017 data (section A.5), there was no time to produce a new set of IC in EE with more data. Since the  $\pi^0$  method was expected not to drive the precision of the IC constants in EE with respect to other available methods, it was decided to focus more on the improvement of the calibration in EB, for which  $\pi^0$ 's have a significant impact.

the former map are lower than unity on average because of the CC, which over-correct the channels' energy, resulting in a measured  $\pi^0$  mass larger than the true one. Again, it should be stressed that the absolute IC constants do not have a particular physics meaning as far as the calibration is concerned: what really matters is the set of constants normalized to unity in  $\eta$ -rings.

In both cases, one can notice that there is no visible pattern related to the borders of modules and supermodules. However, a peculiar regular pattern is observed, which seems to follow the location of trigger towers (TT) in EB (for example, the blue squares in Fig. A.17a). As already mentioned, a TT in EB is a matrix of  $5 \times 5$  crystals and, in this respect, it should be pointed out that the blue squares visible in A.17a correspond to the 4 crystals around each of the four vertices of the  $5 \times 5$  matrix identifying a TT. The effect is induced by the SR thresholds: indeed, as detailed in section A.3.4, the SR selects crystals belonging to TT satisfying the criteria illustrated in table A.1. This implies that photons hitting ECAL in the center of TT have higher probability to survive the SR selection, provided that their energies satisfy the aforementioned criteria. On the other hand, photons which deposit their energy in several TT are more likely to be suppressed by the SR or to have less RecHits in the geometrical  $3 \times 3$  matrix used by the clustering algorithm to define them (see section A.4.2). Consequently, photons at borders of TT are generally reconstructed with lower energy, since part of it is not read out due to the SR. The effect is enhanced at the vertex of the TT, since the photon's energy is spread along more than two towers.

This might seem in contradiction with the observation that the IC constants are actually lower at the TT borders, which implies a larger invariant mass measured in those channels. However, one must keep in mind that while the SR induces a bias towards lower values in the energy of photons, the offline selection still requires that photons pass the criteria listed in table A.2, in particular the  $p_T$  thresholds. This means that only the most energetic photons among those hitting ECAL in the vicinity of TT borders will survive the full selection dictated by the SR and the offline requirements. Hence, the corresponding invariant mass is biased towards larger values and the IC constants are consequently lower.

This effect is more subtle than the one induced by the gaps between modules and cannot be easily corrected for using simulations. Indeed, in principle the CC should already make up for it, but actually it is not the case due to some underlying differences between simulated and real events which cannot be simply traced back to a geometrical origin. Therefore, a technique based on data was adopted to remove the bias induced by the SR, which consists in the following steps:

- take the map with the IC constants before they are normalized<sup>7</sup> (Fig. A.17a);
- normalize the constants to unity in each single module of each supermodule (Fig. A.17c) (this step is meant to avoid correcting for  $\eta$ -dependent effects in the following);
- fold the previous normalized map into a single supermodule, thus averaging the IC constants among crystals sharing the same position inside each supermodule (this is done separately for EB+ and EB- to avoid averaging effects which might differ between them due to their geometrical structure) and eventually replicate such map into the full EB, obtaining the one shown in Fig. A.17d, where all supermodules are equal by definition;

<sup>7</sup>It was actually observed that no significant difference is found in the final result if one starts from the normalized map shown in Fig. A.17b.



- finally, divide the map of IC normalized to unity in  $\eta$ -ring (Fig. A.17b) by the one obtained in the previous step and normalize it again to unity in each  $\eta$ -ring.

The method illustrated above relies on the assumption that the effect induced by the SR is symmetric under translations along supermodules. Therefore, the basic idea is to isolate the bias on the IC by averaging over different supermodules and remove it by means of the ratio. The main advantage of this procedure is that it does not rely on any external input and can be applied to any set of IC constants. The drawback is that it does not directly address the underlying source, but is rather an ad-hoc effective correction applied *a-posteriori* on the IC constants.

The outcome of this approach is the IC map in Fig. A.17e, where the initial bias that was visible in Fig. A.17b is substantially removed. These IC constants were combined with the results obtained with other calibration methods and contributed in the improvement of the ECAL energy resolution, as discussed in next section.

## A.5 Inter-calibration campaign using 2017 data

IC constants were derived using data collected in 2017 and exploiting all the methods described in section A.3.3. The IC constants were derived using  $9.8 \text{ fb}^{-1}$  for the  $\pi^0$  method, while all the available 2017 data (comprising about  $42 \text{ fb}^{-1}$ ) were used for the other methods based on electrons from Z and W bosons, so to reduce the statistical uncertainty that would otherwise limits the precision of such methods.

The IC constants obtained from the different methods were combined into a single set of IC constants. The combination reduces the total uncertainty on the final constants. The evaluation of the total uncertainty on each method in the combination is performed by solving a system of  $N$  equations, where  $N$  is the number of methods that have been used. Assuming uncorrelated uncertainty between different methods, one can write the system as

$$\begin{aligned}\sigma_{Zee}^2 + \sigma_{E/p}^2 &= \sigma^2(\text{IC}_{Zee} - \text{IC}_{E/p}) \\ \sigma_{Zee}^2 + \sigma_{\pi^0}^2 &= \sigma^2(\text{IC}_{Zee} - \text{IC}_{\pi^0}) \\ \sigma_{\pi^0}^2 + \sigma_{E/p}^2 &= \sigma^2(\text{IC}_{\pi^0} - \text{IC}_{E/p})\end{aligned}$$

where the right-hand-side is defined as the RMS of the difference of IC constants between any two methods. Solving the system eventually yields

$$\begin{aligned}\sigma_{Zee}^2 &= \frac{1}{2} [ \sigma^2(\text{IC}_{Zee} - \text{IC}_{E/p}) + \sigma^2(\text{IC}_{Zee} - \text{IC}_{\pi^0}) - \sigma^2(\text{IC}_{E/p} - \text{IC}_{\pi^0}) ] \\ \sigma_{E/p}^2 &= \frac{1}{2} [ \sigma^2(\text{IC}_{Zee} - \text{IC}_{E/p}) - \sigma^2(\text{IC}_{Zee} - \text{IC}_{\pi^0}) + \sigma^2(\text{IC}_{E/p} - \text{IC}_{\pi^0}) ] \\ \sigma_{\pi^0}^2 &= \frac{1}{2} [ -\sigma^2(\text{IC}_{Zee} - \text{IC}_{E/p}) + \sigma^2(\text{IC}_{Zee} - \text{IC}_{\pi^0}) + \sigma^2(\text{IC}_{E/p} - \text{IC}_{\pi^0}) ]\end{aligned}$$

where the left-hand-side is the total uncertainty on each method. The formulas above can be used to derive the IC precision as a function of  $i\eta$  or  $\eta$ -ring.

The precision reached by each calibration method in EB is shown in Fig. A.18. The precision obtained in the combination is better than 0.3% for  $|\eta| < 0.8$  and is lower than 1% in the rest of EB. The uncertainty on the IC constants provided by each method is generally dominated by systematic uncertainties, except at high  $\eta$ , where the worsening of

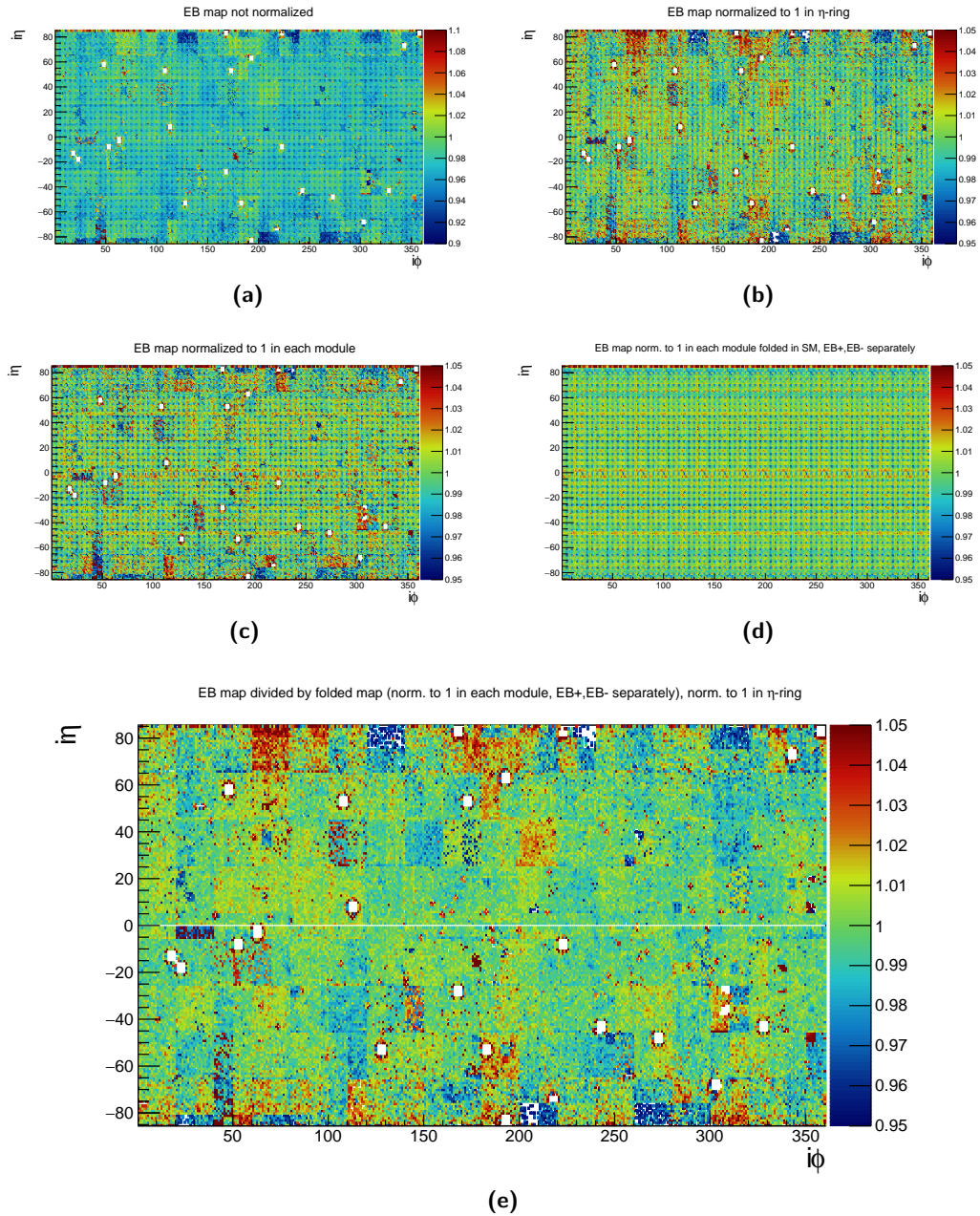


**Figure A.17.** Scheme of the application of the residual corrections on IC constants in EB to deal with the bias induced by the SR. Starting from the map of absolute IC constants (a), they are normalized to unity in each  $\eta$ -ring (b., In both cases a pattern is observed, which is correlated with the location of the trigger towers (TT). To remove it, the map in (a) is normalized to unity in each module (separately for each supermodule) obtaining the map in (c). This map is folded into a single supermodule (separately for EB+ and EB-) and then replicated back in each supermodule, resulting in (d). Eventually, the final IC map is obtained dividing the IC constants in (b) by those in (d), resulting in the map shown in (e). The latter was also normalized again to unity in each  $\eta$ -ring.

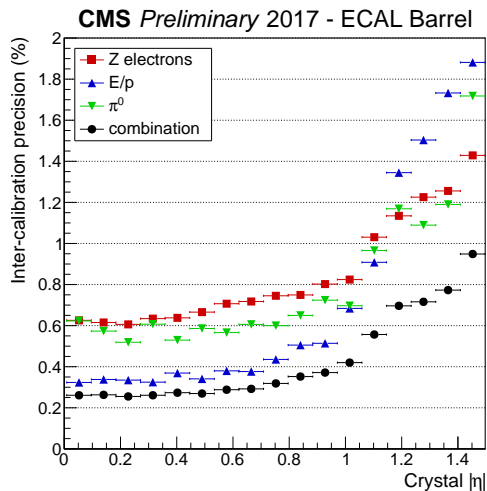


**Figure A.18.** Precision of the IC constants and their combination in EB. The  $Z \rightarrow ee$  method is mainly limited by the statistical uncertainty, while the precision of the  $\pi^0$  method suffers from larger systematic uncertainties. The  $E/p$  methods provides the best precision in the central EB, where a copious number of electrons is available and the amount of material upstream of ECAL is minimal. However, the precision of this method is significantly degraded at larger  $\eta$  due to the significantly lower size of the collected event sample and the substantial electron bremsstrahlung that spoils the measurement of electron momentum  $p$  with the tracker.

the precision (especially in the fourth module) originates mainly from the larger statistical uncertainty. For the  $E/p$  method, the significant loss of precision is also a consequence of the degradation of electron track resolution due to large bremsstrahlung, which is induced by the substantial amount of material upstream of ECAL. The  $\pi^0$  method reaches the lowest statistical uncertainty, ranging between 0.1% and 0.4% in EB (larger at higher  $\eta$ ) and about 1% in EE using less than  $10 \text{ fb}^{-1}$  of data. However, it is limited by larger systematic uncertainties due to energy containment and pileup with respect to other methods using electrons from decays of  $W$  and  $Z$  bosons.

The calibration based on the full 2017 data (except for the  $\pi^0$  method, as already stated) helped improve the electron energy resolution with respect to the calibration conditions available at the end of 2017. Figure A.19 shows the energy resolution for low and high bremsstrahlung electrons, as a function of electron pseudorapidity. The distinction between the two cases is based on the  $R_9$  variable defined in section A.3.1. The resolution is extracted from an unbinned likelihood fit to  $Z \rightarrow ee$  events, using a Voigtian (Landau convoluted with Gaussian) as the signal model. The observed resolution gets worse at higher  $\eta$  in EB due to the larger amount of material upstream of ECAL, although a general improvement bigger than 10% is observed in the entire acceptance region (the improvement is slightly lower for low  $R_9$  electrons, as the resolution is also affected by additional systematic uncertainties due to the emitted radiation). It can also be observed that it is degraded in the vicinity of the  $\eta$  cracks between ECAL modules (indicated by the vertical lines in the plot).

## A.6 Prospects for calibration of full Run II dataset

LHC will stop operations by the end of 2018 and enter a phase of upgrades during the so-called *Long-Shutdown 2*, preparing for the next Run II foreseen to start in 2021. During this period, CMS data collected during all Run II will be analyzed. To support this task, a new inter-calibration campaign is foreseen, involving all the data collected between 2016 and 2018.

All the methods already discussed in this chapter will be adopted to fulfill this commitment. Moreover, several additional improvements in the IC techniques will be scrutinized

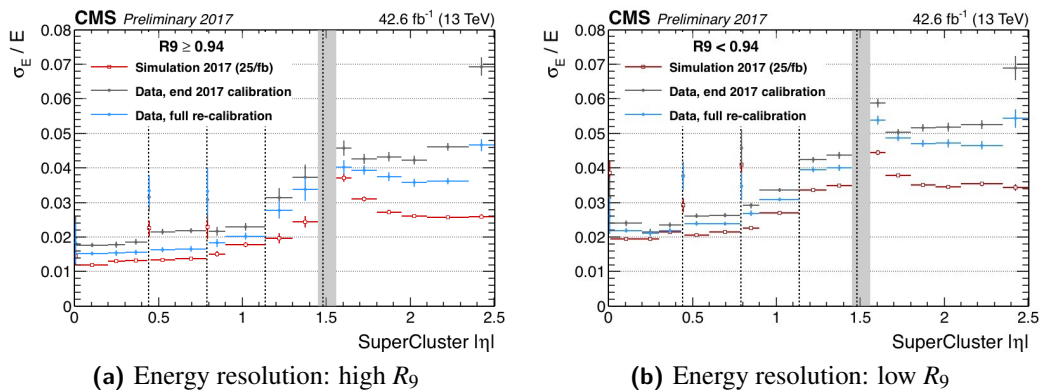


**Figure A.19.** Energy resolution measured from the invariant mass of electron pairs in  $Z \rightarrow ee$  events for low (left) and high (right) bremsstrahlung electrons. The resolution, which is generally better in the former case, is significantly improved after applying the calibration constants derived using the full 2017 dataset (blue dots) with respect to the conditions available at the end of 2017 (grey dots), for which only time dependent effects were corrected for. The ECAL conditions used in the simulation (red dots) reflect the status of the detector as predicted after  $25 \text{ fb}^{-1}$  of data taking in 2017. The vertical dotted bars indicate the borders between ECAL modules in EB, which induce a degradation of the observed resolution.

and studied in details, leading to even better performance in the reconstruction of electron and photons.

Among the expected improvements in the offline calibration, the  $\eta \rightarrow \gamma\gamma$  channel will complement the  $\pi^0$  method. Moreover, a general optimization of the  $\pi^0$  clustering algorithm will be studied as well. This might include the implementation of an energy sharing between overlapping cluster, or a further tuning of the photon selection. At the same time, the optimization of the performance of the dedicated  $\pi^0/\eta$  trigger system will be performed as well.

The calibration is extremely important to maintain the excellent energy resolution and guarantee the stability of the energy scale in all the ECAL. Compared to other calibration methods based on electrons from decays of Z and W bosons, the  $\pi^0$  method benefits from the copious production of  $\pi^0$  particles, which allows to calibrate the detector with higher spacial granularity and negligible statistical uncertainty.

Maintaining and possibly improving the excellent performance of ECAL is a paramount goal for the Higgs boson physics program. Indeed, electron and photons provide a clean experimental signature and allow the measurement of the properties of the Higgs boson with unprecedented precision. Moreover, they are fundamental ingredients to probe the possible existence of new heavy resonances with masses at the TeV scale and decaying into lepton or photon pairs. At the same time, ECAL also plays a key role in SM measurement regarding the properties of W and Z bosons. In turn, these measurements can help improve other analyses through a better understanding of the electroweak sector, as the production of weak bosons is the main source of irreducible backgrounds in searches for new physics.

# Bibliography

- [1] F. Englert and R. Brout, *Broken symmetry and the mass of gauge vector mesons*, *Phys. Rev. Lett.* **13**, (1964) 321; doi:10.1103/PhysRevLett.13.321.
- [2] G. S. Guralnik, C. R. Hagen, and T. W. B. Kibble, *Global conservation laws and massless particles*, *Phys. Rev. Lett.* **13**, (1964) 585; doi:10.1103/PhysRevLett.13.585.
- [3] P. W. Higgs, *Broken symmetries, massless particles and gauge fields*, *Phys. Lett.* **12**, (1964) 132; doi:10.1016/0031-9163(64)91136-9.
- [4] P. W. Higgs, *Broken symmetries and the masses of gauge bosons*, *Phys. Rev. Lett.* **13**, (1964) 508; doi:10.1103/PhysRevLett.13.508.
- [5] S.L. Glashow, *Partial Symmetries of Weak Interactions*, *Nucl.Phys.* **22**, (1961) 579.
- [6] M. Banner et al. [UA2 Collaboration], *Observation of single isolated electrons of high transverse momentum in events with missing transverse energy at the CERN  $p\bar{p}$  collider*, *Phys. Lett. B* **122**, (1983) 476.
- [7] G. Arnison et al. [UA1 Collaboration], *Experimental observation of lepton pairs of invariant mass around  $95 \text{ GeV}/c^2$  at the CERN SPS collider*, *Phys. Lett. B* **126**, (1983) 398.
- [8] ATLAS Collaboration, *Observation of a new particle in the search for the Standard Model Higgs boson with the ATLAS detector at the LHC*, *Phys.Lett.B* **716**, (2012) 1; doi:10.1016/j.physletb.2012.08.020
- [9] CMS Collaboration, *Observation of a new boson at a mass of  $125 \text{ GeV}$  with the CMS experiment at the LHC*, *Phys.Lett.B* **716**, (2012) 30; doi:10.1016/j.physletb.2012.08.021
- [10] CMS Collaboration, *Observation of a new boson with mass near  $125 \text{ GeV}$  in  $pp$  collisions at  $\sqrt{s} = 7$  and  $8 \text{ TeV}$* , *JHEP* **6**, (2013) 81; doi:10.1007/JHEP06(2013)081
- [11] CMS Collaboration, *The CMS experiment at the CERN LHC*, *JINST* **3**, (2008) S08004; doi:10.1088/1748-0221/3/08/S08004.
- [12] C. Patrignani et al. (Particle Data Group), *Chin. Phys. C*, **40**, 100001 (2016).
- [13] CDF and D0 Collaborations, *Combination of CDF and D0 W-Boson Mass Measurements*, *Phys. Rev. D* **88** (2013) 052018; arXiv:1307.7627 [hep-ex].
- [14] M. Baak et al., *The global electroweak fit at NNLO and prospects for the LHC and ILC*, *Eur. Phys. J. C* **74** (2014) 3046; arXiv:1407.3792 [hep-ph].

- [15] J. Haller et al., *Update of the global electroweak fit and constraints on two-Higgs-doublet models*, arXiv:1803.01853v1 [hep-ph] .
- [16] ATLAS Collaboration, *Measurement of the W-boson mass in pp collisions at  $\sqrt{s}=7\text{ TeV}$  with the ATLAS detector*, *Eur.Phys. J. C* **70** (2018) 110; doi:10.1140/epjc/s10052-017-5475-4
- [17] J. Haller, A. Hoecker, R. Kogler, K. Monig, T. Peiffer, J. Stelzer, *Update of the global electroweak fit and constraints on two-Higgs-doublet models*, *Eur.Phys.J.C* **78** (2018) 675; doi:10.1140/epjc/s10052-018-6131-3; arXiv:1803.01853v1 [hep-ph].
- [18] CMS Collaboration, *W-like measurement of the Z boson mass using dimuon events collected in pp collisions at  $\sqrt{s} = 7\text{ TeV}$* , CMS-PAS-SMP-14-007, CERN, Geneva, 2016, <http://cds.cern.ch/record/2139655>.
- [19] H1 and ZEUS Collaboration, *Deep inelastic scattering at HERA*, *Acta Phys. Polon. Supp.* **6**, (2013) 709.
- [20] Jonathan Pumplin et al., *New generation of parton distributions with uncertainties from global QCD analysis*, *JHEP* **07**, (2002) 12; arXiv:0201195 [hep-ph].
- [21] R. D. Ball et al., *Parton distributions with LHC data*, *Nucl.Phys.B* **867**, (2013) 244; doi:10.1016/j.nuclphysb.2012.10.003.
- [22] V. N. Gribov, L. N. Lipatov, *Deep inelastic e-p scattering in perturbation theory*, *Sov. J. Nucl. Phys* **15**, (1972) 438.
- [23] Y. L. Dokshitzer, *Calculation of the structure functions for deep inelastic scattering and  $e^+e^-$  annihilation by perturbation theory in quantum chromodynamics*, *Sov. Phys. JETP* **46**, (1977) 641.
- [24] G. Altarelli and G. Parisi, *Asymptotic freedom in parton language*, *ucl. Phys. B* **126**, (1977) 298.
- [25] S. Carrazza, S. Forte, Z. Kassabov, J. I. Latorre, J. Rojo, *An Unbiased Hessian Representation for Monte Carlo PDFs*, *Eur. Phys. J. C* **75**, (2015) 369, arXiv:1505.06736v3 [hep-ph].
- [26] E. Mirkes, *Angular decay distribution of leptons from W bosons at NLO in hadronic collisions*, *Nucl.Phys.B* **387**, (1992) 3.
- [27] J. C. Collins, D. E. Soper and G. F. Sterman, *Transverse Momentum Distribution in Drell-Yan Pair and W and Z Boson Production*, *Nucl. Phys. B* **250**, (1985) 199.
- [28] G. A. Ladinsky and C. P. Yuan, *The Nonperturbative regime in QCD resummation for gauge boson production at hadron colliders*, *Phys. Rev. D* **50**, (1994) R4239; arXiv:9311341 [hep-ph].
- [29] C. Balazs and C. P. Yuan, *Soft gluon effects on lepton pairs at hadron colliders*, *Phys. Rev. D* **56**, (1997) 5558; arXiv:9704258 [hep-ph].
- [30] S. Catani et al., *Vector boson production at hadron colliders: transverse-momentum resummation and leptonic decay*, *JHEP* **12**, (2015) 047; arXiv:1507.06937 [hep-ph].

- [31] T. Becher, M. Neubert and D. Wilhelm, *Electroweak Gauge-Boson Production at Small  $q_T$ : Infrared Safety from the Collinear Anomaly*, *JHEP* **02**, (2012) 124; arXiv:1109.6027 [hep-ph].
- [32] E. Manca, O. Cerri, N. Foppiani, G. Rolandi, *About the rapidity and helicity distributions of the  $W$  bosons produced at LHC*, *JHEP* **12**, (2017) 130; arXiv:1707.09344v2 [hep-ex].
- [33] H1 and ZEUS Collaborations, *Combination of measurements of inclusive deep inelastic  $e^\pm p$  scattering cross sections and QCD analysis of HERA data*, *Eur. Phys. J. C* **75**, (2015) 580; arXiv: 1506.06042 [hep-ex].
- [34] ATLAS Collaboration, *Studies of theoretical uncertainties on the measurement of the mass of the  $W$  boson at the LHC*, ATL-PHYS PUB-2014-015 (2014); <https://cdsweb.cern.ch/record/1956455>.
- [35] J. C. Collins and D. E. Soper, *Angular distribution of dileptons in high-energy hadron collisions*, *Phys. Rev. D* **16**, (1977) 2219; doi:10.1103/PhysRevD.16.2219.
- [36] R. Ellis, W. Stirling, B. Webber, *QCD and collider physics*, *Camb. Monogr. Part. Phys. Nucl. Phys. Cosmol.* **8**, (1996) 1.
- [37] S. van der Meer, *Calibration of the effective beam height in the ISR*, Technical Report, CERN-ISR-PO-68-31. ISR-PO-68-31, CERN, Geneva, 1968.
- [38] S. Dasu et al., *The TriDAS project. Technical design report, vol. 1: The trigger systems*, 2000.
- [39] CMS Collaboration, *Particle-Flow Event Reconstruction in CMS and Performance for Jets, Taos, and MET*, *Tech. Rep.* CMS-PAS-PFT-09-001, CERN, 2009. Geneva, Apr 2009.
- [40] CMS Collaboration, *Description and performance of track and primary vertex reconstruction with the CMS tracker*, *JINST* **9**, (2014) P10009; arXiv:1405.6569; doi:10.1088/1748-0221/9/10/P10009.
- [41] W. Adam, R. Frühwirth, A. Strandlie, and T. Todorov, *Reconstruction of Electrons with the Gaussian-Sum Filter in the CMS Tracker at the LHC*, *J. Phys. G* **31**, (2005) N9; <http://dx.doi.org/10.1088/0954-3899/31/9/N01>.
- [42] M. Cacciari, G. Salam, and G. Soyez, *The anti- $k_t$  jet clustering algorithm*, *JHEP* **08**, (2008) 063; arXiv:0802.1189; doi:10.1088/1126-6708/2008/04/063.
- [43] CMS Collaboration, *CMS luminosity measurements for the 2016 data taking period*, Physics Analysis Summary CMS-PAS-LUM-17-001.
- [44] J. Alwall, R. Frederix, S. Frixione, V. Hirschi, F. Maltoni, O. Mattelaer, H.-S. Shao, T. Stelzer, P. Torrielli, M. Zaro, *The automated computation of tree-level and next-to-leading order differential cross sections, and their matching to parton shower simulations*, *JHEP* **07**, (2014) 079; arXiv:1405.0301v2 [hep-ph].

- [45] T. Sjöstrand, S. Mrenna, and P. Skands, *A Brief Introduction to PYTHIA 8.1*, *Comput. Phys. Commun.* **178**, (2008) 852; arXiv:0710.3820v1 [hep-ph].
- [46] J. Alwall et al., *MadGraph/MadEvent v4: The New Web Generation*, *JHEP*, **09**, (2007) 028; arXiv:0706.2334v1 [hep-ph].
- [47] S. Alioli, P. Nason, C. Oleari, and E. R., *NLO single-top production matched with shower in POWHEG: s- and t-channel contributions*, *JHEP* **09**, (2009) 111; doi:10.1007/JHEP02(2010)011
- [48] S. Agostinelli et al., *GEANT4: A Simulation toolkit*, *Nucl. Instrum. Meth. A*, **506**, (2003) 250.
- [49] CMS Collaboration, *Electron and Photon performance in CMS with the full 2017 data sample and additional 2016 highlights for the CALOR 2018 Conference*, CMS-DP-2018-017; <https://cds.cern.ch/record/2320638>.
- [50] CMS Collaboration, *Performance of electron reconstruction and selection with the CMS detector in proton-proton collisions at  $\sqrt{s} = 8$  TeV*, *JINST* **10** (2015) P06005; doi:10.1088/1748-0221/10/06/P06005.
- [51] M. Cacciari, G. P. Salam, *Pileup subtraction using jet areas*, *Phys. Lett. B* **659**, (2008) 119; doi:10.1016/j.physletb.2007.09.077.
- [52] M. Oreglia, *A study of the reactions  $\psi' \rightarrow \gamma\gamma\psi$* , Ph.D. Thesis, Stanford University, (1980), SLAC Report SLAC-R-236, <http://www.slac.stanford.edu/pubs/slacreports/slac-r-236.html>.
- [53] CMS Collaboration, *Performance of CMS muon reconstruction in pp collision events at  $\sqrt{s} = 7$  TeV*, *JINST* **7**, (2012) P10002; doi:10.1088/1748-0221/7/10/P10002; arXiv:1206.4071.
- [54] M. Abadi et al., *TensorFlow: Large-scale machine learning on heterogeneous systems*, <https://www.tensorflow.org/about/bib>; TensorFlow official web page: <https://www.tensorflow.org/>.
- [55] F. James, *MINUIT: Function Minimization and Error Analysis Reference Manual*, CERN document server, <https://cdsweb.cern.ch/record/2296388/>.
- [56] G. Cowan, K. Cranmer, E. Gross, O. Vitells, *Asymptotic formulae for likelihood-based tests of new physics*, *Eur. Phys. J. C* **71**, (2011) 1554; arXiv:1007.1727v3 [physics.data-an].
- [57] R. Barlow, C. Beeston, *Fitting using finite Monte Carlo samples*, *Comp. Phys. Comm* **77**, (1993) 219; doi:10.1016/0010-4655(93)90005-W.
- [58] CMS Collaboration, *Measurement of the differential cross section and charge asymmetry for inclusive  $pp \rightarrow W^\pm + X$  production at  $\sqrt{s} = 8$  TeV*, *Eur. Phys. J. C* **76**, (2016) 469; doi:10.1140/epjc/s10052-016-4293-4.
- [59] ATLAS Collaboration, *Measurement of the W charge asymmetry in the  $W \rightarrow \mu\nu$  decay mode in pp collisions at  $\sqrt{s} = 7$  TeV with the ATLAS detector*, *Phys. Lett. B* **701**, (2011) 31; arXiv:1103.2929v1 [hep-ex].



- [60] S. Chatrchyan et al. [CMS Collaboration], *Energy calibration and resolution of the CMS electromagnetic calorimeter in pp collisions at  $\sqrt{s} = 7$  TeV*, *JINST* **8**, P09009 (2013); arXiv:1306.2016v2 [hep-ex].
- [61] CMS Collaboration, *CMS: The electromagnetic calorimeter. Technical design report*, CERN-LHCC-97-33, CMS-TDR-4.
- [62] V. Khachatryan et al. [CMS Collaboration], *Observation of the diphoton decay of the Higgs boson and measurement of its properties*, *Eur. Phys. J. C* **74**, (2014) 3076; arXiv:1407.0558v2 [hep-ex].
- [63] S. Chatrchyan et al. [CMS Collaboration], *Measurement of the properties of a Higgs boson in the four-lepton final state*, *Phys. Rev. D* **89**, 092007 (2014); arXiv:1312.5353v3 [hep-ex].
- [64] P. Adzic et al., *Reconstruction of the signal amplitude of the CMS electromagnetic calorimeter*, *Eur. Phys. J. C* **C46S1** (2006) 26.
- [65] E. Di Marco [CMS Collaboration], *CMS electromagnetic calorimeter calibration and timing performance during LHC Run I and future prospects*, CMS-CR-2014-410 (2014); <http://cds.cern.ch/record/1975982>.
- [66] CMS Collaboration, *Validation of 2015 laser corrections with electrons*, CMS-DP-2015-065 (2015); <https://cds.cern.ch/record/2116255>
- [67] CMS Collaboration, *CMS ECAL with 2017 data*, CMS-DP-2018-015 (2018); <https://cds.cern.ch/record/2319285>
- [68] S. Chatrchyan et al. [CMS Collaboration], *Energy calibration and resolution of the CMS electromagnetic calorimeter in pp collisions at  $\sqrt{s} = 7$  TeV*, *JINST* **8**, P09009 (2013); arXiv:1306.2016v2 [hep-ex].
- [69] N. Almeida et al., *Data filtering in the readout of the CMS Electromagnetic Calorimeter*, *JINST* **3**, P02011 (2008); <https://doi.org/10.1088/1748-0221/3/02/P02011>